



Methane Emissions in Kuwait: Plume Identification, Isotopic Characterisation & Inventory Verification

A thesis submitted for the degree of Doctor of
Philosophy at the University of London

Aliah AlShalan

Department of Earth Sciences,
Royal Holloway, University of London

June, 2019

Declaration of Authorship

I hereby confirm that this thesis and the work presented in it is entirely my own.
Where I have consulted the work of others, this has been clearly stated.

Signed:

Date:

Abstract

National and EDGAR inventories suggest that the dominant sources of methane in Kuwait are leaks from gas flaring and distribution, with additional smaller emissions from landfills, sewage (wastewater) treatment and ruminant animals. In 2012 it was considered by the US EPA to be one of the top global emitters. New measurements during 2015 and 2016 suggest that the inventories differ greatly from observations.

Regular weekly bag samples have been collected from 3 sites in Kuwait, one NW of the city, one to the SE and one in the city from the rooftop of Kuwait College of Science. These take turns to have the highest recorded mole fractions, depending on wind direction. Associated with higher mole fraction is a consistent depletion in ^{13}C of methane, pointing to a national source mix with $\delta^{13}\text{C}$ of -55.9‰ . This is significantly different from the calculation using inventories that suggest a source mix ranging from -52.0 to -50.3‰ .

Mobile plume identification using a Picarro G2301 analyser, coupled with Tedlar bag sampling for isotopic analysis, reveals that by far the largest observed source of methane in Kuwait is from landfill sites ($\delta^{13}\text{C}$ of -58‰), with smaller contributions from fossil fuel industry (-50‰), wastewater treatment (-49‰) and ruminant animals (cows, -62‰ ; camels -60‰ , sheep -64‰).

Many of these isotopic signatures are close to those observed for the same source categories in other countries, for example landfill emission signatures have the same range as those calculated for UK and Hong Kong (-60 to -55‰), even to the level that older closed and capped landfills emit smaller amounts of methane at more enriched values (-55 to -50‰), due to small % of topsoil oxidation.

The isotopic mass balance and mobile observations suggest that the inventories, particularly EDGAR, are in error and that the main source of methane, following significant reductions in methane flaring and venting by Kuwait Oil Company (KOC) in recent years, are biogenic sources, mainly landfill. Our findings suggest that many more top down measurements must be made to verify emissions inventories, particularly in Middle Eastern countries where a significant proportion of emissions are unverified calculations of fossil fuel emissions.

***T**o THE SOUL OF MY*

***F**ATHER*

Acknowledgement

I would like to express my deepest sincere gratitude to my supervisors Dr. Dave Lowry, Dr. Rebecca Fisher and Prof. Euan Nisbet for the guidance, encouragement and advice they have provided throughout the period of this Ph.D. Special thanks are dedicated to my advisor Dr. Natalie Grassineau for her great help and advice. Also, thanks to my supervisor Prof. Mohammed Al-Sarawi, Department of Earth and Environmental Sciences, Kuwait University for his great help and support during the Kuwait campaign.

This project was partially funded by the Kuwait Foundation for the Advancement of Sciences (KFAS) under project code “P115-64SC-01”. KFAS is thanked for the Kuwait campaign grant that forms a significant part of this research.

I would specially like to thank the member of the National Assembly of Kuwait Council, Mr. Abdallah Al-Kandari for his great assistance and moral support throughout the period of this Ph.D.

Special thanks go to the personnel of Atmospheric Group at RHUL, for their endless support and help. Without a particular order Dr. Giulia Zazzeri, Dr. Rebecca Brownlow, Dr. James France and Mr. Mathias Lanoisellé are particularly thanked for their assistance in the use of software and all instruments in the Greenhouse Atmospheric Laboratory at RHUL. Dr. Giulia Zazzeri is also thanked for her help during the Kuwait Campaign.

My deep thanks also go out to Noora Al-Bannay, Anil Ganti, and Shafi Trumboo, Environmental Monitoring Information Systems of Kuwait (eMISK), Environmental Public Authority of Kuwait (EPA) for providing necessary maps used in this research.

Thanks to Eng. Salah Al-Ansari, Metrological Department, State of Kuwait for providing all the meteorological data. Sausan Khader, Department of Earth and Environmental Sciences, Kuwait University and Eng. Ala'a Esmail, Kuwait Institute for Scientific Research (KISR) are acknowledged for their great assistance with field sampling.

Teaching and support staff members of Earth Science Department, Royal Holloway, University of London are thanked for their help.

Last but not the least, I would like to deeply thank my mother, brothers and sisters, without whom I would not have the encouragement to complete this journey.

Contents

<i>Abstract</i>	I
<i>Acknowledgements</i>	IV
<i>Contents</i>	VI
<i>List of Figures</i>	XI
<i>List of tables</i>	XXII
Chapter 1. Introduction	1
1.1 Methane's Role as a Greenhouse Gas	3
1.2 The State of Kuwait: Study Area	4
1.3 Previous Studies of Methane Emissions in Kuwait	5
1.4 Greenhouse Gas Emission Inventory of Kuwait	7
1.5 Research Aims and Objectives	8
1.6 Thesis Outline	10
Chapter 2. Methane: Literature Review	12
2.1 Sources of Atmospheric Methane	13
2.1.1 Biogenic sources	15
2.1.2 Thermogenic sources	15
2.1.3 Pyrogenic sources	15
2.2 Sinks of Atmospheric Methane	16
2.2.1 Atmospheric methane sink	16
2.2.2 Soil methane sink	17
2.3 Quantifying Atmospheric Methane Budget	18
2.3.1 Bottom-up estimate	19
2.3.2 Top-down estimate	19
2.3.3 Comparisons of bottom-up and top-down estimates	20
2.4 Global Growth of Methane	21
2.5 Global Methane Emissions	25
2.5.1 Methane from natural sources	25
• Wetlands	26
• Hydrates	26
• Termites	27
• Geological sources	27
• Other natural sources	28

2.5.2 Methane from anthropogenic sources	28
• Rice cultivation	29
• Biomass burning	29
• Fossil fuels	30
• Solid waste disposal and landfill	31
• Sewage Rice	32
• Enteric fermentation: ruminants	33
• Manure management	34
2.6 Isotopic Analysis of Methane Sources	35
Chapter 3. Methodology	39
3.1 Sample Collection	39
3.1.1 Kuwait sampling campaign	41
3.2 Sample Analysis	42
3.2.1 Picarro Mobile System	42
• <i>Instrument calibration</i>	45
3.2.2 Royal Holloway University of London Atmospheric Laboratory	48
• Measurement of methane concentration: Picarro Cavity Ring-Down spectrometer	48
• <i>Instrument calibration</i>	50
• Isotope measurement techniques: Continuous Flow Gas Chromatography Isotope Ratio Mass Spectrometry	51
• <i>Instrument performance</i>	53
• <i>Instrument calibration</i>	55
3.3 Data Analysis	56
3.3.1 Keeling Plot approach	56
3.3.2 Miller-Tans approach	59
• Regression and error	60
3.3.3 Methane concentration maps and mole fraction plots	61
3.3.4 Openair application	62

Chapter 4: Kuwait Natural Gas Analysis: Fossil Fuel Production and Use	64
4.1 Oil Fields in Kuwait	64
4.1.1 Oil operation facilities	66
4.1.2 Gas operation facilities	66
4.1.3 Oil production	67
4.1.4 Gas flaring	68
4.1.5 Materials and Methods	69
4.2 Kuwait Refineries	74
4.2.1 Surveys of the three refineries	76
4.3 Al-Ahmadi Town	84
4.3.1 Surveys of Al-Ahmadi Town	86
4.3.2 Isotopic signature for Kuwait natural gas	91
4.4 Discussion	92
4.5 Fuel Combustion Emissions from Vehicles	98
4.6 Summary	100
Chapter 5: Analysis of Methane Emissions from Kuwait Landfill Sites	101
5.1 Landfill Methane Emissions	101
5.2 Landfill Sites in Kuwait	102
5.3 Kuwait Campaign	106
5.3.1 Al-Jahra landfill	110
5.3.2 The South 7 th Ring Road Landfill	112
5.3.3 Mina Abdullah Landfill	117
5.3.4 Kead (Construction) landfill	119
5.3.5 The Al-Sulaibiya landfill	120
5.3.6 Al-Qurain landfill	123
5.3.7 Jleeb Al-Shuyoukh landfill	127
5.4 Discussion	131
5.5 Summary	135
Chapter 6: Sewage Treatment	137
6.1 Kuwait Wastewater Treatment Plant	137
6.1.1 Primary treatment	138

6.1.2 Secondary treatment	139
6.1.3 Tertiary treatment	140
6.1.4 Sludge processing	141
6.2 Rigaa Wastewater Treatment Plant	141
6.2.1 4 th May 2015	145
6.2.2 7 th January 2016	145
6.2.3 7 th March 2017	145
6.3 KM30 Industrial Wastewater Plant	147
6.3.1 5 th May 2015	148
6.4 Umm Al-Hyman sewage Treatment Plant	149
6.4.1 17 th March 2017	150
6.5 Discussion	154
6.6 Summary	155
Chapter 7: Ruminants	156
7.1 Cows	158
7.2 Sheep	161
7.3 Camels	162
7.4 Discussions of Ruminants Emissions	164
7.4.1 Ruminants eructation	165
7.4.2 Ruminants rumen	165
7.4.3 Sampling technique	165
7.5 Summary	169
Chapter 8: Ambient Methane Measurements in Kuwait: Long Term Study	170
8.1 Long-Term Methane Measurements	171
8.2 Backward Trajectories	172
8.3 Air Sampling Sites	175
8.3.1 Al-Mutla site	184
8.3.2 Khaldiya site	186
8.3.3 Fahaheel site	188
8.4 Miller-Tans Plots	190
8.5 Diurnal Measurements in Al-Rabya	192
8.5.1 5 th – 6 th January 2016	194
8.5.2 18 th – 19 th July 2016	196

8.5.3 17 th – 18 th October 2016	198
8.6 Summary	200
Chapter 9: Discussion	202
9.1 Kuwait Methane Measurements Comparison with NOAA Baseline Observatories	202
9.2 Satellite Observation of Atmospheric Methane	205
9.3 Evaluation of the EDGAR Emissions Database for Kuwait	210
9.4 Kuwait Inventory by Kuwait EPA	215
9.5 Verification of Inventories	216
Chapter 10: Conclusions	221
10.1 Key Findings	221
10.2 Recommendations for Future Studies and Mitigations of Methane Emissions in the Middle East	223
References	224
Appendices	258

List of Figures

Figure 1.1 Total annual anthropogenic greenhouse gas (GHG) emissions for the period 1970 to 2010. IPCC, 2014	2
Figure 1.2 Kuwait State located in the Northeast end of the Arabian Peninsula. Source: Emisk.com, 2018.	5
Figure 2.1 SCIAMACHY Satellite map for period 2003 to 2005, shows the variation in methane column average mixing ratio for the Northern Hemisphere and the Southern Hemisphere. Source: IUP.uni-bremen.de.	13
Figure 2.2 Global methane sources and sinks for the period 2000 to 2009. Source: Ciais et al. 2013	18
Figure 2.3 Global growth of methane in the atmosphere for the last three and half decades. Source: https://www.esrl.noaa.gov/gmd/ccgg/gallery/figures/index.html	22
Figure 2.4 Methane growth rate (ppb y ⁻¹) by latitude for the period 2002 to 2018, showing the post-2007 global methane rise. Source: https://www.esrl.noaa.gov/gmd/ccgg/gallery/figures/index.html	24
Figure 2.5 3D representation of the latitudinal distribution of atmospheric methane in the boundary layer for the period 2008 to 2017. Source: https://www.esrl.noaa.gov/gmd/ccgg/gallery/figures/index.html	25
Figure 2.6 Isotopic ranges of $\delta^{13}\text{C}$ for CH_4 for a variety of natural and anthropogenic CH_4 sources. source: France et al, 2016.	37
Figure 2.7 Characterization plot of $\delta^{13}\text{C}\text{-CH}_4$ versus $\delta^2\text{H}\text{-CH}_4$ showing the distribution of methane sources. Source: Sherwood et al, 2017	38
Figure 3.1 show the sampling method (Tedlar bag and battery-operated diaphragm pump)	40
Figure 3.2 Air sampling in Al-Mutla area, Kuwait.	41
Figure 3.3 GIS plot of methane mole fractions in ppm recorded for 2 nd to 7 th May 2015 showing the route of the 6-days of surveys in Kuwait.	42
Figure 3.4 shows A) Schematic set up of the RHUL Picarro mobile measurement system and all the physical connections by (Zazzeri et al. 2015) B) Vehicle used in the Kuwait sampling campaign	43

List of Figures

Figure 3.5 shows the Picarro mobile measurement system set up in this study	44
Figure 3.6 show the calibrated against measured values of CH ₄ for three standard tanks measured before and after the Kuwait campaign using the Picarro mobile system.	46
Figure 3.7 Google Earth view of methane plumes detected around Al-Qurain landfill on 4 th of May 2015. The high peak of CH ₄ is 11.45 ppm.	47
Figure 3.8 show the G1301 Picarro CRDS (Cavity Ring-Down Spectroscopy) analyser at the RHUL Atmospheric Laboratory connected to three international standard air cylinders for calibration.	50
Figure 3.9 Picarro 1301 CRDS Target values from 2015 to 2017 at RHUL	51
Figure 3.10 Trace Gas preconcentrator coupled with IsoPrime mass spectrometer.	52
Figure 3.11 Schematic of the Trace Gas in the CH ₄ analysis set-up. Black arrows indicate direction of flow of helium and the air sample during CH ₄ analysis. Grey arrows show the default helium flow between analyses (Fisher et al., 2006).	52
Figure 3.12 Graphical illustration of the Keeling plot method From Pataki et al,2003	58
Figure 3.13 Miller-Tans plot based on all the isotopic values measured and the background values for each season in this study. Further detail in chapter (8).	60
Figure 3.14 Shows an example of A) Polar plot for the methane mole fraction and B) Pollution Rose for the measurement $\delta^{13}\text{C}$ values by using the Openair application (http://www.openair-project.org).	63
Figure 4.1 The Oil Fields in the state of Kuwait (source from eMISK,2018).	65
Figure 4.2 Oil production from 2012/2013 to 2015/2016	67
Figure 4.3 KOC gas flaring reduction over the years (Ibrahim, 2015)	68

List of Figures

Figure 4.4 shows Kuwait natural gas production during 2000 to 2010 (www.eia.gov)	69
Figure 4.5 Samplings were collected from (A) an active rig and (B) low pressure flare facilities at ground level in the oil fields of Kuwait.	70
Figure 4.6 Google map showing the location of the air samples in Sabriyah and Ar-Raudhatain in North Kuwait City on 7 th of March and 27 th of October 2016. Pushpins represent samples locations with different mole fractions and yellow square represent the gathering center (GC) and green square booster.	71
Figure 4.7 Kuwait National Petroleum Company (KNPC) refineries: Mina Al-Ahmadi (MAA), Mina Abdullah (MAB) and Shuaiba (SHU). (Source Emisk, 2018)	74
Figure 4.8 Methane mole fractions of the intersected plumes during the survey on 5 th May 2015 downwind of the refineries. Red series represents the North to South route at 8:33 - 8:37 am (GMT) and the Blue series represents South to North route at 8:41 - 8:46 am (GMT)	77
Figure 4.9 ArcGIS plot of CH ₄ mole fraction recorded downwind of the refineries on 5 th May 2015. (1) Mina Al-Ahmadi (MAA), (2) Mina Abdullah (MAB) and (3) Shuaiba (SHU) Yellow pushpins represent the air samples locations and red arrow indicates the wind direction (ESE)	78
Figure 4.10 Google Earth view of methane mole fraction columns measured along the King Abdul-Aziz Highway downwind the refineries and the two main methane plumes were detected will discussed in following figures. Black arrow indicates the wind direction.	79
Figure 4.11 ArcGIS plot of CH ₄ mole fractions in ppm recorded on 6 th May 2015 downwind of refineries and two main methane plumes were detected. (1) Mina Al-Ahmadi (MAA), (2) Mina Abdullah (MAB) and (3) Shuaiba (SHU). Yellow pushpins represent the air sampling locations and red arrow indicates the wind direction.	80
Figure 4.12 Methane mole fractions of the repeated plume intersection during the survey on 6 th May 2015, downwind of the refineries. Red series represents the North to South route at 12:30 – 12:33 pm (GMT) and the Blue series represents South to North route at 12:54 – 12:57 (GMT), Black arrow indicates the wind direction. A) before the time lag correction; B)	

List of Figures

After time lag correction. The peak represents multiple measurements recorded when the vehicle was stopped to collect samples.	81
Figure 4.13 Methane mole fractions of the repeated plume intersect during the survey on 6 th May 2015, downwind of the refineries. Red series represent the North to South route at 12:34 - 12:39 am (GMT) and the Blue series represents South to North route at 12:47 to 12:54 am (GMT), Black arrow is the wind direction. A) Before the time lag correction; B) After time lag correction.	82
Figure 4.14 Keeling plot based on samples collected downwind of the three refineries on 6 th May 2015	83
Figure 4.15 Map shows the three main explosions that occurred in 2010, (Alkhaledi et al. 2015)	84
Figure 4.16 Al-Ahmadi ridge zone with north (NTF) and south tank farms (STF). Reference:(Alkhaledi et al. 2015)	85
Figure 4.17 Google Earth view of methane mole fraction columns measured along the public roads in Al-Ahmadi Town on 5 th May 2015. Yellow pushpins represent the air sample locations and the mole fraction of the air sample bags (ppm) and black arrow indicates the wind direction (SE)	86
Figure 4.18 Vents distributed around the residential houses in Al-Ahmadi Town	87
Figure 4.19 ArcGIS shows the Picarro mobile system rout in block 1 in Ahmadi Town on 5 th of May 2015. Black arrow indicates the wind direction (SSE), the yellow pushpins represent the air samples location, and the green circle are the vents that been showed in figure 4.16	88
Figure 4.20 ArcGIS shows the Picarro mobile system route around Al-Ahmadi Town (5 th May 2015). Black arrow indicates the wind direction, the red square shows the zoomed area of the next map	89
Figure 4.21 ArcGIS shows the Picarro mobile system route in Block 1, South Ahmadi Town (5 th May 2015). Red arrow indicates the wind direction	89

List of Figures

Figure 4.22 Keeling plot based on the samples collected in Al-Ahmadi Town on 5th May 2015	90
Figure 4.23 Great Burgan field. Source:(Alsharhan & Nairn 1997) eMISK,2018.	91
Figure 4.24 Bernard diagram to classify natural gas origin by using the molecular ratio of the natural gas: C1/C2+C3) against $\delta^{13}\text{C}-\text{CH}_4$ (‰). This plot is modified after (Aali et al. 2006) results, based on the original figure of (Bernard et al. 1978) . The red star represents the sample from the Greater Burgan field in this study which confirmed the thermogenic origin of the Kuwait gas.	94
Figure 4.25 Keeling plot based on the car exhaust samples	99
Figure 5.1 Location of Landfill sites (closed and active) in Kuwait in relation to urban area. Source: eMISK.com	103
Figure 5.2 (A) Area of closed and open landfill sites in Kuwait (km ²). (B) Areas of individual landfill sites in Kuwait (km ²). source: Al-Ahmad,2012.	103
Figure 5.3 Show the dumping of mixtures of waste materials in Kuwait.	104
Figure 5.4: The contribution associated with CH ₄ emissions at both the a) sector and b) activity levels in Kuwait 1994. (Source: the Kuwait's Initial National Communications under the United Nations Framework Convention on Climate Change report, November 2012.)	106
Figure 5.5 ArcGIS Plot of the route of the Kuwait Campaign over 6 Days: 2nd-7th of May 2015.	107
Figure 5.6 The Seven landfills that were surveyed by Picarro mobile system in the Kuwait Campaign during the period 2 nd to 7 th of May 2015. Source: eMISK.com	108
Figure 5.7 Al-Jahra active Landfill source: eMISK.com	110
Figure 5.8 ArcGIS plot of Methane Mole Fractions (ppm) in Al-Jahra active landfill on the 2 nd of May 2015. The black markers are the locations of the air samples collected and red arrow is wind direction.	111

List of Figures

Figure 5.9 Keeling plot based on the air samples collected from Al-Jahra landfill site on 2 nd of May 2015	112
Figure 5.10 The South 7th Ring Road active Landfill. (source: Emisk.com)	113
Figure 5.11 ArcGIS plot of Methane mole fractions (ppm) in South 7 th Ring Road active landfill site on 3 rd of May 2015. The yellow markers are the locations of air samples collected	114
Figure 5.12 Keeling plot based on the samples collected on the South 7 th Ring Road landfill site on 3 rd of May 2015.	114
Figure 5.13 ArcGIS map of methane mole fractions (ppm) in the South 7 th Ring Road landfill site. The black markers are the location of the air samples collected. The red arrow represents the wind direction on 4 th of May 2015	115
Figure 5.14 ArcGIS map of methane mole fractions (ppm) in the south 7 th Ring Road landfill site. The red arrow represents the wind direction on 7 th of May 2015.	116
Figure 5.15 Mina Abdullah active landfill site. Source: eMISK	117
Figure 5.16 ArcGIS map of methane mole fractions (ppm) in the Mina Abdullah landfill site. The black markers are the location of the air samples collected and red arrow the wind direction.	118
Figure 5.17 Keeling plot based on the samples collected on Mina Abdullah landfill	118
Figure 5.18 Kabad Construction Landfill Source: eMISK	119
Figure 5.19 ArcGIS map shows methane mole fractions (ppm) in Kabad construction landfill site that is located in the southwest with nearby South Seven ring road landfill site for comparison.	120
Figure 5.20 Al-Sulaibiya Landfill site location in relation to the urban area. Source: eMISK	121
Figure 5.21 ArcGIS map of methane mole fractions (ppm) in the Al-Sulaibiyah landfill site. The red arrow represents wind direction	122

List of Figures

Figure 5.22 Keeling plot based on the samples collected on Al-Sulaibiya landfill site	122
Figure 5.23 Al-Qurain Closed Landfill site related to the urban area. Source: eMISK	123
Figure 5.24 ArcGIS map of methane mole fractions (ppm) in the Al-Qurain landfill site. The red markers are the location of the air samples collected. The red arrow represents the wind direction.	124
Figure 5.25 Keeling plot based on the samples collected on Al-Qurain landfill	125
Figure 5.26 Al-Qurain landfill and the 300 boreholes of the gas system	126
Figure 5.27 Collection of gas samples from boreholes in Al-Qurain Landfill site	127
Figure 5.28 Jleeb Al-Shuyoukh landfill site related to the urban area. Source: eMISK	128
Figure 5.29 ArcGIS plot of methane mole fractions (ppm) in the Jleeb Al-Shuyoukh Landfill site. The black markers are the locations of the air samples collected. The red arrow represented the wind direction	129
Figure 5.30 Keeling Plot based on the samples collected on Jleeb Al-Shuyoukh Landfill in the Kuwait campaign on May 2015	129
Figure 5.31 One of the boreholes in Jleeb Al-Shuyoukh landfill site	130
Figure 6.1 Map shows the four wastewater treatment plants in Kuwait. Source: Emisk, 2018	138
Figure 6.2 The Headworks Building (Primary treatment) in Al-Reqqa Sewage Treatment Plant.	139
Figure 6.3 Settling Tank (Secondary Treatment) in Al-Reqqa Sewage Treatment Plant	140
Figure 6.4 The structures of Riqqa Sewage Treatment Plant. Red area: represents the primary treatment. Blue and green: secondary treatment, yellow and purple: sludge processing. More detail in the legend	142

List of Figures

Figure 6.5 ArcGIS plot of methane mole fractions in ppm recorded on 4 th May 2015 around Riqqa sewage treatment plant. Black stars are the locations of the air samples collected.	143
Figure 6.6 Keeling Plot based on the air samples collected recorded on 4 th May 2015 around Riqqa sewage treatment plant.	144
Figure 6.7 The trucks and vehicles parked next to Riqqa sewage treatment plant	144
Figure 6.8 Keeling Plot based on the air samples collected on 7 th January 2016 around Riqqa sewage treatment plant	145
Figure 6.9 Keeling Plot based on the air samples collected on 7 th March 2017 around Riqqa sewage treatment plant	146
Figure 6.10 ArcGIS plot of calculated $\delta^{13}\text{C}$ source signatures (‰) for CH_4 elevations on 7 th March 2017 around Riqqa sewage works. The yellow arrow represents the wind direction and the markers are the locations of the air samples collected	147
Figure 6.11 ArcGIS plot of methane mole fractions in ppm recorded on 5 th May 2015 around KM30 sewage works. The red stars are the locations of the air samples collected.	148
Figure 6.12 Keeling Plot based on the air samples collected recorded on 5 th May 2015 around KM30 sewage treatment plant	149
Figure 6.13 Treatment processes in Umm Al-Hayman sewage treatment plant	150
Figure 6.14 Keeling plot for based on the 12 air samples that were collected in Umm Al-Hayman wastewater treatment plant on 17 th March 2017.	151
Figure 6.15 Keeling plot for based on the 3 air samples that were collected outside the Umm Al-Hayman wastewater treatment plant on 17 th March 2017 in Kuwait	151
Figure 6.16 Industrial liquid waste pit located NE Umm Al-Hayman sewage treatment plant. Three samples were collected next to this pit.	152

List of Figures

Figure 6.17 Google earth map for the locations of the 15 air samples collected at Umm Al-Hayman wastewater treatment, A) methane mole fraction (ppm), B) methane isotopic measured for all 15 samples on the 7th of March 2017 with ENE wind direction.	153
Figure 7.1 Animal farming areas in Kuwait State. Source: Emisk, Jun 2018	157
Figure 7.2 ArcGIS plot of methane mole fractions in ppm recorded on 3rd of May 2015 around Al-Sulabiya area. Red arrow represents wind direction NNW.	158
Figure 7.3 Shows the Holstein Friesians cows inside a shed in one of the Al-Sulabiya farm.	159
Figure 7.4 ArcGIS plot methane mole fractions in ppm recorded on 3 rd of May 2015 in cows farm in Al-Sulibiya area, Red arrow represent the wind direction.	160
Figure 7.5 Keeling plot based on samples collected in a cow farm in Al-Sulibiya area on 3 rd of May 2015.	160
Figure 7.6 Google Earth view of methane mole fraction columns measured along the transect downwind of the sheep farm (Al-Mawashi) located in Kabd area on 7 th of May 2015. Yellow markers represent samples collections location and the yellow arrow the wind direction (S-SSE).	161
Figure 7.7 Keeling plot based on air samples collected downwind of sheep farm (Al-Mawashi) on 7 th May 2015.	162
Figure 7.8 Group of 200 camels, next to the public road in Al-Sabya desert area North of Kuwait City	163
Figure 7.9 Keeling plot based on the samples collected of group of camels in the desert on 2 nd May 2015	164
Figure 7.10 Illustration of tracer methodology by (Johnson et al. 1994)	166
Figure 8.1 Google Earth map showing the three sites for collection of air samples (green pushpins) in Kuwait during 2015 and 2016.	170

List of Figures

Figure 8.2 Backward trajectory model for Kuwait, calculated for a duration of 120 hrs air movement.	172
Figure 8.3 Backward trajectory model for air arriving at Kuwait City, calculated for a duration of 120 hrs of air movement. (A) the air mass is coming from Iraq and Syria, (B) coming from Iran.	173
Figure 8.4 Backward trajectory model for air arriving at Kuwait City, calculated for a duration of 120 hrs air movement. (A) coming from Saudi Arabia and (B) from the Arabian Gulf.	174
Figure 8.5 shows Al-Mutla where samples were collected for the period of 2015-2016 (Source: eMISK, 2018)	175
Figure 8.6 Shows Khaldiya site in the Kuwait University, College of Science. (Source: eMISK, 2018).	176
Figure 8.7 Shows the location of the Fahaheel site (Source: eMISK, 2018)	177
Figure 8.8 Methane mole fraction for period the 2015 and 2016 for three sites in Kuwait. The minimum period is highlighted by the in yellow shaded area in summer and the maximum by the blue shade area in winter.	179
Figure 8.9 Methane isotopic signatures values for period 2015 and 2016 for three sites in Kuwait.	181
Figure 8.10 Shows the $\delta^{13}\text{C-CH}_4$ values and the methane mole fractions measurements for the air samples collected in 2015 and 2016 from three sites (Al-Mutla, Khaldiya and Fahaheel)	182
Figure 8.11 Polar plot of methane mole fractions (ppm) recorded for 2015 and 2016 in Al-Mutla site, Kuwait	184
Figure 8.12 A) Measured $\delta^{13}\text{C}$ values, B) Calculated $\delta^{13}\text{C}$ source signatures split by wind direction for 2015 and 2016	185
Figure 8.13 Polar plot of methane mole fraction (ppm) recorded for 2015 and 2016 in Khaldiya	186
Figure 8.14 A) Measured $\delta^{13}\text{C}$ values, B) Calculated $\delta^{13}\text{C}$ source signatures split by wind direction for 2015 and 2016 at Khaldiya.	187

List of Figures

Figure 8.15 Polar plot of methane mole fraction (ppm) recorded for 2015 and 2016 in Fahaheel site, Kuwait	188
Figure 8.16 A) Measured $\delta^{13}\text{C}$ values, B) Calculated $\delta^{13}\text{C}$ source signatures split by wind direction for 2015 and 2016 at Fahaheel.	189
Figure 8.17 Miller-Tans plot based on all the isotopic values measured and the background values for each season	190
Figure 8.18 Miller-Tans plots for each site a) Al-Mutla, b) Khaldiya and c) Fahaheel for 2015 and 2016 in Kuwait.	191
Figure 8.19 shows location of Al-Rabya Residential Area (yellow star) and the major sources of air emissions in Kuwait (Source: eMISK, 2017)	193
Figure 8.20 Keeling plot based on samples collected in Al-Rabya area on 5 th – 6 th January 2016.	194
Figure 8.21 Backward trajectory model for Al-Rabya for air a moving on 6 th January 2016 calculated for a duration of 72 hrs air movement.	195
Figure 8.22 Methane mole fractions and $\delta^{13}\text{C}$ for air collected in Al-Rabya on 5 th to 6 th January 2016, blue line represents methane mole fractions, orange line is $\delta^{13}\text{C}$ and green shaded zone shows that the highest CH_4 mole fraction sample has ^{13}C -depleted signature.	195
Figure 8.23 Methane mole fractions and $\delta^{13}\text{C}$ on 18 th to 19 th July 2016 at Al-Rabya, blue line represents methane mole fractions, orange line is $\delta^{13}\text{C}$ and green shaded zone shows that the highest CH_4 mole fraction sample has ^{13}C -depleted signature	196
Figure 8.24 Keeling plot based on samples collected in Al-Rabya area on 18 th – 19 th July 2016	197
Figure 8.25 Backward trajectory model for air a moving at Al-Rabya on 19 th July, calculated for a duration of 72 hrs air movement.	197
Figure 8.26 Keeling plot based on samples collected in Al-Rabya area on 17 th – 18 th October 2016	198
Figure 8.27 Backward trajectory model for Al-Rabya calculated for 72 hrs air movement.	199

List of Figures

Figure 8.28 Methane mole fractions and $\delta^{13}\text{C}$ measured in Al-Rabya 17 th – 18 th October 2016, blue line presented methane mole fractions, orange line is $\delta^{13}\text{C}$ and green shaded zone shows that the highest CH_4 mole fraction sample has a ^{13}C -depleted signature.	199
Figure 9.1 (A) NOAA greenhouse gas reference network sites, (B) NOAA/ESRL/GMD station location, that is the only station in the Middle East and the closet to Kuwait State. Source: NOAA.gov	203
Figure 9.2 Comparison of long-term measurements of three sites in Kuwait and the closest NOAA site.	204
Figure 9.3 Global methane for the period 2003 to 2005. Reference: IUP.uni-bremen.de.	206
Figure 9.4 GOSAT satellite observation of atmospheric methane for A) Jun 2015 and B) Jun 2016. Red box represent Kuwait location Sorces: GOSAT.nise.go.jp	207
Figure 9.5 GOSAT satellite observation of atmospheric methane For A) December, 2015 and B) December, 2016. Red box represent Kuwait location Sorces:GOSAT.nise.go.jp	208
Figure 9.6 Methane concentration measurements data from GOSAT. Sources: GOSAT.nise.go.jp	209
Figure 9.7 EDGAR data for Kuwait methane emissions for all sectors from 1990 to 2012. Source: www.edgar.jrc.europa.eu,2016	211
Figure 9.8 EDGAR data for all source category for Kuwait (in red) and other countries in the same region. Source: www.edgar.jrc.europa.eu,2016	212
Figure 9.9 Crude oil production for Kuwait and other countries for the period 1970 to 2017. Source: OPEC,2018	213
Figure 9. 10 EDGAR 2012 data for global methane emissions for all sectors. Source: www.edgar.jrc.europa.eu,2016	214

List of Tables

Table 1.1 Total greenhouse gases emissions (Gg) of Kuwait State. Source: EPA,2012	8
Table 2.1 Global methane source and sink estimates (Tg CH ₄ yr ⁻¹) by using bottom-up and top-down approaches. Source: (Saunio et al. 2016).	14
Table 3.1 shows the calibration of methane mole fraction using the Picarro mobile system at the RHUL lab before and after Kuwait campaign.	45
Table 3.2 Show the Internal Secondary standards that was used in this study	56
Table 4.1 Air samples collected from North Oil Fields on 7 th March 2016, Kuwait.	72
Table 4.2 Air samples collected from North Kuwait Oil Fields on 27 th October 2016	73
Table 4.3 Air samples collected during the survey by using Picarro mobile system on the 5 th of May 2015.	77
Table 4.4 Air samples collected downwind of the refineries during the survey by using Picarro mobile system on the 6 th of May 2015	83
Table 4.5 Isotopic signatures of natural gas from previous studies of Middle East gas reservoirs and some national gas distribution systems	97
Table 4.6 Fossil fuel related isotopic signatures in the state of Kuwait	100
Table 5.1 Quantities and rate of soil waste recieved at MSW landfill sites in Kuwait from 1997 to 2011. (Sourece: Al-Ahmad, 2012).	105
Table 5.2 Landfill sites that were surveyed during Kuwait campaign in 2015 with the date and time and locations of the collected air samples and the mole fractions in (ppm) of methane of the air bag samples.	109
Table 5.3 Boreholes of Al-Qurain landfill with the concentrations of the methane (%) and the $\delta^{13}\text{C}$ signatures.	126
Table 5.4 Location of Jleeb Al-Shuyoukh boreholes and the concentrations of the methane (%) with the $\delta^{13}\text{C}$ signature	130
Table 5.5 Landfill sites that have been surveyed during Kuwait Campaign on May 2015 with the maximum mole fraction of methane (ppm) and the calculated $\delta^{13}\text{C}$ signature.	136
Table 6.1 Methane isotopic signatures in the wastewater treatment plants in Kuwait	155

List of Tables

Table 7.1 Annual statistical bulletin of the livestock in state of Kuwait during 2015-2016. Source: The Public Authority of Agriculture and Fish Resources/ Statistics Department 2015-2016.	156
Table 7.2 Literature isotopic value of ruminants from a range of previous studies.	158
Table 7. 3 Isotopic signatures of methane from ruminants in Kuwait State of this study.	169
Table 8.1 Summary of measurements for samples collected at their sites (2015-2016)	183
Table 8.2 $\delta^{13}\text{C}$ and methane mole fraction values for the diurnal studies that were carried out in Kuwait State during 2016.	200
Table 9.1 Methane isotopic signatures for difference sources in Kuwait.	216
Table 9.2 Estimated landfill signature in Kuwait.	217
Table 9.3 Methane emissions from inventories and verification	219

C***HAPTER 1***

I***NTRODUCTION***

1. Introduction

The Earth's atmosphere is changing due to the emission of pollutants and greenhouse gases (GHG). Quantifying greenhouse gases plays a crucial role in understanding global climate change. Direct effect of these gases occurs when they absorb infrared radiation, thus trapping heat and potentially changing the planet's temperature. The most important greenhouse gases include carbon dioxide (CO₂), methane (CH₄), nitrous oxide (N₂O), and several other halocarbons such as hydrofluorocarbons (HFCs) and sulfur hexafluoride (SF₆). Although CO₂ and CH₄ occur naturally in the atmosphere, their atmospheric concentrations have changed, and are expected to continue changing because of human activities. There is now consensus that the accumulation of these anthropogenic greenhouse gases will lead to major climate change.

The Intergovernmental Panel on Climate Change (IPCC) use the Global Warming Potential (GWP) concept to allow comparisons of the effect of different greenhouse gases on global warming. It compares the direct climate forcing of different greenhouse gases to that of CO₂. More specifically, it is a measure of how much energy can be absorbed by the emissions of 1 ton of a given gas over a specific period or time, relative to the emissions of 1 ton of CO₂ (IPCC AR5 2014). Emissions of greenhouse gases are often given either in gigagrams (Gg) or in teragrams (Tg).

Atmospheric methane (CH₄) is a powerful greenhouse gas. It is the second most important anthropogenic greenhouse gas contributing to climate change after CO₂ (Wuebbles & Hayhoe 2002; Saunio *et al.* 2016). CH₄ global emissions are estimated at around 550 Tg/yr (Kirschke *et al.* 2013), but they represent only 4% of the global emissions of CO₂ in carbon mass flux units (Saunio *et al.* 2016). While CO₂ contributes about 50% of the enhanced greenhouse effect, CH₄ is responsible for approximately 15-20% (0.48W m⁻²) of the global warming produced by all greenhouse gases since 1750 (Saunio *et al.*, 2016; Ciais *et al.*, 2013; Wuebbles and Hayhoe, 2002). This is attributed to the large warming potential per molecule of CH₄ compared to CO₂ (IPCC AR5 2014). Reducing methane emissions can therefore

play a vital role in reducing the overall emissions of greenhouse gases. Many studies have been conducted on methane emissions from numerous anthropogenic and natural sources (e.g. Badr *et al.* 1991; Kirschke *et al.* 2013; Zazzeri *et al.* 2015, 2017; Hwang *et al.* 2016).

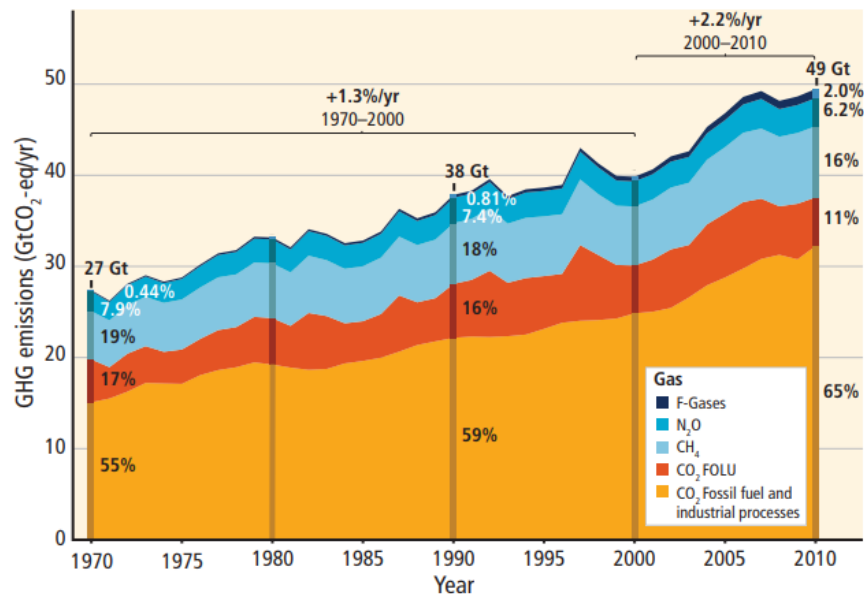


Figure 1.1 Total annual anthropogenic greenhouse gas (GHG) emissions for the period 1970 to 2010. IPCC,2014. (FOLU refers to Forestry and Other Land Use)

Methane emissions quantifications from these sources are often based on emission factor and model calculations (IPCC 2006). It is well known that the global methane budget can be derived from “bottom-up” estimates (inventories) or “top-down” inverse modelling (Kirschke *et al.* 2013; Bergamaschi *et al.* 2015; Sauniois *et al.* 2016). However, several studies have shown that there is a gap between the global methane budget derived from these estimates with the difference varying from one source type to another (Kirschke *et al.* 2013; Sauniois *et al.* 2016). The importance of isotopic analysis as a tool that links methane emissions to specific sources and in verifying inventories has been supported by several studies (Chanton *et al.* 1999, 2000; Levin *et al.* 1999; Bousquet *et al.* 2011; Townsend-Small *et al.* 2012; Zazzeri *et al.* 2015; Fisher *et al.* 2017).

1.1 Methane's Role as a Greenhouse Gas

CH₄ is about 28 times more powerful at warming the atmosphere than CO₂ over a 100-year horizon (IPCC AR5 2013). CH₄ lifetime in the atmosphere is short and estimated around 9±2 years compared with 100 years for CO₂. Hence, atmospheric methane concentrations can be more quickly reduced than other gases such as CO₂, making it a good target for climate change mitigation (Saunois *et al.* 2016).

CH₄ is emitted from several human-induced sources such as landfills, agricultural activities, wastewater treatment, oil and natural gas system and coal mining. In addition, CH₄ is a principle component of natural gas and an important source of energy. Consequently, the prevention or capture and use of CH₄ emission can provide a potential energy source and environmental benefits.

The United Nations Framework Convention on Climate Change (UNFCCC) is the globally recognised platform calling for actions on reduction of anthropogenic greenhouse gases including methane. The Kyoto protocol of the UNFCCC targets a control on the emissions of the greenhouse gases including CH₄ in order to reduce global warming. The Intergovernmental Panel on Climate Change (IPCC) guidelines in 2006 for National Greenhouse Gas Inventories are an important step for national estimates of emissions and removal of greenhouse gases. The guidelines mitigate against global climate change in four sectors including (1) Energy; (2) Industrial processes and product use, (3) Agriculture, forestry and other land use; and (4) Waste (IPCC 2006).

The most up-to-date IPCC special report on the impact of global warming (IPCC 2018) warns that human activities are estimated to have caused approximately 1°C warming above pre-industrial levels in 2017, with a likely range of 0.8°C to 1.2°C. In addition, global warming is likely to reach 1.5°C between 2030 and 2052 if it continues to increase at the current rate without any efforts to control it.

1.2 The State of Kuwait: Study Area

The State of Kuwait covers an area of 17,818 km² in the northeastern end of the Arabian Peninsula. It is located between latitudes 28°30' and 30°5' North and longitudes 46°33' and 48°30' East and consists of a mainland where the capital Kuwait City is located and nine uninhabited islands in the Arabian Gulf. The State of Kuwait shares a 495 km border with Saudi Arabia to the south and a 195 km border with Iraq to the north and west. The coast line extends for 325 km along the mainland and 175 km along the islands (Environment Public Authority (EPA) 2012). The State of Kuwait has a current population of approximately 4.5 million. The overwhelmingly urban population of Kuwait has grown steadily over the past two decades with total population growth of about 4.1% per year between 1994 and 2011. Kuwait has a hyper-arid desert climate, hot and dry with a rainfall average ranging from 75 to 130 millimeters a year. Average daily high temperature ranges from 42°C to 46°C in summer with humidity exceeding 95% from mid-August to September (EPA 2012; WMO 2018; Kuwait Meteorological Center 2018).

Kuwait's economy is comparatively rich but highly dependent on oil and gas exports. Kuwait is a major oil supplier with oil companies accounting for 95% of exports, 50% of gross domestic products (GDP) and 90% of government revenue. Kuwait holds approximately 101.5 billion barrels (bbl) of oil reserves, around 7% of global oil reserves. Approximately 1.8 trillion cubic meters (m³) of natural gas reserves have been proven. Current production capacity of gas in Kuwait is about 3.15 million barrels per day (EPA 2012; OPEC ASB 2018).

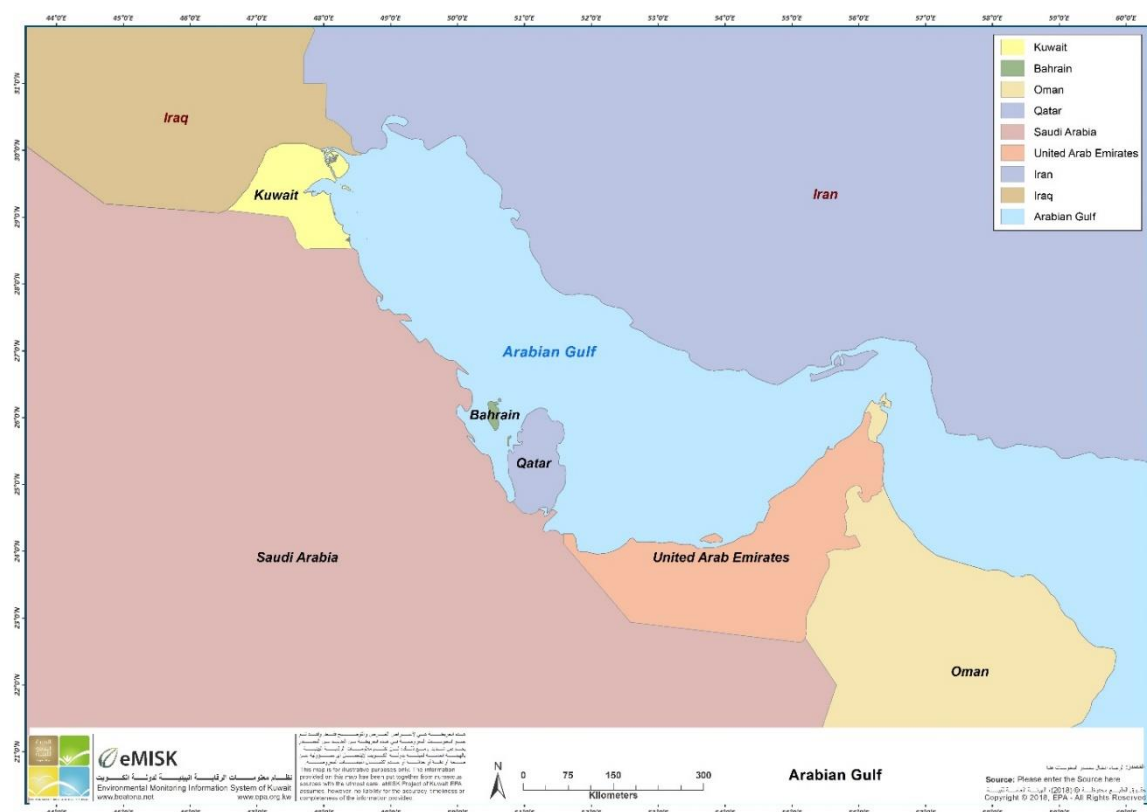


Figure 1.2 Kuwait State located in the Northeast end of the Arabian Peninsula. Source: Emisk, 2018.

1.3 Previous Studies of Methane Emissions in Kuwait

Kuwait is a major oil producing country and its economy directly depends on its export of crude and refined products. These activities result in the emission of gaseous pollutants to the atmosphere. Research on methane emissions in Kuwait are scarce, and mainly focus on gas concentration, distribution and characterisation from oil and gas related activities (Al-Hamad & Khan 2008; Al-Hamad *et al.* 2008a, b, 2009) and landfill sites (Al-Yaqout *et al.* 2005; Al-Ahmad *et al.* 2012; Al-Saffae & Al-Sarawi 2018).

Sources of methane in oil activities include oil production, transport, refineries, storage and utilisations (Al-Hamad *et al.* 2008a). The impact of greenhouse gas (GHG) emissions from flaring activities at oil production facilities at North Kuwait oil fields has been studied by Al-Hamad *et al.* (2008). They used the Industrial Source Complex (ISCST3) Dispersion Model to simulate the mean predicted ground level concentrations of methane. The modelling results show that most elevated CH₄ occurs in winter in the early morning, when the inversion layer, temperature and wind speed are low, suppressing the dispersion. Overall, the recorded levels of pollutants in the winter period were higher than summer.

Methane and other hydrocarbon gas emissions resulting from flaring in Kuwait oilfields have also been studied by Al-hamad *et al.* (2008b). Their study covered all of Kuwait's oil producing zones and showed that emissions of flaring pollutants were associated with oil field related operations such as gathering centers, booster stations, tank areas as well as other activities related to oil productions.

Kuwait is among the highest per capita waste generators in the world with around 1.4 - 1.5 kg/day per capita. More than 2 million tons of solid waste are generated each year. Kuwait has 18 landfills, of which 14 sites are closed and 4 sites are still in operation.

There have been several studies on greenhouse emissions from landfills in Kuwait (Al-Yaqout *et al.* 2005; Al-Ahmad *et al.* 2012; Al-Saffae & Al-Sarawi 2018). However, most of these studies have mainly focused on the characterisation, concentration and distribution of gases, largely from Jleeb Al-Shuyoukh and Al-Qurain landfills. Al-Yaqout *et al.* (2005) have analysed the gas contents (CH₄ and CO₂) of a closed, Al-Qurain landfill based on samples collected from boreholes. They found very high landfill gas production ranging from 149-567 ml/min. Typical gas flow rate in the landfill was 312 ±126 ml/min with 52.5 ±3.2% of CH₄ and 36.1 ±2.8 % of CO₂.

All the previous studies have focused on a particular source and there have been no studies mapping the distribution of methane emissions across the country.

1.4 Greenhouse Gas Emission Inventory of Kuwait

Kuwait's first greenhouse gas inventory, also known as Initial National Communication (INC) under the United Nations Framework Convention on Climate Change, was developed in 2012 by the Environment Public Authority (EPA), following the revised IPCC 1996 Guidelines in combination with the IPCC's Good Practice Guidance and Uncertainty Management in National Greenhouse Gas Inventories (IPCC, 2000). The report used 1994 as the base year for the mitigation analysis mainly because of the availability of high quality-controlled data. A 26-year planning period (1994-2020) was chosen for the evaluation of greenhouse gases in Kuwait.

The overall greenhouse emissions in Kuwait according to the inventory are summarized in Table 1.1. Total methane emissions were 129.19 Gg CH₄, which include 92.69 Gg from energy and 33.80 Gg from waste with additional smaller emissions 2.70 Gg from agricultural activities. No emissions were encountered from industrial processes, solvent and other product use and land-use change and forestry. Sewage treatment was not considered as a source of greenhouse gases.

The inventory shows that 95.3 % of all greenhouse emissions in Kuwait in 1994 were from energy-related activities, including combustion of fossil fuels and the release of fugitive emissions from oil and gas operations and industrial processes accounted for 2.1% of emissions. Waste management contributed 2.4% whereas agriculture accounted for only 0.2%. The focus of greenhouse mitigations was therefore, on the energy sector.

SHORT SUMMARY REPORT FOR NATIONAL GREENHOUSE GAS INVENTORIES (Gg)							
GREENHOUSE GAS SOURCE AND SINK CATEGORIES	CO ₂	CO ₂	CH ₄	CH ₄	N ₂ O	N ₂ O	Total
	Emissions	Removals		21 CO ₂ eq		310 CO ₂ eq	CO ₂ eq
1 Energy							
A Fuel Combustion	28,856		1.69	35.5	0.17	52.7	28,944
B Fugitive Emissions from Fuels	0		91.00	1,911.0		0.0	1,911
Energy total							30,855
2 Industrial Processes	668		0.00	0.0	0.00	0.0	668
3 Solvent and Other Product Use	0			0.0	0.00	0.0	0
4 Agriculture	0		2.70	56.7	0.03	9.3	66
5 Land-Use Change & Forestry	0	22	0.00	0	0.00	0.0	-22
6 Waste			33.80	709.8	0.24	74.4	784
7 Other	0	0	0.00	0	0.00	0.0	0
Total	29,524	22	129.19	7,501	0.44	136.4	32,373

Table 1.1 Total greenhouse gases emissions (Gg) of Kuwait State. Source: EPA,2012

1.5 Research Aims and Objectives

This study focuses on methane emissions in Kuwait. The research, for the first time in Kuwait uses high-precision methane isotopic analysis of $\delta^{13}\text{C}$ coupled with mole fraction measurement in order to link isotopic signatures to methane emission sources in Kuwait. The research involves the use of Cavity Ring-Down Spectroscopy (Picarro analyser) for methane plume identification in Kuwait and further analysis of Tedlar bag samples in the RHUL Greenhouse Gas Laboratory. The use of the Picarro analyser and the fact that the data used in this study are internationally calibrated are of great advantage.

Methane stable isotopic analysis will be used to improve source identification, to gain better understanding of the gap between global methane budgets that result from bottom-up emission inventories and budget estimates from top-down observation (Zazzeri *et al.* 2015; Fisher *et al.* 2017). Methane sources such as gas leaks and landfills can have widely different C isotopic ratios (Schwietzke *et al.* 2016; Zazzeri *et al.* 2017). The C isotopic ratios enable distinction by providing insight into the methane origin. Atmospheric measurements of isotopic signatures can be used to

apportion emissions from different sources.

The main aim of this research is a better understanding of the distribution and strengths of methane sources in Kuwait and identification of targets for future mitigation.

The objectives to achieve this aim are summarised below and discussed in more detail in the following chapters of this thesis.

- 1) To locate and identify the sources of methane emissions in Kuwait.

This will be achieved by undertaking a week-long mobile measurement survey.

- 2) To characterise the isotopic signature of methane emission sources in Kuwait.

This will be achieved by collection of air samples in methane plumes identified during the survey for later isotopic analysis.

- 3) To assess the proportionate contribution of the main methane sources in Kuwait to the local atmospheric methane budget.

This will be achieved by weekly sampling at 3 sites across the country for 2 years for subsequent analysis of mole fractions and isotopes.

- 4) To compare the results of this research to the national (e.g. EPA) and global (i.e. Emissions Database for Global Atmospheric Research (EDGAR) emissions database for atmospheric (methane) emissions.

This will be achieved by mass-balance modeling of the isotopic signatures identified during aims 2 and 3 above.

1.6 Thesis Outline

This research consists of ten chapters: those following this introduction are outlined below:

Chapter 2 presents a review of literature on methane. It provides an overview of global methane sources and sinks as well as global emissions growth of methane for three decades. This chapter also discusses and compares different methane inventories and methane quantification methods based mainly on the standardised IPCC (IPCC 2006) methodologies.

Chapter 3 presents the materials and methods used to understand methane emissions in Kuwait. The chapter also describes sampling procedures, instrument performance and calibrations, error and uncertainty. Sample analysis using Keeling and Miller-Tans approaches, as well as polar plot and pollution rose construction from the Openair application are also described.

Chapter 4 describes the analysis of methane emissions from natural gas systems (oil exploration, production, gathering, transmission, processing, exportation) in Kuwait. It presents Kuwait's oil fields and facilities oil and gas production and oil refineries. The chapter also discusses sampling procedures, and isotopic signature of Kuwait natural gas in oil field surveys.

Chapter 5 presents the analysis of methane emissions from landfill sites in Kuwait. It describes seven surveyed landfill sites, including their location, characteristics and isotopic signatures of emissions. The chapter also discusses the results of the analysis and compares them with the previous studies in Kuwait.

Chapter 6 presents the results of methane emissions from sewage (wastewater) treatment in Kuwait. It describes Kuwait's sewage treatment, sample analysis and isotopic characterisation.

Chapter 7 presents the results of methane production by ruminant animals in Kuwait, including cows, sheep and camels. The chapter describes and discusses

sampling techniques, analysis and isotopic characterisation of the ruminant's methane emissions.

Chapter 8 presents the results of ambient methane measurement in Kuwait. It describes long term methane measurements at three sampling sites; Al-Mutla, Khaldiya and Fahaheel with details of sampling analysis and isotopic characterisation.

Chapter 9 discusses the results of the previous chapters. It compares the results of this thesis with inventories and other available methane measurements from the region. The chapter also attempts to verify the available bottom up methane inventories for Kuwait

Chapter 10 presents the key conclusions of this research.

C_{CHAPTER 2}

M_{ETHANE – LITERATURE REVIEW}

2. Methane: Literature Review

Methane is the most abundant (reactive/organic) trace gas in the atmosphere with a short steady state lifetime, approximately 9.3 years (range 7.1–10.6; Kirschke *et al.* 2013; Voulgarakis *et al.* 2013). Methane is a major contributor to the enhanced greenhouse effect with a strong influence on tropospheric and stratospheric chemistry. It also plays an important role in the regulation of stratospheric and tropospheric ozone levels. Methane oxidation is a major source of water in the stratosphere (IPCC AR4 2007). In the troposphere, methane consumes about 25% of all hydroxyl and affects both carbon monoxide and ozone concentrations (Thompson 1992). OH is considered a major sink of methane. About 90% of CH₄ destruction occurs via OH radicals (Bergamaschi *et al.*, 2000).

Methane is emitted to the atmosphere by natural and anthropogenic sources. About two-thirds of methane is emitted by human activities and the remainder from natural sources (Nisbet *et al.* 2014). The main natural sources of methane are wetlands, oceans, termites and clathrates (Dlugokencky *et al.* 2011). Wetlands are the largest natural methane source of 164 Tg yr⁻¹, about 30% of total global emissions (Bridgham *et al.* 2013). Anthropogenic methane (fossil fuel exploitation, ruminant animals, rice agriculture, landfill, waste management and biomass burning) account for 54-72% of the global total emissions (Bridgham *et al.* 2013).

This chapter presents a review of literature on methane. It provides an overview of global methane sources and sinks, methane emissions quantifications and the global emissions growth of methane for the last three decades. This chapter also discusses and compares different methane inventories based mainly on the standardised IPCC (IPCC 2006a) methodologies.

2.1 Sources of Atmospheric Methane

The global atmospheric methane budget is determined by a wide range of sources balanced by a much smaller number of sinks (Van Amstel 2012). Methane sources and sinks vary with latitude. The global methane source strength in the Northern Hemisphere is roughly three times greater than in the Southern Hemisphere (Simpson *et al.* 2002; Nisbet *et al.* 2014). Figure 2.1 shows that the Northern Hemisphere methane emissions are higher due to sources including wetlands, natural gas, biomass fires and agriculture, with larger land surface area and higher population in this hemisphere. Methane sources vary inter-annually according to the meteorology (La Niña events) and seasonal changes. Seasonal cycles in the Northern Hemisphere have more interaction among methane sources and sinks which make it more complex than the Southern Hemisphere (Dlugokencky *et al.* 1994).

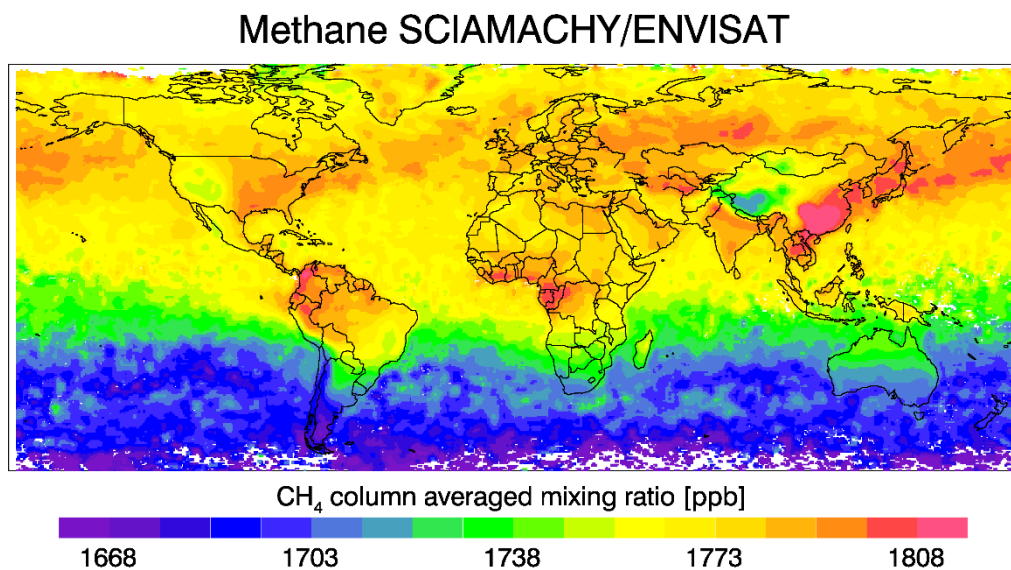


Figure 2.1 SCIAMACHY Satellite map for the period 2003 to 2005, shows the variation in methane column average mixing ratio for the Northern Hemisphere and the Southern Hemisphere. Source: www.IUP.uni-bremen.de

All methane sources can broadly be grouped into three types based on emitting processes: biogenic, thermogenic and pyrogenic sources (Kirschke et al. 2013; Saunio et al. 2016; Cicerone and Oremland 1988). Each of these categories can have both a natural and anthropogenic origin (Ciais et al. 2014). Global of

methane sources are more diverse than the sinks. Total emissions for 2012 are estimated at 568 Tg CH₄ yr⁻¹ (542-582) and 756 CH₄ yr⁻¹ (609-916) based on top-down and bottom-up estimates respectively (Saunois et al. 2016).

Table 2.1 summarises all methane sources and sinks. It compares decadal global methane emissions from natural and anthropogenic sources as well as methane sinks based on the study of Kirschke *et al.* (2013) and Saunois *et al.* 2016. Methane emissions were calculated using both bottom-up and top down approaches

	Kirschke et al. (2013) bottom-up	Kirschke et al. (2013) top-down	Bottom-up			Top-down		
Period of time	2000–2009	2000–2009	2000–2009	2003–2012	2012	2000–2009	2003–2012	2012
Natural sources	347 [238–484]	218 [179–273]	382 [255–519]	384 [257–524]	386 [259–532]	234 [194–292]	231 [194–296]	221 [192–302]
Natural wetlands	217 [177–284]	175 [142–208]	183 [151–222]	185 [153–227]	187 [155–235]	166 [125–204]	167 [127–202]	172 [155–201]
Other natural sources	130 [45–232]	43 [37–65]		199 [104–297]		68 [21–130]	64 [21–132]	49 [22–137]
Other land sources	112 [43–192]			185 [99–272]				
Fresh waters	40 [8–73]			122 [60–180]				
Geological (onshore)	36 [15–57]			40 [30–56]				
Wild animals	15 [15–15]			10 [5–15]				
Termites	11 [2–22]			9 [3–15]				
Wildfires	3 [1–5]			3 [1–5]				
Permafrost soils (direct)	1 [0–1]			1 [0–1]				
Vegetation				e				
Oceanic sources	18 [2–40]			14 [5–25]				
Geological (offshore)	–			12 [5–20]				
Other (including hydrates)	–			2 [0–5]				
Anthropogenic sources	331 [304–368]	335 [273–409]	338 [329–342]	352 [340–360]	370 [351–385]	319 [255–357]	328 [259–370]	347 [262–384]
Agriculture and waste	200 [187–224]	209 [180–241]	190 [174–201]	195 [178–206]	197 [183–211]	183 [112–241]	188 [115–243]	200 [122–213]
Enteric fermentation & manure	101 [98–105] ^a		103 [95–109] ^b	106 [97–111] ^b	107 [100–112] ^b			
Landfills & waste	63 [56–79] ^a		57 [51–61] ^b	59 [52–63] ^b	60 [54–66] ^b			
Rice cultivation	36 [33–40]		29 [23–35] ^b	30 [24–36] ^b	29 [25–39] ^b			
Fossil fuels	96 [85–105]	96 [77–123]	112 [107–126]	121 [114–133]	134 [123–141]	101 [77–126]	105 [77–133]	112 [90–137]
Coal mining	–	–	36 [24–43] ^b	41 [26–50] ^b	46 [29–62] ^b			
Gas, oil & industry	–	–	76 [64–85] ^b	79 [69–88] ^b	88 [78–94] ^b			
Biomass & biofuel burning	35 [32–39]	30 [24–45]	30 [26–34]	30 [27–35]	30 [25–36]	35 [16–53]	34 [15–53]	35 [28–51]
Biomass burning	–	–	18 [15–20]	18 [15–21]	17 [13–21]			
Biofuel burning	–	–	12 [9–14]	12 [10–14]	12 [10–14]			
Sinks								
Total chemical loss	604 [483–738]	518 [510–538]				514 ^d	515 ^d	518 ^d
Tropospheric OH	528 [454–617]							
Stratospheric loss	51 [16–84]							
Tropospheric Cl	25 [13–37]							
Soil uptake	28 [9–47]	32 [26–42]				32 [27–38]	33 [28–38]	36 [30–42]
Sum of sources	678 [542–852]	553 [526–569]	719 [583–861]	736 [596–884]	756 [609–916]	552 [535–566]	558 [540–568]	568 [542–582]
Sum of sinks	632 [592–785]	550 [514–560]				546 ^c	548 ^c	555 ^c
Imbalance		3 [–4–19]				6 ^c	10 ^c	14 ^c
Atmospheric growth		6				6.0 [4.9–6.6]	10.0 [9.4–10.6]	14.0 []

^a Manure is now included in enteric fermentation & manure and not in waste category.

^b For IIASA inventory the breakdown of agriculture and waste (rice, enteric fermentation & manure, landfills & waste) and fossil fuel (coal, oil, gas & industry) sources use the same ratios as the mean of EDGAR and USEPA inventories.

^c Total sink is deduced from global mass balance and not directly computed.

^d Computed as the difference of global sink and soil uptake.

^e Uncertain but likely small.

Table 2.1 Global methane source and sink estimates (Tg CH₄ yr⁻¹) using bottom-up and top-down approaches. Source: (Saunois et al. 2016).

2.1.1 Biogenic sources

Biogenic sources are the major methane contributors (64% - 76%) and comprise methane-generating archaea (methanogens) (Neef *et al.* 2010). Biogenic methane results from the decomposition of organic matter by archaea in anaerobic environments such as natural rice paddies and wetlands, digestive system of ruminants and termites, oxygen poor fresh water, waste-water facilities and organic waste deposits (e.g. sewage, landfill) (Van Amstel 2012; Kirschke *et al.* 2013).

2.1.2 Thermogenic sources

Thermogenic sources account for 19% - 30% and form as a result of the breakdown of buried organic matter deep in the Earth's crust due to excess heat and pressure (Neef *et al.* 2010). These include methane formed over millions of years through geological process. Thermogenic methane is emitted from subsurface to the atmosphere in two ways; through natural features such as marine and terrestrial geological gas seeps, and through the exploitation and distribution of fossil fuels (coal, oil, natural gas), natural gas production, transmission and distribution, and oil production and refining (Van Amstel 2012; Kirschke *et al.* 2013). Methane hydrates can be of biogenic or thermogenic origin (Kirschke *et al.* 2013; Sauniois *et al.* 2016).

2.1.3 Pyrogenic sources

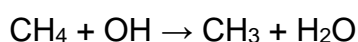
Pyrogenic sources are minor and only account for 4% - 6% (Neef *et al.* 2010). Pyrogenic methane is produced because of incomplete combustion of biomass (wildfires) and of biofuels (fuel burning).

2.2 Sinks of Atmospheric Methane

The methane sinks are both atmospheric and soil sinks (Figure 2.2). An overview of the atmospheric methane sinks is given by Reay *et al.* (2007a). The total size of the global methane sink is estimated to be 500-600 Tg CH₄ yr⁻¹ (Reay 2007a; Saunio *et al.* 2016). Methane total sink uncertainties are in order of 20-40% (Kirschke *et al.* 2013).

2.2.1 Atmospheric methane sink

The primary atmospheric sink for methane is its oxidation by hydroxyl radicals (OH), a chemical reaction that occurs mostly in the troposphere (Ehhalt 1974; Kirschke *et al.* 2013; Reay *et al.* 2018). OH alone is responsible for the removal of 500 Tg CH₄ each year, almost 90% of the global CH₄ sinks and 9% of the total CH₄ burden in the atmosphere (Wuebbles & Hayhoe 2002). Hence, this reaction is very important in determining the rate of CH₄ removal from the atmosphere. In addition, it limits the radiative forcing potential of CH₄ and contributes to the production of peroxy radicals, which can lead to the formation of ozone, and thus induce a further indirect effect of CH₄ climate forcing (Van Amstel 2012; Reay *et al.* 2007a). The initial reaction of methane (CH₄) and hydroxyl (OH) produce methyl (CH₃) and water as in the following equation

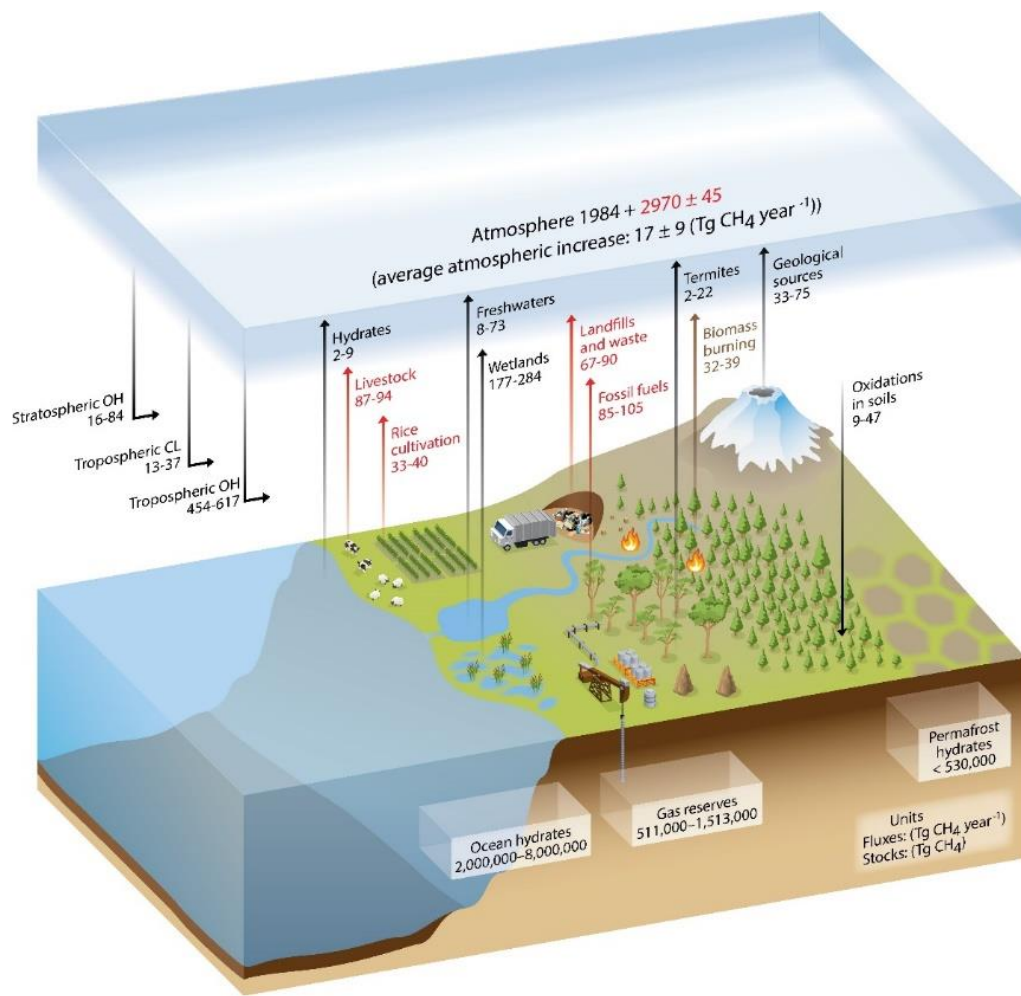


The reaction is more complex in the advanced stages, involving more reactions that eventually lead to both increased water vapour and production of CO₂ (Reay *et al.* 2007a). Another minor sink is the reaction of CH₄ with Chlorine (Cl) radicals in the stratosphere and in the surface water of seas (Allan *et al.* 2005). Direct quantification of OH in the atmosphere is difficult due to the complex atmospheric physics and chemistry that produce OH and its short lifetime (Reay *et al.* 2007; Shallcross *et al.* 2007)

2.2.2 Soil methane sink

Despite soils in wetlands and rice paddies acting as major sources of methane, drier soils can be active CH₄ sinks with CH₄ removed by oxidation (Dunfield 2007; Reay *et al.* 2007a). This accounts for 5% of the total methane sink, approximately 30 Tg CH₄ yr⁻¹ (Wuebbles, & Hayhoe 2002). Kirschke *et al.* (2013) estimated that soils represent a sink for CH₄ of 28 (9-47) Tg CH₄ yr⁻¹. CH₄ is predominantly removed by aerobic bacteria (methanotrophs) in the soil that use the CH₄ as a source of energy and carbon (Dutaur & Verchot 2007; Van Amstel 2012). Methane removal by soil is a small but important flux in the global methane budget. Whether the soil acts as a source or a sink is determined by several factors including water content, pH, soil temperature and organic matter (e.g. nitrate) concentration (Hütsch *et al.* 1994). Forest soils are often strong CH₄ sinks as transpiration by trees helps to keep soil water contents low, creating the aerobic conditions required by methanotrophs. However, when soil becomes waterlogged such as in winter or due to deforestation, anaerobic conditions dominate, leading to growth of CH₄ producing archaea and so the soil becomes a source of CH₄ (Reay *et al.* 2007a).

De Visscher *et al.* (2012) described the importance of the soil methane sink in human-made environments such as landfills and rice fields where biological oxidation plays a crucial role in reducing CH₄ emissions. Although these 'source' areas produce vast amount of CH₄, methanotrophs can limit the actual release of CH₄ to the atmosphere to less than 10% (Reay *et al.* 2007a).



Reay DS, et al. 2018.
Annu. Rev. Environ. Resour. 43:165-92

Figure 2.2 Global methane sources and sinks for the period 2000 to 2009.
Source: Ciais *et al.* 2013

2.3 Quantifying the Atmospheric Methane Budget

Measurement and monitoring of methane emissions are crucial for the development and verification of emission inventories. Methane estimates occur along spatial and temporal resolutions ranging from large-scale global assessments (e.g. global, continental and regional) of annual emissions, to small scale estimates of individual sources over short time scales. There are two general approaches for estimating methane emissions for a specific area: 'bottom-up' and top-down' estimates.

2.3.1 Bottom-up estimate

The bottom-up estimate (inventories) such as the US Greenhouse Gas Inventory (USEPA 2017), the National Atmospheric Emissions Inventory (NAEI 2018) for the UK and Emissions Database for Global Atmospheric Research (EDGAR) (Crippa *et al.* 2018) have been developed by multiplying average emission factors (amount of emission per unit of activity; IPCC 2006a) for each known source category by the activity data (Hsu *et al.* 2010; Schwietzke *et al.* 2014; Höglund-Isaksson 2017). Bottom-up estimates allow for direct measurements of methane sources and link emissions to specific sources. However, they require accurate emissions factors and comprehensive accounting of activity data (IPCC 2006a; NASEM 2018). This technique can produce finer spatial resolution and more detailed emissions for a given source, but the large number of sources and the variability of emission factors are a challenge for this technique (Karion *et al.* 2013).

The IPCC guidelines (IPCC 2006a) provided a tiered system of bottom-up estimates, consisting of three tiers that can be used by countries to produce national inventories of greenhouse emissions. Tier 1 is the simplest and involves basic equations and default values for emission factors and activity parameters. Tier 2 uses specific parameters and more detailed calculations to produce inventories. It allows for incorporation of country-specific emission factors and activity data. Tier 3 is the most complex method of producing inventories and mainly used for countries with good and annually updated data and advanced methodologies. It uses more advanced country-specific parameters with complex equations. Uncertainties are largely associated with emission factors and activity data.

2.3.2 Top-down estimate

Top-down approaches were basically developed in an attempt to evaluate and reduce uncertainties associated with the bottom-up approaches (Bergamaschi *et al.* 2015; Fairley & Fischer 2015). Top-down estimates, also known as ‘inverse modelling’ involve using atmospheric concentration measurements combined with inverse modelling to estimate methane emissions and sinks. This technique has widely been used to estimate methane emissions on global scale (Mikaloff

Fletcher *et al.* 2004; Bousquet *et al.* 2006; Bousquet *et al.* 2011; Kirschke *et al.* 2013; Bergamaschi *et al.* 2015; Houweling *et al.* 2017; Janssens-Maenhout *et al.* 2017). Top-down measurement techniques to estimate methane emissions utilise aircraft, satellite or ground based measurements (Morino *et al.* 2011; Karion *et al.* 2013).

Source identification is more problematic when using top-down estimates as it tends to estimate total methane rather than identify specific sources. One way to improve methane source identification is the use of isotopic measurements (e.g. Fisher *et al.* 2017).

2.3.3 Comparisons of bottom-up and top-down estimates

Generally, there are some gaps between global methane budgets that are derived from “bottom-up” inventory estimates and budgets derived from “top-down” observation (Kirschke *et al.* 2013; Saunois *et al.* 2016). Many studies have compared these two approaches to estimate and validate GHG emissions (Kirschke *et al.* 2013; Nisbet *et al.* 2014; Saunois *et al.* 2016; Tsuruta *et al.* 2016). They found that bottom-up approaches suggest larger global emissions than top-down, mostly due to the large natural emissions from individual sources such as wetland and some individual emissions reported by the bottom-up approach being overestimated (Kirschke *et al.* 2013; Saunois *et al.* 2016). The overestimation most likely results from estimation errors of natural source and sink extrapolation or double counting of some natural sources such as wetlands (Saunois *et al.* 2016).

At the global scale, the total methane emissions inferred from top-down estimates are 568 Tg CH₄ yr⁻¹ (range 542–582) for the year 2012 (top down) with a slightly smaller value of 558 Tg CH₄ yr⁻¹ (range 540–568) for the 2003–2012 decade (Saunois *et al.* 2016). However, global methane emission estimates from bottom-up approach are higher with a much larger range of 736 Tg CH₄ yr⁻¹ (596–884) for the same 2003-2012 decade (Saunois *et al.* 2016). Top -down estimates of the methane sink for 2003-2012 are 548 Tg CH₄ yr⁻¹ (Saunois *et al.* 2016). The top-down approach estimates a difference of 8 Tg CH₄ yr⁻¹ between total sources and sinks for the 2000-2009 decade, whereas bottom-up calculates a larger difference of 46 Tg CH₄ yr⁻¹ (Kirschke *et al.* 2013). Natural methane sources differ

greatly between bottom-up and top-down estimates, whereas anthropogenic sources are much more consistent (Kirschke *et al.* 2013; Saunio *et al.* 2016). Uncertainties for anthropogenic emissions appear smaller than the emissions from natural sources and the uncertainties on source categories appear larger for top-down inversions than for bottom-up inventories and models (Tsuruta *et al.* 2016).

2.4 Global Growth of Methane

Global atmospheric growth of methane has been the subject of many studies (Dlugokencky *et al.* 1998, 2011; Kirschke *et al.* 2013; Nisbet *et al.* 2014, 2016; Saunio *et al.* 2016; Schaefer *et al.* 2016; Reay *et al.* 2018). IPCC has also summarised global trends of methane in the second, third, fourth and fifth assessment reports. The global atmospheric methane concentration is determined by the balance between the emission sources and the photochemical destruction by the hydroxyl radical (Bousquet *et al.* 2006). Trends and inter-annual variability in OH concentration can be significantly impacted by methane emission (IPCC AR5, 2014).

The growth of methane in the atmosphere is largely related to increasing anthropogenic emissions (IPCC AR4 2007). The column-averaged atmospheric CH₄ concentration can be mapped by remote sensing from the surface using ground-based Fourier Transform Spectrometers (e.g. TCCON, <http://www.tccon.caltech.edu/>) and from space by several satellite instruments such as the Scanning Imaging Spectrometer for Atmospheric Cartography - SCIAMACHY, 2003–2012 (Frankenberg *et al.* 2008), and the Greenhouse gases Observing SATellite – GOSAT, since 2009 (Morino *et al.* 2011).

The trapped air bubbles in ice cores formed during cold glacial periods provide a continuous record of the atmospheric concentrations of methane over the past 400,000 years and more (Louergue *et al.* 2008). The ice-core records show that CH₄ abundance has varied from 350 ppb during glacial periods up to 700-800 ppb during interglacial periods (Denman *et al.* 2007; Dlugokencky *et al.* 2011), suggesting that methane concentration has more than doubled during the warm interglacial periods. This has proved the impact of climate change on atmospheric methane (Dlugokencky *et al.* 2011).

After 1750, atmospheric CH₄ levels have generally risen with time. They have significantly increased by a factor of 2.7 from 700 ppb during the pre-industrial periods to 1859 ppb by 2017 (WMO, 2018; IPCC AR5 2013, 2014). The increase has been largely attributed to anthropogenic emissions (IPCC AR5 2014) as well as other factors such as meteorological feedback and changes in CH₄ lifetime (Dlugokencky *et al.* 2011).

Figure 2.3 shows the global CH₄ records over the last three and a half decades since the start of detailed global GHG monitoring by NOAA (https://www.esrl.noaa.gov/gmd/ccgg/trends_ch4/). From the 1980s to 1992, atmospheric methane was rising sharply by >10 ppb per year and around 14 ppb in 1984 (Dlugokencky *et al.* 1998, 2011; Nisbet *et al.* 2014). This high growth rate was attributed to the strong increase in anthropogenic emissions in the post-War years (Dlugokencky *et al.* 1998).

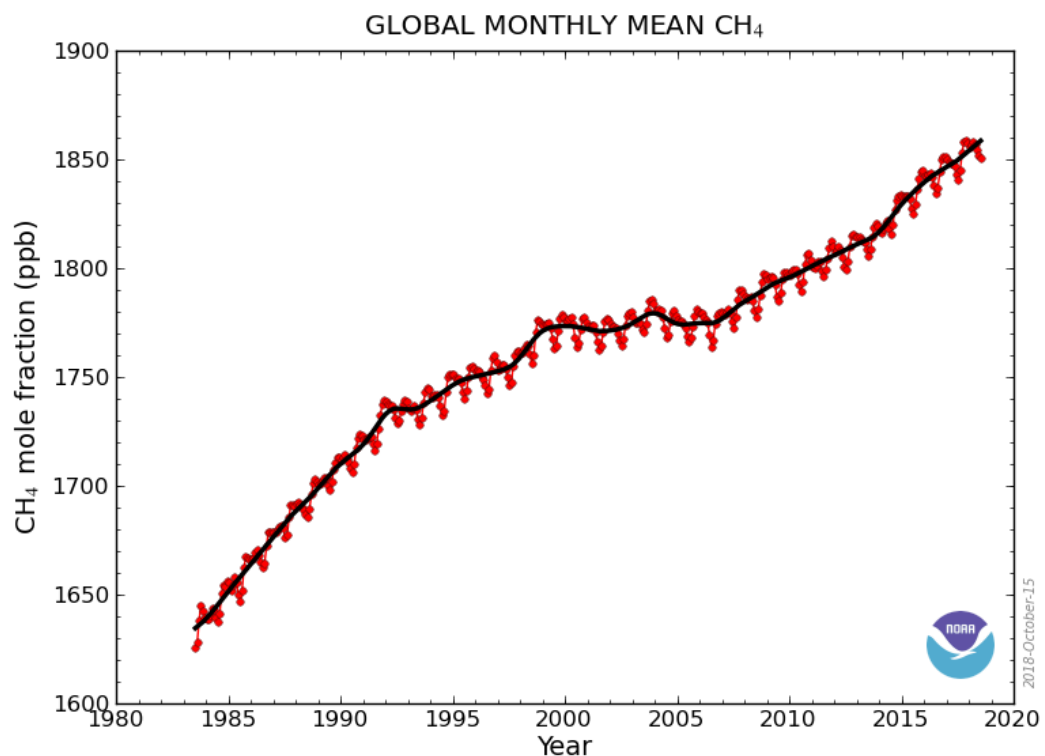


Figure 2.3 Global growth of methane in the atmosphere for the last three and half decades. Source:
<https://www.esrl.noaa.gov/gmd/ccgg/gallery/figures/index.html>

In 1991/1992, the eruption of Mt. Pinatubo and the major El Niño event had a strong impact on both methane sources and sinks (Dlugokencky *et al.* 1998). Following this event, methane growth rate decreased in 1992 due to decrease in the emissions from northern wetlands and from the fossil fuel sector of the former Soviet Union (Dlugokencky *et al.* 1998, 2001).

Strong methane growth resumed due to the largest El Niño event and the boreal biomass burning during the period 1997-1998. Growth increased globally from an average of 3.9 ppb per year during 1995-1997 to 12.7 ± 0.6 ppb in 1998 (Dlugokencky *et al.* 2001, 2011; Simmonds *et al.* 2005; Bousquet *et al.* 2006; Rigby *et al.* 2008)

During the late 1990s, methane growth rate decreased to 2.6 ± 0.6 ppb in 1999 (Dlugokencky *et al.* 2001, 2011). This decrease in the CH₄ growth rate was caused by the decline in anthropogenic emissions (Bousquet *et al.* 2006). The atmospheric methane growth rate increased again in 1999-2000 due to anthropogenic emissions related to the Chinese economy booming (Bousquet *et al.* 2006) with stable mixing ratios from 2000-2006 (Rigby *et al.* 2008; Frankenberg *et al.* 2011). A small increase occurred in 2002-2003 related to biomass burning in Boreal regions (Simmonds *et al.* 2005; Dlugokencky *et al.* 2009).

Apart from the strong impact of both the 1991-1992 Mt. Pinatubo eruption and the 1997-1998 El Niño event, the overall trend in methane growth from 1983 to 2006 shows a clear trend towards equilibrium (Dlugokencky *et al.* 2009; 2011; Nisbet *et al.* 2016).

The current methane rate is different and has been sustained since 2007. Renewed growth started near the beginning of 2007 (Fig. 2.4) with an increase in methane growth during 2007-2009 due to the imbalance of sources and sinks (Frankenberg *et al.* 2011). Global growth rate increased in both hemispheres during 2006-2007 with stronger emissions in the northern hemisphere (Fig. 2.4) (Rigby *et al.* 2008).

In 2007, the globally averaged mole fraction of CH₄ increased by 8.3 ± 0.6 ppb with the largest growth at high northern latitudes (Figure 2.4) (Dlugokencky *et al.*

2009). An increase in the atmospheric methane growth in 2008 was observed in the tropics (Dlugokencky *et al.* 2009). This increase was attributed to the tropical La Niña events and tropical wetlands, the largest sources in the global methane budget. After 2009 atmospheric methane increased with growth rate of 4-5 ppb/year (Sussmann *et al.* 2012; IPCC AR5 2013).

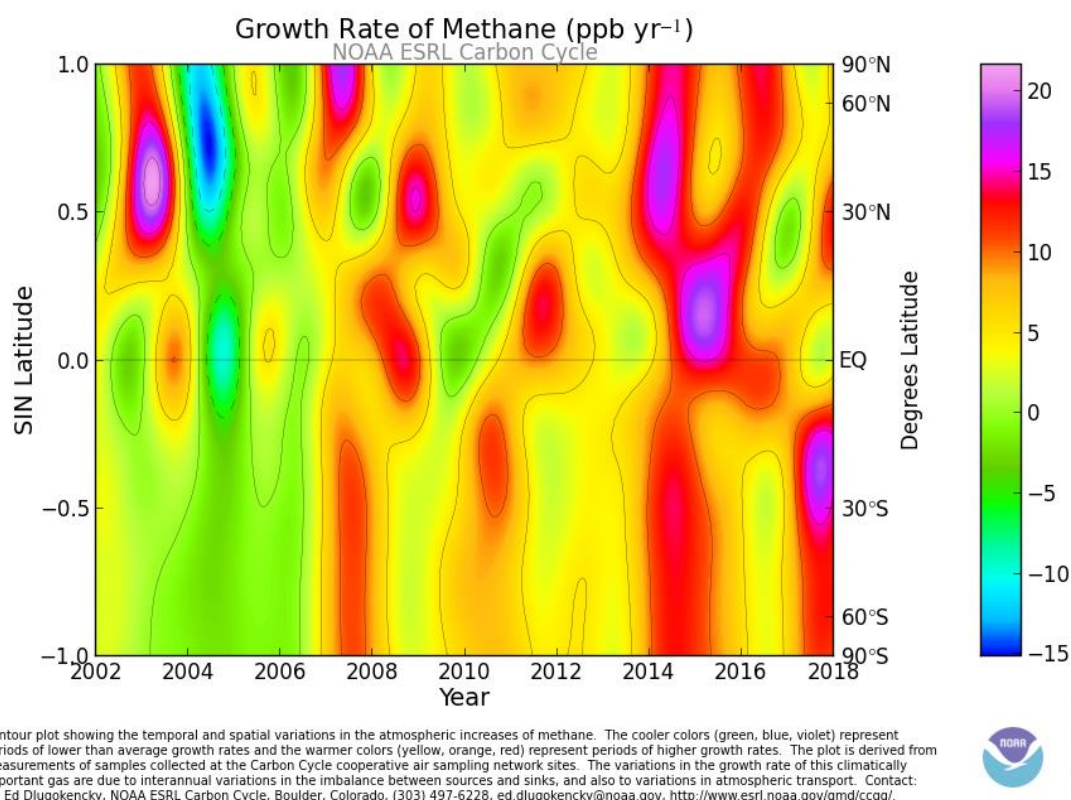


Figure 2.4 Methane growth rate (ppb y⁻¹) by latitude for the period 2002 to 2018, showing the post-2007 global methane rise. Source: <https://www.esrl.noaa.gov/gmd/ccgg/gallery/figures/index.html>

Overall, the globally averaged mole fraction of methane in the atmosphere increased by 5.7 ± 1.2 ppb yr⁻¹ from 2007 to 2013 (Nisbet *et al.* 2016). Negative shifts in carbon isotopic values ($\delta^{13}\text{C}$) over this time period were also documented by Nisbet *et al.* (2016) and Schaefer *et al.* (2016). In 2014, an extreme methane growth rate at 12.5 ± 0.4 ppb, associated with a further shift to more negative isotopic values, was observed at most latitudes (Figure 2.5) (Nisbet *et al.* 2016). The post-2007 methane rise was primarily attributed to the increased emissions from biogenic sources (Nisbet *et al.* 2016; Schaefer *et al.* 2016) with significant

contribution from rice paddies and ruminants in the tropics and likely a small contribution from fossil fuels, rice-harvested area, and animal populations (Nisbet *et al.* 2016). Nisbet *et al.* (2016) showed that tropical wetlands were probably the major components of the recent methane growth, whereas Schaefer *et al.* (2016) postulated that agriculture was the dominant contributor to methane rise. There have also been suggestions that the rise could be explained by decreases in OH (Rigby *et al.* 2017) or increases in fossil fuel emissions (Worden *et al.* 2017).

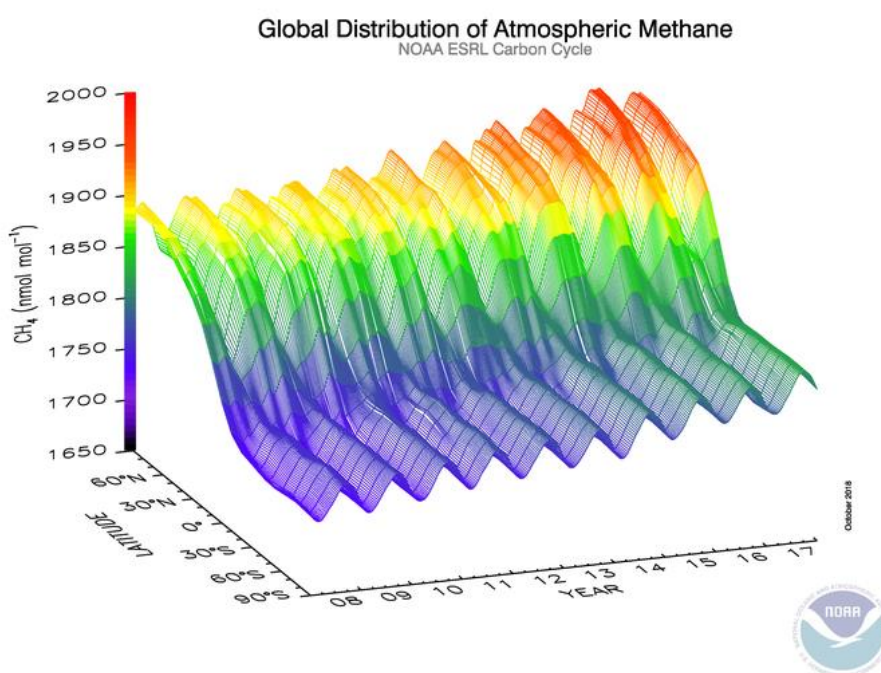


Figure 2.5 3D representation of the latitudinal distribution of atmospheric methane in the boundary layer for the period 2008 to 2017.

Source:

<https://www.esrl.noaa.gov/gmd/ccgg/gallery/figures/index.html>

2.5 Global Methane Emissions Sources

2.5.1 Methane from natural sources

Natural methane sources contribute around 40% of total methane emissions. Natural emissions are mainly from wetlands, which account for most of the total natural emissions with a mean emissions estimate of 187 Tg CH₄ yr⁻¹ (Sauniois

et al. 2016). Inter-annual CH₄ emissions from wetlands can greatly vary and can cause variations in the global CH₄ fluxes (Kirschke *et al.* 2013; Saunio *et al.* 2016). A small contribution to the global methane budget comes from other sources such geological sources, freshwater, termites and wildfires. All these sources can potentially grow or diminish in response to environmental change (Reay *et al.* 2018).

Wetlands

In wetland environments methane is formed under anaerobic conditions by microbial decomposition of organic materials. The sensitivity of this source is largely controlled by temperature, water table level and the substrate availability. Hence, future predictions of emissions are difficult. Generally, emissions would be expected to rise in warm and stagnant wetlands with high water table level and organic-rich soil (Christensen *et al.* 2003; Van Amstel 2012; Christensen & Panikov, 2002). Anaerobic conditions occur in waterlogged soil; in shallow lakes, peat areas and rice fields. The produced methane can be diffused while escaping from subsurface to the atmosphere. Consequently, the diffused methane is partially oxidised by methanotrophic microbes. Most of the methane is expected to oxidise if it diffuses upwards through the water column (Van Amstel 2012). Van Amstel (2012) suggested that most (90%) of the atmospheric methane in swamps and lakes escapes by bubbling up through the water column.

Estimates of natural wetland give a wide range from 155-235 Tg CH₄ yr⁻¹ (Saunio *et al.* 2016). Top-down and bottom-up estimates are 172 and 187 Tg CH₄ yr⁻¹ (Saunio *et al.* 2016) for the year 2012. (Bloom *et al.* 2010) suggested that tropical wetlands contributed 50-60 % of global emissions over 2003-2005.

Hydrates

Methane molecules captured or blocked in a water crystal structure are known as methane hydrates or clathrates. It is estimated that one cubic metre of hydrate can contain at least 170 cubic metres of methane (Van Amstel 2012). Methane hydrates have been invoked as an agent of climate change (Kennete *et al.* 2003). They are commonly found under certain temperature, pressure and depth conditions in permafrost regions and under continental margins and below sub-

sea and land permafrost (Maslin *et al.* 2010; Shakhova *et al.* 2010). Hydrate dissociation in response to reduced pressure or increased temperature can potentially produce rapid release of methane that has been trapped for very long time periods (Westbrook *et al.* 2009). Several studies suggested that methane emissions from hydrates are increasing but it is poorly known how much is being released and how much avoids oxidation in the water column and ends up to the atmosphere. Kirschke *et al.* (2013) suggested that hydrate emissions were approximately 6 (2-9) Tg/yr for the three decades 1980-2009. Saunio *et al.* (2016) estimate <2 (0-5) Tg CH₄ yr⁻¹.

Termites

Production and emission of methane by termite occurs via methanogenesis by microbial degradation of organic matter in their guts. Termites play a crucial role in many ecosystems. Their main food is both living and dead plants and their basic diet consists of wood and foliage (Sanderson 1996). Since the discovery of termite emitted methane, several studies have addressed their contribution to the global methane budget. An early study (Zimmerman *et al.* 1982) estimated that termites contribute between 75 – 310 Tg CH₄ yr⁻¹. Later studies have shown a much lower contribution. Kirschke *et al.* (2013) estimated termite emissions of 11 (2-22) Tg CH₄ yr⁻¹ for the period 1980-2009. There is only small inter-decadal variability but large global variability with the major contributors to the global termite source being Africa (30%) and tropical South America (36%). More recently, Saunio *et al.* (2016) estimated 9 (3-15) Tg CH₄ yr⁻¹ for the decade 2003-2012.

Geologic sources

Methane may be formed in many geological environments either via methanogenesis or thermogenic processes. Several studies have shown that major methane emissions are mainly related to hydrocarbon production in sedimentary basins with some related to geothermal/volcanic settings (Etiope *et al.* 2008). Four main geological sources are distinguished: microseepage, terrestrial microseeps, marine seeps and geothermal /volcanic fluxes. These have been described by several authors (Judd *et al.* 1999; Etiope *et al.* 2007, 2008). Global estimates of methane emissions from geological sources were

around 54 (33-75) Tg CH₄ yr⁻¹ (Kirschke *et al.* 2013) for the period 1980-2009 based on a bottom-up approach. More recent work by Saunio *et al.* (2016) only estimates 14 (5-25) Tg CH₄ yr⁻¹ for the year 2012 based on a bottom-up approach.

Other natural sources

Additional natural sources of methane include both vegetation and wildfires. Keppler *et al.* (2006) first reported, from laboratory experiments that terrestrial plants can produce and emit methane directly under anaerobic conditions. There has been since, growing and convincing evidence that plants can produce methane even in the presence of oxygen (Keppler *et al.* 2009; Wishkerman *et al.* 2011; Liu *et al.* 2015) Bruhn *et al.* 2012. Trees are an important pathway for CH₄ produced in soils to be transported to the atmosphere (Pangala *et al.* 2015). Keppler *et al.* (2009) estimated global emissions from vegetation between 0 and 50 Tg CH₄ yr⁻¹.

Biomass burning in the boreal forests produce and emit methane to the atmosphere. Natural wildfires occur in tropical regions as well as America, Eurasia and Australia (Kasischke & Bruhwiler 2003). Global methane emissions from wildfires are estimated at 3 (1-5) Tg CH₄ yr⁻¹ for the decade 2000-2009 (Denman *et al.* 2007; Kirschke *et al.* 2013) and for 2003-2012 (Saunio *et al.* 2016).

2.5.2 Methane from Anthropogenic sources

Anthropogenic sources have received more attention than natural sources as the substantial addition of human induced greenhouse gases during the past century has contributed to climate change (IPPC 2013a). Top down estimates of methane emissions attribute around 60% of total global methane to anthropogenic sources (Saunio *et al.* 2016). Total emissions of anthropogenic methane have been estimated at 352 (340-360) Tg CH₄ yr⁻¹ for the 2003-2012 decade. Anthropogenic sources comprise a wide range of human activities such as rice paddy agriculture, waste disposal, landfills, sewage, livestock and fossil fuel extraction, storage, transformation, transportation and use, including oil, natural gas and coal mining (Ciais *et al.* 2013; NASEM 2018). Anthropogenic sources are dominated by

agriculture and fossil fuel related emissions with estimated mean methane emissions of 197 Tg CH₄ yr⁻¹ and 134 Tg CH₄ yr⁻¹ respectively.

Types of anthropogenic sources and their global methane emissions estimates. are listed in Table 2.1.

Rice Cultivation

Rice cultivation is an important anthropogenic source of methane and most of world's rice grows in flooded fields. Aerobic decomposition of organic matter depletes the oxygen in the soil, resulting in anaerobic conditions in which methane is formed by methanogenic archaea (Reay *et al.* 2010; Van Amstel, 2012; Saunio *et al.* 2016). The produced methane escapes to the atmosphere primarily via diffusive transport but also through bubbling and transport through plants (Van Amstel, 2012; Saunio *et al.* 2018). Methane production depends on the soil types, rice variety, periods of flooding, and climate (Van Amstel, 2012). Estimates of global methane emissions from rice cultivation are variable but have significantly declined with time. These variations have been attributed to the lack of data regarding the irrigated and rain-fed areas as well as about deep-water and upland rice (Van Amstel, 2012). Earlier studies (Matthews & Fung 1987) suggested a global emission of 40 – 160 Tg CH₄ yr⁻¹ whereas more recent studies suggested only 25-60 Tg CH₄ yr⁻¹ (Reay *et al.* 2010). Based on the IPCC fifth assessment report (Ciais *et al.* 2013), rice paddies account for 33-40 Tg CH₄ yr⁻¹. Saunio *et al.* (2016) estimate the range from 24-36 Tg CH₄ yr⁻¹ for the 2003-2012 decade. The majority (90%) of rice paddy methane emissions comes from Asian monsoon countries, and around 50% from just India and China (Yan *et al.* 2009; Reay *et al.* 2018).

Biomass burning

Biomass burning, or the burning of vegetation, can include the deliberate burning of living and/or dead vegetation. Methane is produced and emitted because of incomplete combustion in cooler and/or oxygen-deficient fires (Levine 2010). Anthropogenic burning is thought to be more important (90%) than natural fires (Page *et al.* 2002). Compounds released from biomass in the form of carbon monoxide, methane, non-methane hydrocarbons, oxides and nitrogen have

impacts on the climate (Van Amstel, 2012). Every biomass fire consists of four phases of combustion; flaming, pyrolysis, smouldering and glowing. These phases depend on the biomass type and conditions during the fire. A large quantity of methane is produced particularly during the smouldering phase (Van Amstel, 2012). The majority (90%) of global biomass burning occurs in tropical forests of South America and Southeast Asia and in the savannas of Africa and South America (Page *et al.* 2002; Kirschke *et al.* 2013). The IPCC (Ciais *et al.* 2013) estimate of methane emissions from biomass ranges between 32-39 Tg CH₄ yr⁻¹. The expected future global temperature increase of 2-4°C due to the projected increase in greenhouse gases will likely lead to an increase in the level of fire activity throughout the world's forests thus causing an increase in methane emission (Reay *et al.* 2010).

Fossil Fuels

Oil and gas systems are one of the leading sources of anthropogenic CH₄ emissions, accounting for 23% of the total global CH₄ emission in 2010 (USEPA 2012). Methane can leak during field exploration and production, operation of vents and flares, production of natural gas and oil, compression of gas for transport and oil tanker loading and transport (IPCC 2006b; Van Amstel, 2012). The fossil fuel industry is estimated to emit 96 (85-105) Tg CH₄ yr⁻¹ of methane into the atmosphere for the period 2000-2009 based on the bottom-up estimate (Kirschke *et al.* 2013). Saunio *et al.* (2016) estimated a fossil contribution of 80 (78-94) Tg CH₄ yr⁻¹ to the global methane budget. The escape of natural gas (>90% methane; Wuebbles & Hayhoe, 2002) during extraction, transport and combustion processes can be a significant source of methane.

Global emissions from oil and natural gas systems are expected to rise 56% between 2010 and 2030 (USEPA 2013). Van Amstel (2012) estimated a total emission of 15 Tg CH₄ yr⁻¹ and 45 Tg CH₄ yr⁻¹ from oil vents and gas leaks respectively. Methane leakage from the oil and gas system can practically be reduced to the minimum by capturing the methane emitted during drilling processes and re-injecting it back underground, use of high pressured pipes for gas transmission and use of Glycol for gas drying (Van Amstel 2012). Methods for estimation of methane emissions from fossil fuel are explained in detail by the

IPCC guidelines (IPCC 2006b).

Solid waste disposal and landfill

Treatment and disposal of municipal and industrial waste produce considerable amounts of biogenic methane (CH₄) and carbon dioxide (CO₂) as well as smaller amounts of non-volatile organic compounds, nitrous oxide (N₂O) and carbon monoxide (CO) (IPCC 2006c). Methane is formed in response to microbial processes occurring in organic matter within the waste under anaerobic conditions. The time lag of methane production and emission depends on the waste water contents, temperature and the presence of readily degraded materials such as food waste (Börjesson *et al.* 2001; Van Amstel 2012). The produced methane contributes approximately 3 to 4% to the annual global anthropogenic emissions (IPCC 2006c).

Methane is continuously produced from landfills for several years. Based on the IPCC fifth assessment report (Ciais *et al.* 2013), landfills and waste contributed between 67 to 90 Tg CH₄ yr⁻¹ for the period 2000-2009. Van Amstel (2012) estimated lower values of 36 Tg CH₄ yr⁻¹ for 1990 and 46 Tg CH₄ yr⁻¹ for 2010. More recently, Saunio *et al.* (2016) estimated a range from 52 to 63 Tg CH₄ yr⁻¹, about 18% of total global anthropogenic emissions.

According to the IPCC guidelines (IPCC 2006a), methane emissions from solid waste disposal sites can be estimated based on the widely accepted First Order Decay (FOD) or time dependent model. The model assumes that methane production potential depends solely on the amount of the Degradable Organic Carbon (DOC) in the waste, which typically declines slowly over time. Hence, the highest methane emissions occur in the first few years after waste is deposited in a disposal site, then gradually decays throughout a few decades as the degradable carbon material is consumed (Einola *et al.* 2007; IPCC 2006a).

The amount of methane that is oxidized before emission to the atmosphere is directly affected by the thickness, temperature, physical properties and moisture content of the cover soil layer (Börjesson *et al.* 2001; Bogner & Matthews 2003). Even with a substantial soil cover a small fraction of CH₄ generated will diffuse through fissures/cracks, escaping the oxidation process through the cover soil.

The CH₄ generated at landfills can be recovered and combusted in a flare or through installation of a gas extraction pipeline network, extracted to produce energy.

Based on the IPCC report (IPCC 2006c), the uncertainty in the estimate of the CH₄ emission from landfills lies in two areas, uncertainty due to the methodology of the model itself, and uncertainty attributed to each of the input parameters. Although the FOD is widely used, it is important to note that it is a simple model of a very complex and poorly understood system. The period between deposition of the waste and full production of CH₄ involves a series of complex reactions that change over time and the reaction rate varies according to the landfill conditions. Moreover, parameters such as thickness and temperature may vary even within the same landfill.

Sewage

Sewage or wastewater can be a source of methane when disposed or treated anaerobically. Methane is emitted from a variety of domestic, commercial and industrial liquid wastes (IPCC 2006d; Van Amstel, 2012). Domestic sewage is defined as wastewater from household water use, whereas industrial wastewater is produced by industrial activity. Centralised anaerobic wastewater treatment plants are becoming more desirable, particularly in developed countries (van Eekert et al. 2010).

The potential amount of methane generated in different waste types and the actual emitted methane from the different types of treatment depends primarily on the quantity of degraded organic materials in the wastewater, temperature, storage time and treatment type. The most common parameters used to measure the organic component of the sewage are Chemical Oxygen Demand (COD) and Biological Oxygen Demand (BOD) (IPCC 2006d; van Eekert *et al.* 2010). Wastewater with higher COD or BOD generally yields more CH₄ than those with lower COD or BOD (IPCC 2006d). Methane emissions from sewage treatment systems were estimated by Van Amstel (2012) based on the growth of sewage treatment. His global estimate is 30 Tg CH₄ yr⁻¹ for the year 2010 based on a bottom-up approach.

Doorn et al. (1999) and IPCC (2006d) provide good practice guidelines for CH₄ emission estimation. The IPCC calculates methane emissions from wastewater using the maximum capacity of CH₄ that can be produced from a given quantity of organics (BOD or COD) and a correction factor that indicates the degree to which the treatment and discharge system is anaerobic. Methane estimation steps and equations for both domestic and industrial wastewater are explained in great detail by the IPCC guidelines (IPCC 2006d).

Enteric fermentation; Ruminants

An overview of methane emissions from ruminants is provided by Kelliher and Clark (2010). Farming of ruminants such as cattle, buffalo, goats, sheep, and camels for both meat and dairy products results in a large amount of methane emitted to the atmosphere (Johnson *et al.* 2002). Methane is formed by anaerobic microbial activity in their digestive systems. Ruminants have a four-part stomach with two anterior chambers, which enables an intensive microbial fermentation that produces methane. They develop symbiotic relationships with methanogens in order to break down cellulose to produce carbohydrates that are largely used for energy. Methane is produced as a by-product of this process (Reay *et al.* 2010). The vast majority of methane is released through the mouth of the multi-stomached ruminants, approximately 87% through eructation and respiration (Sauniois *et al.* 2016).

The amount of CH₄ produced by ruminants is strongly influenced by the total weight of animal and their diet (Sauniois *et al.* 2016; IPCC 2006e). Sauniois *et al.* (2016) inferred a range of 97-111 Tg CH₄ yr⁻¹ of global methane emissions from ruminants for the decade 2003-2012 and included both enteric fermentation and manure management. The IPCC fourth assessment report (IPCC AR4 2007) and Van Amstel (2012) have estimated global methane emissions by ruminants to be 84 Tg CH₄ yr⁻¹ (year 2000) and 74 Tg CH₄ yr⁻¹ (year 2010) respectively.

Quantification of methane emissions from ruminants has been studied worldwide (Grainger *et al.* 2007; Ji & Park 2012). Methods for measuring and estimating methane emission from ruminants are reviewed by Storm *et al.* (2012) and Grainger *et al.* (2007). Methodologies range from simple animal respiration chambers to modelling techniques. The IPCC (IPCC 2006e) guidelines provide a

comprehensive methodology together with the necessary equations for quantifying emission inventories. Emissions are simply estimated by multiplying the number of animals by an emission factor for a specific livestock population. The accuracy of the emission estimate is positively related to the quality of the data.

Manure management

Methane emissions from animal manure tend to be smaller than enteric emissions. The primary organic matter composition of manure gives rise to potential CH₄ emission when treated in liquid-based systems like lagoon or manure tanks (Reay *et al.* 2010; Van Amstel 2012). When manure is kept in contact with oxygen (i.e. spread in the field or paddock), it tends to decompose aerobically, hence producing little CH₄ (Van Amstel 2012; Sauniois *et al.* 2016). Animal manure emissions are often included in the total ruminant methane emissions but tend to be separated when methane mitigation is considered (Reay *et al.* 2010). The manure management system of each country strongly influences the production and emissions of methane (Van Amstel 2012).

Parameters such as ambient temperature, moisture, and manure storage influence the growth of archaea that produce CH₄ (Sauniois *et al.* 2016). Manure CH₄ emissions are also influenced by the amount and composition of the manure and the manure portion that decomposes anaerobically (Reay *et al.* 2010). Estimates of CH₄ emissions from manure can be carried out by multiplying the amount of manure per animal category and/or country with an emission factor for the defined livestock population (van Eekert *et al.* 2010).

2.6 Isotopic Analysis of Methane Sources

The isotopic composition of methane is determined by specific chemical and physical properties that typically yield valuable information regarding the relative strength of methane sources and sinks and their contribution to the atmospheric methane budget (Wuebbles, & Hayhoe 2002). $\delta^{13}\text{C}$ refers to the ratio of $^{13}\text{C}:^{12}\text{C}$ relative to the Vienna Pee Dee Belemnite (VPDB) standard (Wuebbles & Hayhoe 2002; Sherwood *et al.* 2017). The isotopic signatures are given by the deviation of the sample isotopic ratio $[(^{13}\text{C}/^{12}\text{C})_{\text{Sample}}]$ relative to a given standard $[(^{13}\text{C}/^{12}\text{C})_{\text{Standard}}]$ and are expressed as per mil (‰) using the following equation (Kirschke *et al.* 2013; Saunio *et al.* 2016).

$$\delta^{13}\text{C} = \left(\left[\frac{(^{13}\text{C}/^{12}\text{C})_{\text{Sample}}}{(^{13}\text{C}/^{12}\text{C})_{\text{Standard}}} \right] - 1 \right) \times 1000$$

The ratio of deuterium (D) to hydrogen (H) in the methane (δD) can also provide insights into the origin of detected CH_4 emissions but much less data is available than for $\delta^{13}\text{C}$ (Dlugokencky *et al.* 2011; Zazzeri *et al.* 2015, 2017; Townsend-Small *et al.*, 2016). Isotopic composition is important to understand changes in atmospheric methane emissions and provide additional information on the source and sink distribution. Isotopes can also be useful in determining methane oxidation (Liptay *et al.* 1998). Isotopic measurements carry valuable information about CH_4 sources because they may be enriched or depleted in $\delta^{13}\text{C}$ or δD relative to the ambient background air (Dlugokencky *et al.* 2011). The global mean of the carbon isotopic composition of atmospheric methane ($\delta^{13}\text{C}$) is -47‰ and this signature varies temporally and spatially (Wuebbles, & Hayhoe 2002; Fisher *et al.* 2006).

All three types of methane sources have distinct isotopic $\delta^{13}\text{C}$ signatures; -70 to -50 ‰ for biogenic, -55 to -25 ‰ for thermogenic and -35 to -10‰ for pyrogenic sources (e.g. Dlugokencky *et al.*, 2011, Kirschke *et al.* 2013). ^{13}C depleted or light CH_4 is typically produced by biological sources, whereas ^{13}C -enriched or heavy methane is emitted mainly from pyrogenic and thermogenic sources such as coal mining and biomass burning (e.g. Zazzeri *et al.* 2015). Biological sources vary isotopically depending on the production pathway and the amount of methane oxidation that takes place before emission. The isotopic signatures of different methane sources have been studied by many authors in different places (e.g.

Liptay *et al.* 1998; Lowry *et al.* 2001; Fisher *et al.* 2006, 2017; Dlugokencky *et al.* 2011; Zazzeri *et al.* 2015; France *et al.* 2016; Schwietzke *et al.* 2016).

Even for a particular source category however there can be variations in the isotopic signatures. Methane emissions from natural gas have variable isotopic signatures due to the formation characteristics such as temperature of the gas production, for example West-Siberian pipeline emissions are around -50‰, whereas in the North Sea they are around -35‰ to -25‰ (Lowry *et al.* 2001; Dlugokencky *et al.* 2011). The wetland emission signatures vary with latitude between -70‰ and -60‰ at high northern latitudes and typically -60‰ to -50‰ in tropical climates (Dlugokencky *et al.* 2011). Pangala *et al.* (2017) studied the emissions of soil methane transported through trees and found that the average $\delta^{13}\text{C}$ value is -66 ± 6 ‰. Each type of plant has a distinctive isotopic composition affecting methane released from either burning or digestion. C3 and C4 plants have different isotopic signatures related to different photosynthetic pathways. C3 plants have a carbon isotope composition between -35‰ and -21‰ and the C4 plant pathway -20‰ to -10‰ (Reeburgh, 2003). The digestion of these plants by ruminants results in different isotopic signatures during eructation. Ruminants eating C3 plants emit methane with $\delta^{13}\text{C}$ of -70‰ to -60‰ and -55‰ to -50‰ for those digesting C4 plants (Dlugokencky *et al.* 2011), representing a fractionation of about 35‰ from the source vegetation to the produced methane. Figure 2.6 show a range of isotopic methane signatures for both natural and anthropogenic sources.

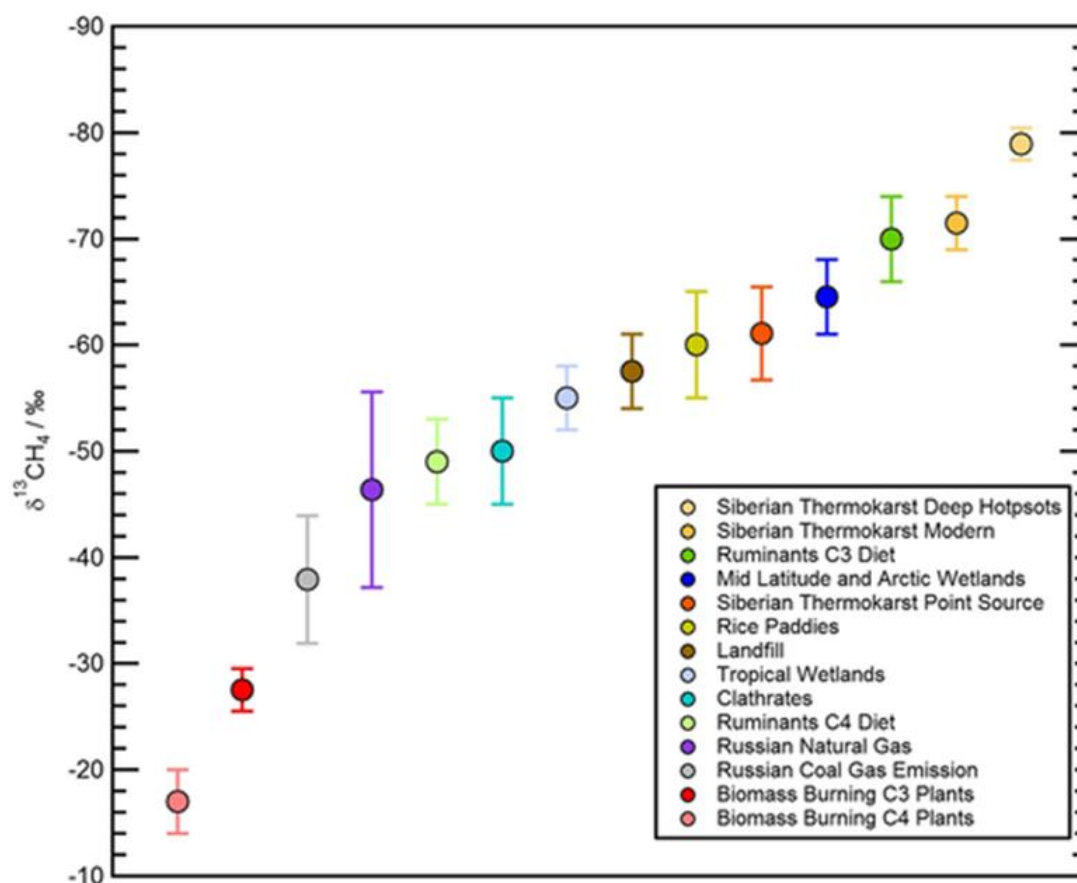


Figure 2.6 Isotopic ranges of $\delta^{13}\text{C}$ for CH_4 for a variety of natural and anthropogenic CH_4 sources. source: France et al,2016.

Sherwood *et al.* (2017) have recently set up a comprehensive CH_4 source signature database that allows much more accurate characterisation of globally and regionally representative isotopic source signatures from fossil fuels (conventional natural gas, shale gas, and coal), microbial (wetlands, rice paddies, ruminants, termites, and landfills and/or waste) and biomass burning sources. The database consists of 10,706 samples from 190 published references, of which 8734 are fossil fuels and 1972 are non-fossil (Figure 2.7), which represents a large bias considering the proportion of emission from fossil sources. The 2017 version of their database can be accessed from the NOAA Earth System Research Laboratory link: (<https://www.esrl.noaa.gov/gmd/ccgg/arc/?id=123>). Several studies have also shown that the previous global CH_4 budget models have mostly relied on poorly constrained $\delta^{13}\text{C}$ values (Schwietzke *et al.* 2016; Sherwood *et al.* 2017).

Much of the methane isotope data that have been published have been from studies in the US and Europe and there have not been many measurements of the isotopic signature of methane emissions from the Middle East. As many of the sources have isotopic signatures that can vary regionally then it will be important to add isotopic signatures from emissions in this region to the global database.

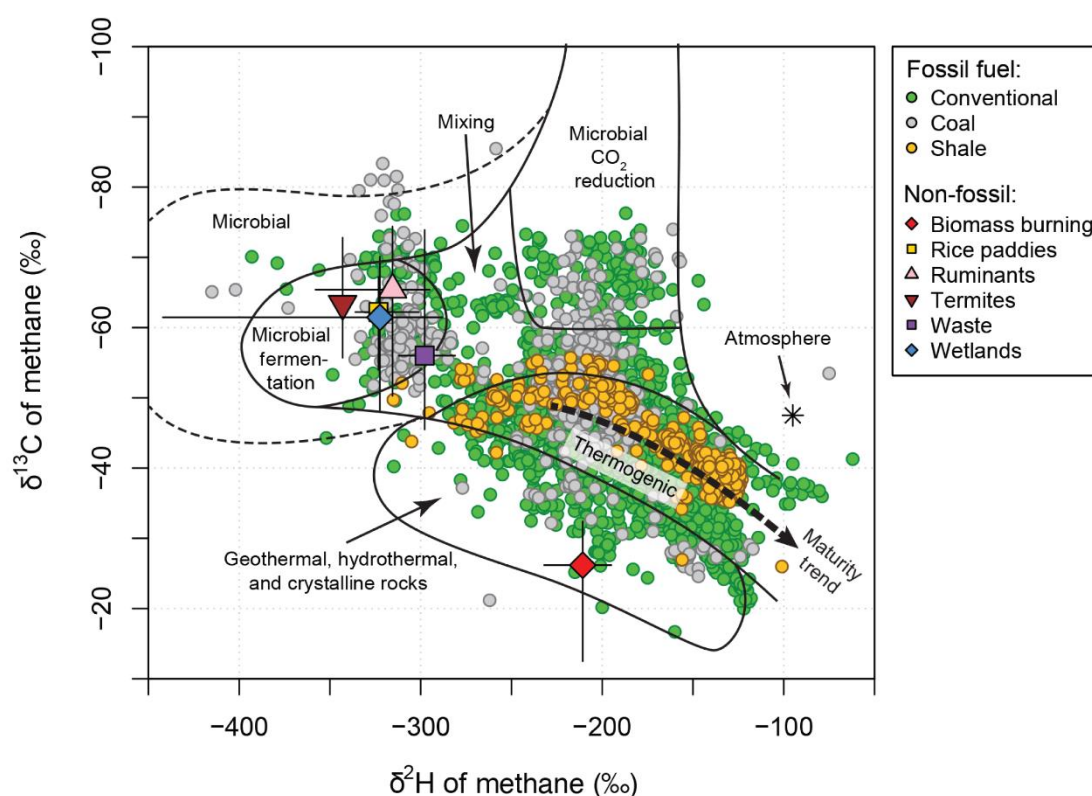


Figure 2.7 Characterisation plot of $\delta^{13}\text{C}\text{-CH}_4$ versus $\delta^2\text{H}\text{-CH}_4$ showing the distribution of methane sources. Source: Sherwood et al., 2017

C_{HAPTER 3}

M_{ETHODOLOGY}

3. Methodology

Some sources responsible for methane plumes are isotopically distinct. Thus, the actual methane source and its contribution to the atmospheric methane budget can be identified by measuring the carbon isotopic composition of methane in air samples (Levin *et al.* 1999; Dlugokencky *et al.* 2011). The importance of isotopic analysis as a tool that links methane emissions to specific sources and in verifying inventories has been supported by several studies (Levin *et al.* 1999; Lowry *et al.* 2001; Fisher *et al.* 2006; Townsend-Small *et al.* 2012; Zazzeri *et al.* 2015, 2017).

3.1 Sample Collection

Air sample collection in Kuwait was carried out in four different ways: 1) 6 days sampling during the Kuwait mobile campaign, 2) diurnal sampling, 3) site-specific sampling (e.g. landfills and oil fields) and 4) regular (weekly) sampling over two years - 2015 and 2016. Samples were collected in 3-litre Tedlar bags (SKC Ltd) using a battery-operated micro diaphragm pump (KNF Neuberger Ltd.). The air sampling tube was flushed with ambient air for 10 seconds to prevent contamination. Each bag took approximately 35 seconds to be filled. All the bags were 75% full and carefully sealed to avoid contamination or leakage and expansion during the shipment to Royal Holloway laboratory for analysis. Figure 3.1 shows the sampling method.



Figure 3.1 The sampling method (Tedlar bag and battery-operated diaphragm pump)

Three sampling sites were selected for the weekly methane measurements in Kuwait. Methane measurement was carried out upwind (Al-Mutla) and downwind (Fahaheel) at 2 metres above the ground as shown in Figure 3.2. The third sampling site was on the roof of the Department of Earth and Environmental Sciences at Kuwait University at 6 meters above ground (Khaldiya).

All air samples collected in Kuwait were shipped to Royal Holloway University of London (RHUL) Greenhouse Gas Laboratory for analysis.



Figure 3.2 Air sampling in Al-Mutla area, Kuwait.

3.1.1 Kuwait sampling campaign

The $\delta^{13}\text{C}$ signatures of the methane sources in Kuwait were carefully defined. Investigation of methane sources required a dedicated sampling campaign. This campaign was carried out from 2nd to 7th of May 2015 and targeted the methane emissions sources in the State of Kuwait. Many sources were investigated during this campaign such as landfills, sewage treatment plants, refineries, oil fields and animals. The Picarro mobile system was used in this campaign. The instrument was shipped to the Department of Earth and Environmental sciences, Kuwait University, Faculty of Sciences on 29th of April 2015 and tested in an air-conditioned laboratory on 1st of May, 2015. The mobile Picarro was set up in a 4X4 vehicle on 2nd of May 2015, when the first survey of this campaign commenced. Figure 3.3 shows the route for all surveys covered during this campaign. Methane plumes were measured while driving on public roads around the target area where possible. Air samples were collected downwind and upwind and across the source plume. In this campaign various potential sources were investigated on the same day. For urban areas with multiple methane sources, this method is particularly valuable. Several studies have also used this method (Phillips *et al.* 2013; Zazzeri *et al.* 2015, 2017).

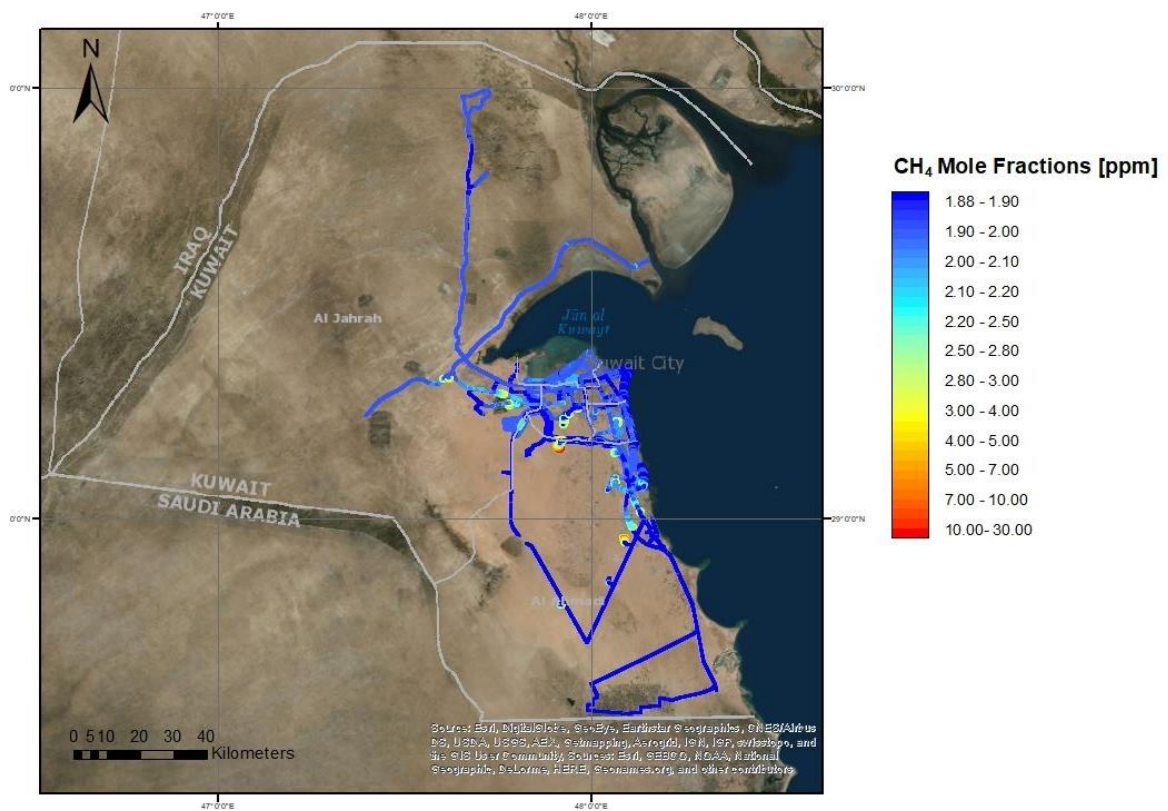


Figure 3.3 GIS plot of methane mole fractions in ppm recorded for 2nd to 7th May 2015 showing the route of the 6-days of surveys in Kuwait.

3.2 Sample Analysis

3.2.1 Picarro mobile system

Measurement of the methane (CH₄) concentration utilised monitoring equipment consisting of a high-precision mobile Picarro G2301 CRDS (Cavity Ring-Down Spectrometer) analyser. The system is capable of measuring carbon dioxide (CO₂) and methane (CH₄) concentrations at ppb sensitivity with negligible drift, as well as water vapour in percentage (%) every 3 seconds.

The Mobile Picarro G2301 is equipped with an A0491 Mobile Module, consisting of an analyser pump, control systems for a Climatronics sonic anemometer and a GPS receiver. A high-resolution Garmin GPS16X was used to record the location and time stamp data of each measurement. The anemometer was mounted on the roof of a vehicle at an elevation of 2.2 m above the ground. The system consists of two air inlets (Figure 3.4A.), the GPS receiver and anemometer. With the aid of three fully charged 12 V, 110 Ah lead-acid, re-chargeable batteries, the Picarro instrument can run for up to 9 hours. Figure 3.5 shows a simple arrangement of the Mobile Picarro components and sampling used in this study. This configuration can always be modified to fit the vehicle used for each measurement campaign.

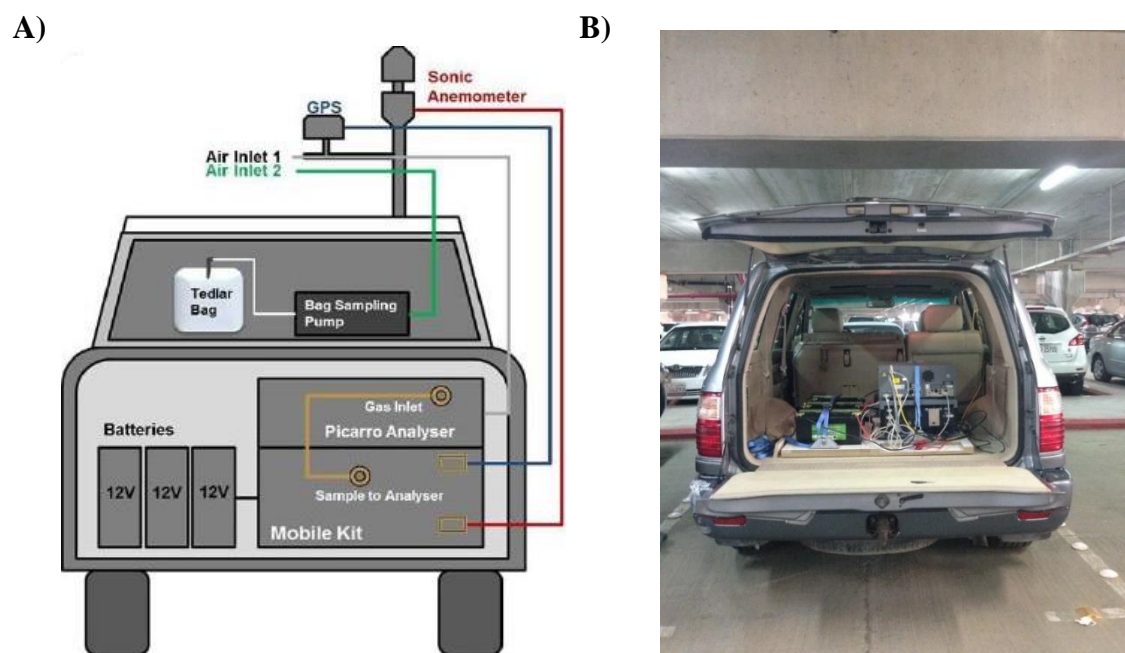


Figure 3.4 shows A) Schematic set up of the RHUL Picarro mobile measurement system and all the physical connections by (Zazzeri *et al.* 2015) B) Vehicle used in the Kuwait sampling campaign

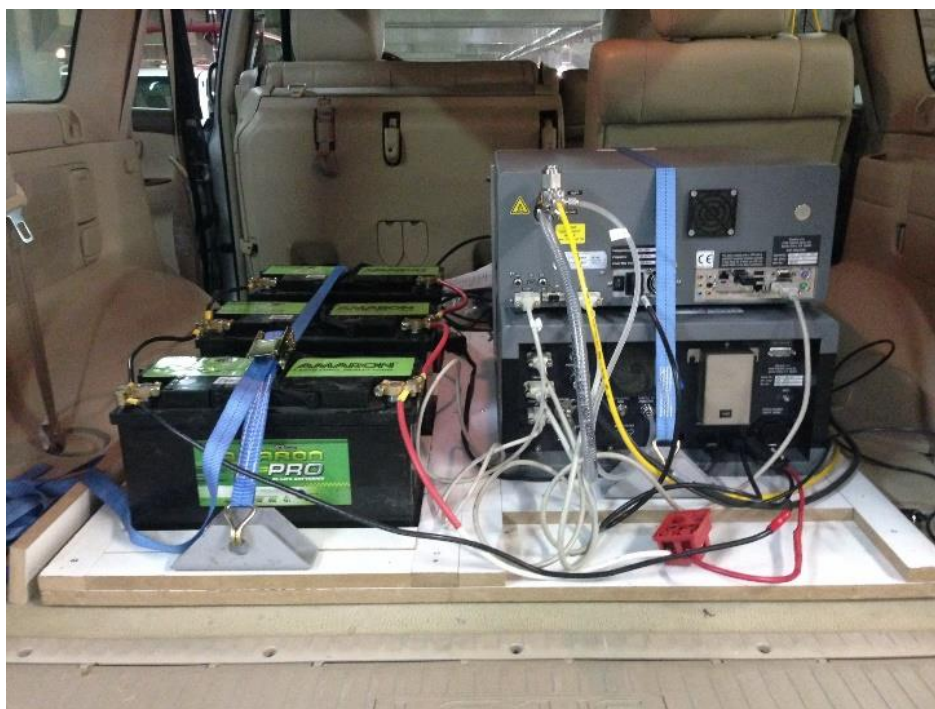


Figure 3.5 The Picarro mobile measurement system set up in this study

The first air inlet of the Mobile Picarro (inlet 1; Figure 3.4A) is a $\frac{1}{4}$ " outer diameter and 1.83 m length Nylon tube with blocked end and a series of 2 mm diameter holes drilled into the first 30 cm to allow air ingress (Picarro 2012). The flow is split so approximately 300 cc/min of the air flows through a 2 μ m Swagelok filter to the Picarro, and the rest vents after the mobile module pump. Flow split plays a crucial role in reducing the lag time between the air entering the inlet and the measurement. The second air inlet (inlet 2; Figure 3.4A) is $\frac{1}{4}$ " outer diameter Nylon tube attached to a battery-operated diaphragm pump (KNF Neuberger). This inlet is used to collect plume and background air samples that are analysed for mole fraction and $\delta^{13}\text{C}$ of methane later in the RHUL greenhouse gas laboratory.

The Picarro analyser can be connected to a laptop, tablet or even smart phone via Wifi connection to a 3G or 4G system. This allows continuous observation of the measured CO₂ and CH₄ mole fractions by the passenger during travel. The fact that the measured CO₂ and CH₄ can be displayed in real time on Google Earth allows on-site geospatial visualisation of the gas plumes (Figure 3.7). Approximately 7 seconds delay time between the instantaneous GPS location and the display of Picarro concentrations has been calculated by measuring the time lag of the CO₂ peak arrival.

Instrument calibration

Good comparability between measurements is essential. The Picarro Mobile 2301 instrument was calibrated before it was shipped to Kuwait in the RHUL greenhouse gas laboratory against three calibration standards, two from National Oceanic and Atmospheric Administration (NOAA; <http://www.esrl.noaa.gov/gmd/cc1/>) and one from Max Planck Institute Jena Gas Lab, and this was repeated after the instrument was returned to RHUL after the campaign had finished. Results have shown ± 0.5 ppb precision and Table 3.1 shows the mole fraction of the standards before and after the Kuwait campaign. The drift in measurements between the 2 calibrations was small (less than 0.0009 ppm).

STANDARDS	KNOWN CH₄ (PPM)	MEASURED CH₄ (PPM) 30/3/2015	MEASURED CH₄ (PPM) 14/5/2015
NOAA10	1.8497	1.8530	1.8533
NOAA12	1.9936	1.9965	1.9974
TR-RHUL-2011-3	2.0007	2.0044	2.0043

Table 3.1 Calibration of methane mole fraction using the Picarro mobile system at the RHUL lab before and after Kuwait campaign.

All raw data from the mobile Picarro were converted by using Equation 3.1 as derived in Figure 3.6

$$\text{Corrected CH}_4 \text{ ppm} = (0.99927 \times \text{Raw CH}_4 \text{ ppm}) - 0.00205 \quad (3.1)$$

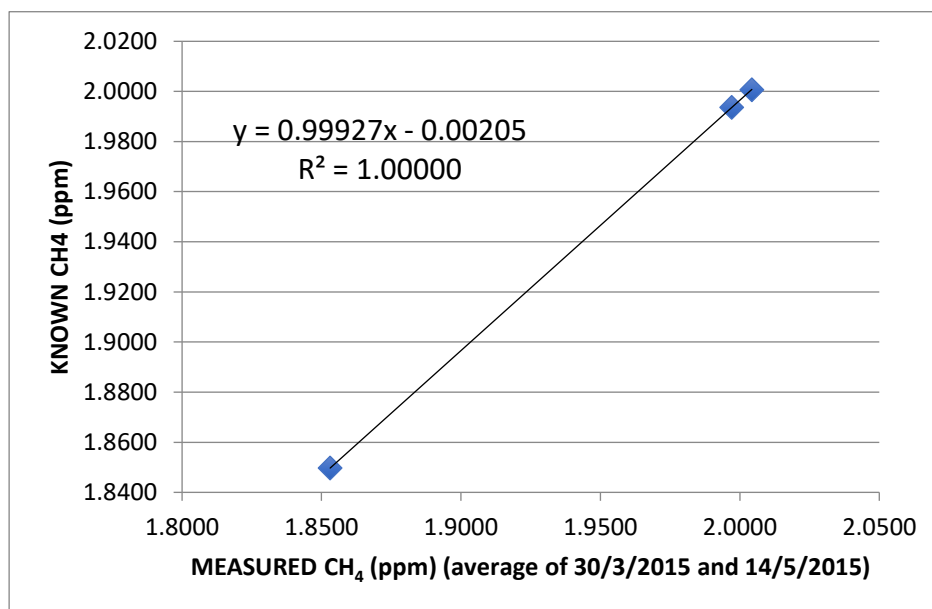


Figure 3.6 The calibrated against measured values of CH₄ for three standard tanks measured before and after the Kuwait campaign using the Picarro mobile system.

Methane concentrations at the sites of interest were investigated by driving downwind and using Google Earth to visualise the mole fractions in real time. An example of the sampled data displayed on Google Earth is shown in Figure 3.7. At some locations, the bisection of the plume perpendicular to the wind direction allowed mapping of the Gaussian shape.

Once the methane plume was identified, 3L Tedlar bags were filled at both close to the plume centre and at plume edges. Tedlar bag samples were generally collected across the plume by stopping the vehicle whenever methane mole fractions were detected above the background. In some cases, it wasn't possible to stop so some samples were collected while driving. The speed at which samples were collected while driving ranged between 25 km/hr, in urban area and sources sites as landfills

and 60 Km/h for the highway. In addition, 'background' samples were collected away from plumes.

After each measurement survey, the raw data produced by the Mobile Picarro analyser was directly obtained via USB for analysis. The acquired raw file comprises the following; (1) measurements of the CO₂ and CH₄ mole fractions in ppm; (2) GPS coordinates (longitude and latitude) in degrees; (3) water content in percentage; and (4) wind speed and direction (wind vector). The raw file was converted into a KML file and visualised on Google Earth where the total series of mole fractions were reproduced as shown in Figure 3.7.

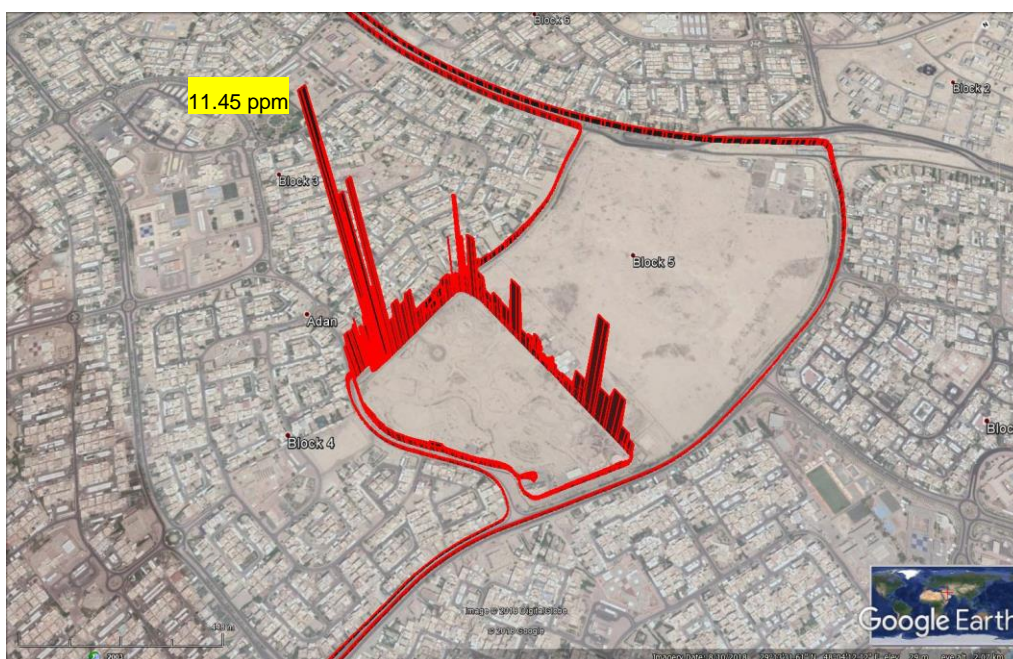


Figure 3.7 Google Earth view of methane plumes detected around Al-Qurain landfill on 4th of May 2015. The high peak of CH₄ is 11.45 ppm.

Prior to each survey, independent estimation of wind direction and speed via the Meteorological Department, Directorate General of Civil Aviation of the state of Kuwait (www.met.gov.kw) allowed assessment of the accessibility of the downwind area of the source. During the survey, the sampling route was directed by the instantaneous visualisation of mole fractions. Although the Google Earth display of the data shows the methane plume location, it does not actually represent the plume

size due to poor visualisation. Therefore, mole fraction data were re-plotted during post-analysis using GIS software. Satellite images of the sites were used as base maps to better display the mole fraction range and give a clearer spatial representation of the data.

3.2.2 Royal Holloway University of London Atmospheric Laboratory

The RHUL Greenhouse Gas Laboratory has high precision measurement equipment for ambient air greenhouse gas analysis. Methane mole fraction was measured (ppm) using a Picarro G1301 Cavity Ring-Down Spectrometer. The Trace Gas – Isoprime spectrometer system (CF-GC-IRMS) was used to measure methane isotopic ratio. This section describes both instruments in more details.

Measurement of Methane Concentration: Picarro Cavity Ring-Down Spectrometer

Methane mole fractions of air in bag samples were measured using a Picarro G1301 optical analyser (Figure 3.8) which provides CH₄ and CO₂ mole fractions in parts-per-million (ppm) and water content in percentage (%) (<http://www.picarro.com>). The mobile measurements used a Picarro G2301. Picarro analysers use optical absorption spectroscopy of the target gas or gases to determine concentration. They are based on cavity ring-down spectroscopy (CRDS), an optical technique in which direct measurement of infrared absorption loss in a sample cell is used to quantify the concentration of the gas (Crosson 2008). The difference between CRDS and other conventional direct absorption techniques is in precision and sensitivity, since CRDS uses an effective pathlength of many kilometres in an optically stable cavity (Crosson 2008). This long pathlength is produced using high reflectivity mirrors, which support a continuous traveling light wave (Engeln *et al.* 1998; Crosson 2008). The principle of direct absorption techniques of the CRDS is governed by the Beer-Lambert law which suggests that light attenuates exponentially as it travels through a sample. Thus, the intensity of the transmitted light is directly related to the absorption coefficient and the effective path length of the light through the sample (Swinehart 1962).

The cavity inside the Picarro instrument consists of a closed chamber with two highly reflective mirrors. It also serves as a small-sized ($<10\text{ cm}^3$) flow cell into which the gas sample is introduced (Yoshida *et al.* 2014; Zazzeri *et al.* 2015). When the laser is on, a beam enters the cavity and because of the reflections, the cavity is quickly filled with circulating laser light. After multiple reflections the light intensity decays to zero in an exponential fashion as it bounces off the mirrors. The resulting decay in light intensity, called a 'ring-down' is measured with respect to the time using a fast photo-detector (<http://www.picarro.com>). The exponential decay of light intensity is proportional to all the losses inside the cavity. The concentration of the target gas species is determined by alterations in the decay 'ring-down' time of light intensity (<http://www.picarro.com>).

To achieve the high precision measurements of the Picarro instrument, the cavity optical path length can be increased to 15-20 km using multi-pass geometries (Rella *et al.* 2015). This long path length results in greater absorption by gases within the cavity and thus greater ring-down decay time. This allows high precision measurements with uncertainty depending on the analyte gas (Crosson 2008; Mønster *et al.* 2014). The temperature and pressure of the gas are highly controlled in the Picarro instrument (Crosson 2008). Gas stability together with a proper calibration of the instrument allow accurate measurements to be delivered (Crosson 2008; Richardson *et al.* 2012; Yoshida *et al.* 2014). Further description of the instrument is presented in the Picarro website (<http://www.picarro.com>) and (Mønster *et al.* 2014).

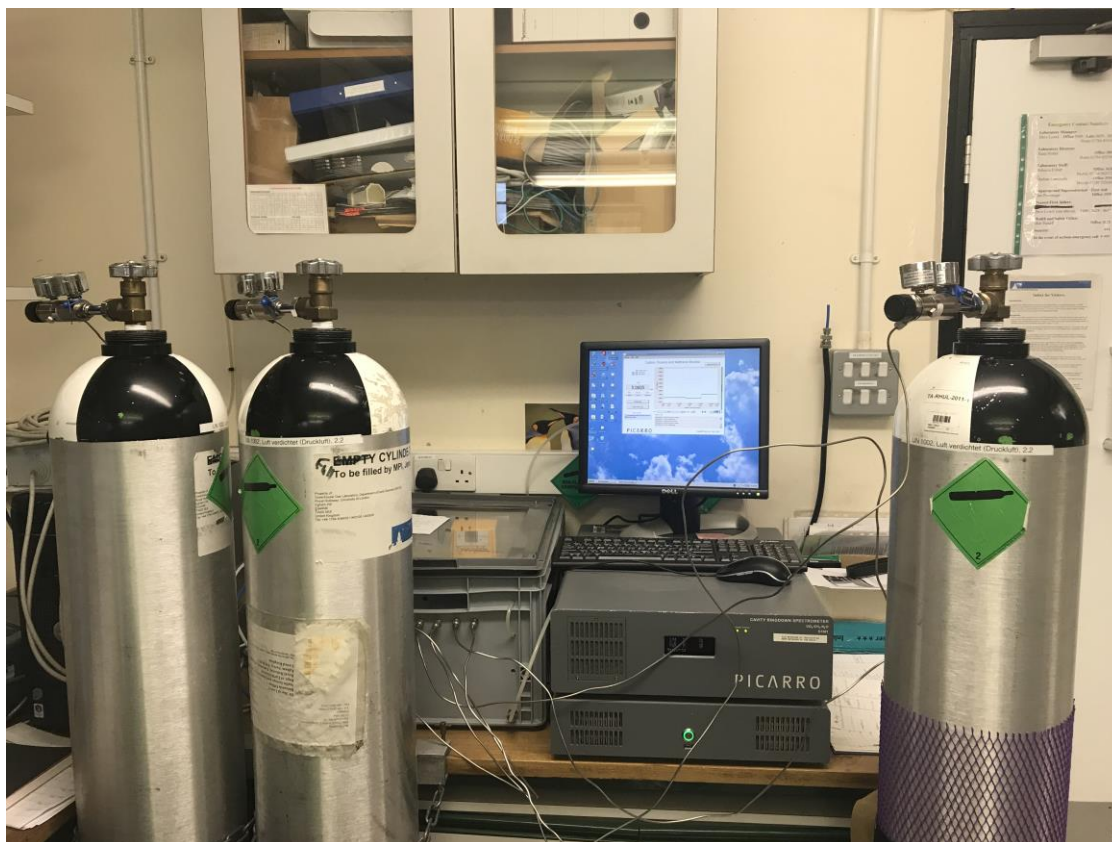


Figure 3.8 The G1301 Picarro CRDS (Cavity Ring-Down Spectroscopy) analyser at the RHUL Atmospheric Laboratory connected to three international standard air cylinders for calibration.

Instrument calibration

In the atmospheric laboratory at RHUL, the Picarro G1301 instrument is calibrated weekly using three international standards obtained from the Max-Planck Institute, Jena Gas lab of dry air with methane mole fractions (2.0918, 1.9124 and 1.8092 ppm) on the NOAA04 scale (Dlugokencky et al. 2005). Each standard is run for 18 minutes with the last 10 minutes averaged with typical standard deviation of 0.26 ppb. A target gas is measured once a week for 18 minutes and the last 10 minutes averaged. The standard deviation of target gas measurements gives the repeatability in Figure 3.9. Over 30 months the same target gas was measured with

a standard deviation of 0.27 ppb. This represents the long term precision. The Picarro CRDS measured linearly up to 20 ppm. However, air samples with higher mole fraction must be diluted with nitrogen before analysis.

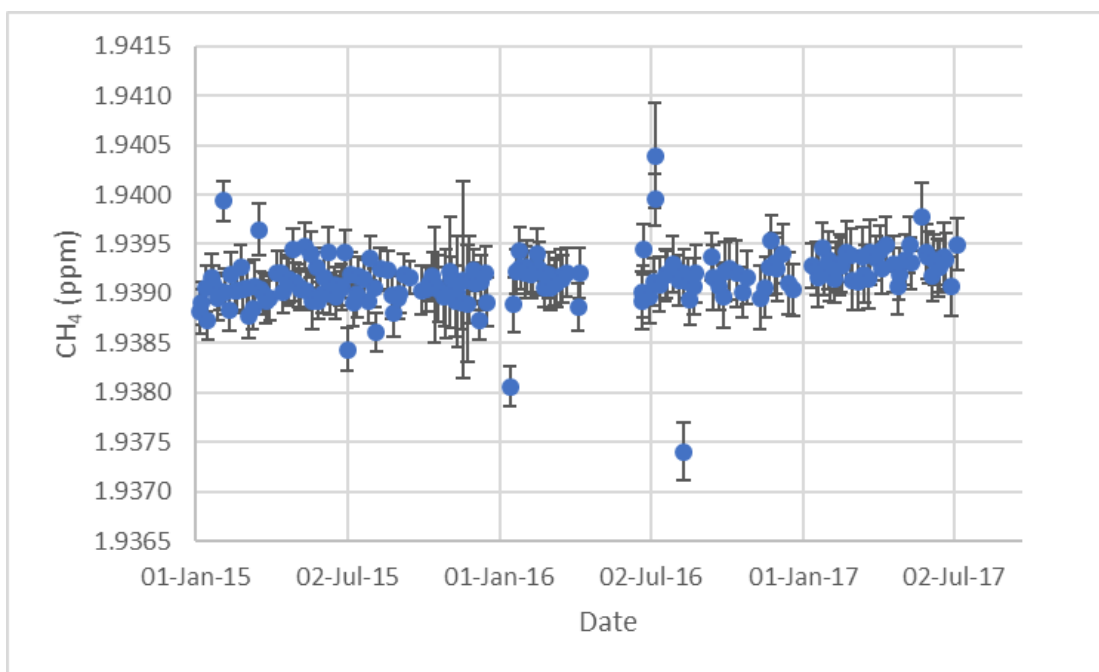


Figure 3.9 Picarro 1301 CRDS Target values from 2015 to 2017 at RHUL

Isotope Measurement Techniques: Continuous Flow Gas Chromatography Isotope Ratio Mass Spectrometry

The Isoprime Trace Gas Preconcentrator together with the Isoprime stable Isotope ratio mass spectrometer (CF-GC-IRMS) shown in Figure 3.10 were used for high-precision isotopic ratio measurements of methane (Fisher *et al.* 2006; Zazzeri *et al.* 2017). Trace Gas 1 system was installed at Royal Holloway University of London (RHUL) in March 2003 (Fisher *et al.* 2006). The second system, currently used for most measurements, was installed in 2010.

A schematic of the Trace Gas in the CH₄ analysis set up is shown in Figure 3.11 with the instruments connected in a continuous-flow set-up.



Figure 3.10 Trace Gas preconcentrator coupled with IsoPrime mass spectrometer.

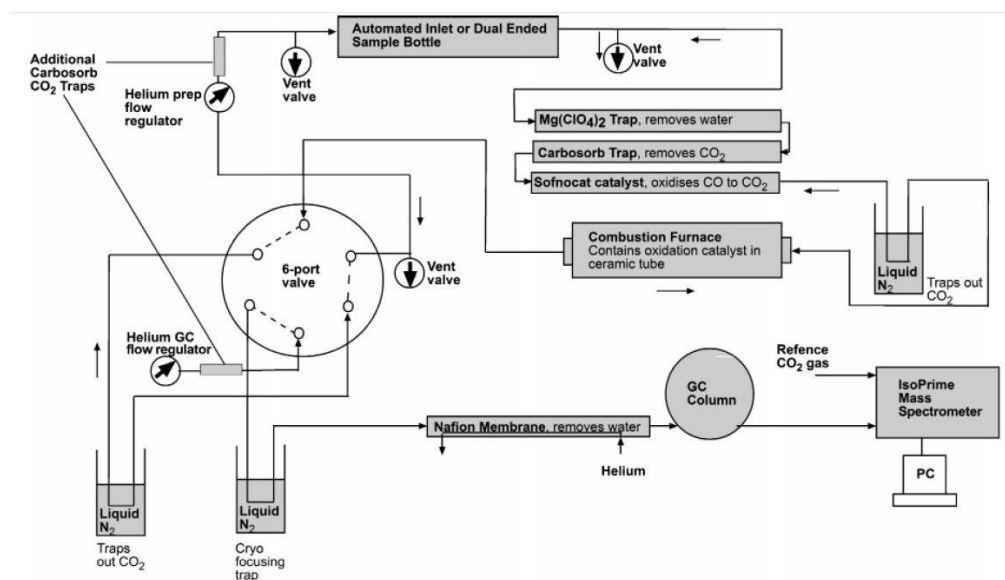


Figure 3.11 Schematic of the Trace Gas in the CH₄ analysis set-up. Black arrows indicate direction of flow of helium and the air sample during CH₄ analysis. Grey arrows show the default helium flow between analyses (Fisher et al., 2006).

Instrument performance

For CH₄ analysis, air samples enter the Trace Gas through a 75 ml sample volume with automated valves. These valves are controlled by a computer running Ion Vantage software. During the analysis, the air sample is first dried. A 20 mL/min flow of helium transports the sample through a sequence of chemical traps (Fisher *et al.* 2006). Water and CO₂ are removed through magnesium perchlorate and Carbosorb chemical traps (Elemental Microanalysis Ltd). The Sofnocat catalyst (Molecular Products Ltd.) in the Trace Gas oxidises CO to CO₂ and the resultant CO₂ is then frozen in a liquid nitrogen cryotrap held at -196°C (Fisher *et al.* 2006; Zazzeri *et al.* 2015). The cryotrap consists of nickel tube loops wrapped with glass-coated electrical heater elements. These heating elements, under control of the computer software, automatically switch on when the traps are raised out of the liquid nitrogen.

The flow continues to the combustion furnace, where the CH₄ is oxidised into CO₂. The resultant CO₂ is cryogenically trapped in the liquid nitrogen to increase the concentration of trace gases to detectable levels (Fisher *et al.* 2006). The cryofocused gas is swept out of the trap through a Nafion membrane to remove any water produced during the oxidation step. Prior to entering the ion source in the mass spectrometer, the CO₂ is isolated from any residual gas components using a 25m PoraPLOT Q GC column (0.32mm i.d.) (Fisher *et al.* 2006; Zazzeri *et al.* 2015).

The separated gas is then carried through to the ion source at a flow rate of 0.3 mL/min, to measure its isotopic ratio (Fisher *et al.* 2006). The mass spectrometer consists of three main parts; (1) ion source where multiple ions are generated from the carried gas; (2) analyser where the ions are electrically accelerated and deflected by a magnetic field according to their mass-to-charge ratio; and (3) a detector system where the relative abundance of each ion is recorded (Brenna *et al.* 1997).

In the case of CO₂, the data comprises three ions with their corresponding masses (mass 44, 45, 46) (Meier-Augenstein 1999; Zazzeri *et al.* 2015). These are aligned through three different slits where an electrical current together with the current ratios are measured. The $\delta^{13}\text{C}$ value for the measured sample is then quantified by comparing the resultant ratios to a reference gas. Isotopic measurements are made relative to a CO₂ gas cylinder reference (Fisher *et al.* 2006; Zazzeri *et al.* 2015).

This research has used the continuous flow isotope-ratio mass spectrometry (CF-GC-IRMS) technique to analyse $\delta^{13}\text{C}$ of methane in air from the 3 L Tedlar bags air samples that have been collected in Kuwait State and shipped to the RHUL Lab. Measurement of atmospheric methane samples with mole fractions up to 7 ppm were carried out immediately without a dilution. However, air samples with higher mole fraction levels (>7 ppm) such as those from landfill boreholes or from the oil gas field were first diluted in the RHUL laboratory. 1L Tedlar bags were partly filled with the high concentration sample. This was diluted with zero grade nitrogen (which is scrubbed of methane) to mole fractions between 2 and 5 ppm as that is the most suitable range for isotopic analysis.

The carbon isotope ratio ($\delta^{13}\text{C}$) for CH₄ analysis was measured in triplicate to high precision ($\pm 0.05\text{‰}$) which was achieved by Fisher *et al.* (2006). Fisher *et al.* (2006) introduced minor modifications to the CF-IRMS to increase the efficiency of the oxidation step in the combustion furnace, and better gas handling, thus, allowing high-precision isotopic analysis of methane (CH₄) and carbon dioxide (CO₂). The main change was the use of a catalyst consisting of palladium powder on quartz wool in the furnace at a temperature of 790°C which has the highest possible repeatability and accuracy compared with other catalysts which were tested at specific temperature and flow rate (Fisher *et al.* 2006; Zazzeri *et al.* 2015). The precision and accuracy for both CH₄ and CO₂ analysis were further enhanced by using a fixed and automated inlet system which reduces sample contamination with laboratory air and eliminates variations in pumping time.

The great advantage of the instrument compared to conventional methods (e.g. Lowe *et al.* 1994) which require a long time for the analysis is that each analysis of

75 cc of air only takes approximately 20 minutes. Furthermore, the isotopic precision of the instrument is significantly higher than the one obtained from the current laser-based isotopic measurement system, such as the CRDS analyser (within 1 ‰ for $\delta^{13}\text{C}$ of CH_4 (Phillips *et al.* 2013)).

The raw values of the $\delta^{13}\text{C}$ were calibrated against the internal secondary standard. This enables corrections to be made to sample results whenever there is a drift in $\delta^{13}\text{C}$ of CH_4 of the secondary standard over the time of analysis (≈ 0.05 ‰). Correction for each measured value was estimated from the difference between the correct value of the secondary standard and the mean isotopic value of the secondary standard measured regularly each day.

Instrument calibration

At the beginning of each day, an internal secondary standard is run four times or until the measurements are stable. After every two samples an internal secondary standard is analysed again to check for any drift. The internal secondary standard is a tank of ambient air which has been calibrated by measurement comparison with a cylinder of air from NOAA that has been measured by the INSTAAR laboratory at the University of Colorado (Nisbet *et al.* 2016).

The raw data are calibrated against the secondary standard in use at the time of analysis. The estimated isotopic values of these are shown in table 3.2. Each day, the results of the measured value shown in the batch report analyses are corrected by the difference between the true (in table) value and the mean measured isotopic value of the secondary standard. The drift correction can be made against the difference of mean of secondary standard for the day and the true value of the secondary standard.

<i>Standard</i>	<i>Value (‰)</i>	<i>Dates</i>
<i>RHS673</i>	-47.43	24/2/14 to 3/9/15
<i>RHS676</i>	-47.61	4/9/15 to 24/8/16
<i>RHS677</i>	-47.81	23/8/16 to 16/10/17
<i>RHS681</i>	-47.97	18/10/17 to 21/5/18

Table 3.2 The Internal Secondary standards used in this study

3.3 Data Analysis

This research has followed the analysis described by (Keeling 1958, 1961) and (Miller & Tans 2003) to quantify the isotopic signature of each individual plume. Many studies have successfully used the Keeling and Miller-Tans plots to determine the $\delta^{13}\text{C}$ signature of a source in specific settings (Pataki *et al.* 2003; Rella *et al.* 2015; Zazzeri *et al.* 2015, 2017; Arata *et al.* 2016; Wang *et al.* 2018). However, in order to obtain correct results, use of both methods needs to be selected carefully (Miller & Tans 2003; Vardag *et al.* 2016).

3.3.1 Keeling plot approach

The Keeling method (Keeling 1958, 1961) was introduced for relating changes in the $\delta^{13}\text{C}$ and mole fraction values to the isotopic signature of a source. It has been used to interpret various sub-systems of the global carbon cycle (Keeling 1958, 1961;

Pataki *et al.* 2003; Sturm *et al.* 2005; Fisher *et al.* 2006; Zazzeri *et al.* 2015, 2017). The Keeling approach assumes that the isotopic composition of both the background and source remains constant during the sampling period. It is based on the principles of mass conservation. Thus, the atmospheric mole fraction of a gas in the lower boundary layer can be expressed by the following equation (Pataki *et al.* 2003; Zazzeri *et al.* 2015).

$$C_a = C_b + C_s \quad (3.2)$$

Where c_a is the observed mole fraction of the gas in the ecosystem, c_b is the background atmospheric mole fraction; and c_s is the additional mole fraction of the gas produced by the source (Pataki *et al.* 2003; Zobitz *et al.* 2006).

Given mass conservation, the following equation can be obtained

$$\delta^{13}C_a C_a = \delta^{13}C_b C_b + \delta^{13}C_s C_s \quad (3.3)$$

The source input to the atmosphere can be calculated from the combination of the two previous equations as follows

$$\delta^{13}C_a = c_b (\delta^{13}C_b - \delta^{13}C_s) (1/c_a) + \delta^{13}C_s \quad (3.4)$$

Where the values of $\delta^{13}C_a$ and $1/c_a$ refer to the y-and-x best fit line values respectively. The $\delta^{13}C_s$ refer to the integrated value of the CH₄ source in the ecosystem as shown in Figure 3.12 (Pataki *et al.* 2003). Plotting $\delta^{13}C_a$ and $1/c_a$ yields a y intercept of the $\delta^{13}C_s$ that is the isotopic value at which the methane mole fraction tends to infinity (Pataki *et al.* 2003; Vardag *et al.* 2016). This may reasonably give the isotope signature for the methane source responsible for the excess over background.

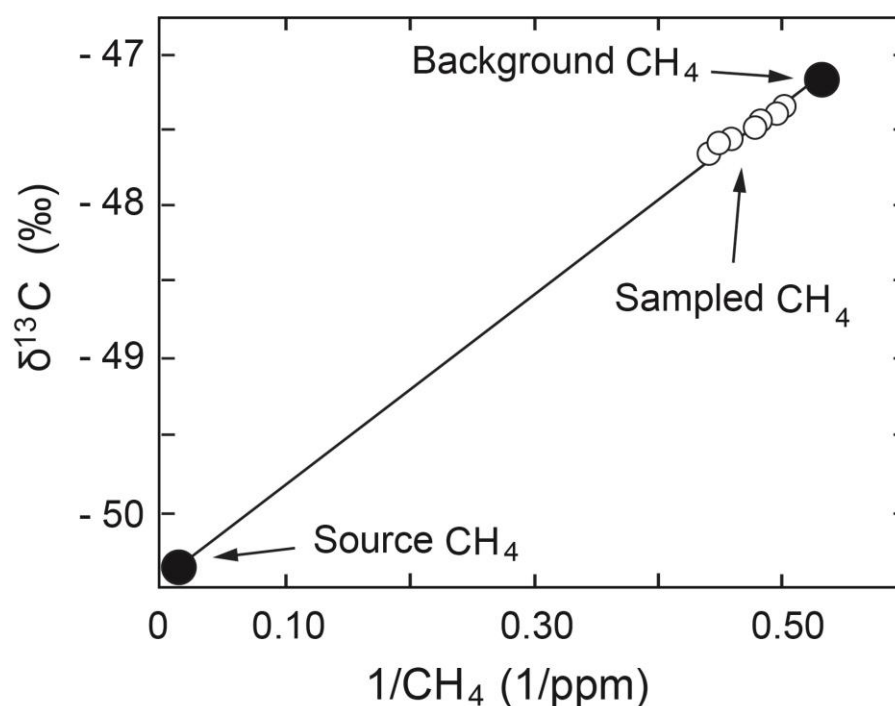


Figure 3.12 Graphical illustration of the Keeling plot method from Pataki *et al* (2003).

In this study, the Keeling plot method (Keeling 1958) was employed to calculate the isotopic signature of the methane source responsible for the excess over a constant background. This was achieved by plotting the $\delta^{13}\text{C}_a$ values (‰) (y-axis) against the inverse of methane mole fractions (ppm) ($1/c_a$; x-axis) (Pataki *et al.* 2003). The isotopic signature of the source has been interpreted from the regression line. Following the Keeling plot approach, every methane source was assigned an isotopic signature.

3.3.2 Miller-Tans approach

Miller and Tans (2003) have suggested an alternative approach for calculating isotope signature discrimination from atmospheric measurements of CH₄ and $\delta^{13}\text{C}$. Unlike the Keeling plot method, the Miller-Tans method is more flexible and allows for straightforward specification of the background values of both CH₄ and $\delta^{13}\text{C}$. Hence, this approach becomes necessary when the background is not constant through the time or space relevant to the measurements.

Miller and Tans (2003) rearranged equations (3.2) and (3.3) in which the background values of CH₄ and $\delta^{13}\text{C}$ must be specified and derived a new equation

$$\delta^{13}\text{C}_a \text{C}_a = \delta^{13}\text{C}_s \text{C}_s - c_b (\delta^{13}\text{C}_b - \delta^{13}\text{C}_s) \quad (3.5)$$

$$\delta^{13}\text{C}_a \text{C}_a - \delta^{13}\text{C}_b \text{C}_b = \delta^{13}\text{C}_s (\text{C}_a - \text{C}_b) \quad (3.6)$$

Equation (3.6) is more flexible and explicit than equation (3.4) where the background values can take different forms and could be constant or vary with time (Miller & Tans 2003). This research used the Miller-Tans approach to calculate the isotopic signature of a long-term study of the three-sites sampling for 2015 and 2016 (Figure 3.13).

The $\delta^{13}\text{C}_a \cdot \text{C}_a - \delta^{13}\text{C}_b \cdot \text{C}_b$ values (ppm.‰) (y-axis) were plotted against $\text{C}_a - \text{C}_b$ (ppm) values (x-axis) and the isotopic composition was determined from the slope ($\delta^{13}\text{C}_s$) (Miller & Tans 2003; Zobitz *et al.* 2006).

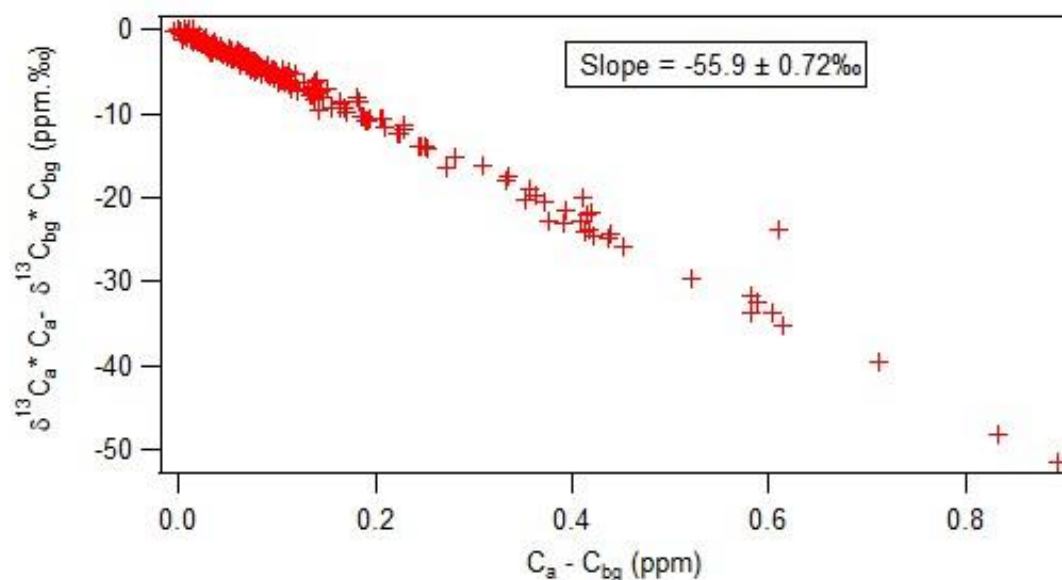


Figure 3.13 Miller-Tans plot based on all the isotopic values measured and the background values for each season in this study. Further detail in chapter (8).

Regression and Error Analysis

During the construction of the Keeling plot, a linear regression of the data must be obtained to compute the line intercept of the Keeling plot. Thus, the question of how to perform this regression becomes crucial. Several studies (Miller & Tans 2003; Pataki *et al.* 2003; Zobitz *et al.* 2006; Leng *et al.* 2007) have shown that the uncertainty associated with source signature calculation is more related to the suitability of the model to the analysed data rather than the analytical precision of both $\delta^{13}\text{C}$ and CH_4 and measurements. For example, the application of the classical ordinary least squares approach (OLS), also known as Model I regression (Miller & Tans 2003) which relies on the assumption that the independent variable is measured without error could be problematic in the calculation of the regression line. Not allowing for errors in the OLS method results in a smaller absolute magnitude of the slope or intercept than other approaches which allow for errors in both X and Y (Leng *et al.* 2007).

Since atmospheric data are often measured with errors for both X and Y variables (Pataki *et al.* 2003; Leng *et al.* 2007) an alternative regression model must be implemented to overcome the uncertainty and less precision of the OLS method. There are several models that allow errors in both CH₄ and $\delta^{13}\text{C}$ (Pataki *et al.* 2003; Leng *et al.* 2007) but yield small differences in the slopes and intercepts. These are the Orthogonal Distance Regression (ODR) and the Geometric Mean Regression (GMR, also known as reduced or standard major axis regression or Model II regression) (Miller & Tans 2003; Pataki *et al.* 2003). Further details on these methods and their drawbacks are explained by Pataki *et al.* (2003) and Miller & Tans (2003).

In this study, error on each point of the Miller-Tans approach was calculated using an error propagation method. In addition, a simple and widely used approach that can accommodate for the heteroscedastic measurement errors was used. This is known as the BCES method (stands for Bivariate Correlated Errors and intrinsic Scatter) (Akritas & Bershadsky 1996). The publicly available BCES regression program (<http://www.astro.wisc.edu/~mab/archive/stats/stats.html>) was used to calculate the intercept and thus the $\delta^{13}\text{C}$ value of the methane source. This technique allows for measurement errors on both variables and provides the least-biased estimates of regression slope (Akritas & Bershadsky 1996).

3.3.3 Methane mole fraction maps and plots

In order to properly visualise the methane mole fraction range, GIS ArcMap 10.2 software was used to generate maps displaying measured methane in ppm (Figure 3.3). The raw data produced by the Picarro analyser after each measurement campaign were calibrated and re-plotted. An Excel file with 5 columns, comprising CO₂ and CH₄ mole fraction measurements, longitude, latitude and date was generated and imported into ArcMap. The Excel file was then converted into a shape file with the longitude, latitude and CH₄ assigned to the x-y-z fields respectively. Having created the shape file, a colour ramp was selected in ArcMap and intervals were setup.

In this study, templates in ArcMap were modified to show mole fraction ranges with different colours to allow best visualisation. Scanned maps and images were georeferenced and used as base maps for the survey route and mole fractions. The mole fraction maps produced were eventually exported to various image formats such as JPEG and PDF files.

3.3.4 Openair application

Openair is an R (www.r-project.org) package primarily developed for air quality data analysis, but can also generally be used in the atmospheric sciences (Carslaw & Ropkins 2012; Carslaw 2015; Agustine *et al.* 2017; Masiol *et al.* 2017; Zazzeri *et al.* 2017; Al-Rashidi *et al.* 2018). Openair is a free, open-source programming environment which can be downloaded from its official website (<http://www.openair-project.org>). Once downloaded, air quality data to be analysed can be input either from computer files or a monitoring station (Carslaw 2015). More information concerning this software can be obtained from the Openair website (<http://www.openair-project.org>) which provides a comprehensive manual (Carslaw 2015) to support the package.

This study discusses only two functions of the Openair software: Polar plot and pollution rose functions (Figure 3.14). The polar plot function plots a bivariate plot of methane mole fractions in parts-per-million (ppm). Methane mole fractions generally vary by wind direction and speed (Carslaw 2015). The polar plot function is described in more detail elsewhere (Carslaw & Beevers 2013; Uria-Tellaetxe & Carslaw 2014; Carslaw 2015). The pollution rose function on the other hand plots the measured and the calculated $\delta^{13}\text{C}$ source signatures (‰) for the site of interest and splits them by wind direction. See (Carslaw 2015) for further detail.

The data processed and imported in Openair used a .csv (comma separated value) format, which is one of the simple extension files in Microsoft Excel (Carslaw 2015). Excel files with five columns, comprising; time, date, wind speed, wind direction and either methane concentrations (for polar plot) or $\delta^{13}\text{C}$ source signature (for pollution rose) were generated and imported into Openair as .csv format. The meteorological

data (wind speed and direction) for two consecutive years (2015 and 2016) were obtained from the official website of the Kuwait Meteorological Department (<http://www.met.gov.kw>).

Seasonal background mole fractions were selected and source signatures for each individual weekly sample were calculated using the ‘Lever’ rule (Thom et al, 1993; Fisher et al, 20016) according to the following equation:

$$\delta^{13}\text{C}_{\text{source}} = (\delta^{13}\text{C}_{\text{air}} \times c_{\text{air}} - \delta^{13}\text{C}_{\text{background}} \times c_{\text{background}}) / \Delta c$$

Where (Δc) is the difference in mixing ratio (c) between the selected background and the sampled air (c_{air}). $\delta^{13}\text{C}_{\text{air}}$ differs from $\delta^{13}\text{C}_{\text{background}}$ depending on the isotopic signature of the CH_4 from emission sources that are mixed with background air.

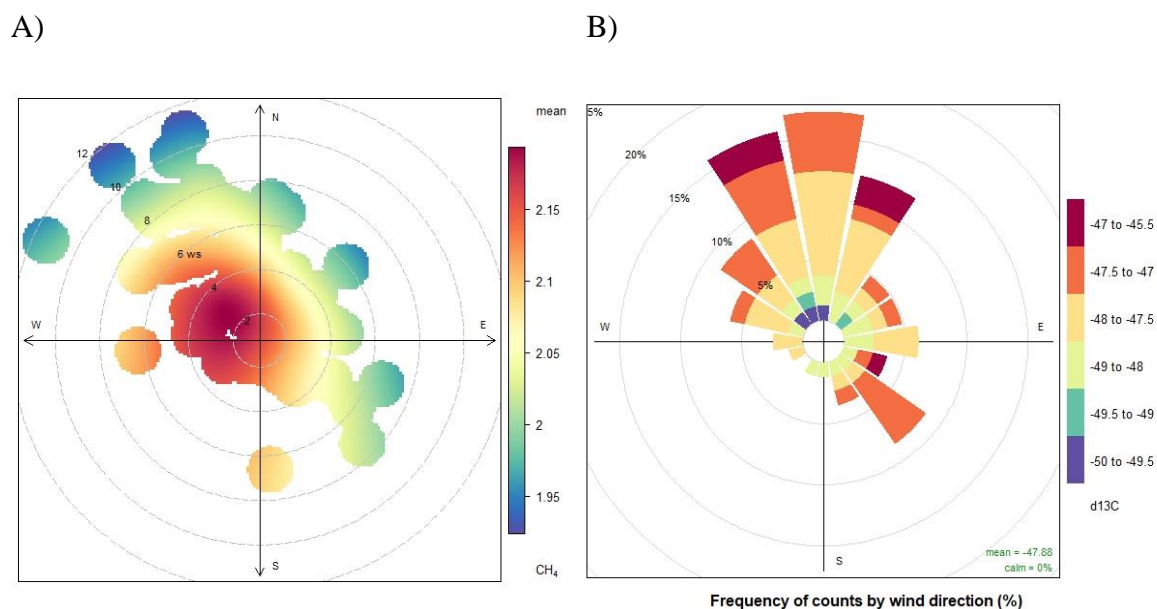


Figure 3.14 Example of A) Polar plot for the methane mole fraction and B) Pollution Rose for the measurement $\delta^{13}\text{C}$ values by using the Openair application (<http://www.openair-project.org>).

C***HAPTER 4***

K***UWAIT NATURAL GAS ANALYSIS: FOSSIL FUEL PRODUCTION AND USE***

4. Kuwait Natural Gas Analysis : Fossil Fuel Production and Use

The chapter discusses the methane emissions from natural gas systems (oil exploration, production, gathering, transmission, processing, exportation) in the State of Kuwait.

The exploration and production activities, refining, transportation, and distribution involve many distinct operations, each of which represents a potential source of fugitive emission that may be attributed to equipment leaks; evaporation losses; disposal of waste gas by flaring or venting, and accidents or equipment failures. The Kuwait Oil Company (KOC) is primarily responsible for the exploration and production of oil and gas within Kuwait and the refining of crude oil is done by the Kuwait National Petroleum Company which is a subsidiary. According to the methane emissions inventory for Kuwait, fugitive emissions accounted for 71% of methane emissions in the year 1994 (Environment Public Authority 2012).

Höglund-Isaksson (2017) simulated global methane and ethane emissions for the period 1980 to 2012 and found that oil production is a much larger contributor than natural gas production of methane and ethane emissions.

The research presents a case study of a gas leak from an unknown source in Al-Ahmadi Town. It discusses the results of vehicles emissions and measurements of the methane mole fraction and the $\delta^{13}\text{C}$ source-specific isotopic signatures of oil field and refinery emissions.

4.1 Oil Fields in Kuwait

There are more than twelve developed oil fields spread over the State of Kuwait (Figure 4.1). These oil fields are divided into four main parts: North, West, South and East Fields. The production and export of oil and gas are managed by the Kuwait Oil Company (KOC).



4.1.1 Oil operation facilities

KOC has the responsibility for exploration operation, onshore and offshore surveys, drilling of test wells and the development of producing wells in addition to crude and natural gas exploration. The main structures of the KOC oil and gas operation facilities are the following:

- Oil Wellheads: there are approximately fifteen different types of wellhead structures installed in oil fields.
- Oil Flow lines and Corridors: These multi-phase pipelines transmit the well productions (Oil, water and gas) to the gathering centers. The flow lines are laid above-ground along organized corridors.
- Gathering Center: In KOC oil fields there are around 26 Gathering Centers operating and receiving the crude oil from various wellheads that are spread over the oilfields. The Gathering Centers stabilize the crude oil by a multi-stage stabilization process and separate the gas and the water from the crude oil.

4.1.2 Gas operation facilities

- Gas systems and functions

Gas separated at High Pressure (HP) and Low Pressure (LP) from the Gathering Centers is transmitted to the booster stations by respective HP and LP gas networks. Tank Vapours (TV) are compressed in the Gathering Centers by the Tank Vapour Compressor (TVC). At the Booster Stations, the HP and LP gases are compressed for further transmission to the LPG (Liquefied Petroleum Gas) plant. The condensate recovered from the compressed and cooled gases is dehydrated and routed to the LPG Plant via pipelines.

- Booster stations

These are installed to fully utilize the separated gas from the Gathering Centers which was previously wasted to flare. Booster Stations receive the gas from various Gathering Centers and compress it; separate the condensate from the gas stream; and dehydrate the compressed gas and condensate. These compressed gases and condensate are transmitted through pipelines to the Mina Al-Ahmadi LPG Plant. At Mina Al-Ahmadi the transmitted gas and liquid is processed to recover Gasoline and Liquefied Petroleum Gas which are exported.

4.1.3 Oil production

The Capacity of Crude Production reached 3.017 Million Barrels of Oil Per Day (MMBOPD) at the end of 2016, which is higher than the 2015/2016 target of 3 MMBOPD (Figure 4.2). Efforts are aimed to increase crude production capacity to 3.65 MMBOPD by 2020 (Kuwait Oil Company 2016).

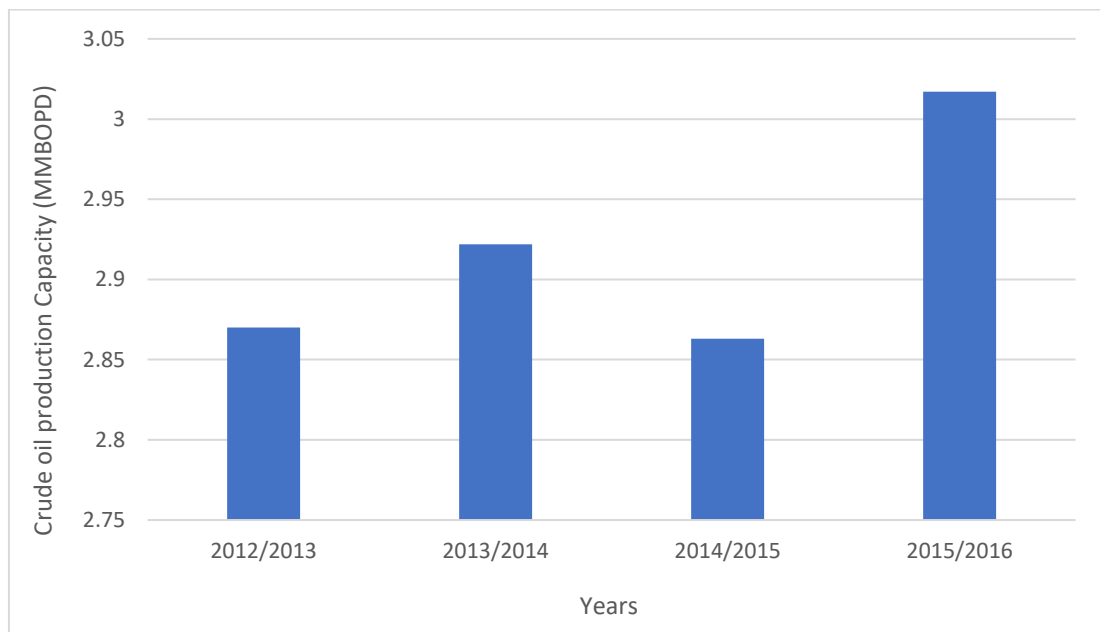


Figure 4.2 Oil production from 2012/2013 to 2015/2016

The North Kuwait operation achieved a Crude Production Capacity of approximately 709 MBOPD during 2016. In the South and East Kuwait asset, Crude Production Capacity (CPC) reached approximately 1,706 MBOPD. For the West Kuwait asset, CPC reached approximately 534 MBOPD. The total daily average of Associated and Non-Associated gas production reached 1.737 Million standard cubic feet per day (MMSCFD) against the target of 1.530 MMSCFD (Kuwait Oil Company 2016).

4.1.4 Gas flaring

KOC won the “Gas Flaring Reduction Excellence Award 2015” as part of the World Bank Global Gas Flaring reduction (GGFr) initiative, due to a reduction in flaring to 1% of produced gas. Figure 3.4 shows the KOC gas flaring percentage (Ibrahim ,2015). Globally, flaring of associated gas generated declined from 20 % to 12% for the period 1990 and 2010 (Höglund-Isaksson 2017). This is parallel with an increase in Kuwait gas production according to the Energy Information Administration (www.eia.gov) during the period from 2000 to 2010.

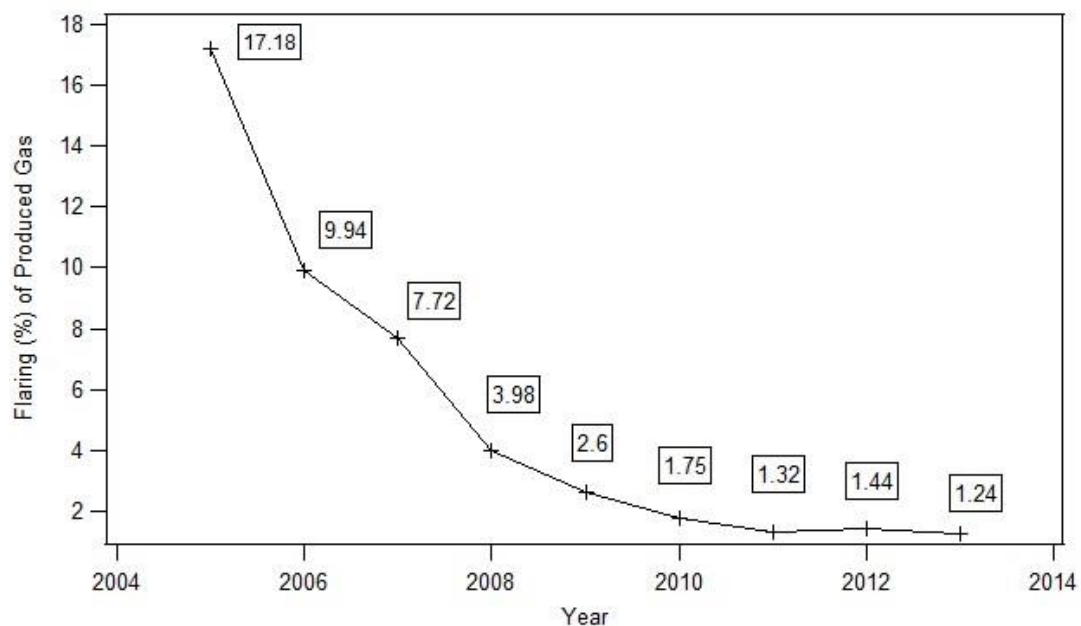


Figure 4.3 KOC gas flaring reduction over the years (Ibrahim, 2015)

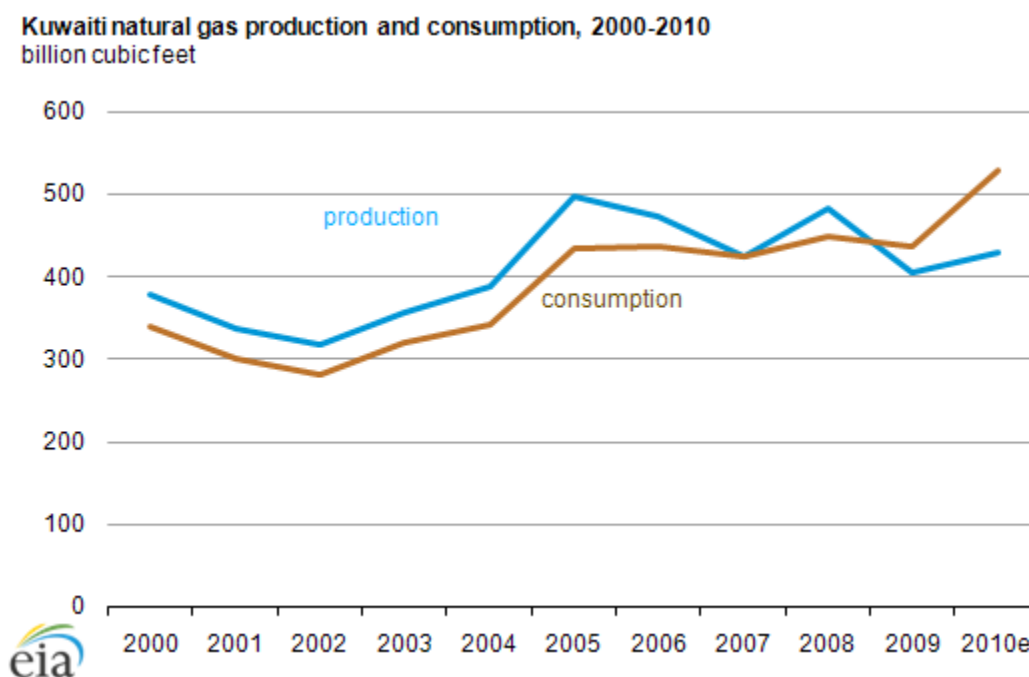


Figure 4.4 Kuwait natural gas production during 2000 to 2010 (www.eia.gov)

4.1.5 Materials and methods

To assign a representative $\delta^{13}\text{C-CH}_4$ signature to emissions from natural gas, the oil fields have been surveyed and their emissions isotopically characterised. The following sections discuss the methane emissions from natural gas from Kuwait oil fields.

In order to identify methane sources from the oil and gas sector, Höglund-Isaksson (2017) located the sources of methane emissions released during oil extraction and due to unintended leakage along the production process chain from the well head to storage. Mitchell *et al.* (2015) and Marchese *et al.* (2015) investigated methane emissions from 114 gathering centers and 16 processing plants in the USA natural gas system. Based on these studies different facilities were investigated during the sampling in Kuwait oil fields. Figure 4.5 shows some of the facilities that were investigated during sampling: Gathering Center, Booster, active rig and ground low

pressure flare and high-pressure flare.

A)



B)



Figure 4.5 Samplings at (A) an active rig and (B) low pressure flare facilities at ground level in the oil fields of Kuwait.

The first field visit to the KOC North oil fields was conducted on 7th of March 2016. Due to KOC security restrictions the site could not be accessed with the Picarro mobile system and instead a vehicle was provided by KOC to enter the site and samples were collected using a small gas pump.

Samples were collected from different facilities around the Sabriyah and Ar-Raudhatain oil fields. 21 air samples were collected in 3L Tedlar bags using a diaphragm gas pump (KNF NMP830KNDC) operated by a 6V battery. Sampling was done upwind and downwind of each facility. Bags were shipped to RHUL for analysis of methane mole fraction and $\delta^{13}\text{C}\text{-CH}_4$ (Figure. 4.6).

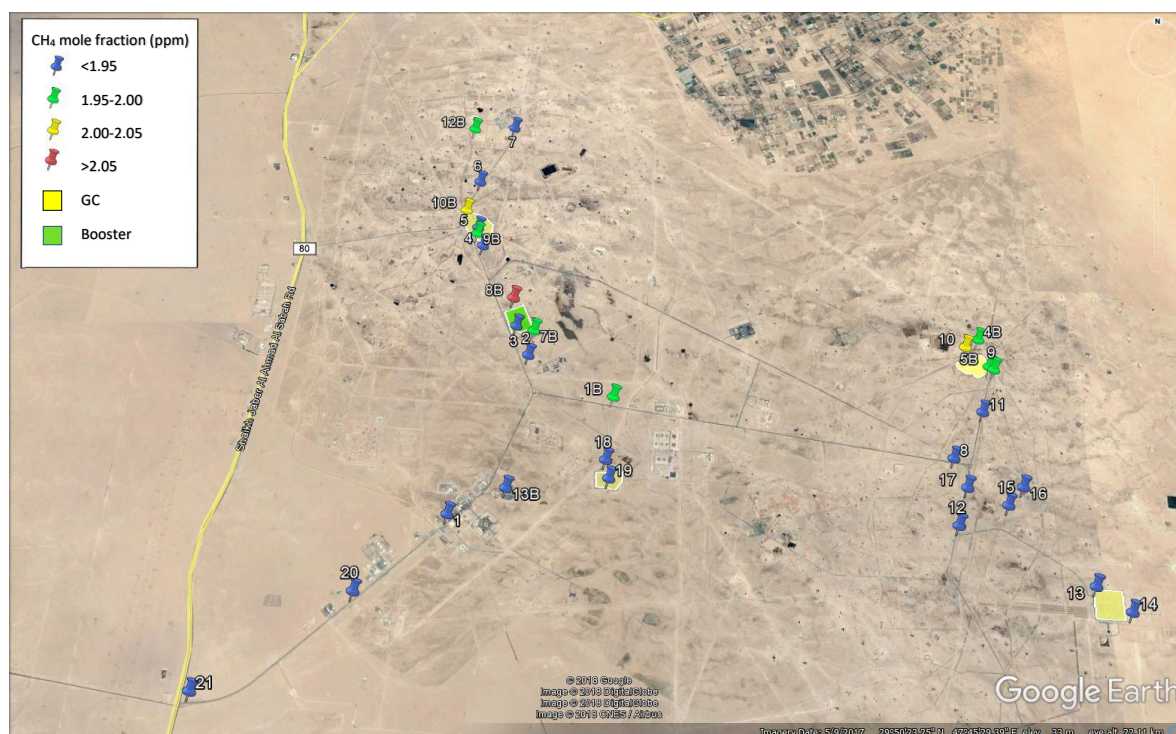


Figure 4.6 Google map showing the location of the air samples in Sabriyah and Ar-Raudhatain in North Kuwait City on 7th of March and 27th of October 2016. Pushpins represent sample locations with different mole fractions. The yellow square represents a gathering center (GC) and the green square a booster station.

CH₄ mole fractions of all the air samples were measured using a Picarro G1301 CRDS analyser (see chapter 3) at the Royal Holloway University of London Laboratory. Methane mole fractions ranged from 1.91 to 1.92 ppm in most samples. Table 4.1 summarises the mole fractions of methane sampled in the oil fields in North Kuwait. Wind speed was recorded at 60 km/h from N-NW direction. No methane plumes were evident on this day. All the samples were at the background level except sample number 9 and 10 which showed the highest concentration of 1.96 and 2.0 ppm, respectively upwind and downwind of Gathering Center 23 in Sabriyah oil fields.

<i>Name</i>	<i>Kuwait local Time</i>	<i>Latitude °N</i>	<i>Longitude °E</i>	<i>Tempe- rature °C</i>	<i>Wind Direction</i>	<i>CH₄ Mole Fraction (ppm)</i>	<i>SD ppm</i>	<i>δ¹³C ‰</i>	<i>SD ‰</i>
<i>sample 1</i>	09:40	29.8068	47.7243	41.1	N-NW	1.9206	0.0365	-47.42	0.03
<i>sample 2</i>	09:52	29.8415	47.7401	41.1	N-NW	1.9200	0.0299	-47.42	0.02
<i>sample 3</i>	09:54	29.8481	47.7366	41.2	N-NW	1.9197	0.0448	-47.36	0.05
<i>sample 4</i>	10:00	29.8669	47.7266	41.5	NW	1.9280	0.0478	-47.50	0.04
<i>sample 5</i>	10:05	29.8714	47.7249	41.4	NW	1.9235	0.0414	-47.26	0.05
<i>sample 6</i>	10:10	29.8831	47.7243	41.3	NW	1.9253	0.0419	-47.48	0.09
<i>sample 7</i>	10:15	29.8977	47.7320	41.5	N	1.9155	0.0310	-47.37	0.05
<i>sample 8</i>	10:35	29.8226	47.8406	41.5	NW	1.9181	0.0339	-47.23	0.01
<i>sample 9</i>	10:40	29.8423	47.8521	41.5	NW	1.9646	0.0287	-47.43	0.02
<i>sample 10</i>	10:48	29.8429	47.8503	41.7	NW	2.0076	0.0393	-47.65	0.03
<i>sample 11</i>	10:50	29.8328	47.8484	42.0	NW	1.9151	0.0432	-47.42	0.04
<i>sample 12</i>	10:55	29.8088	47.8404	42.2	NW	1.9128	0.0426	-47.56	0.05
<i>sample 13</i>	11:00	29.7980	47.8696	42.2	NW	1.9117	0.0569	-47.52	0.04
<i>sample 14</i>	11:05	29.7934	47.8767	42.1	NW	1.9120	0.0318	-47.46	0.03
<i>sample 15</i>	11:12	29.8133	47.8521	42.1	NW	1.9142	0.0356	-47.53	0.05
<i>sample 16</i>	11:16	29.8172	47.8559	42.1	NW	1.9140	0.0494	-47.48	0.03
<i>sample 17</i>	11:22	29.8166	47.8431	42.6	NW	1.9194	0.0270	-47.40	0.07
<i>sample 18</i>	11:40	29.8193	47.7598	42.6	NW	1.9147	0.0486	-47.59	0.01
<i>sample 19</i>	11:42	29.8155	47.7607	42.6	NW	1.9164	0.0370	-47.44	0.03
<i>sample 20</i>	12:00	29.7910	47.7052	43.0	NW	1.9150	0.0355	-47.45	0.05
<i>sample 21</i>	12:07	29.7714	47.6732	43.0	NW	1.9114	0.0440	-47.44	0.03

Table 4.1 Air samples collected from North Kuwait Oil Fields on 7th March 2016.

A second field visit to North Kuwait Oil field for sampling was carried out on 27th of October 2016. 14 air samples were collected upwind and downwind from different facilities around Sabriyah and Ar-Raudhatain oilfields. The range of the methane mole fractions was 1.9 to 2.08 ppm. Wind speed was around 14 km/h from S-SE direction and the temperature was 32 °C. The maximum concentration of 2.07 ppm was found downwind of the Booster installation and the methane mole fraction was 2.02 ppm downwind of Gathering Center 15 and 2.01 ppm downwind of the active rig in Sabriyah oil field (Table 4.2).

Name	Kuwait local Time	Latitude °N	Longitude °E	Temperature °C	Wind Direction	Wind Speed (Km/h)	CH ₄ mole fraction (ppm)	SD ppm	δ ¹³ C ‰	SD ‰
Sample 1	11:46	29.8330	47.7611	32	S-SE	14	1.9570	0.0251	-47.65	0.032
Sample 2	11:56	downwind of active rig		32	S-SE	14	2.0099	0.0634	-47.40	0.03
Sample 3	12:05	29.8424	47.9833	32	S-SE	14	2.0006	0.0304	-47.77	0.02
Sample 4	12:15	29.8491	47.8491	33	S-SE	14	1.9979	0.0469	-47.69	0.06
Sample 5	12:18	29.8513	47.8502	32	S-SE	14	1.9927	0.0360	-47.53	0.03
Sample 6	12:20	downwind of active rig		33	S-SE	14	1.9886	0.0373	-47.67	0.06
Sample 7	12:42	29.8472	47.7411	32	S-SE	14	1.9920	0.0355	-47.77	0.03
Sample 8	12:50	29.8547	47.7355	32	S-SE	14	2.0758	0.0373	-47.81	0.01
Sample 9	12:55	29.8700	47.7250	32	S-SE	14	1.9773	0.0479	leaked	
Sample 10	13:00	29.8758	47.72166	32	S-SE	15	2.0243	0.0405	-47.63	0.06
Sample 11	13:05	downwind of active rig		32	S-SE	14	1.9705	0.0477	-47.54	0.04
Sample 12	13:12	29.8972	47.7216	32	S-SE	14	1.9720	0.0473	-47.46	0.03
Sample 13	13:32	29.8127	47.7372	32	S-SE	15	1.9541	0.0551	-47.43	0.04
Sample 14	13:45	B.G		32	S-SE	14	1.9093	0.0265	-47.40	0.03

Table 4.2 Air samples collected from North Kuwait Oil Fields on 27th October 2016

The isotopic signature of the methane source is normally characterised using the Keeling plot method (see Chapter 3) but the range in methane mole fraction was not large enough to allow identification of the source signature using this method.

4.2 Kuwait Refineries

Kuwait National Petroleum Company, a subsidiary of Kuwait Petroleum Company (KPC), is Kuwait's only refining company. KNPC provides all the fuels, including gasoline, diesel, kerosene and gas for local and international markets. KNPC operates three refineries, namely Mina Al-Ahmadi, Mina Abdullah and Shuaiba with a total capacity of 936,000 barrels per day for crude oil (Figure 4.7).

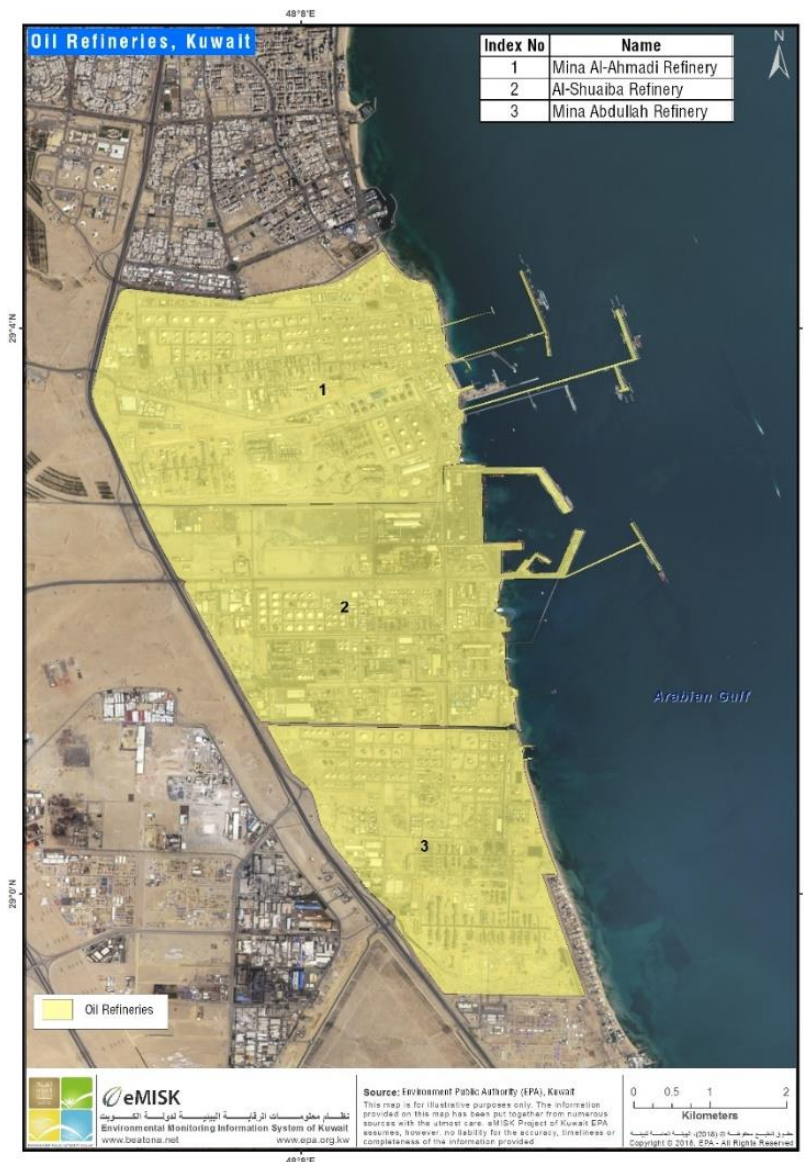


Figure 4.7 Kuwait National Petroleum Company (KNPC) refineries: Mina Al-Ahmadi (MAA), Mina Abdullah (MAB) and Shuaiba (SHU). (Source Emisk, 2018)

Each refinery has its own features. Shuaiba is the world's first all-hydrogen refinery, MAA is one of the world's largest refineries and MAB has high conversion capabilities.

- Mina Al Ahmadi refinery

Mina Al Ahmadi Refinery (MAA) is located directly on the seashore and covers a total land area of 10.5 km². MAA was built in 1949 with 25,000 barrels per day (bpd) capacity to supply the local market with gasoline, diesel and kerosene. Over the years, MAA increased its capacity to 466,000 bpd of crude oil and 2,458 Million of cubic feet of gas per day (MMSCFPD) of gas processing. MAA produces almost all kinds of petroleum by-products, such as gasoline, kerosene, diesel, bitumen, naphtha, LPG, and sulphur. The flare recovery unit is registered in UN's Clean Development Mechanism. The majority of products are exported to international markets while a part of the production is for local market (www.KNPC.com)

- Mina Abdullah refinery

Mina Abdullah Refinery (MAB) is located 53 km south of Kuwait along the Gulf coast and covers an area of approximately 7.835 km². It has a production capacity of 270,000 bpd of crude oil. MAB produces almost all kinds of petroleum by-products, such as naphtha, kerosene, low-sulphur gas-oil, coke, fuel oil, and sulphur.

- Shuaiba refinery

Shuaiba Refinery (SHU) is the first national oil refinery in the region located 50 km south of Kuwait City. It was built in 1966 and commissioned in April 1968. SHU occupies an area of 1.232 km² in Shuaiba Industrial Area. The production capacity is around 200,000 bpd of crude oil. Shuaiba Refinery was destined for closure in April 2017; however, the tanks and export facilities would be utilized as part of Clean Fuel Project. SHU refinery is connected through a network with MAB and MAA. The export facilities at MAA are used for exporting SHU products (www.KNPC.com).

- Gas liquefaction

Gas Liquefaction is a major activity of the Kuwait National Petroleum Company (KNPC); the company has a Liquefaction Plant at MAA. Gas is naturally produced in some of Kuwait oil fields. First it is sent to Gathering Centers, after that to the Liquefied Natural Gas (LNG) Liquefaction Plant at MAA. The plant has 4 production trains to extract Propane, Butane and Gasoline (www.KNPC.com).

4.2.1 Surveys of the three refineries

As part of the May 2015 Picarro mobile assessment the refineries were surveyed twice along the same downwind transect through the emission plumes from the refineries, using the mobile Picarro system described in chapter 3. ArcGIS plots were produced to show the methane mole fractions downwind of the three refineries for two different days (5th and 6th May 2015).

On 5th May 2015, the first survey was conducted along the King Abdul-Aziz Highway where methane plumes were encountered around the refineries. Figure 4.8 shows inlet lag-time corrected N-S and S-N transects of the downwind methane plume from the refineries. The main plume had a maximum mole fraction of 2.49 ppm during the survey. The plume was recorded between 29.0612 to 29.0270 latitude (N-S) at 8:33 - 8:37 am (GMT), and the same plume intersected between 29.0231 to 29.0605 (S-N) at 8:41 - 8:46 am (GMT). Vehicle speed was around 60 km/h, because measurements were in a main road so it was not possible to go slower.

The time delay between the instantaneous GPS location and the display of Picarro mole fractions (Zazzeri, 2015) of the plumes are aligned by shifting the mole fractions back by 7 seconds due to the lag between air entering the inlet and the analysis being completed.

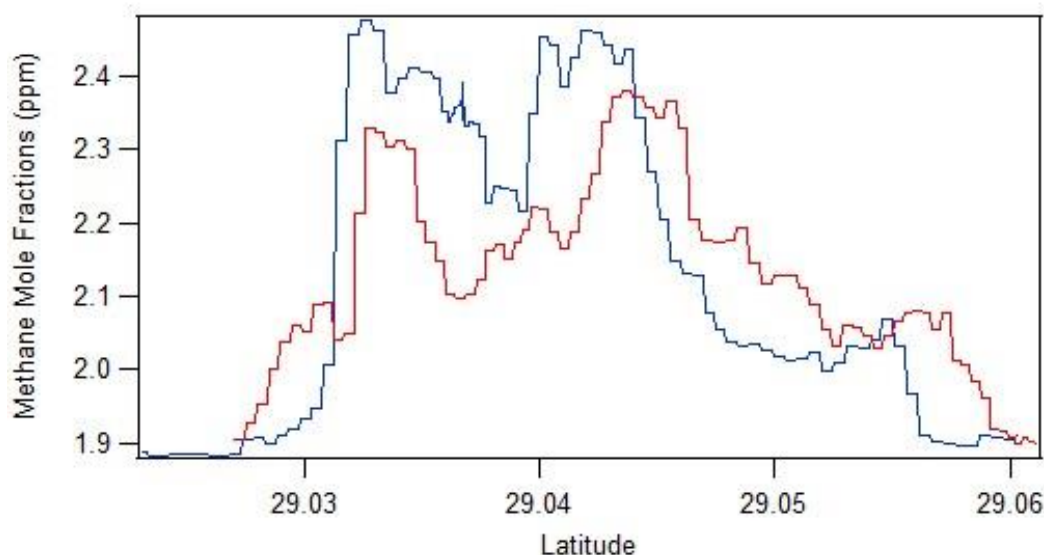


Figure 4.8 Methane mole fractions of the intersected plumes during the survey on 5th May 2015 downwind of the refineries. Red series represents the North to South route at 8:33 - 8:37 am (GMT) and the Blue series represents South to North route at 8:41 - 8:46 am (GMT).

Four samples were collected downwind of the methane plume that was moving WNW from the refineries (Table 4.3). The route of the survey is shown in a GIS map and the yellow pushpins in Figure 4.9 represent location where samples were collected.

<i>Name</i>	<i>Kuwait local Time</i>	<i>Latitude °N</i>	<i>Longitude °E</i>	<i>Wind Direction</i>	<i>CH₄ Mole Fraction (ppm)</i>	<i>SD ppm</i>	<i>δ¹³C ‰</i>
<i>Sample 1</i>	8:39	29.0107	48.1326	154	1.9552	0.0015	-46.80
<i>Sample 2</i>	8:42	29.0323	48.1211	145	2.3626	0.0014	-46.78
<i>Sample 3</i>	9:42	29.0785	48.1410	139	2.3569	0.0016	-49.08
<i>Sample 4</i>	9:44	29.0763	48.1417	133	1.8793	0.0015	-47.04

Table 4.3 Air samples collected during the survey by using the Picarro mobile system on the 5th of May 2015.

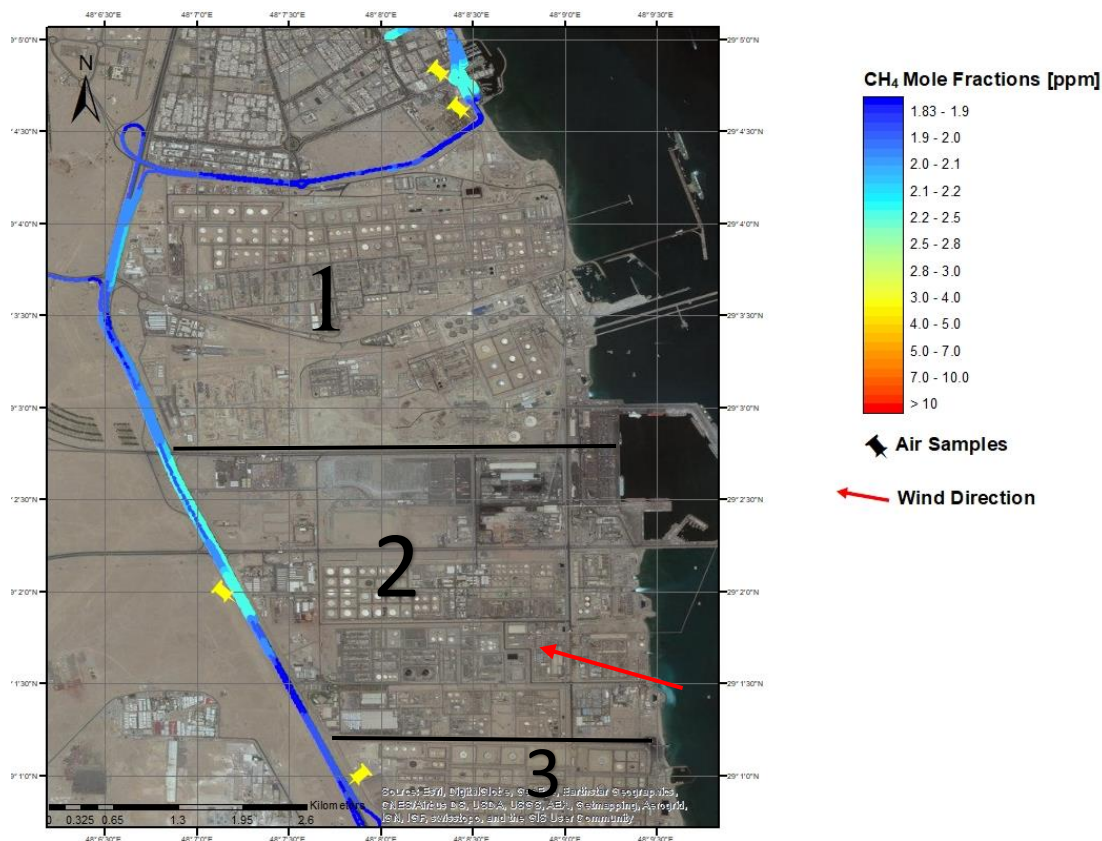


Figure 4.9 ArcGIS plot of CH₄ mole fraction recorded downwind of the refineries on 5th May 2015. (1) Mina Al-Ahmadi (MAA), (2) Mina Abdullah (MAB) and (3) Shuaiba (SHU) Yellow pushpins represent the air sample locations and red arrow indicates the wind direction (ESE)

Another survey was conducted on 6th May 2015. By utilising the Picarro mobile gas analyser, potential source sites were investigated on the same day, driving on the King Abdul-Aziz Highway around the refineries and collecting samples. During the survey, two main methane plumes were detected (Figure 4.10). The repeated plume intersection was along the public road (N-S) at a vehicle speed of around 40-60 km/h. Wind direction was from ESE allowing downwind intersection of plumes from the refineries (Figure 4.11)

The first plume was detected at 12:30 – 12:33 pm (GMT) between 29.0071°N to 29.0178°N and the same plume was observed again on the same road at 12:54 – 12:57 (GMT) between 29.01802°N and 29.0048°N. This was the biggest methane plume that was intercepted downwind of the west side of the refineries with maximum methane mole fractions of 4.40 ppm (Figure 4.12)

The second plume was located between 29.0217°N to 29.0500°N (N-S) at 12:34 - 12:39 am (GMT) and the same plume intersected again at 12:47 to 12:54 am (GMT) between 29.0481°N and 29.0190°N latitude with maximum mole fractions of 2.71 ppm and vehicle speed was around 40 to 50 km/h (figure 4.13).



Figure 4.10 Google Earth view of methane mole fraction columns measured along the King Abdul-Aziz Highway downwind of the refineries showing the two main methane plumes detected. Black arrow indicates the wind direction.

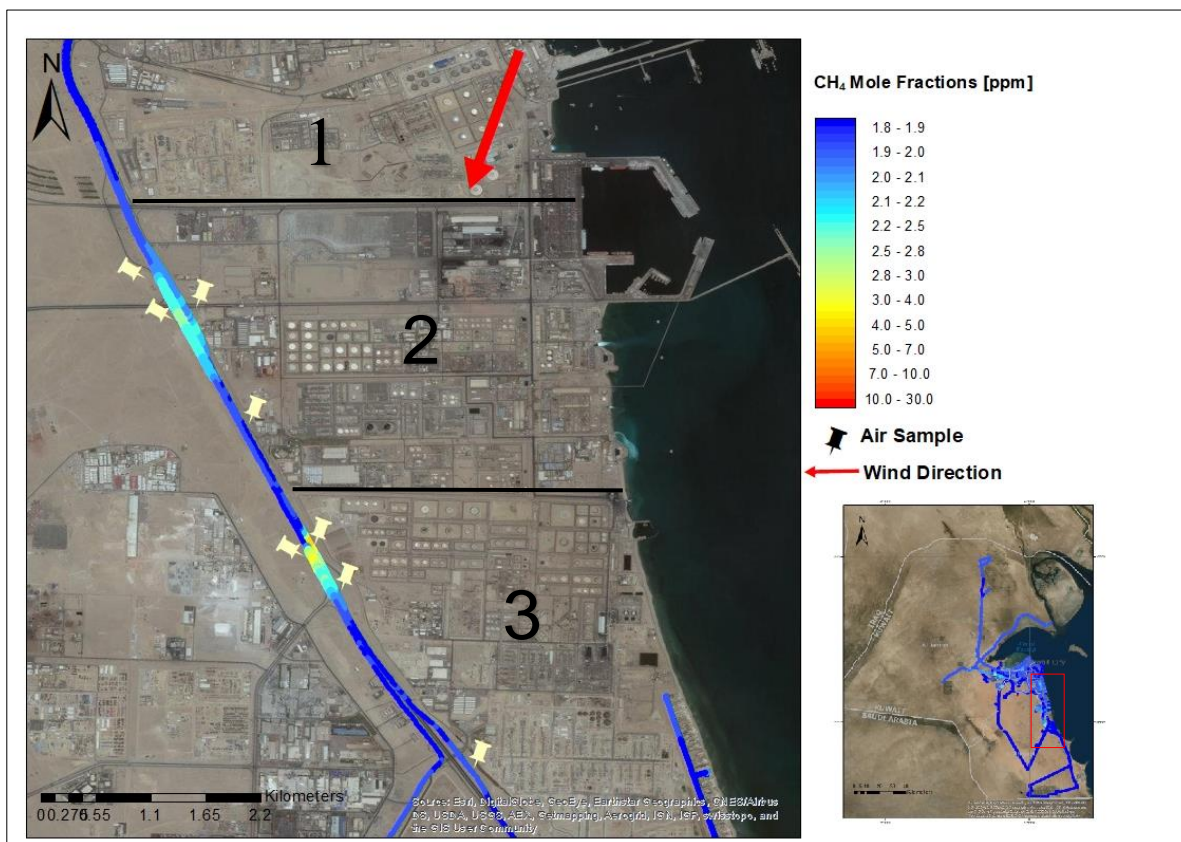


Figure 4.11 ArcGIS plot of CH₄ mole fractions in ppm recorded on 6th May 2015 downwind of refineries and two main methane plumes detected. (1) Mina Al-Ahmadi (MAA), (2) Mina Abdullah (MAB) and (3) Shuaiba (SHU). Yellow pushpins represent the air sampling locations and the red arrow indicates the wind direction.

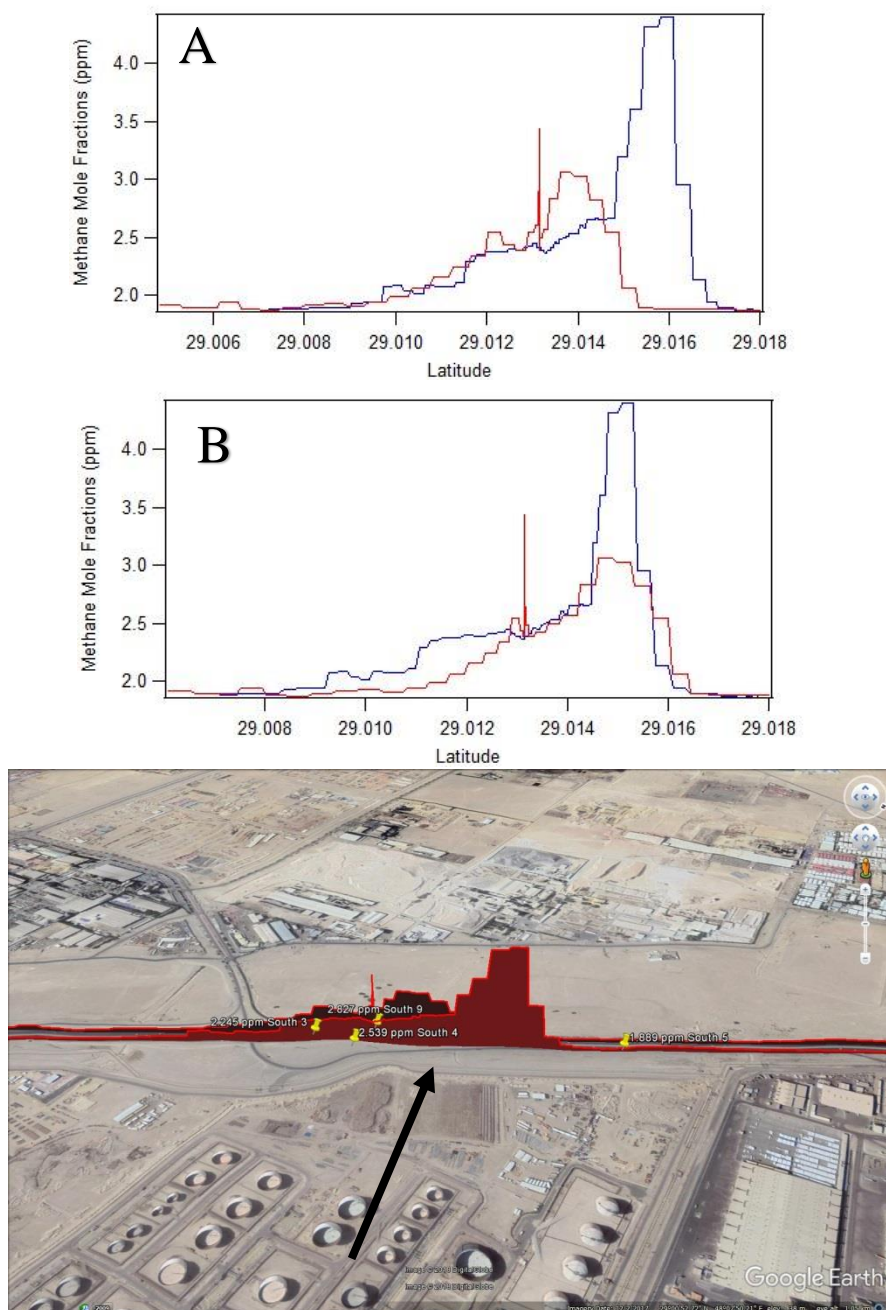


Figure 4.12 Methane mole fractions of the repeated plume intersection during the survey on 6th May 2015, downwind of the refineries. Red series represents the North to South route at 12:30 – 12:33 pm (GMT) and the Blue series represents South to North route at 12:54 – 12:57 (GMT), Black arrow indicates the wind direction. A) before the time lag correction; B) After time lag correction. The peak represents multiple measurements recorded when the vehicle was stopped to collect samples.

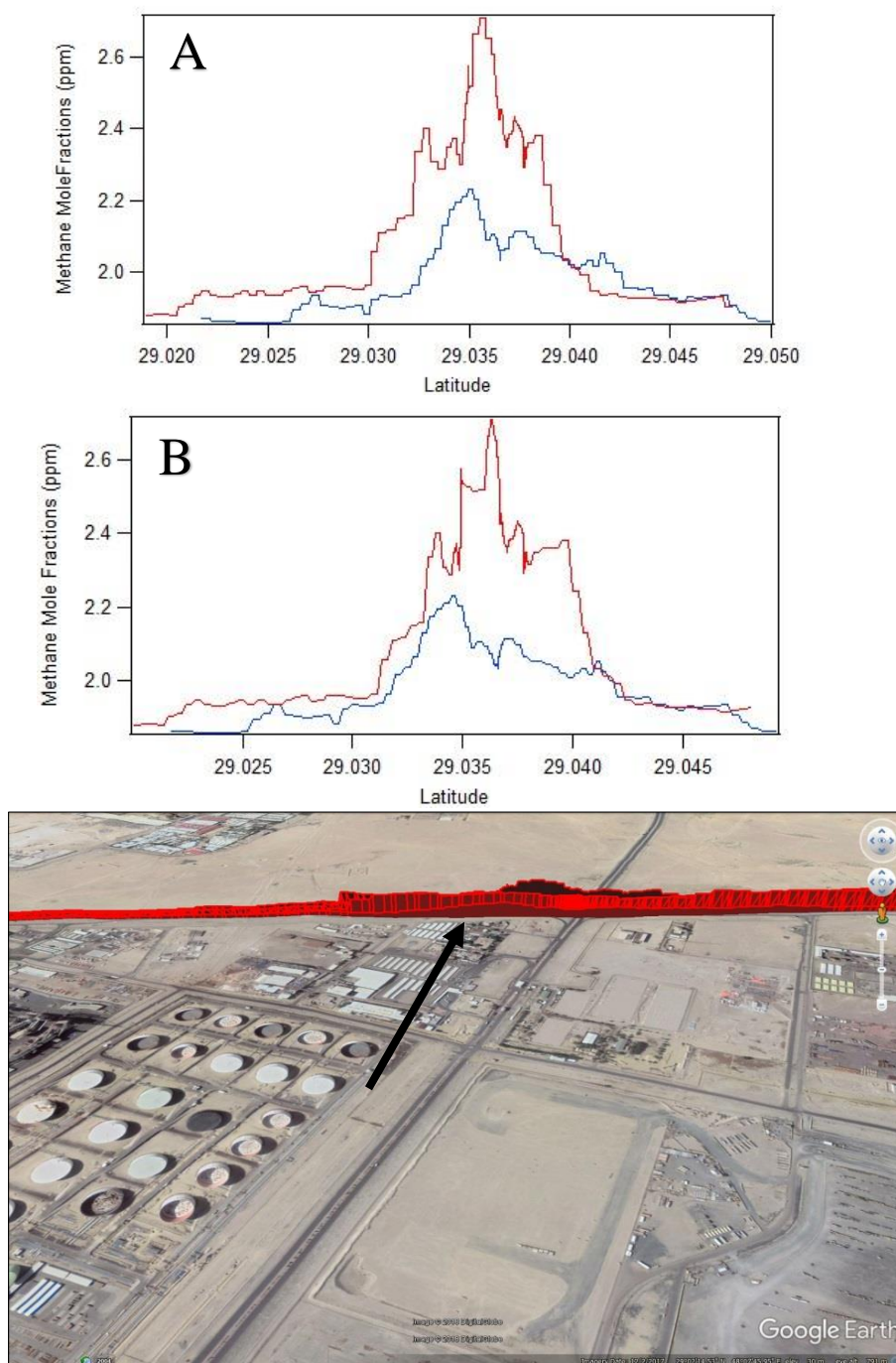


Figure 4.13 Methane mole fractions of the repeated plume intersect during the survey on 6th May 2015, downwind of the refineries. Red series represent the North to South route at 12:34 - 12:39 am (GMT) and the Blue series represents South to North route at 12:47 to 12:54 am (GMT), Black arrow is the wind direction. A) Before the time lag correction; B) After time lag correction.

Table 4.4 shows eight air samples that were collected in sequence while driving to get representative samples of integrated methane emissions downwind of the three refineries (Figure 4. 10). A Keeling plot based on the eight air samples gives an intercept value of $-51.6 \pm 0.5\text{‰}$ (Figure 4.14).

Name	Kuwait local Time	Latitude °N	Longitude °E	Wind Direction	CH ₄ Mole Fraction (ppm)	SD ppm	δ ¹³ C ‰	SD ‰
Sample 1	12:27	28.9963	48.1440	28	1.9025	0.0008	-47.11	0.01
Sample 2	12:31	29.0119	48.1323	26	2.2453	0.0009	-47.91	0.01
Sample 3	12:31	29.0130	48.1317	24	2.5392	0.0015	-48.41	0.05
Sample 4	12:33	29.0177	48.1292	24	1.8893	0.0015	-47.11	0.01
Sample 5	12:36	29.0366	48.1192	24	2.0488	0.0014	-47.38	0.06
Sample 6	12:49	29.0377	48.1178	24	2.3326	0.0009	-47.96	0.04
Sample 7	12:51	29.0349	48.1193	24	2.5340	0.0012	-48.23	0.04
Sample 8	12:55	29.0132	48.1312	24	2.8275	0.0005	-47.95	0.05

Table 4.4 Air samples collected downwind of the refineries during the survey using the Picarro mobile system on 6th May 2015

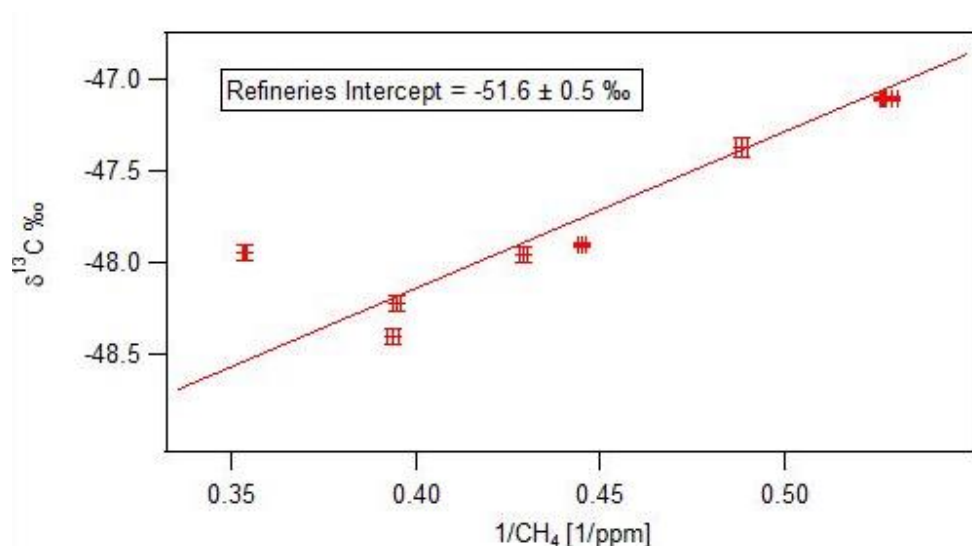


Figure 4.14 Keeling plot based on samples collected downwind of the three refineries on 6th May 2015

4.3 Al-Ahmadi Town

Al-Ahmadi Town is located to the south east of Kuwait City with an area of 5.120 km². This town was built for British expats in the 1940s and is the only area in Kuwait with a piped gas network. Around 1600 residential houses were owned by KOC for their employees' accommodation. In 1950 a gas network was constructed to supply the houses which was later replaced with new corrosion-resistant plastic pipes in 2008. Three gas explosions occurred in 2010: two occurred at different houses that were connected to the KOC natural gas network in north Ahmadi and one occurred at a house in south Al-Ahmadi that was not connected to the network (Figure 4.15). The causes of these accidents were not identified but a few complaints were received due to gas odour in the air, which was assumed to be from a gas leak from the KOC network. Measurements showed high levels of gas within and outside of KOC owned houses (Alkhaledi *et al.* 2015). Al-Ahmadi town consists of many blocks however Block No.1 has suffered from many natural gas leakages in the last decade (Al-rashed 2014).

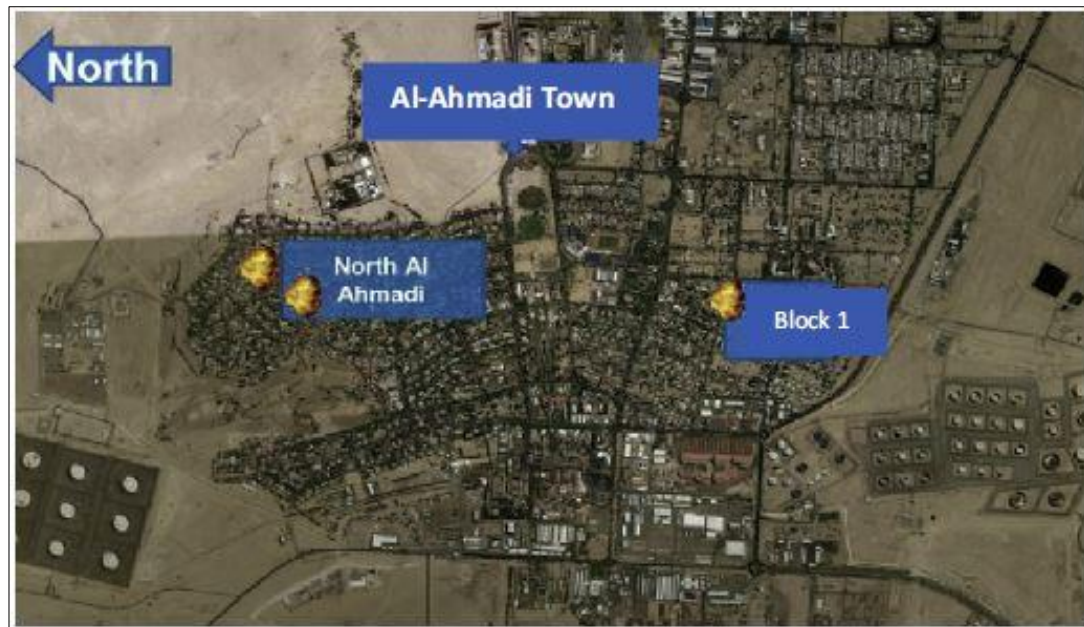


Figure 4.15 Map showing the three main explosions that occurred in 2010, (Alkhaledi *et al.* 2015)

The reasons for the gas leakage in Ahmadi area are either from an artificial source such as the KOC gas pipe network or from a natural geological source. Alkhaledi et al (2015) used fault tree analysis to identify the type and the source of the leakage gas. Four different source hypotheses were investigated: leaks from the natural gas network, leaks from the sewer network, leaks from wells and boreholes in and around the town of Al-Ahmadi, and leaks from underground geological formations. The observation well results showed that the high gas region extends from north to south Al-Ahmadi over the Al-Ahmadi ridge zone. This ridge has an arch-shaped set of geological formations over the hydrocarbon reservoir beneath Al-Ahmadi town. Alkhaledi et al (2015) found that the leaking gas in the Al-Ahmadi incidents is thought to be from natural gas of geological origin that gradually migrated from deep hydrocarbon reservoirs upwards through cap-rock fractures over a long period of time (Figure 4.16). This agrees with the result of Carman (1996) and Alsharhan & Nairn (1997) suggesting that the Burgan oil reservoir structure is an anticlinal dome with 30 fractures.

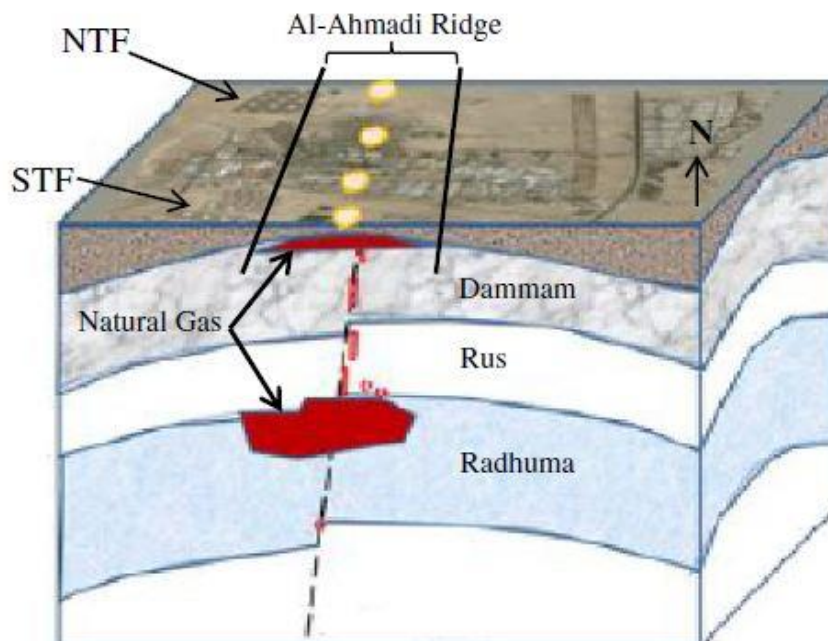


Figure 4.16 Al-Ahmadi ridge zone with north (NTF) and south tank farms (STF). Reference: (Alkhaledi et al. 2015)

4.3.1 Survey of Al-Ahmadi Town

Al-Ahmadi Town was explored using the Picarro mobile system on 5th May 2015. Figure 4.17 shows that peaks of methane were observed at block No1 and four air samples were collected by driving on public roads in the same block.



Figure 4.17 Google Earth view of methane mole fraction columns measured along the public roads in Al-Ahmadi Town on 5th May 2015. Yellow pushpins represent the air sample locations and the mole fraction of the air sample bags (ppm) and black arrow indicates the wind direction (SE)

Many vents have been installed around block 1 since 2010 to avoid dangerous underground build-up of methane. These are distributed around the residential houses in the area (Figure 4.18). These are supervised by KOC to monitor the air quality in the area. Air samples were collected downwind of venting pipes (Figure 4.19).



Figure 4.18 Vents distributed around the residential houses in Al-Ahmadi Town

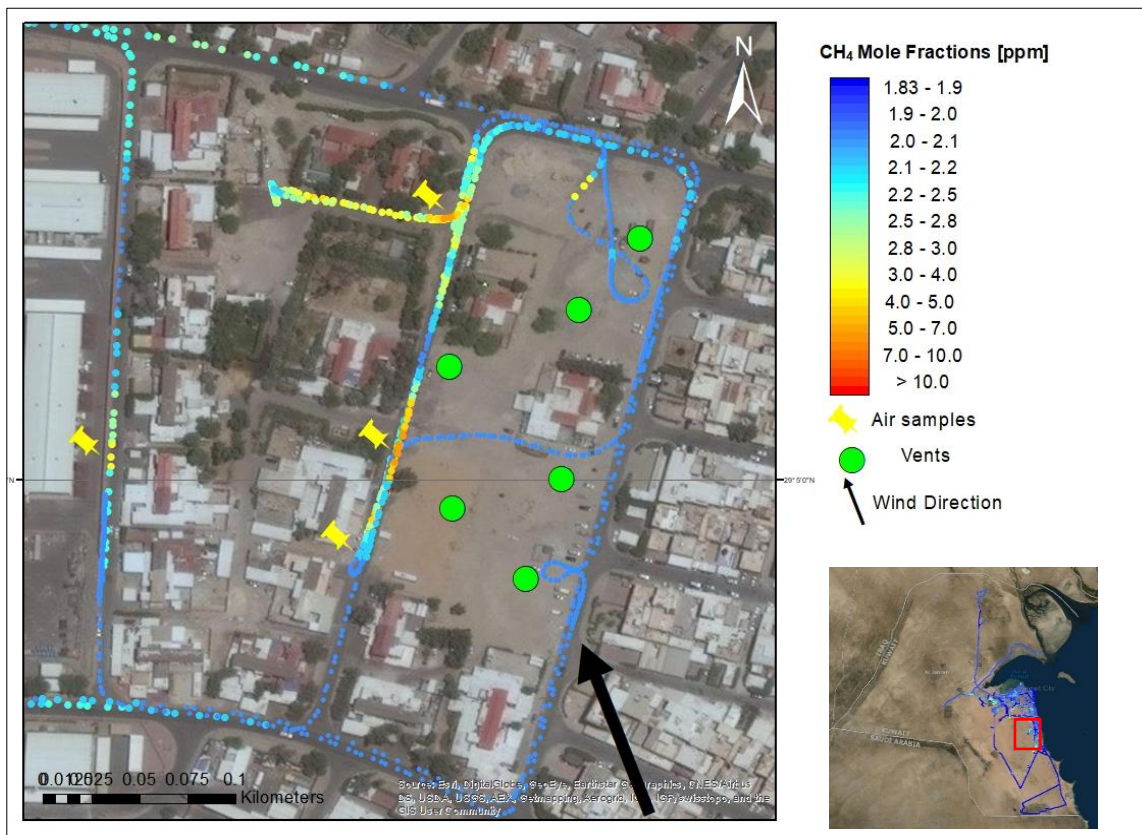


Figure 4.19 ArcGIS showing the Picarro mobile system route in block 1 in Ahmadi Town on 5th of May 2015. Black arrow indicates the wind direction (SSE), the yellow pushpins represent the air sample locations, and the green circles are the vents shown in figure 4.16

Figures 4.20 and 4.21 show that methane emission peaks are observed in Block 1 around the houses in the south of Al-Ahmadi Town. The maximum methane mole fraction measured was 9.01 ppm in this block during the survey.

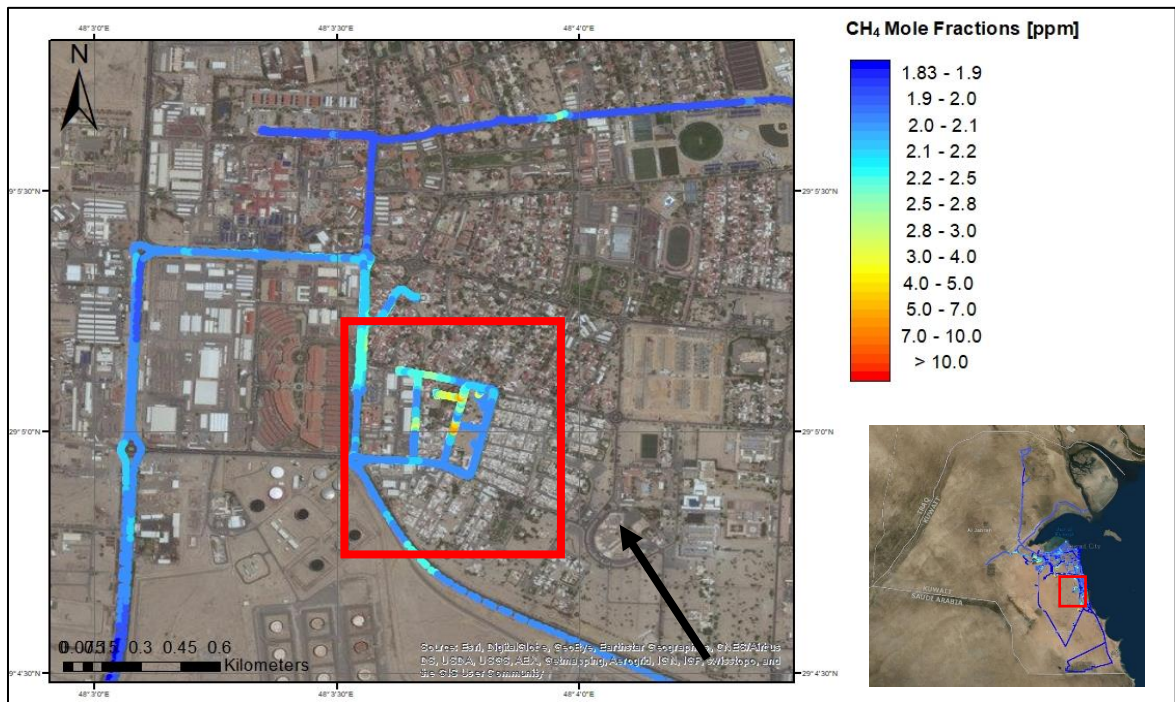


Figure 4.20 ArcGIS showing the Picarro mobile system route around Al-Ahmadi Town (5th May 2015). Black arrow indicates the wind direction, the red square shows the zoomed area of the next map

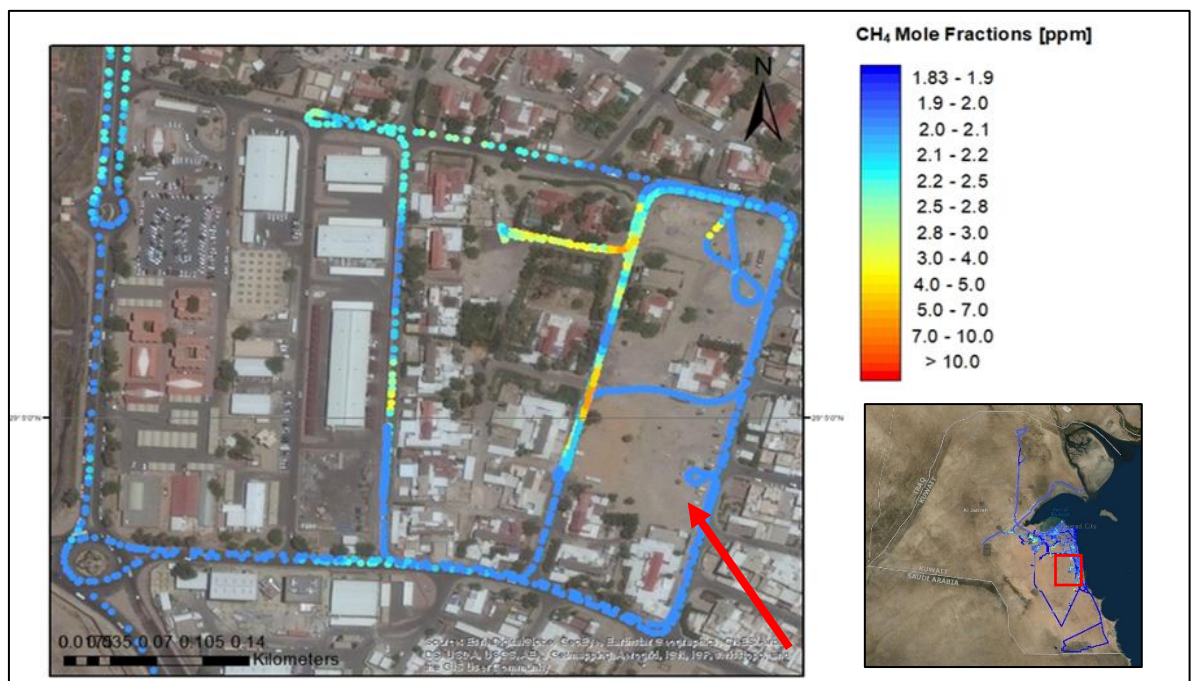


Figure 4.21 ArcGIS showing the Picarro mobile system route in Block 1, South Ahmadi Town (5th May 2015). Red arrow indicates the wind direction.

The $\delta^{13}\text{C}\text{-CH}_4$ source signature resulting from the Keeling plot (figure. 4.22) based on the air samples collected in Block 1, south Ahmadi Town is $-50.0 \pm 0.2 \text{ ‰}$. Based on the $\delta^{13}\text{C}\text{-CH}_4$ source signature, it is not possible to determine whether gas is from the pipe network or natural geological sources.

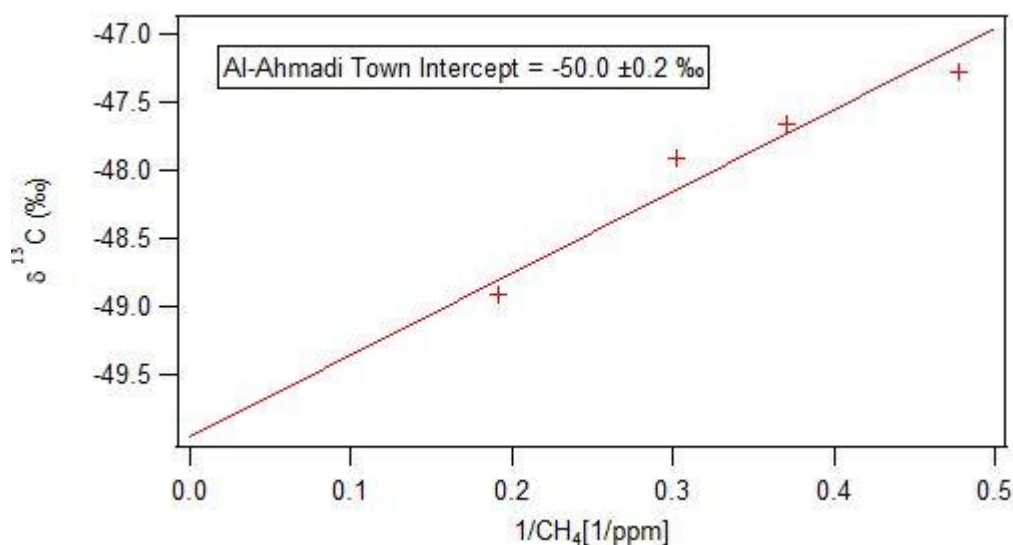


Figure 4.22 Keeling plot based on the samples collected in Al-Ahmadi Town on 5th May 2015

4.3.2 Isotopic signature for Kuwait natural gas

A natural gas sample was provided by the KNPC laboratory, from the Al-Ahmadi field and the Greater Burgan field which is the biggest oil field in Kuwait and the second-largest producing field in the world. The Greater Burgan field is an oval dome of some 750 km² and a high ellipticity of 0.7 and a slight elongation striking north. The structure is cut by nearly 30 faults. The largest fault identified has a 73 m throw (Alsharhan & Nairn 1997). The Greater Burgan oil field is located to the south and subdivided into the Burgan, Magwa, and Ahmadi sectors (Figure. 4.23).

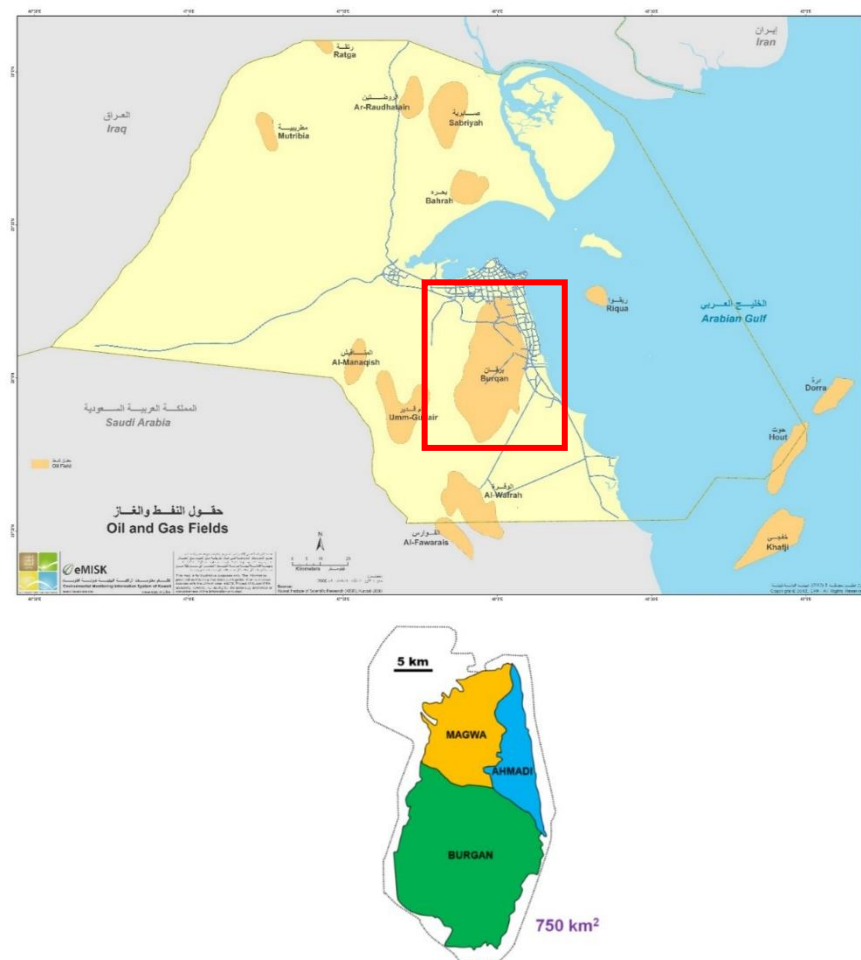


Figure 4.23 Great Burgan field. Source:(Alsharhan & Nairn 1997) , eMISK,2018.

The gas sample contained C1-Methane 64.3%, C2-Ethane 9.27%, and C3-Propane 6.51% (data from KNPC). Methane $\delta^{13}\text{C}$ was measured by GC-IRMS at RHUL. The $\delta^{13}\text{C}\text{-CH}_4$ source for Kuwait natural gas based on this sample is $-48.9 \pm 0.2\text{‰}$ (5 separate dilutions of 1 concentrated gas sample).

4.4 Discussion

The global fossil fuel industry contributes 15 to 22 % of methane emissions to the total atmospheric methane budget (Schwietzke *et al.* 2016). Another study shows that the global measurements of $^{14}\text{CH}_4$ estimated the fossil (energy) methane emissions at 9 – 27% of the total methane emission (Chen & Prinn 2006). There are many sources for methane emissions in the gas industry. Gathering Centers are a potential source of the methane emissions in natural gas systems. Marchese *et al.* (2015) and Mitchell *et al.* (2015) measured the methane emissions from natural gas gathering centers and processing plants in the United States. The studies showed that the methane emission and the distributions mainly for gathering facilities are negatively correlated with facility throughput. This variation in methane emissions appears to be due to differences between inlet and outlet pressure, as well as venting and leaking equipment. A minority of facilities contribute most of the emissions (known as a fat tail). For example, 30% of gathering facilities contribute 80% of the total emissions (Mitchell *et al.* 2015). A methane emission study was conducted by the Health, Safety and Environmental Department in KOC for two Gathering Centers (Gathering Center 25 and Gathering Center 27) and one Booster Station (BS-131). This study revealed very low methane emissions of about 37 million cubic feet per year (MMcf/year) from Gathering Center (25) and it showed that the main methane sources for this facility are the flare emissions of 27.9 MMcf /year (Ibrahim, 2015) even though KOC flare emission have been recently greatly reduced.

Methane emissions from natural gas as a part of production declined by approximately 2 to 8 % over the past three decades (Schwietzke *et al.* 2016). Schwietzke *et al.* (2016) suggest that methane emissions from natural gas are greater than inventories by 20 to 60 %.

Stable isotope ratios are one of the geochemical tools commonly used to link the natural gases to their sources. Stable carbon isotopic signatures of natural gas are influenced by environmental conditions such as temperature, soil moisture content or dissolved inorganic carbon at the time of formation (Whiticar 1996). There are variable isotopic signatures of methane in natural gas. Formation temperature of the gas reservoir is the main influence on the methane isotopic signatures. The thermal maturity is one of the primary controls on gas chemistry. More mature gases tend to be drier and isotopically heavier (Arouri *et al.* 2010). There are many studies undertaken on the natural gas origin based on the field data collected for different gas types: a) shallow, low-temperature bacterial gases, b) higher temperature “thermogenic” gases, often associated with oil and c) coal-bed and shale-hosted gases (Rice 1992; Tang *et al.* 2000). The stable C isotopic signatures are formed by bacterial processes (biogenic) or generated from Type I and II kerogen by thermogenic processes (non-biogenic) (Whiticar *et al.* 1986; Whiticar 1996). A Bernard plot (Figure. 4.24) determines the origin of natural gases by using $C_1/(C_2+C_3)$ ratio and $\delta^{13}C$ values of methane. The $\delta^{13}C$ composition of bacterial methane ranges from -120 to -50‰ (Pallasser 2000) whereas thermogenic methane typically has $\delta^{13}C > -50‰$. Sherwood *et al.* (2017) assume a $\delta^{13}C$ value of -50 or -55‰ as the limit between thermogenic and microbial CH_4 . Recent work extends the thermogenic field to isotopically lighter values (-67‰). Based on previous work, the isotopic signature of this study $-48.9 \pm 0.2‰$ falls within the thermogenic origin field.

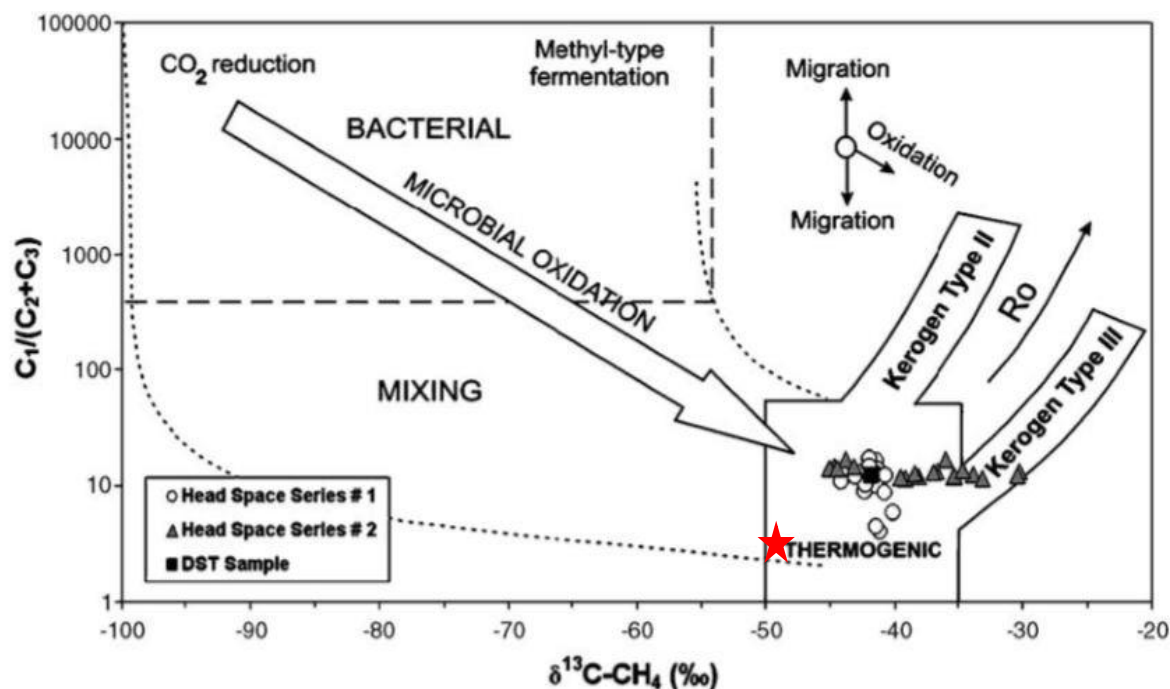


Figure 4.24 Bernard diagram to classify natural gas origin by using the molecular ratio of the natural gas: $C_1/(C_2+C_3)$ against $\delta^{13}C-CH_4$ (‰). This plot is modified after Aali *et al.* (2006) results, based on the original figure of Bernard *et al.* (1978). The red star represents the sample from the Greater Burgan field in this study which confirmed the thermogenic origin of the Kuwait gas.

The United Kingdom is directly supplied with gas of thermogenic gas origin from North Sea fields through the gas network. North Sea fields have a very distinctive and heavier isotopic values ranging from -37 to -25 ‰ (Lowry *et al.* 2001; Dlugokencky *et al.* 2011). A study of SE England natural gas plumes carried out during 2013-2014 showed $\delta^{13}C-CH_4$ for the natural gas to be -36‰ (Zazzeri 2015). RHUL laboratory measured natural gas network samples from European countries give values of -29.5 ± 0.9 ‰ for a sample from Holland and -47.6 ± 0.9 ‰ for a sample from Italy (Zazzeri 2015). Around 3356 CH_4 leaks were identified across Boston City in the US with average $\delta^{13}CH_4$ values of -36.8‰ (Phillips *et al.* 2013). In southwest Germany, the natural gas isotopic signature was calculated to be -50.8 ± 2.8 ‰ (Levin *et al.* 1999). Lowry *et al.* (2001) measured the gas of St. Petersburg, Russia and

found the $\delta^{13}\text{C}$ isotopic values of the natural gas ranged from -51.5 to -48.5‰. This is due to the mixing of the shallow West Siberian gas of biogenic origin (-64 to -58‰) with deep reserves of thermogenic origin (-50 to -38‰). In Heidelberg, the isotopic signatures of natural gas from the distribution network were changing seasonally according to the supply sources which lead to $\delta^{13}\text{C}$ values to be more depleted (-50‰) in summer due to the supply source mainly from Russian pipelines while in winter the values were more enriched (-30‰) with the supply coming from North Sea (Levin *et al.* 1999).

The world's largest gas field in Iran was studied by Aali *et al.* (2006) to investigate the origin of the gas in the Upper Permian Dalan Formation by evaluating the $\delta^{13}\text{C}$ values of methane. In this study two series of head space gas samples were collected at 2670 – 3149 m depth during the drilling phase in the South Pars field. The average $\delta^{13}\text{C}$ values of methane were -41.9 ‰ for first series and -37.8‰ for the second series. Another study on one of the largest natural gas provinces in Iran shows that the $\delta^{13}\text{C}$ values of methane range from -42.5 ± 0.2 ‰ to -37.2 ± 0.2 ‰ (Sabeti & Rabbani 2015). Stable isotopic compositions of natural gas were analysed from two gas fields in Eastern Kopeh-Dagh in Iran (Saadati *et al.* 2016). These studies show an overall range of $\delta^{13}\text{C}$ values from -43 to -32 ‰ indicating that the Iranian gas fields are a source of thermogenic emissions.

The $\delta^{13}\text{C}$ methane values tend to increase with depth of formation (Berner & Faber 1996; Lakshmi *et al.* 2014). Galimov & Rabbani (2001) studied the Late Permian Dalan Formation Zone D, E; Early Triassic Kangan and Lower Zone of the Dalan Formation (Zone G) in Southern Iran for characterisation of the chemical and isotopic composition of the gases to interpret the origin of these gases. They found gases from Kangan Formation within 1801-1983 m depth and upper part of the Dalan Formation (Zone D, E) at 2036-2328 m depth to be uniform in chemical and isotopic characteristics. The measured $\delta^{13}\text{C}$ values varied from -40.6 to -40.3 ‰ for Kangan Formation and -41.3 to -40 ‰ for the Dalan Formation (Zone D, E). Methane content in the gas varied from 84.4 to 87.6% for these formations. Gases from the Lower Zone (G) of the Dalan Formation at depth 3600-3655m showed significantly different characteristics with a $\delta^{13}\text{C}$ signature of -26.2‰. This is similar to the results of the

study by Worden and Smalley (1996) of the Khuff Formation in Abu Dhabi. They reported that methane $\delta^{13}\text{C}$ values of -45 to -40‰ were found within shallower zones (< 4300 m) and in deeper horizons gases (> 4300 m) the methane $\delta^{13}\text{C}$ signature was -23‰.

In a study by Jenden *et al.* (2015) natural gas samples were collected from Permian Khuff reservoirs along the east coast of Saudi Arabia and in the Arabian Gulf between 1997 and 2013. Reservoir depths range from 3000 m to > 5200 m at temperatures of 100 °C to more than 150°C. Methane $\delta^{13}\text{C}$ ranges from -40‰ to -35‰ and can be as low as -48‰ in Paleozoic gases elsewhere in Saudi Arabia. $\delta^{13}\text{C}\text{-CH}_4$ isotopic signature of natural gas in Oman ranges from -42.3 ‰ to -38.1‰ found in the Khazzan and Saih Rawl field (Millson *et al.* 2008).

The methane $\delta^{13}\text{C}$ values of the Ghazal field, Saudi Arabia ranged between -45.3 to -28.2 ‰. Table 4.5 summarises the $\delta^{13}\text{C}$ values of methane from all the previous studies gas reservoirs in the Middle East, and selected studies of gas distribution networks.

Region	Site / country	$\delta^{13}\text{C}$ (‰)	Author
Europe	SE England, UK	-38.5 to -35.7	(Zazzeri 2015)
	Heidelberg, Germany	-50.8	(Levin <i>et al.</i> 1999)
	Holland	-29.5	(Zazzeri 2015)
	Italy	-47.6	(Zazzeri 2015)
	West Siberian	-64 to -38	(Lowry <i>et al.</i> 2001)
	North Sea	-37 to -25	(Lowry <i>et al.</i> 2001; Dlugokencky <i>et al.</i> 2011)
USA	Boston, USA	-36.8	(Phillips <i>et al.</i> 2013)
Middle East	Southern Iran	-41.2 to -26.2	(Galimov & Rabbani 2001)
	Abu Dhabi, UAE	-45 to -23	(Worden & Smalley 1996)
	South Pars, Iran	-41.9 to -37.8	(Aali <i>et al.</i> 2006)
	Khazzan , Oman	-42.3 to -38.1	(Millson <i>et al.</i> 2008)
	Ghazal, Saudi Arabia	-45.3 to -28.2	(Arouri <i>et al.</i> 2010)
	Kuwait	-48.9	This study

Table 4.5 Isotopic signatures of natural gas from previous studies of Middle East gas reservoirs and some national gas distribution systems

4.5 Fuel Combustion Emissions from Vehicles

Vehicles emit methane enriched in ^{13}C (Fisher, 2006). The methane $\delta^{13}\text{C}$ signatures of vehicles vary from -22 to -9 ‰ (Chanton *et al.* 2000). The combustion efficiency of the engine and the $\delta^{13}\text{C}$ of the fuel are the main factors that control the $\delta^{13}\text{C}$ methane produced by gasoline automobile engines (Zazzeri 2015). Methane $\delta^{13}\text{C}$ from cars in Heidelberg in Germany was -22.8‰ (Levin *et al.* 1993). Another study by Levin *et al.* (1999) showed the methane $\delta^{13}\text{C}$ isotopic values from car exhaust around -28.0 ± 2.4 ‰.

Fisher (2006) carried out a study of car exhaust emissions near RHUL. The results gave a methane $\delta^{13}\text{C}$ of -20.1 ± 1.7 ‰. Methane emissions from car exhaust are related to the $\delta^{13}\text{C}$ of the hydrocarbon mix of fuel used and the age of vehicle (Lowry *et al.* 2001). The most modern cars produce methane enriched with $\delta^{13}\text{C}$ due to the recent improvements in the efficiency of fuel combustion. There is an inverse relationship between methane concentrations and the $\delta^{13}\text{C}$ values. Higher combustion efficiencies mean less methane is produced and it is $\delta^{13}\text{C}$ enriched. This relationship was studied by Chanton *et al.* (2000) and Nakagawa *et al.* (2005). The values of $\delta^{13}\text{C}$ from automobile exhaust for 16 different ages cars (1979 to 1997) were between -20 and -10‰ with an average of -15.4 ± 4.1 ‰ (Chanton *et al.* 2000). This trend agrees with Nakagawa *et al.* (2005) who found that $\delta^{13}\text{C}$ -CH₄ values for modern cars were enriched by more than 10 ‰ (-11 to -9 ‰) compared to older cars (-21 ‰). According to the isotope fractionation effects associated with oxidation over metal catalysts in the catalytic converter of modern vehicles, $\delta^{13}\text{C}$ values of CH₄ in automobile exhaust increased in accordance with the model year of the engine.

In a study carried out for car emissions in Kuwait, five samples were collected from the exhaust of a single car (Range Rover Sport 2016). The car engine had been running for 3 minutes before samples were collected within 0.5 to 2 m of the exhaust pipe. The methane mole fractions for these air samples from the car ranged from 2.1 to 4.8 ppm. Based on the samples, the methane $\delta^{13}\text{C}$ value calculated by Keeling plot analysis for this vehicle was -13.3 ± 1.0 ‰ (Figure. 4.25). This value is comparable with the -10.9 ± 2.3 ‰ calculated by Zazzeri (2015) for 10 different cars.

The $\delta^{13}\text{C}$ values vary by engine age. In the 1990s the signatures were more depleted (-28 to -22‰) and during the early 2000s reached -20.0‰. The most recent values are more enriched with ^{13}C of > -15 ‰. This change may be due to high combustion efficiency of the engine in modern cars.

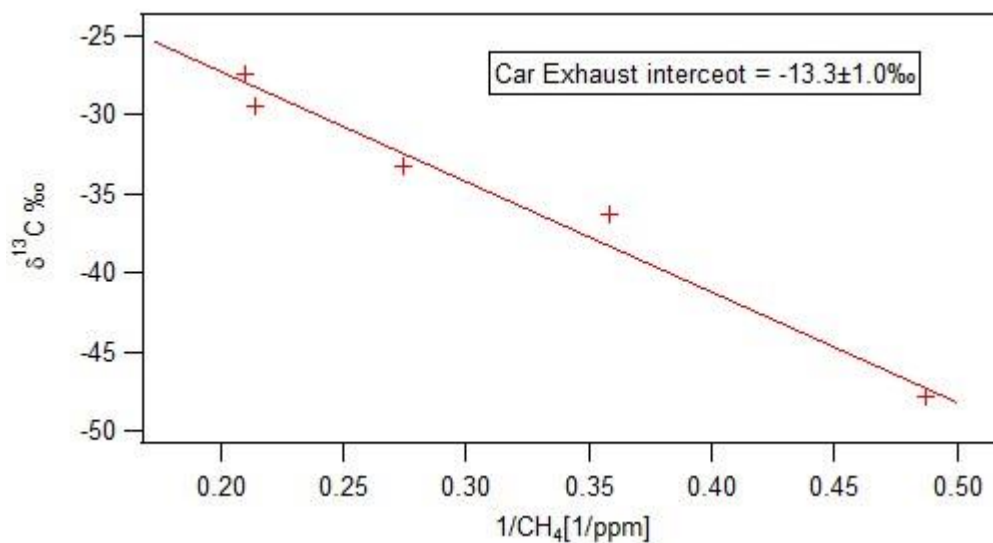


Figure 4.25 Keeling plot based on the car exhaust samples

4.6 Summary

The methane isotopic signature for Kuwait natural gas has been constrained to a value of $-48.9 \pm 0.2\text{‰}$. All the gas plumes and gas samples fall within the range -52 to -49‰ . According to the Bernard diagram, this is consistent with thermogenic gas because the gas contains high ethane and propane (Figure. 4.20). Table 4.3 summarises the $\delta^{13}\text{C}$ source signature of methane plumes sampled downwind of the refineries. Methane isotopic values of the Al-Ahmadi gas leaks, the Al Ahmadi oil field sample from Greater Burgan, plus fuel combustion emissions from a vehicle using fuel from Kuwait petrol station supply are presented in Table 4.6.

<i>Gas installation</i>	<i>$\delta^{13}\text{C}$ source signature (‰)</i>
Al-Ahmadi Town (gas leakage)	$-50.0 \pm 0.2\text{‰}$
Refineries	$-51.6 \pm 0.5\text{‰}$
Ahmadi oil field (Greater Burgan)	$-48.9 \pm 0.2\text{‰}$
<i>Car exhaust</i>	$-13.1 \pm 1.0\text{‰}$

Table 4.6 Fossil fuel related isotopic signatures in the state of Kuwait

C***HAPTER 5***

A***NALYSIS OF METHANE EMISSIONS FROM KUWAIT LANDFILL SITES***

5. Analysis of Methane Emissions from Kuwait Landfill Sites

Landfills have been considered as one of the main sources of methane gas emissions encountered during the surveys in the State of Kuwait. This chapter discusses landfill sites in the State of Kuwait. The chapter will introduce the landfill sites in Kuwait and present the results of the measured mole fraction of methane and the $\delta^{13}\text{C}$ source isotopic signatures.

5.1 Landfills Methane Emissions

Landfilling has long been the common method for final disposal of solid waste. All types of waste removal activity such as recycling and composting eventually leave some residual materials that need to be landfilled (Mc Dougall, 2011). Despite all the technologies, the long-lasting accumulation of waste creates negative impacts on the environment. Methane emissions arise from the anaerobic microbial degradation of organic waste (Christensen, 2011).

Landfills are responsible for 3-7% of global total CH_4 emissions (IPCC, 2013; Chanton *et al.*, 2011). Landfill Gas (LFG) typically consists of 50-60% of methane and 30-40% of carbon dioxide and other trace gases (Wang-Yao *et al.* 2006; Widory *et al.* 2012). However, these proportions change over time. Several studies have calculated the percentage of methane oxidation in landfill cover soils by the use of stable isotopes (Liptay *et al.* 1998; Chanton *et al.* 1999, 2000; Börjesson *et al.* 2001; Abichou *et al.* 2006; Widory *et al.* 2012).

Methane in the anoxic zone escapes the landfill to the atmosphere either through vents or cracks in the soil cap where no oxidation occurs or by flowing through the cover soil cap where partial oxidation occurs (Liptay *et al.* 1998).

Liptay *et al.* (1998) also determined the methane oxidation in landfill cover soils using stable isotopes. According to their study, the mean isotopic composition of CH₄, emitted from six New England (United States) landfills was ¹³C enriched (-50.4 to -48.1 ‰), relative to the methane in the anoxic zone landfill (mean values of -56.2 to -55.9 ‰). This was attributed to the oxidation of methane by methanotrophs while it was transported from the landfill to the atmosphere through the soil cap.

5.2 Landfill Sites in Kuwait

In Kuwait, landfilling is the main disposal method for domestic waste. It is estimated to be the largest source of anthropogenic methane (Al-Yaqout & Hamoda 2002). The present state of Municipal Solid Waste (MSW) disposal in Kuwait has been reviewed by several authors (Al-Meshan and Mahrous, 1999 and 2002; Al-Yaqout and Hamoda, 2002; KEPA, 2002; Al-Faraj, 2005; Al-Tahw, 2006; Mugeem, 2009; Abdullah, 2010; Al-Ahmad, 2012). Approximately 90% of all domestic waste is disposed in landfill sites and the remaining fraction is recycled. The landfill sites are not engineered, instead they are voids made by quarrying. The waste comprises household, organic, construction and industrial waste. Most of the landfill sites have been closed for more than 20 years due to operational problems, such as severe public health and environmental issues.

There are 18 landfill sites in Kuwait state of which 14 sites are closed and the other 4 are still operating and receiving municipal waste. These closed landfill sites are located within the city of Kuwait (Figure 5.1), close to human habitation, and generate huge amounts of gases (methane, carbon dioxide, etc.). They cover an area of 17.76 km², about 61% of the total landfill area in Kuwait (Figure 5.2).

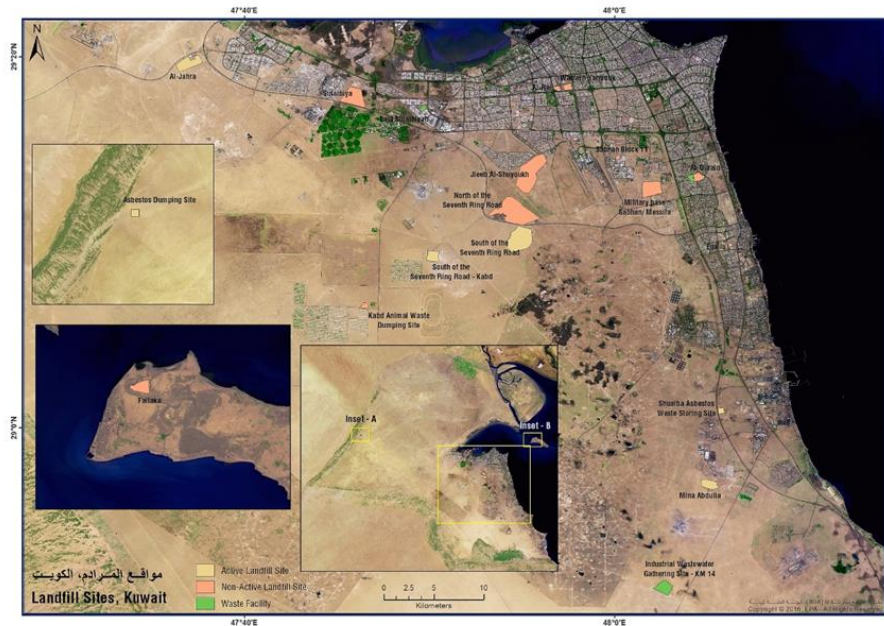


Figure 5.1 Location of Landfill sites (closed and active) in Kuwait in relation to the urban area. Source: eMISK.com

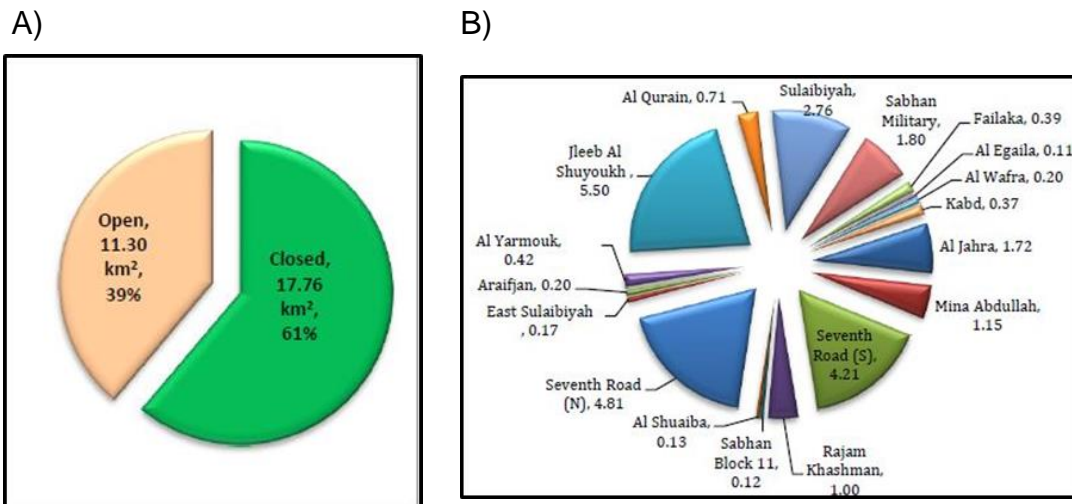


Figure 5.2 (A) Area of closed and open landfill sites in Kuwait (km²). (B) Areas of individual landfill sites in Kuwait (km²). source: Al-Ahmad,2012.

The four sites which are still in operation, cover an area of 11.3 km², about 39% of the total landfill area in Kuwait. Landfills occupy 29.06 km² of the Kuwaiti land, and this area is expected to reach 60 km² by 2025 (Al-Ahmad, 2012). Safe landfill areas were selected on low relief desert areas which were previously used as sand quarries (in a void made by quarrying). The landfills are lacking the operation of safe engineering practices (Figure 5.3).

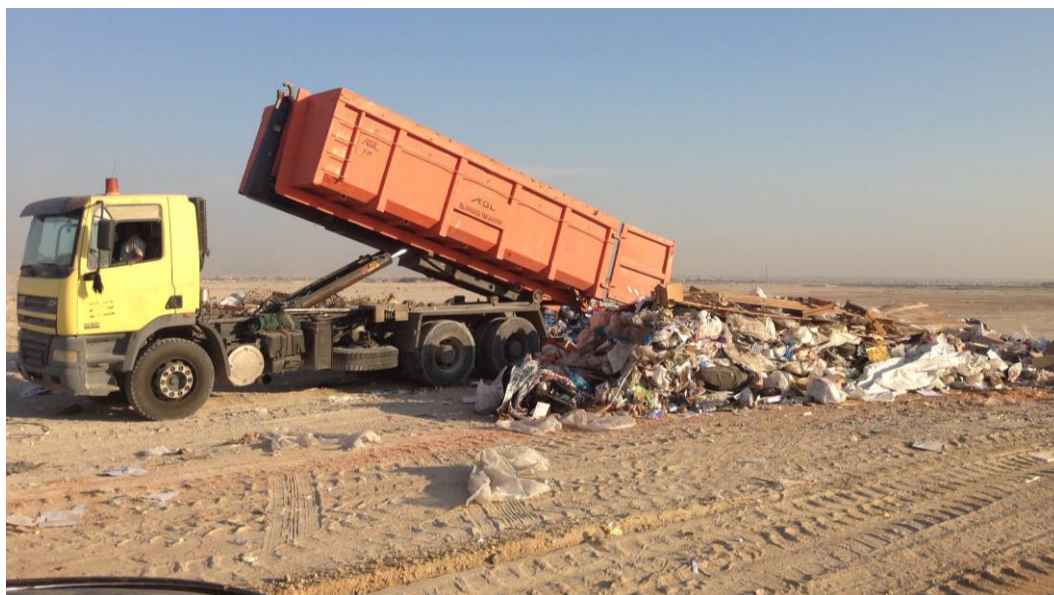


Figure 5.3 Dumping of mixtures of waste materials in Kuwait.

Several studies (Al-Yaqout & Hamoda 2002; Al-Yaqout *et al.* 2002, 2005) on the operational characteristics of solid waste landfills in Kuwait have shown that the landfills are posing serious environmental issues. Annually, more than 1 million tons of Municipal Solid Waste (MSW) are produced in Kuwait with a per capita rate of 1.4 kg/day. Based on the analysis of the refuse composition in Kuwait, the refuse primarily contains 58% of food, 18% of paper, and 12% of plastics (Hamoda,1997).

Since the 1970`s, the amount of solid waste in Kuwait has significantly increased as a result of the population increase. Table 5.1 summarizes the

quantities and rate of soil waste disposal during the period from 2000-2011 at MSW landfill sites (Al-Ahmad, 2012).

According to Kuwait's Initial National Communications under the United Nations Framework Convention on Climate Change report on November 2012, about 26% of the CH₄ emissions (Figure 5.4) in the State of Kuwait in the year of 1994 were from waste disposal.

Year	Household SW (Ton)	Increasing Rate (%)	Construction Waste (Tons)	Increasing Rate (%)	Total (Tons)	Increasing Rate (%)
1997	880685	-	2784500	-	3665185	-
1998	999622	13.5	2685200	-3.5	3684835.5	0.5
1999	1079086	8	2892670	7.5	3971763.9	8
2000	1063697	-1.5	3918240	35.5	4981935.6	25.5
2001	1236771	16	4035390	3	5272177.3	6
2002	1289855	4	4758910	18	6048769.3	14.5
2003	1296365	0.5	3773880	-20.5	5070245.5	-16
2004	1107949	-14.5	4309200	14	5417134.5	7
2005	1113153	0.5	3699050	-14	4812203.5	-11
2006	1288379	16	6972465	88.5	8260859.7	71.5
2007	1558748	21	3926280	-43.5	5485049	-33.5
2008	1310036	-16	4481190	14.1	5791226	-5.6
2009	1153233	-12	2231695	-50.2	3384928	-41.6
2010	1408432	22	1568535	-29.7	2976967	-12.1
2011	1357395	-4	1276589	-18.6	2633984	-11.5

Table 5.1 Quantities and rate of soil waste received at MSW landfill sites in Kuwait from 1997 to 2011. (Source: Al-Ahmad, 2012).

The emissions of landfill gas have always been a major concern to the local communities because of the foul odor and various health and environmental hazards. On a global scale, the emission of methane in LFG contributes to the greenhouse effect and global methane budget.

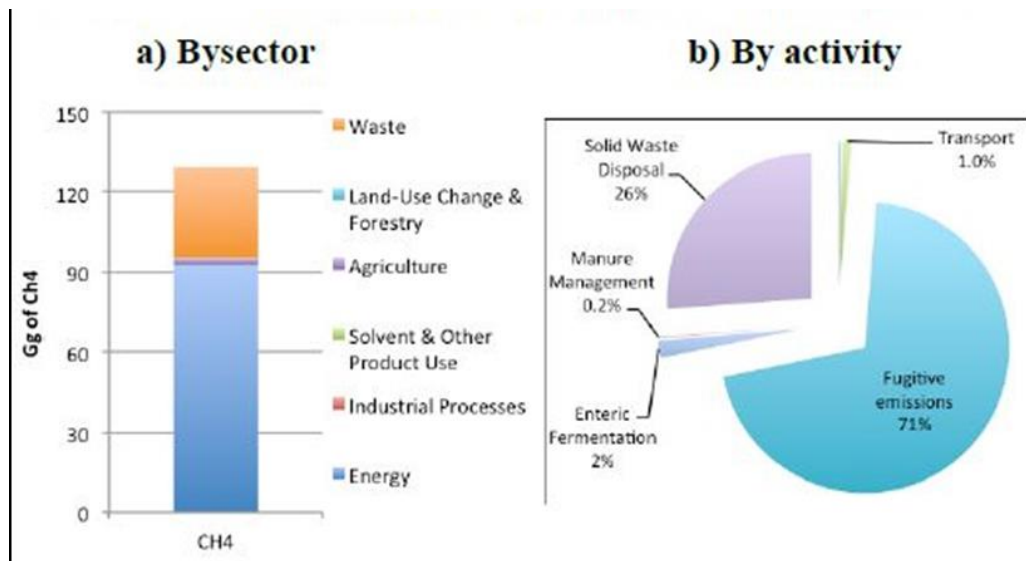


Figure 5.4: The contribution associated with CH₄ emissions at both the a) sector and b) activity levels in Kuwait 1994. (Source: the Kuwait's Initial National Communications under the United Nations Framework Convention on Climate Change report, November 2012.)

5.3 Kuwait Campaign

During the Kuwait mobile campaign introduced in chapter 3, seven landfill sites were included in the route (Figure 5.5). Before every survey, wind direction was checked to verify that the downwind area of the landfill sites was reachable. Methane measurements during the campaign were carried out in May, when the temperature in Kuwait was around 30°C. Figure 5.6 shows the seven landfill sites that have been surveyed in this study, of which four sites are active and three are closed. These are briefly mentioned here and described in more detail in the following section. (1) Al-Jahra landfill, (2) the South Seventh Ring Road landfill, (3) Mina Abdullah landfill, (4) Kabad landfill, (5) Al-Sulabiya landfill, (6) Al-Qurain landfill and (7) Jleeb Al-Shuyoukh landfill.

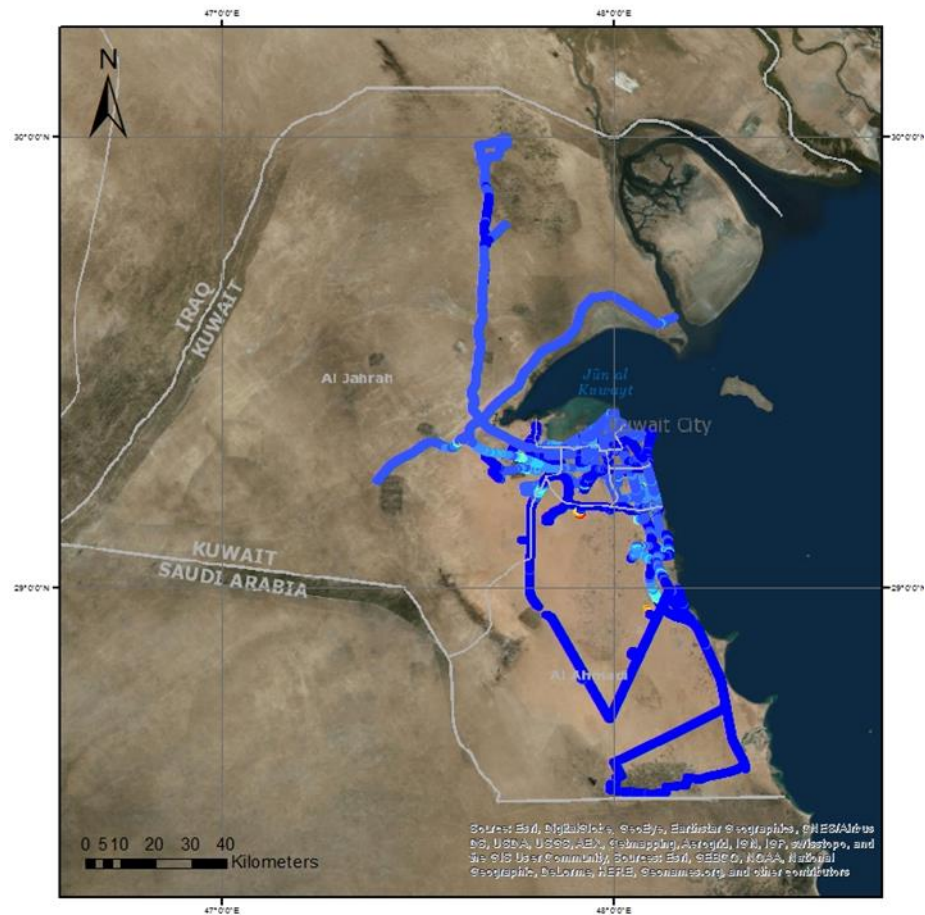


Figure 5.5 ArcGIS Plot of the route of the Kuwait Campaign over 6 Days: 2nd-7th of May 2015.

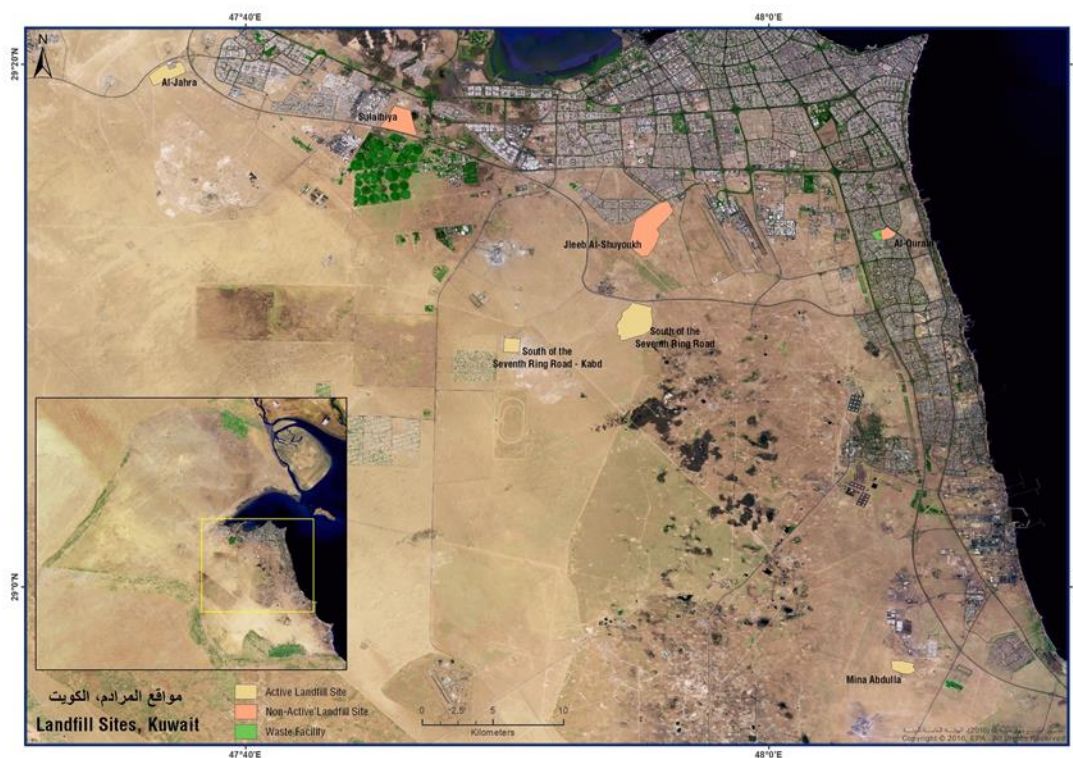


Figure 5.6 The Seven landfills that were surveyed by the Picarro mobile system in the Kuwait Campaign during the period 2nd to 7th of May 2015.
Source: eMISK.com

A summary of all the landfill sites which were surveyed by the Picarro mobile system from the period of 2nd to 7th of May 2015 during the Kuwait campaign is shown in Table 5.2. All sites are located around and within the Kuwait urban area.

Sample Name	Date	Time UT	Latitude °N	Longitude °E	CH ₄ Mole fraction (ppm)
Al-Jahra Landfill	2/5/2015	12:00:00	29.312	47.578	1.98
	2/5/2015	12:02:00	29.326	47.604	2.16
	2/5/2015	12:17:00	29.326	47.617	5.51
	2/5/2015	12:24:00	29.329	47.618	2.93
Al-Sulabiya Landfill	3/5/2015	8:08:00	29.279	47.692	1.89
	3/5/2015	8:44:00	29.290	47.765	2.49
	3/5/2015	8:45:00	29.290	47.764	2.99
South of 7 th Ring Road Landfill	3/5/2015	11:06:00	29.166	47.912	11.92
	3/5/2015	11:11:00	29.165	47.914	20.18
	3/5/2015	11:17:00	29.165	47.915	34.34
	3/5/2015	11:22:00	29.169	47.908	6.18
	3/5/2015	11:26:00	29.174	47.916	1.93
	3/5/2015	11:29:00	29.178	47.916	1.90
Al-Qurain Landfill	4/5/2015	7:14:00	29.226	48.066	3.64
	4/5/2015	7:28:00	29.225	48.070	2.40
	4/5/2015	7:30:00	29.227	48.069	2.24
	4/5/2015	7:34:00	29.226	48.067	3.73
South 7 th Ring Road Landfill	4/5/2015	8:44:00	29.182	47.915	3.21
	4/5/2015	8:47:00	29.182	47.932	1.91
Jeleeab AL-Shuyoukh Landfill	4/5/2015	11:38:00	29.220	47.923	2.58
	4/5/2015	11:44:00	29.220	47.924	1.92
	4/5/2015	11:51:00	29.229	47.926	2.54
	4/5/2015	11:55:00	29.231	47.924	2.34
Mina Abdullah Landfill	5/5/2015	10:20:00	28.947	48.089	3.08
	5/5/2015	10:23:00	28.953	48.086	3.66
	5/5/2015	10:31:00	28.951	48.089	8.60
	5/5/2015	10:41:00	28.955	48.087	2.72
	5/5/2015	10:43:00	28.953	48.089	6.78

Table 5.2 Landfill sites that were surveyed during the Kuwait campaign in 2015 with the date and time and locations of the collected air samples and the mole fractions in (ppm) of methane in the air bag samples.

5.3.1 Al-Jahra landfill

Al-Jahra landfill is one of the largest non-engineered active landfill sites. It is very close to a highly populated city in Kuwait, Al-Jahra. This landfill site started operating in 1986 and it covers an area of approximately 1.98 km² (Figure 5.7). Al-Jahra active landfill site mainly receives household solid waste. On the 2nd of May 2015, this landfill was surveyed by the Picarro Mobile System (Figure 5.8). As the Al-Jahra landfill is still active, the area has been affected by methane emissions, and the plume was detected with a recorded maximum mole fraction of 11.34 ppm.

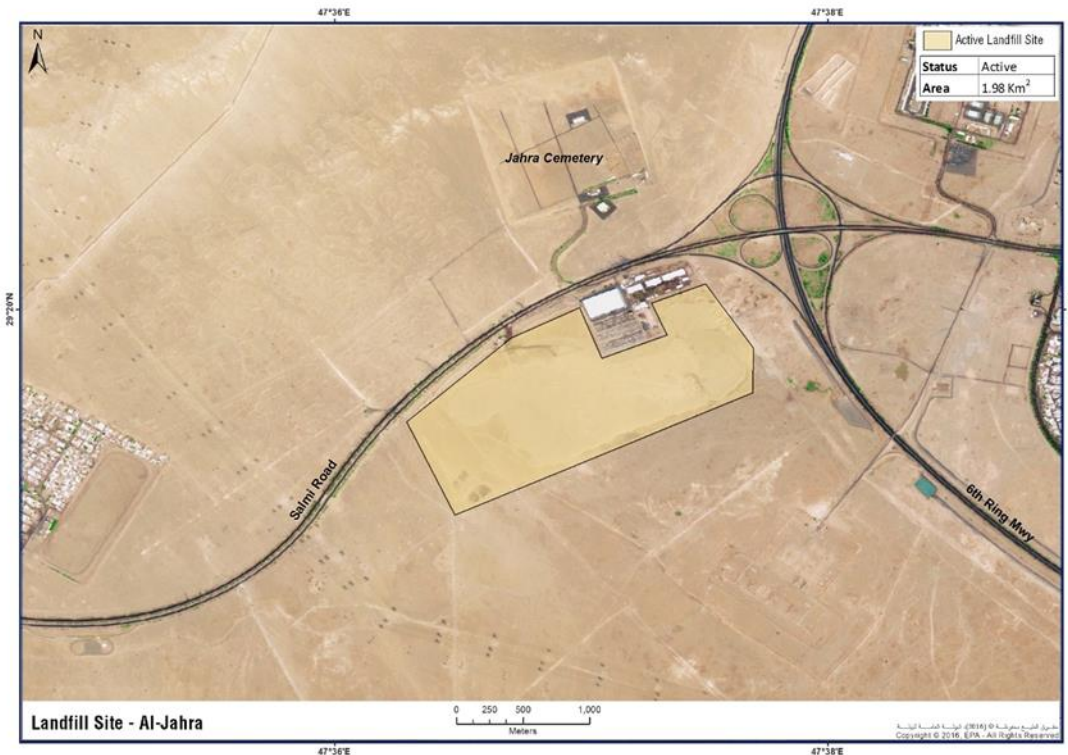


Figure 5.7 Al-Jahra active Landfill source: eMISK.com

Four air samples were collected in the Al-Jahra landfill site of which three were taken at the landfill, and one sample on the transect downwind of the landfill plume to the NE. Air samples were collected through the emissions plume, in order to get at least three samples to represent the integrated methane emissions downwind of the landfill (Figure 5.8). Figure 5.9 shows the Keeling plot analysis based on the samples collected from the area that were affected by Al-Jahra landfill emissions. Samples analysis yielded a source signature of $-59.4 \pm 1.4\%$.

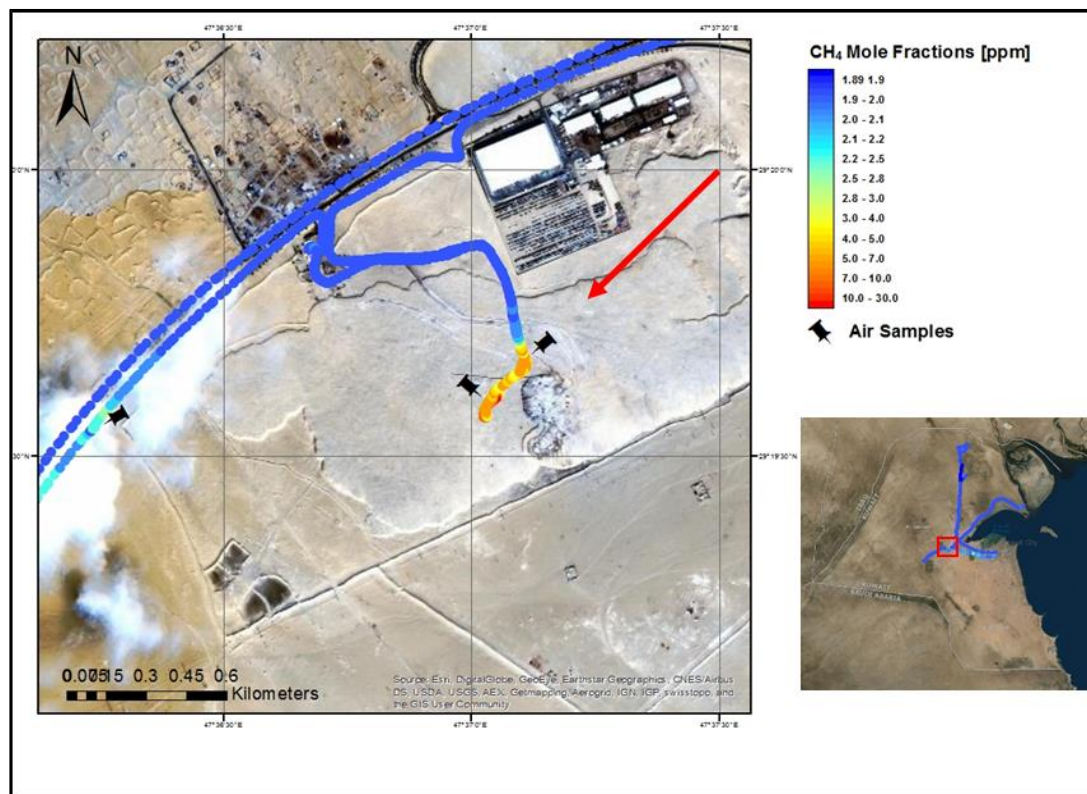


Figure 5.8 ArcGIS plot of Methane Mole Fractions (ppm) in the Al-Jahra active landfill on the 2nd of May 2015. The black markers are the locations of the air samples collected and the red arrow is wind direction.

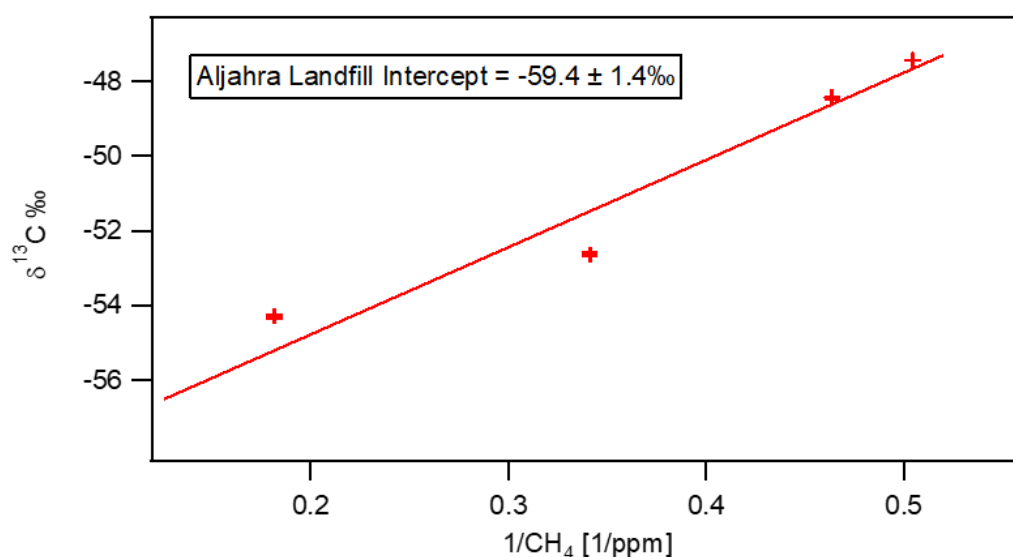


Figure 5.9 Keeling plot based on the air samples collected from the Al-Jahra landfill site on 2nd of May 2015

5.3.2 The South 7th ring road landfill

This active landfill site is located to the south of a public road known as the 7th Ring Road as shown on Figure 5.10. It is about 5.7 km away from a residential area. This landfill site started to operate in 1992 and covers a total area of 4.28 km². On the 3rd of May 2015, this landfill was surveyed when the wind direction was from the NE. It was found that the landfill is still emitting large amounts of methane with a maximum recorded mole fraction of 38.7 ppm, which was the highest value measured in this campaign.

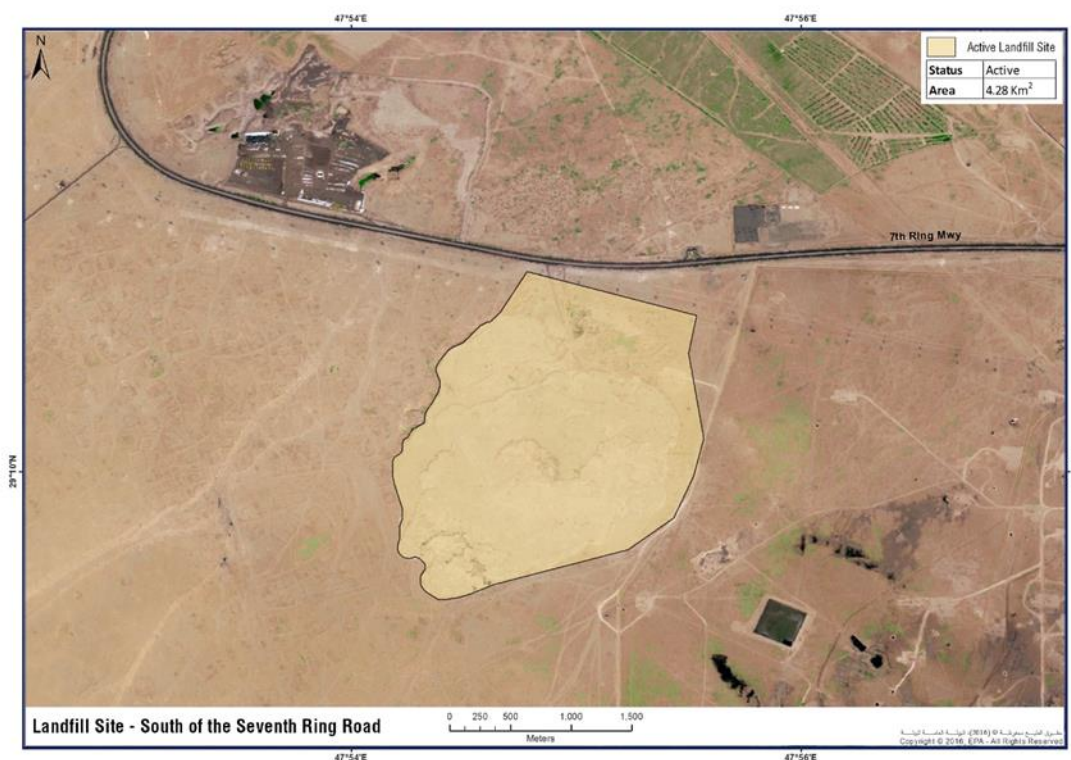


Figure 5.10 The South 7th Ring Road active Landfill. (source: Emisk.com)

Figure 5.11 shows an ArcGIS map with methane mole fractions in the 7th Ring Road landfill site plotted. The six air samples from the site were collected while transecting the main plume at the centre of the landfill. The maximum methane mole fraction measured in this active landfill site was 38.7 ppm. The Keeling plot based on those air samples gives a source signature value of $-58.5 \pm 0.5\%$ (Figure 5.12).

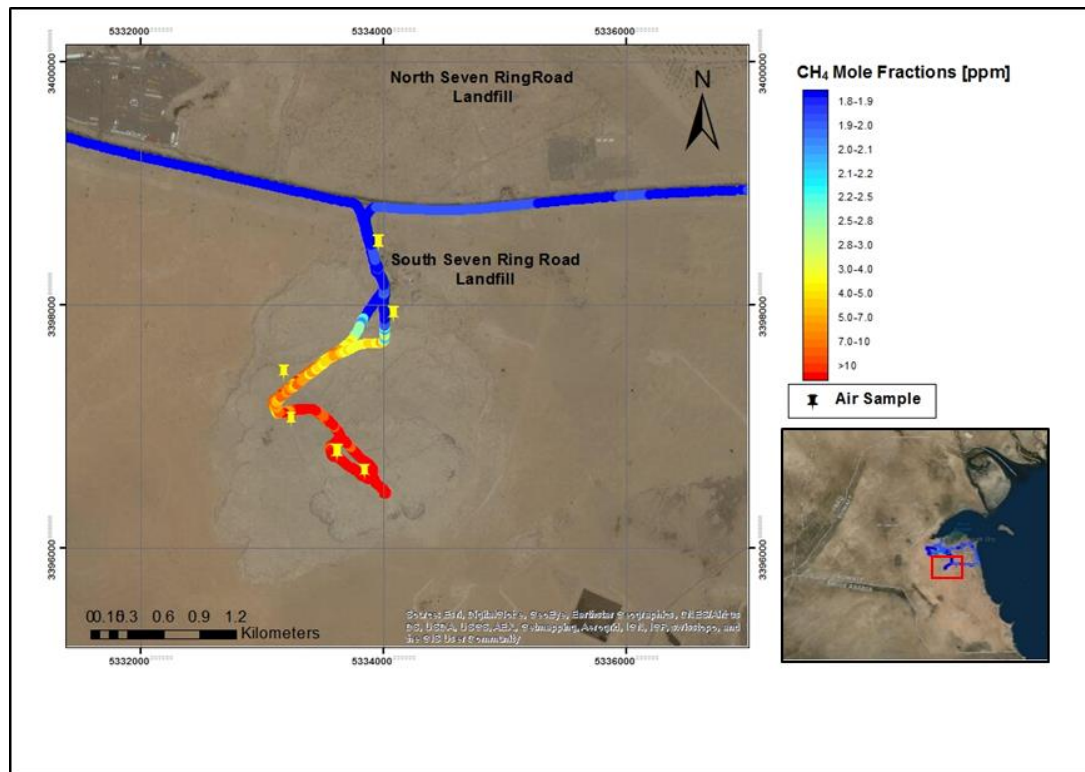


Figure 5.11 ArcGIS plot of Methane mole fractions (ppm) in the South 7th Ring Road active landfill site on 3rd of May 2015. The yellow markers are the locations of air samples collected

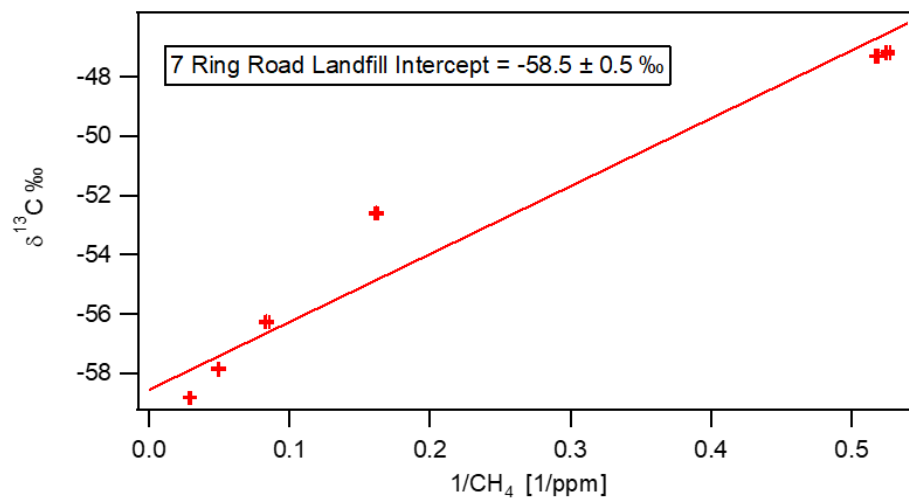


Figure 5.12 Keeling plot based on the samples collected on the South 7th Ring Road landfill site on 3rd of May 2015.

On the 4th of May 2015, when the wind direction was from a SE direction, a high methane peak was detected with a maximum methane mole fraction of 6.35 ppm. The ArcGIS base map as shown in Figure 5.13 illustrates the locations of the landfill site in relation to the main public road from which the methane measurements were taken. Two air samples were collected with mole fractions ranging from 2.5 to 3 ppm.

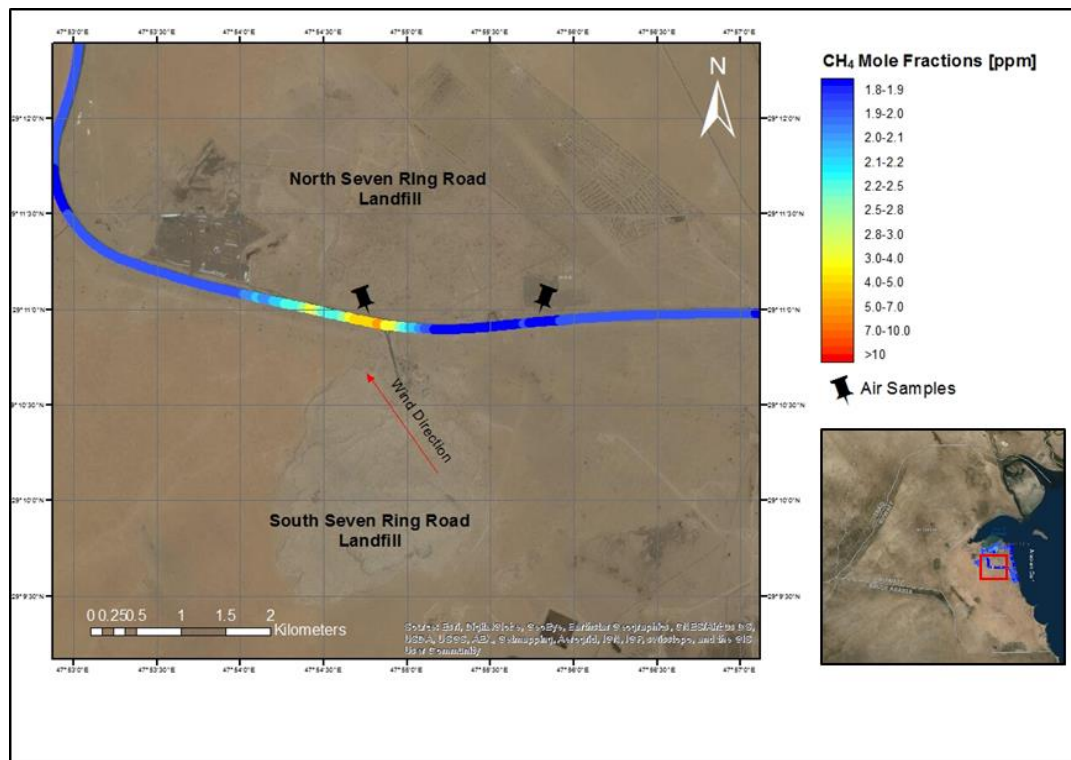


Figure 5.13 ArcGIS map of methane mole fractions (ppm) in the South 7th Ring Road landfill site. The black markers are the location of the air samples collected. The red arrow represents the wind direction on 4th of May 2015

While driving on the 7th of May 2015 and passing next to the 7th South Ring Road active landfill site using the Picarro Mobile System, the wind was coming from S-SE direction. High methane peaks were detected with a maximum mole fraction of 4.6 ppm as shown in the ArcGIS map in Figure 5.14.

The fact that the 7th South Ring Road landfill site has been surveyed three times on three different days has confirmed that this public road is affected by emissions of methane from the landfill site.

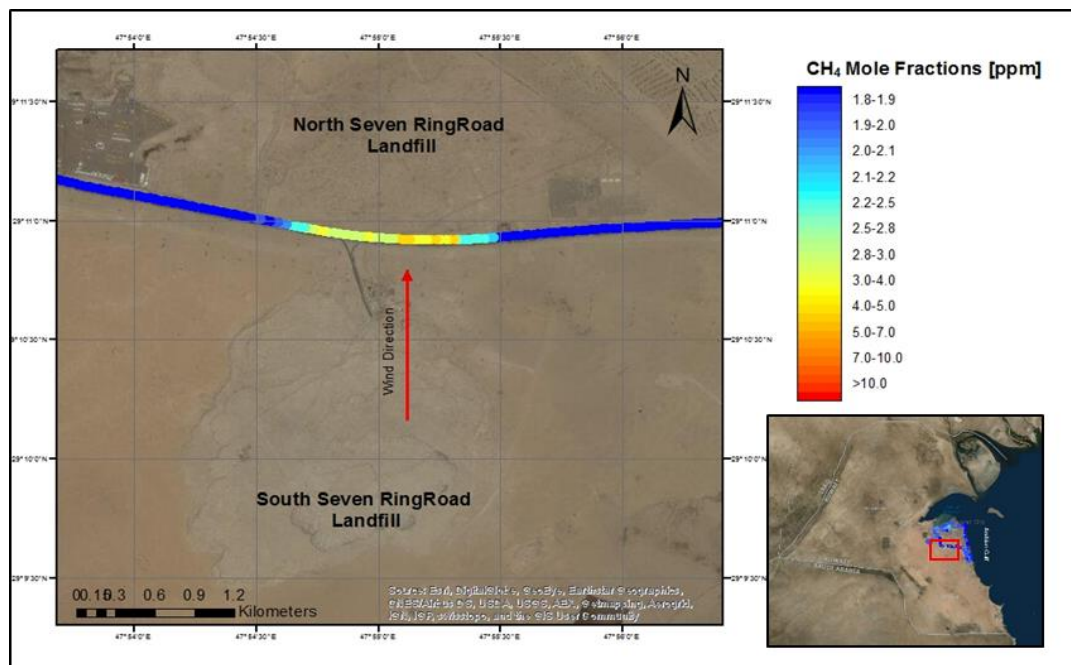


Figure 5.14 ArcGIS map of methane mole fractions (ppm) in the south 7th Ring Road landfill site. The red arrow represents the wind direction on 7th of May 2015.

5.3.3 Mina Abdullah landfill

Mina Abdullah landfill site is an active site that started operating in 1991 with a total area of 1.15 km² and a waste depth of more than 15 m. Although this landfill site is still in operation, only household waste is permitted (Al-Ahmad, 2012). Mina Abdulla landfill site is approximately 4.6 km from the nearest residential area (Figure 5.16). It is surrounded by roads and industrial areas.

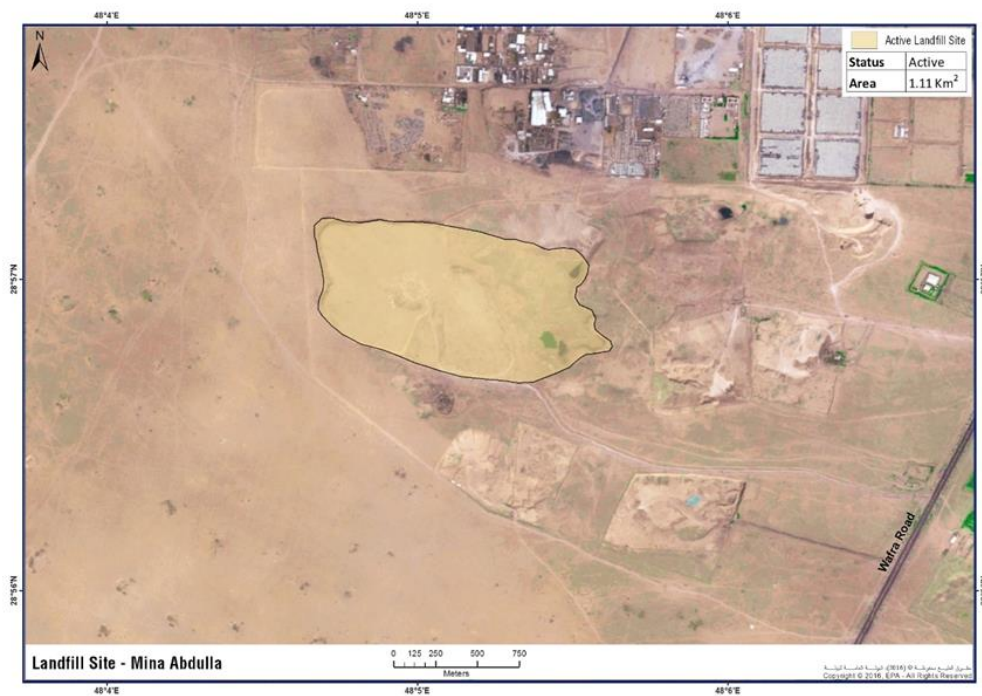


Figure 5.15 Mina Abdullah active landfill site. Source: eMISK

The Mina Abdullah site was surveyed on the 5th of May 2015 while the wind direction was from SE. The methane plume was detected on the landfill site with a maximum mole fraction of 23.8 ppm (Figure 5.16). Five air samples were collected, and analysis yielded a Keeling plot intercept of $-59.2 \pm 1.0\%$ (Figure 5.17).

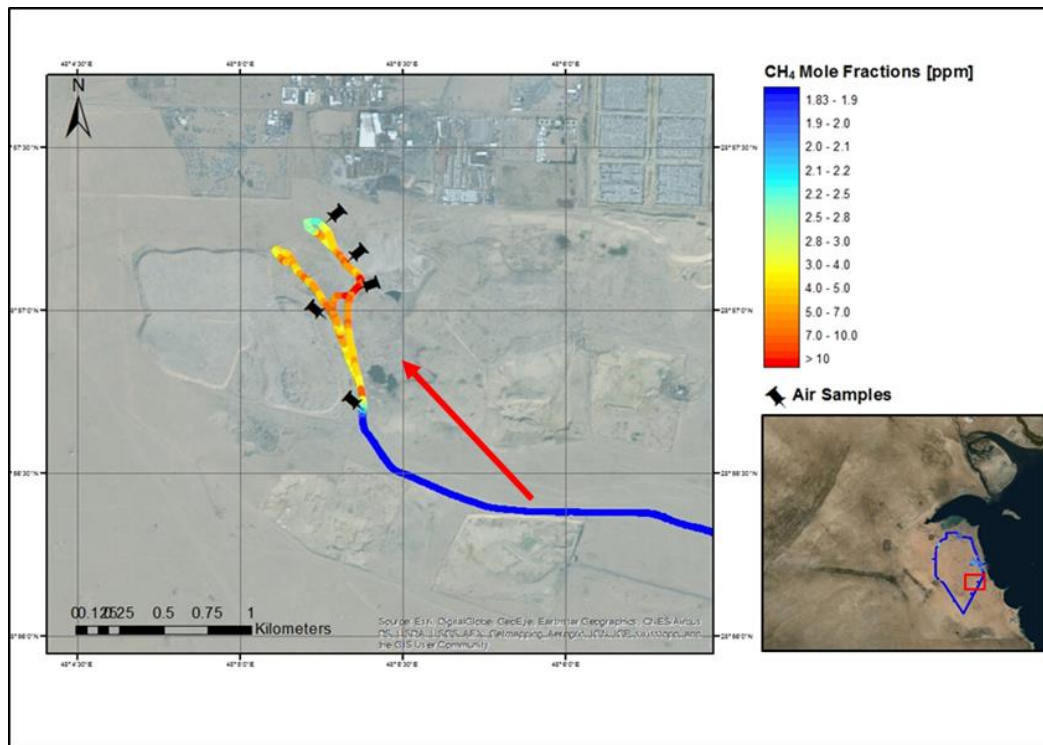


Figure 5.16 ArcGIS map of methane mole fractions (ppm) in the Mina Abdullah landfill site. The black markers are the location of the air samples collected and red arrow the wind direction.

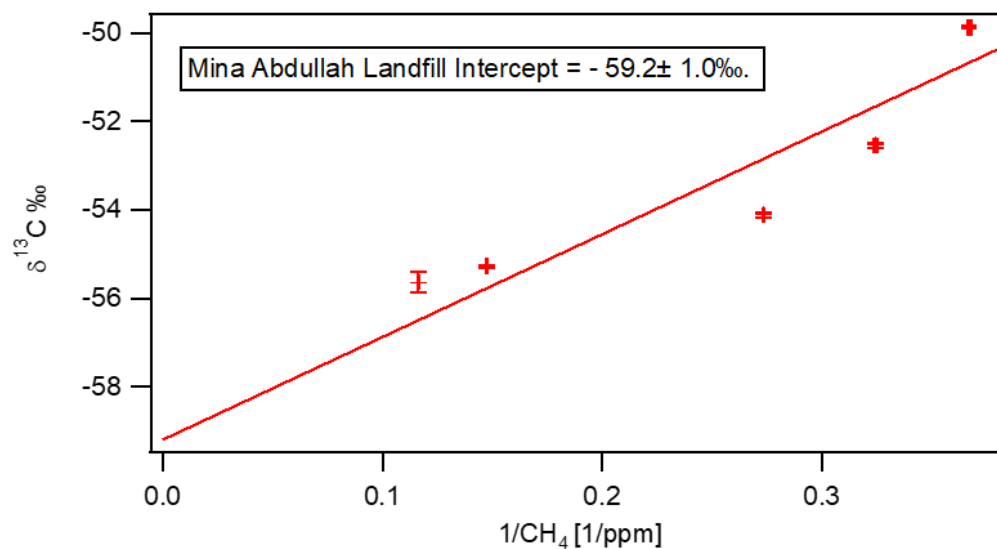


Figure 5.17 Keeling plot based on the samples collected on Mina Abdullah landfill

5.3.4 Kabad (construction) landfill

This landfill is located in the southwest of the South 7th Ring Road landfill site, as shown in the ArcGIS base map (Figure 5.18). This is an active landfill for construction waste with a total area of 1 km². The landfill is relatively new and started operating in 2010 for construction waste. On the 3rd of May 2015, this active landfill was surveyed by the Picarro Mobile System with no emissions recorded from this landfill site. All the methane mole fraction measured from this landfill site were within the background level (Figure 5.19).

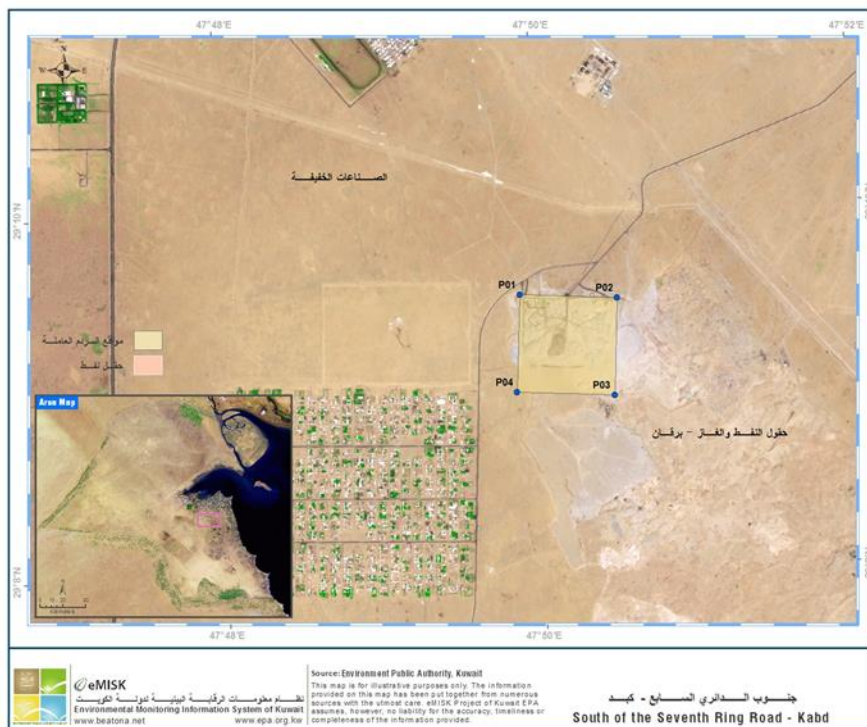


Figure 5.18 Kabad Construction Landfill Source: eMISK

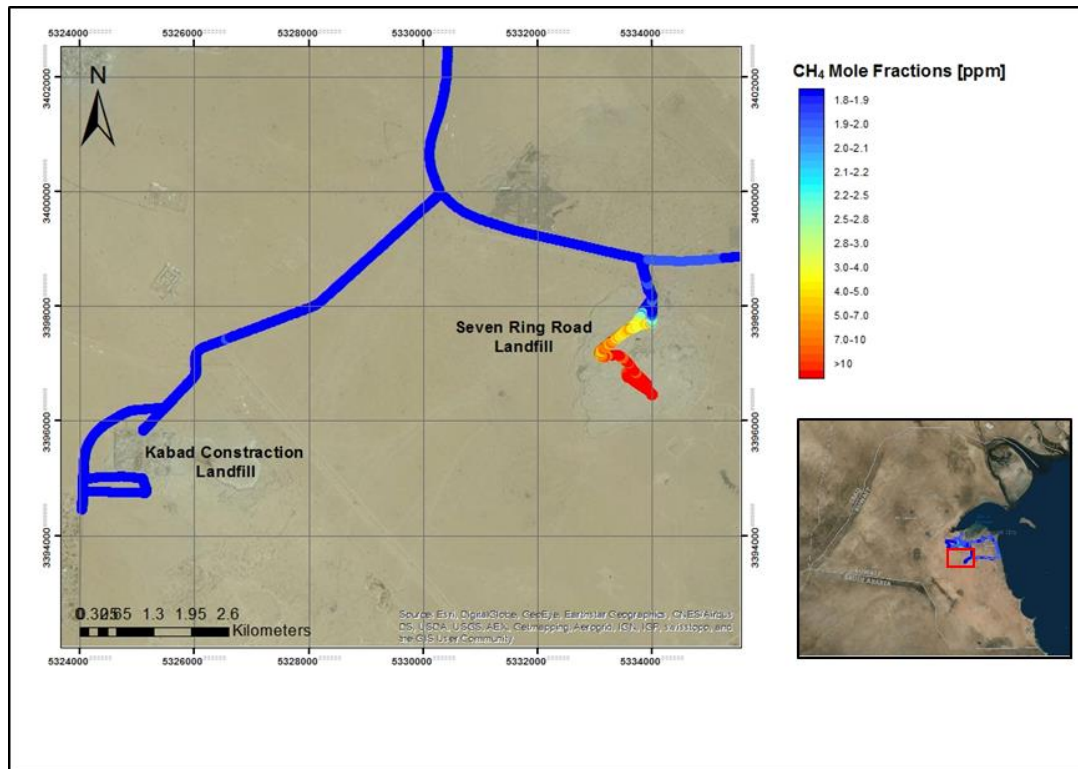


Figure 5.19 ArcGIS map showing methane mole fractions (ppm) in the Kabad construction landfill site that is located in the southwest with nearby South Seven ring road landfill site for comparison.

5.3.5 The Al-Sulaibiya landfill

The Al-Sulaibiya landfill is a closed site, covering an area of approximately 2.78 km². It is located near Al-Sulaibiya industrial area to the south west of Kuwait City (Figure 5.20). The site was used for the dumping of domestic waste and demolition materials from 1980 to 2000. This landfill site received more than 500 tons of waste per day for 20 years.

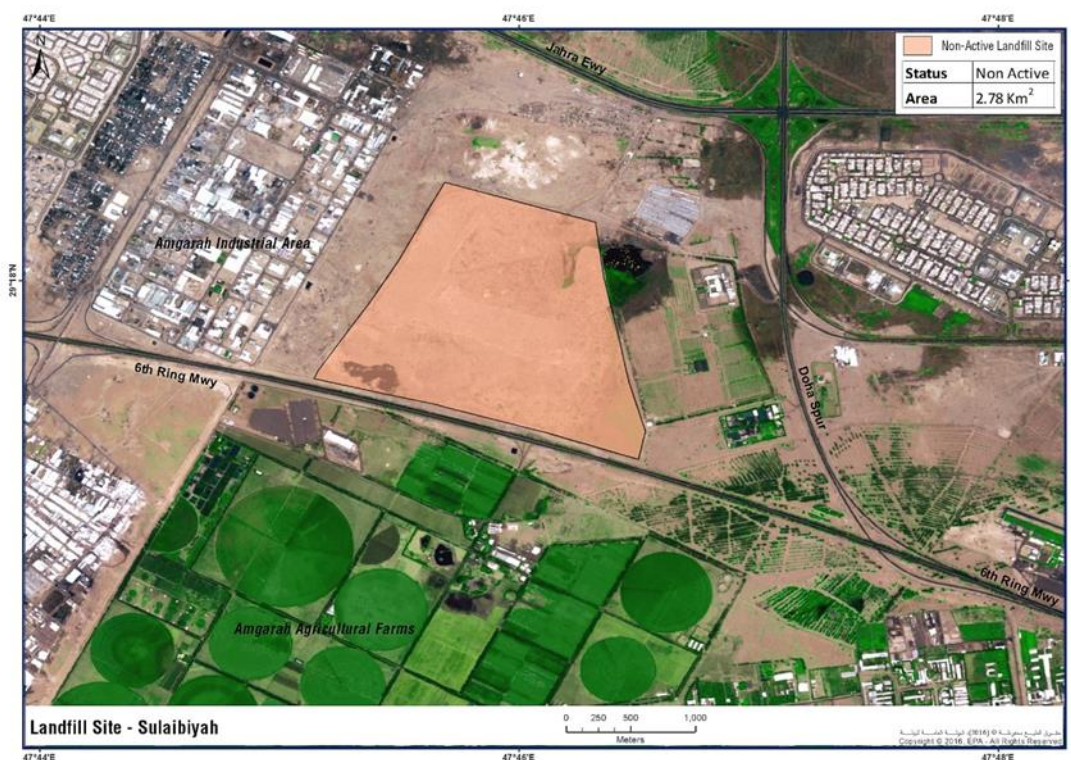


Figure 5.20 Al-Sulaibiya Landfill site location in relation to the urban area. Source: eMISK

On the 3rd of May 2015, the Al-Sulaibiya closed landfill site was surveyed as the wind was coming from the NW direction. The ArcGIS map in Figure 5.21 shows the methane plume that was encountered on the main road. A maximum mole fraction of 3.6 ppm was measured during this survey. Three air samples were collected whilst driving on this main public road on the south of the landfill site with methane mole fractions ranging from 1.9 to 2.99 ppm. The intercept of the Keeling plots based on the analysis of those samples is the most ^{13}C enriched signature found for a landfill site during the campaign, $-51.9 \pm 0.2 \text{ ‰}$ (Figure 5.22). This is likely to result from biogas oxidation in the topsoil cover which causes enrichment in $^{13}\text{C}\text{-CH}_4$.

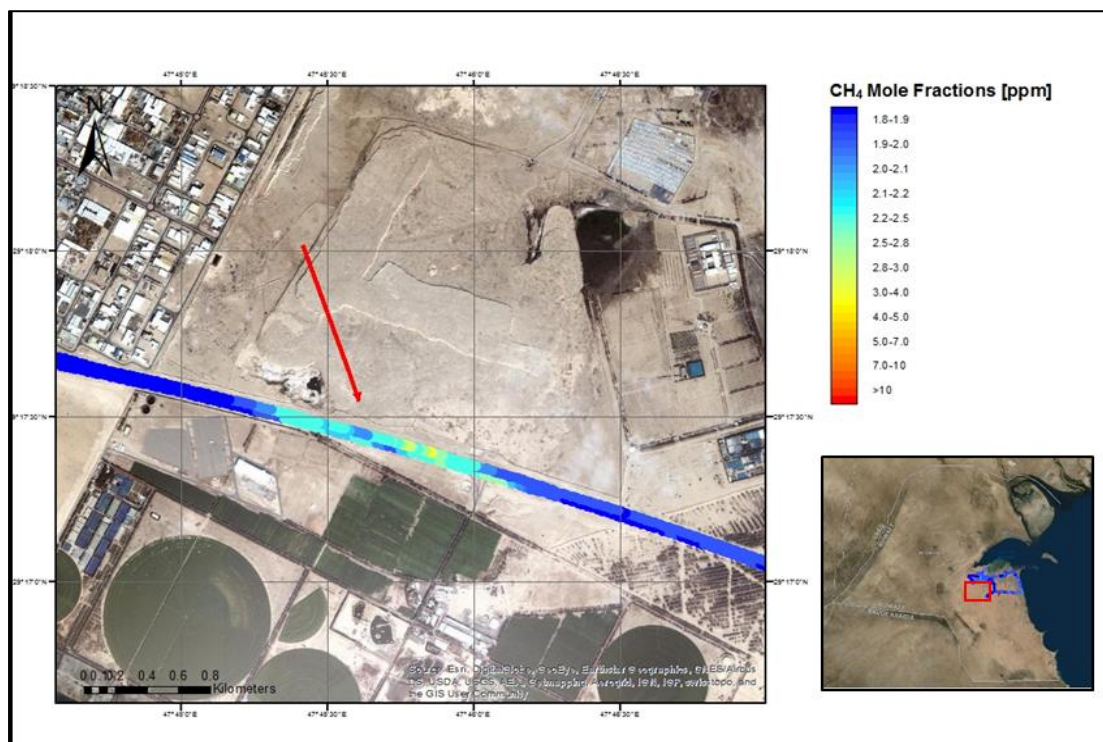


Figure 5.21 ArcGIS map of methane mole fractions (ppm) in the Al-Sulaibiyah landfill site. The red arrow represents wind direction

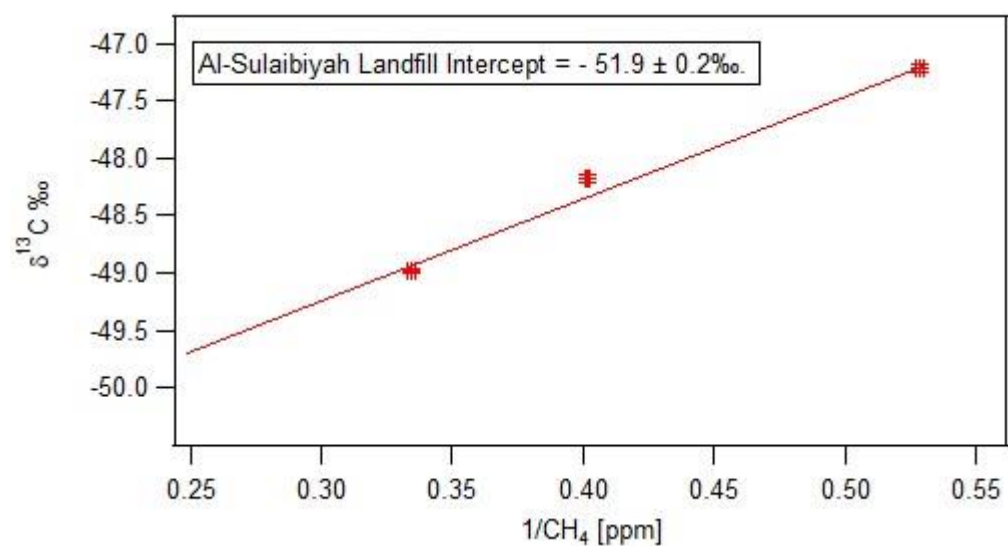


Figure 5.22 Keeling plot based on the samples collected on Al-Sulaibiya landfill site

5.3.6 Al-Qurain landfill

Al-Qurain landfill is an unlined closed landfill located in the Al-Adan residential area, about 15 km to the south east of Kuwait City. The total area of the site is approximately 1 km² (Figure 5.23). The total volume of non-homogenous waste, which was dumped in the site, is about 5 million m³, and the overall depth of the waste layer in the landfill ranged from 5 to 25 m during a 10-year period of operation from 1976 to 1985. This landfill area has suffered from strange and intense odours and the occurrence of flares due to the ignition of methane gas emissions (Al-Yaqout et al, 2002; Al-Yaqout and Hamoda, 2007; Al-Ahmad, 2012).

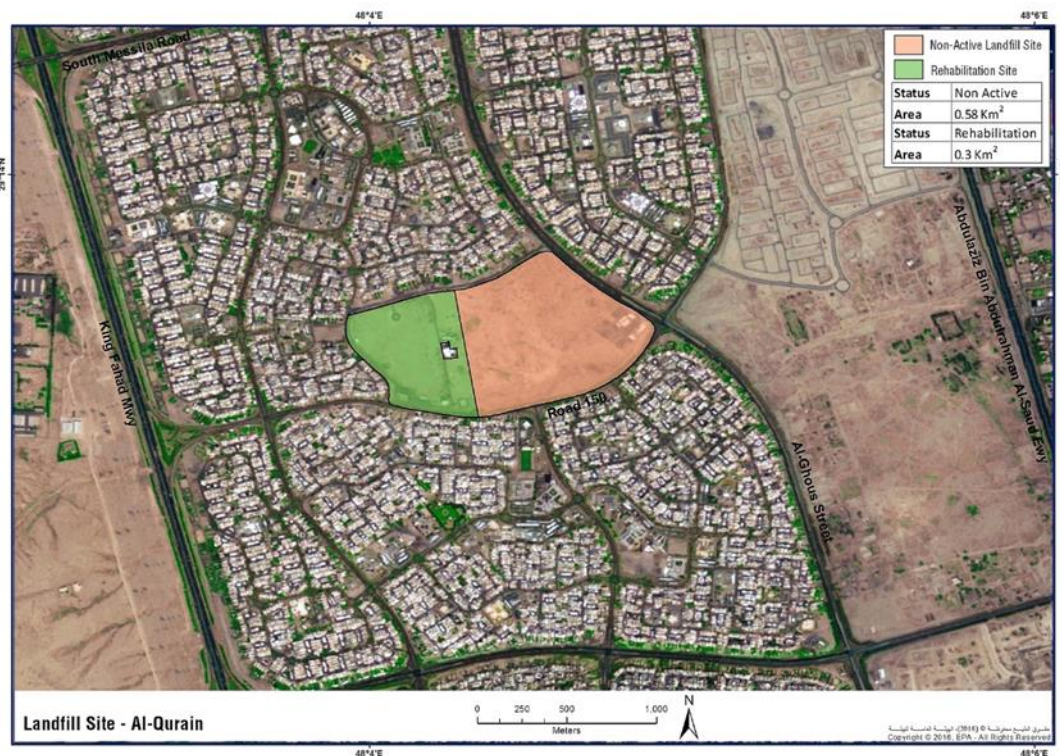


Figure 5.23 Al-Qurain Closed Landfill site related to the urban area.
Source: eMISK

In May 1999, the Environment Public Authority (EPA) initiated a program to reduce the health and environmental impacts of the landfill on the inhabitants of the surrounding residential area. The government solved this problem by; (1) partial removal of the waste, (2) collection of the Landfill Gas (LFG) produced and the pre-treatment of leachate water and (3) the landfill site was capped with 1 metre of soil. 300 vertical gas wells were drilled to depth of 5-20 meters within and outside the site. A gas venting system has been operating since 2001. The gas collection system has been recently established to collect landfill gas and convert it to electrical energy. This site was redeveloped to be used as a public park that would contain some buildings and recreational activities.

Al-Qurain landfill site was surveyed by the Picarro Mobile System on the 4th of May 2015, as the wind was coming from the NW. While driving on the main public road around the landfill site, the methane plume was detected on the NW of the site as shown on the ArcGIS base map Figure 5. 24.

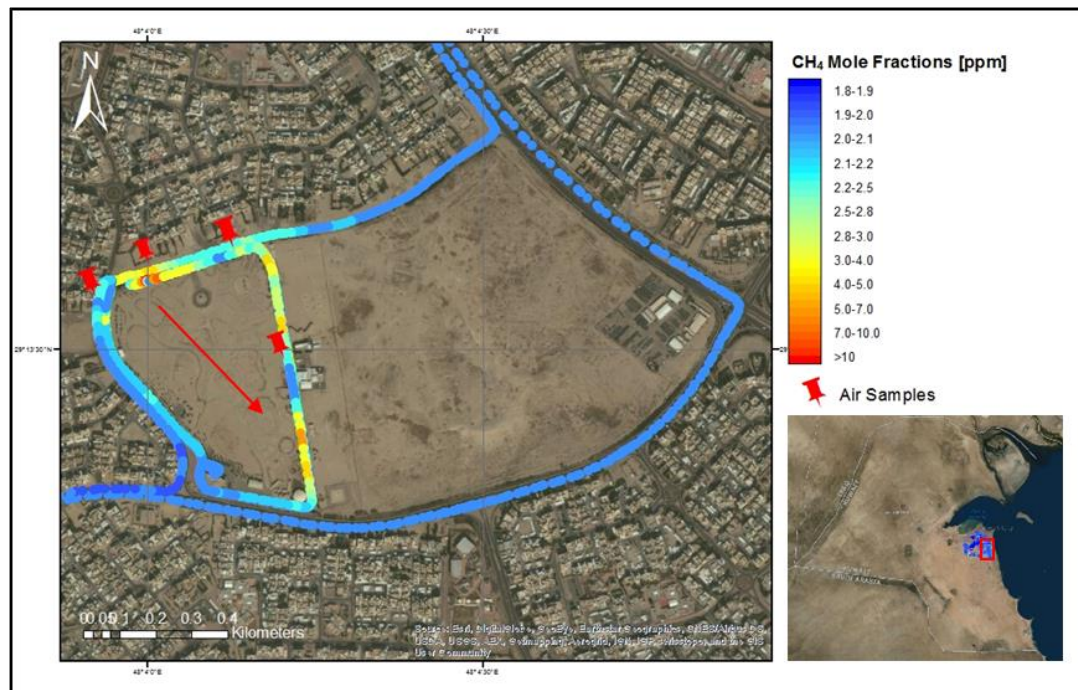


Figure 5.24 ArcGIS map of methane mole fractions [ppm] in the Al-Qurain landfill site. The red markers are the location of the air samples collected. The red arrow represents the wind direction.

Four air samples were collected while transecting the main plume on the NW side of the landfill with maximum methane mole fraction of 11.45 ppm. The calculated source signature based on the Keeling plot analysis of those air samples, was -54.3 ± 0.2 ‰, which is one of the heaviest values found in Kuwait landfills sites (Figure 5.25).

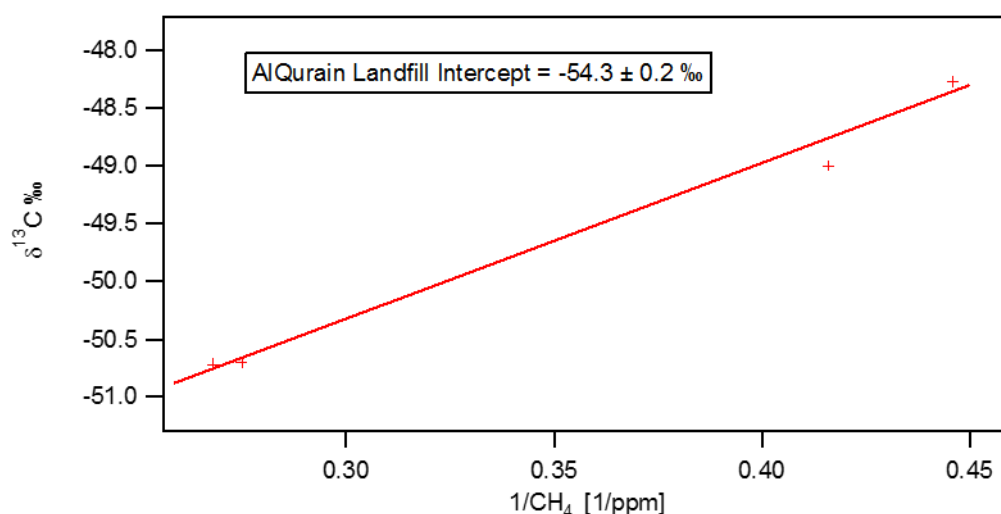


Figure 5.25 Keeling plot based on the samples collected on Al-Qurain landfill

On the 18th of February 2016, the Al-Qurain landfill site was investigated to determine the isotopic signature of gas in the anoxic zone by collecting gas samples from boreholes. There are 300 boreholes (Figure 5.26) for the gas-collecting system as previously mentioned. The following boreholes, 123, 124, and 125, were chosen to represent the methane concentration in Al-Qurain landfill. The borehole valve was opened and connected to a syringe for gas sampling (Figure 5.27). Gas samples were stored in a Tedlar bag and diluted with Nitrogen.

The concentrations of methane were 61.47% ,83.49% and 84.9% in wells 123,124 and 125 respectively. The isotopic signature of the gas ranged from -56.9‰ to -54.0 ‰. Table 5.3 shows methane concentrations and isotopic signatures of each well.



Figure 5.26 Al-Qurain landfill and the 300 boreholes of the gas system

Well number	Methane concentrations [%]	$\delta^{13}\text{C-CH}_4$ [‰]
123	61.5	-56.86 ± 0.06
124	83.5	-56.44 ± 0.06
125	84.9	-53.98 ± 0.07

Table 5.3 Boreholes of the Al-Qurain landfill with the concentrations of the methane (%) and the $\delta^{13}\text{C}$ signatures.



Figure 5.27 Collection of gas samples from boreholes in Al-Qurain Landfill site

5.3.7 Jleeb Al-Shuyoukh landfill

Jleeb Al-Shuyoukh is the largest landfill site in Kuwait with an area exceeding 6 km². It is located in the south of Kuwait City, very close to the International Airport of Kuwait and next to the Abdullah Al-Mubarak residential area (Figure 5.28). This landfill site received 2500 tons of waste per day for more than 20 years. The waste consists of a mixture of house refuse and viscous industrial waste. Approximately 20 million cubic metres of municipal solid waste and 3 million cubic metres of demolition waste were dumped in this site during its operational period between 1970 and 1993. In 2002, one metre of soil layer was installed because of a major burning incident. Fifty boreholes with a depth of up to 29 metres were drilled in 2006 and in March 2008, and measurements of landfill gas composition started.

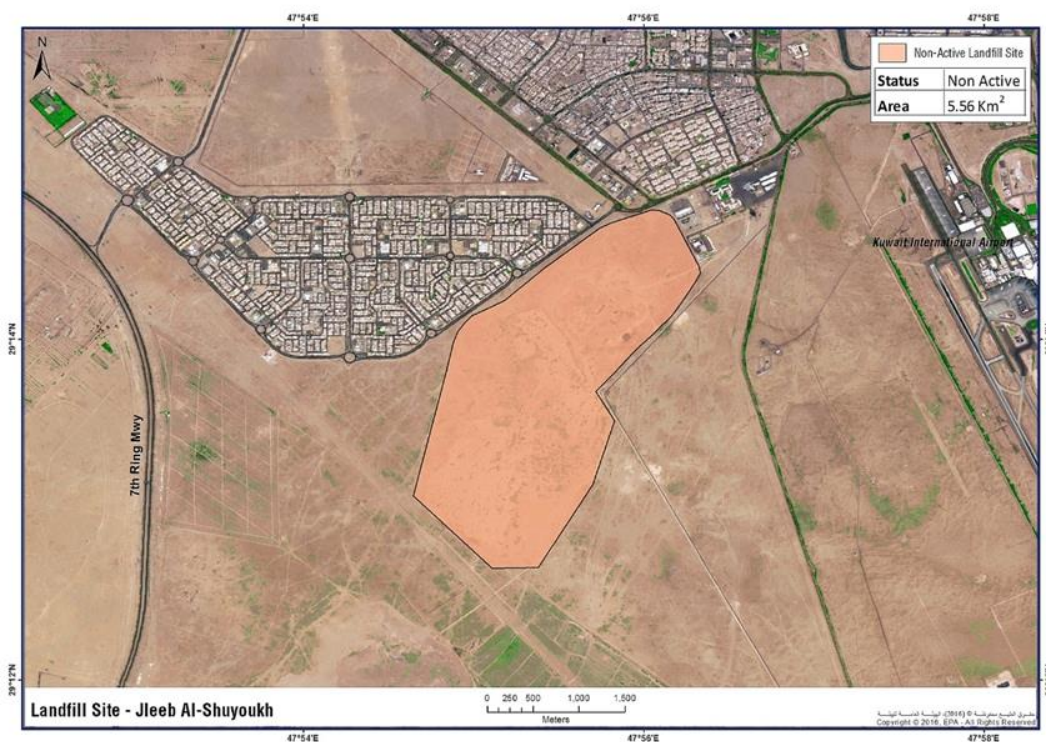


Figure 5.28 Jleeb Al-Shuyoukh landfill site related to the urban area.
Source: eMISK

During the survey with the Picarro Mobile System on the 4th of May 2015, a methane plume was detected, with a recorded maximum mole fraction of 5.2 ppm (Figure 5.29). Figure 5.30 shows that the isotopic signature based on the samples was $-56.4 \pm 1.9\text{‰}$.

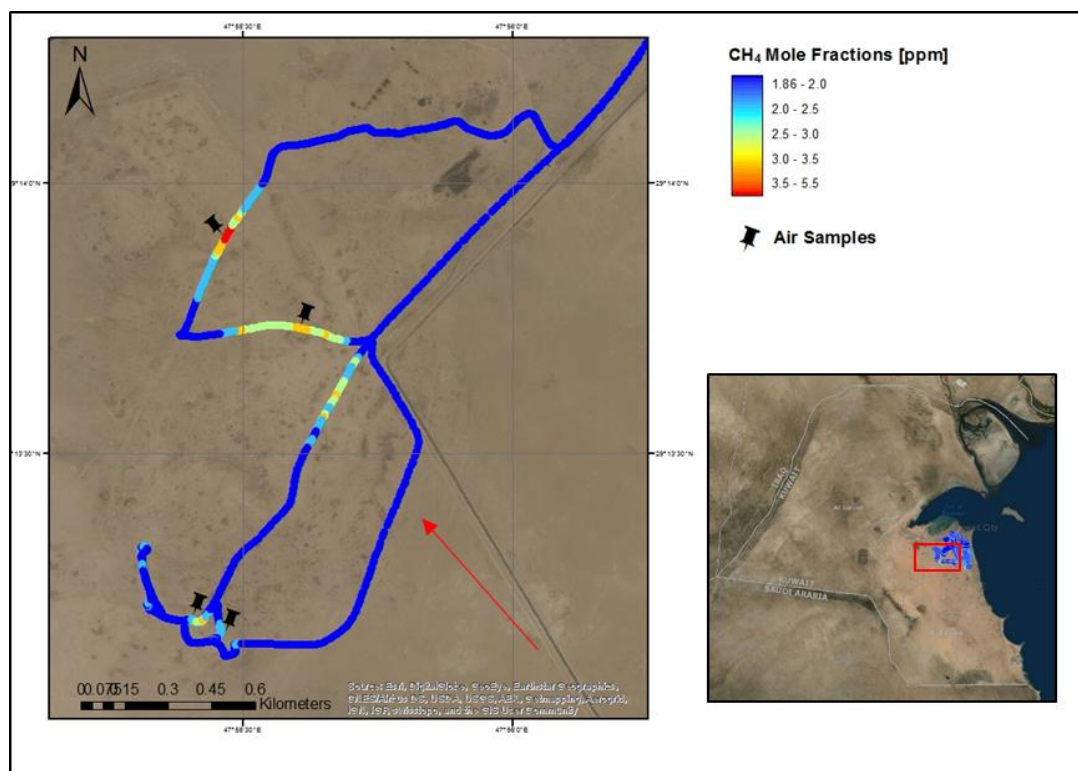


Figure 5.29 ArcGIS plot of methane mole fractions (ppm) in the Jleeb Al-Shuyoukh Landfill site. The black makers are the locations of the air samples collected. The red arrow represented the wind direction

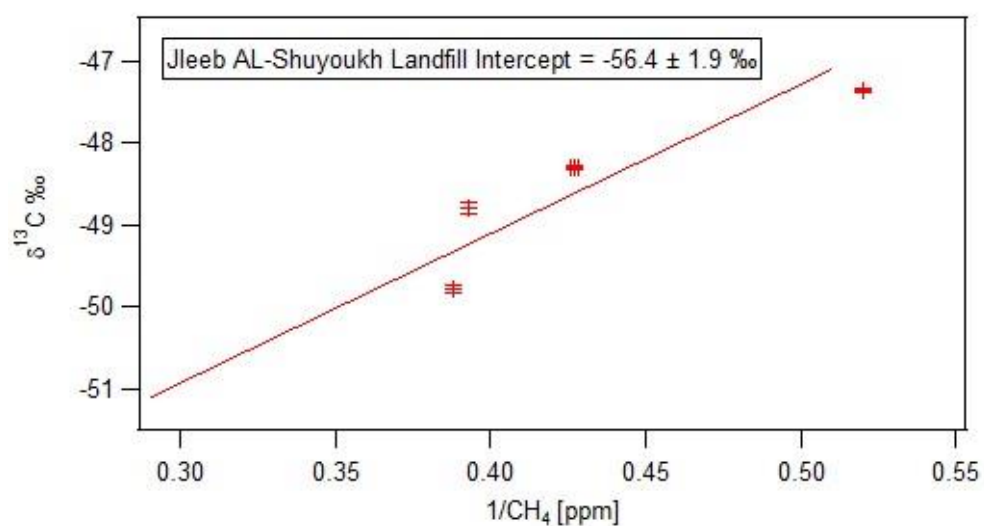


Figure 5.30 Keeling Plot based on the samples collected on Jleeb Al-Shuyoukh Landfill in the Kuwait campaign on 4th May 2015

Boreholes in Al-Qurain landfill site were also studied on the 18th of February 2016 and three air samples were collected from different boreholes (BH16, BH17, BH41) for measuring the concentration and isotopic signature of methane as shown in Table 5.4. One of these samples leaked, and the other two were analysed. Boreholes BH16 and BH17 have concentrations of CH₄ 70.6% and 14.28%, respectively (Figure 5.31).

WELL NO.	Longitude	Latitude	CH ₄	
			Concentration [%]	$\delta^{13}\text{C-CH}_4$
BH16	492274.860	3233552.850	70.6	-58.65 \pm 0.05
BH17	492385.020	3233676.540	14.3	-58.00 \pm 0.07
BH41	492190.520	3233911.860	Leaked	Leaked

Table 5.4 Location of the Jleeb Al-Shuyoukh boreholes and the concentrations of methane (%) with the $\delta^{13}\text{C}$ signature



Figure 5.31 One of the boreholes in the Jleeb Al-Shuyoukh landfill site

5.4 Discussion

This study has investigated the methane mole fraction and $\delta^{13}\text{C}\text{-CH}_4$ from seven landfill sites in the State of Kuwait (Figure 5.1 and Table 5.2). These include four active uncovered sites, namely: Al-Jahra landfill, the 7th Ring Road landfill, Mina Abdullah landfill, and Kabad landfill, and three closed covered landfills: Al-Sulabiya, Al-Qurain and Jleeb Al-Shuyoukh. Methane emissions from landfill sites have also been studied by many authors in Kuwait (Al-Yaqout & Hamoda 2002, 2007, Al-Yaqout *et al.* 2002, 2005; AlAhmad *et al.* 2012; Al-Saffae & Al-Sarawi 2018) and worldwide (Czepiel *et al.* 1993; Liptay *et al.* 1998; Chanton *et al.* 1999; Börjesson *et al.* 2001; Wang-Yao *et al.* 2006; Widory *et al.* 2012). However, previous studies in Kuwait (AlAhmad *et al.* 2012; Al-Saffae & Al-Sarawi 2018) have mainly focused on the characterisation, concentration and distribution of gases from Jleeb Al-Shuyoukh and Al-Qurain landfills using a standard landfill gas analyser such as the GFM handheld analyser (Al-Saffae & Al-Sarawi 2018).

This research uses for the first time in Kuwait, the Picarro analyser and its mobile module which allows high-precision measurements of methane mole fractions down to ppb in plumes emitted from the sites and isotopic analysis to determine the methane isotopic signatures in the emissions.

Rates of landfill emissions depend on several factors such as climatic and environmental conditions, initial (original and primary) waste disposal, type of material landfilled and operational factors (Al-Ahmad *et al.* 2012; Zazzeri 2015). The isotopic composition of CH_4 emitted from landfill sites is controlled by many factors such as the waste materials and age and amount of CH_4 oxidation. The main influence on the $\delta^{13}\text{C}$ isotopic signature of methane emitted from landfill sites is methane oxidation that occurs by methanotrophy in top-soil that covers the sites. The process of methane oxidation within soil is controlled by temperature and moisture content and methanotrophic communities present (Börjesson *et al.* 2001). Börjesson *et al.* (2001) have investigated the effects of different temperatures on the oxidation process in the cover soil of old and newly covered landfills in Sweden with the use of $\delta^{13}\text{C}$ analysis. They found

that, in summer, the emitted CH₄ was ¹³C enriched, relative to the anaerobic-zone methane, and the estimation of CH₄ oxidation amounts between new and old landfills was 41-50% and 60-94%, respectively. No difference in δ¹³C was observed between emitted and anaerobic-zone methane in winter, which is indicative of no soil oxidation.

Seasonal variation of methane oxidation in the landfill cover soil is one of the factors that was studied by Chanton and Liptay (2000). They used the stable isotope technique. They also found that the emissions of methane were high in winter and that the δ¹³C of those emissions from landfill soil surface were about -54‰. In summer, δ¹³C of emitted methane was around -40‰ and the emission was lower. This oxidation percentage varied according to the soil type and temperatures. Oxidation percentage was calculated for 2 Kuwait landfills; Al Qurain and Jleeb Al-Shuyoukh as recorded in Table 5.5, and based on the following equation (Liptay *et al.* 1998; Chanton *et al.* 1999).

$$f_o(\%) = [(\delta E - \delta A) / (a_{ox} - a_{trans}) \times 1000] \times 1000$$

The δ¹³C value of emitted CH₄ from landfill δE is related to the δ¹³C value of methane in the anoxic zone δA as shown in the equation. *f_o* is the percentage of CH₄ oxidised in transit through the cover soil and *a_{ox}* and *a_{trans}* are the isotopic fractionation factor associated with microbial methane oxidation and methane transport respectively.

Liptay *et al.* (1998) and Chanton *et al.* (1999) have assumed that *a_{trans}* = 1 and that δ¹³C value of CH₄ within the anoxic zone is what enters the oxidation zone. The (*a_{ox}*) represents the preference of bacteria to consume CH₄ containing the lighter isotope, leaving the remaining pool enriched in ¹³C (Chanton *et al.* 1999). Liptay *et al.* (1998) studied a variety of soil samples with different sand and clay content and found that this did not greatly affect the fractionation factor for New England landfill soils that averaged 1.022±0.008. This value is similar to previous studies in German landfills and for swamp methanotrophs (Liptay *et al.* 1998). A value of 1.022 ± 0.004 was found for forest soil methane oxidation with a slight temperature dependency (Tyler *et al.* 1994). King *et al.* (1989)

found values of 1.027 and 1.016 for tundra soil. The average of the previous studies was used to calculate the a_{ox} for Kuwait landfills; unfortunately there are no studies of Kuwait soil to determine the fractionation factor for bacterial oxidation

Bergamaschi *et al.* (1998) found around 80% (70-97%) of methane was oxidised during transport through the cover soil. The high values of the isotopic signatures of methane emissions from covered areas are distinctly $\delta^{13}C$ enriched ($-45.9 \pm 8.0\text{‰}$), compared to the isotopic signatures of methane emissions from uncovered areas ($-55.1 \pm 5.2\text{‰}$). They have shown the importance of methane oxidation, which plays only a minor role in the uncovered landfills area and high oxidation capacity in covered areas.

Townsend-Small *et al.* (2016) collected 18 air samples from landfills upwind and downwind from Weld and Larimer counties. Their isotopic analysis shows a source signature of $-58.1 \pm 1.4\text{‰}$ in USA. Zazzeri *et al.* (2015) studied methane emissions from SE England landfills and found that there was no great variability in $\delta^{13}C$ values (-58‰). Zazzeri *et al.* (2015) also found that emissions from old landfills that predate gas extraction are more enriched in $\delta^{13}C$ (toward -50‰).

The results of this study share similarities with the above studies (Bergamaschi *et al.* 1998; Börjesson *et al.* 2001). This research shows that ^{13}C enrichments are associated with covered (closed) landfills such as Al-Sulaibiya -51.9‰ , Al-Quaran -54.3‰ and Al-Jeleep Al-Shuyoukh -56.4‰ . However, uncovered landfills sites show more ^{13}C depletion such as Al-Jahra -59.4‰ , South 7th Ring Road -58.5‰ and Mina Abdullah landfill -59.1‰ . Table 5.5 summarises all the methane mole fraction and $\delta^{13}C\text{-CH}_4$ for all landfill sites that were investigated in this study. The highest mole fraction was encountered from the South 7th Ring Road site 38.7 ppm where the lowest mole fraction from Jleeb Al-Shuyoukh landfill site 5.20 ppm. There were no emissions encountered from the Kabad landfill 1.88 ppm.

Methane concentrations from the Jleeb Al-Shuyoukh and Al-Qurain landfill sites were also studied by several authors based on samples collected from several boreholes (Al-Saffae and Al-Sarawi, 2018; AlAhmad *et al.*, 2012; AlSarawi, 2009). Al-Sarawi (2009) found that the main components of Al Qurain Landfill gas (LFG) were methane with a maximum of 63% and varying concentrations of carbon dioxide, from 1% to 43%.

AlAhmad *et al.* (2012) determined the concentration of CH₄ and CO₂ in both Al-Qurain and Jleeb Al-Shuyoukh landfill sites. In their study, borehole BH16 was among the boreholes they investigated in the Jleeb Al-Shuyoukh landfill. BH16 was classified as the one with the highest concentration of methane gas (from 50% to 60%). A recent study (Al-Saffae & Al-Sarawi 2018) has investigated the properties and distribution of landfill gases at Al-Qurain landfill based on samples collected from 25 boreholes. They found that the dominant gases in the landfill were CH₄, CO₂, H₂O and O₂. Methane (CH₄) concentration was the highest with an average ranging from 40% to 60%.

This study targeted different boreholes from those studied by AlAhmed *et al.* (2012) and Al-Saffar and Al-Sarawi (2018) except from BH16 in Jleeb Al-Shuyoukh landfill. The results of this research are in a good agreement with the above studies. In addition, this study shows that methane mole fraction from borehole BH16 was the highest of 70.6 % in Jleeb Al-Shuyoukh landfill and even more than the methane concentration of 50-60 % measured by AlAhmed *et al.* (2012).

Lowry *et al.* (2001) have also studied methane emissions from boreholes in two different covered landfills in London. Their analysis gave $\delta^{13}\text{C}$ values of -52‰ for the Colnbrook landfill and -51.7 ‰ for the London Road landfill (Ascot). Both of these sites pre-dated gas extraction systems. The results of this study are more ¹³C-depleted (-55.76 ‰ and -58.32‰) than the results of Lowry *et al.* (2001), but are very similar to more modern landfill sites in the UK investigated by Zazzeri *et al.* (2015)

5.5 Summary:

This study uses for the first time the Picarro Mobile system to investigate the methane mole fraction and isotopic signature from seven landfill sites in the state of Kuwait (Figure 5.4 and Tables 5.2). Samples were collected during the Kuwait campaign from 2nd to 7th of May 2015 as summarised in Table 5.5. In this study, the highest value of the methane mole fraction was 38.7 ppm measured in South Seven Ring Road active landfill. Isotopic signatures were in the range from $-59.44 \pm 1.4\text{‰}$ to $-51.9 \pm 0.2\text{‰}$, with an average value of $-56.6 \pm 0.8\text{‰}$.

The average of the isotopic signatures of the three active uncovered landfills (Al-Sulaibiya, Al-Qurain and Jleeb Al-Shuyoukh) is $-59.1 \pm 0.9\text{‰}$, whereas for the three closed covered landfill sites (Al-Jahra, the 7th Ring Road and Mina Abdullah) it is $-54.2 \pm 0.7\text{‰}$. This is associated with methane oxidation within the soil cap of the covered closed landfill sites resulting in enriched $\delta^{13}\text{C}$ methane emitted to the atmosphere. Oxidation rates, calculated from the isotopic difference between borehole gas from depth in the landfill and the signature of methane in surface emissions to atmosphere (shown in Table 5.5) are very low ($<10\%$).

In Kuwait there is no gas extraction system in place in the active landfills and no cover soils, so there is very little oxidation. The old landfills have a thin cover and show small percentages of oxidation (7-9%), but due to warm to hot temperatures all year round the bacteria will remain active and so there is unlikely to be a significant difference between summer and winter isotopic signatures for these sites.

Landfill	Status	Survey date	Max CH ₄ (ppm)	$\delta^{13}\text{C}$ (‰)	$\delta^{13}\text{C}$ (‰) of Boreholes	Cover Soil Oxidation %
Al-Jahra	Active	2 nd May 2015	11.34	-59.4±1.4		
South Seven Ring Road	Active	3 rd May 2015	38.71	-58.5±0.5		
Mina Abdullah	Active	5 th May 2015	28.94	-59.1±1.0		
Al-Sulaibiyah	Closed 1987	3 rd May 2015	3.60	-51.9±0.2		
Al Qurain	Closed 1985	4 th May 2015	11.45	-54.3±0.2	-55.76± 0.06	6.6
Jleeb Al-Shuyoukh	Closed 1993	4 th May 2015	5.20	-56.4 ±1.9	-58.32 ±0.06	8.7
Kabad Construction	Active	3 rd May 2015	1.88	No emissions		

Table 5.5 Landfill sites that have been surveyed during the Kuwait Campaign on May 2015 with the maximum mole fraction of methane (ppm) and the calculated $\delta^{13}\text{C}$ signature.

C***HAPTER 6***

S***EWAGE TREATMENT***

6. Sewage Treatment

About 5% of global methane emissions are produced from sewage treatment (El-Fadel & Massoud 2001). Many studies on the anaerobic wastewater treatment show that a significant amount of methane can be produced in sewer systems, related to the hydraulic retention time and the area to volume ratio of wastewater and the sludge biodegraded under anaerobic conditions (Guisasola *et al.* 2008). Methane is formed by processes of intense biological activity in the absence of oxygen that occur in the influent lines, primary settling, sludge holding tanks and sludge transfer lines (Czepiel *et al.* 1993). Guisasola *et al.* (2008) show that the methane of the sewer system occurs in an aqueous phase until reaching a point of release to the atmosphere

6.1 Kuwait Wastewater Treatment plants

The wastewater treatment plants in Kuwait are using an Aerobic biological reactor system. This is related to the type of bacteria that are involved in the degradation of organic matter. There are many processes and technologies of Aerobic Biological Treatment, the most common and the oldest is the Conventional Activated Sludge Process (ASP) system that is used in Kuwait to treat municipal and industrial wastewater. There are 4 wastewater treatment plants in Kuwait, three of them operate by Tertiary Treatment Stage (Umm Al-Hayman, Riqqa, Kabd), one by Reverse Osmosis (RO) technology (As-Sulaybiyah) and one for the Industrial wastewater treatment plant called KM30 (Figure 6.1). Basically, these start with the removal of the suspended impurities from the raw wastewater followed by an active aerobic sludge biological treatment process, classified as secondary treatment, and end with tertiary treatment.

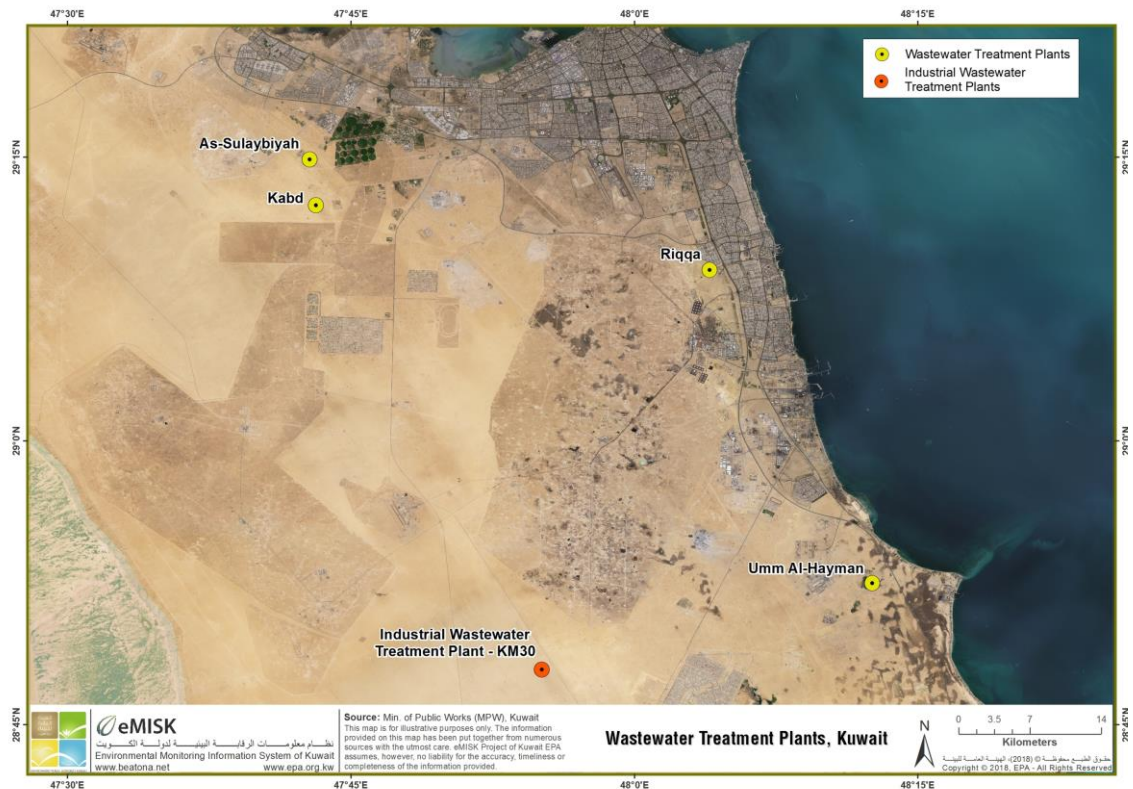


Figure 6.1 Map showing the four wastewater treatment plants in Kuwait.
Source: Emisk, 2018

6.1.1 Primary treatment

Primary treatment is carried out in the Headworks Building (Figure 6.2) where the wastewater is received and treated. The first stage in the primary treatment is screening where the floating and suspended material is first removed from the wastewater using automatic mechanical bar screens. Following on from the screening there is a grit and scum removal stage, using aerated grit chambers to collect the settled grit from the bottom of each chamber. Scum on the surface of the water as well as oil and grease are removed by a scraper in each grit chamber. Gas separation and collection from the headworks building use special exhaust fans and injection in to the aeration tanks and sludge digester.



Figure 6.2 The Headworks Building (Primary treatment) in Al-Reqqa Sewage Treatment Plant.

6.1.2 Secondary treatment

In the Secondary Treatment the polluting materials are removed, and the gases collected from the headwork building and the sludge thickeners. Secondary Treatment is carried out in two steps: the first step is in the aeration tanks where primary treated wastewater is mixed with massive quantities of bacteria and microorganisms, and the whole mix is aerated (Figure 6.3). Aeration activates the bacteria and microorganisms, which in turn start consuming the polluting materials. These bacteria and microorganisms are settled in the settling tanks as sludge. The primary treated water is mixed with the sludge returned from the settling tanks then it flows in to aeration tanks. The mix is aerated in the aeration tanks using air blowers that compress the air into the main headers, and then into an air distribution network located inside the aeration tanks. This compressed air consists of the atmospheric air mixed with the gases collected from the headworks building and the sludge thickeners. The mixed liquid flowing out of the aeration tanks enters secondary settling tanks and a sludge settles in the bottom of these tanks. Part of this settled sludge is returned to the aeration tanks and mixed with the primary treated wastewater. The other part is pumped to the

sludge processing stage. The clear water flowing out of the settling tanks is collected and discharged to the tertiary stage for further treatment.



Figure 6.3 Settling Tank (Secondary Treatment) in Al-Reqqqa Sewage Treatment Plant

6.1.3 Tertiary treatment

The aim of this final treatment stage is to disinfect the treated water and to remove the remaining solid particles from it. This eventually improves the quality of the treated water and makes it suitable for irrigation purposes. The secondary treated water flows from the settling tanks through an open channel injected with chlorine solution (pre-chlorination) to the tertiary treatment stage before reaching the balancing tanks. Water is transferred from the balancing tanks to the sand filtration by using screw pumps. After filtration, the chlorine is added for a second time (post-chlorination) to eliminate any remaining bacteria or microorganisms. This stage is the final process for treating the wastewater before its discharge to irrigation locations.

6.1.4 Sludge processing

Excess sludge produced from the secondary treatment stage is pumped to sludge thickeners that are covered with aluminum domes to prevent emission of odours to the atmosphere. The trapped air inside the cover domes is collected using exhaust fans and injected into the aeration tanks and sludge digesters. Then the thickened sludge is pumped into aerobic digesters. In these digesters, the sludge is mixed and aerated with air blowers. Then, these digested sludges are pumped to sludge drying beds and left to dry completely.

6.2 Riqqa Wastewater Treatment Plant

Riqqa Wastewater Treatment Plant is located on the south side of Kuwait City and serves the 14 adjoining urban areas. It began operation in 1982 with a capacity of 85000 m³ of domestic wastewater per day, using an activated sludge system for secondary treatment. In 1984 a complete tertiary treatment stage was constructed and operated in Riqqa Wastewater Plant with a capacity of 160000 m³/day as a part of a major project for utilization and reuse of tertiary treated water for irrigation purposes. A special upgrading was carried out in 1999 due to the increase in the wastewater quantities discharged to Riqqa plant to 180000 m³/day. Through this upgrading project primary treatment units were added, the number of secondary treatment units was increased, and the aerobic system was modified to collect and treat odorous gases and improve the overall performance of the plant. Also new facilities were added for treating and drying the sludge. The structure of the Riqqa wastewater treatment plant system is shown in Figure 6.4. This site was investigated three times during 2015 to 2017.

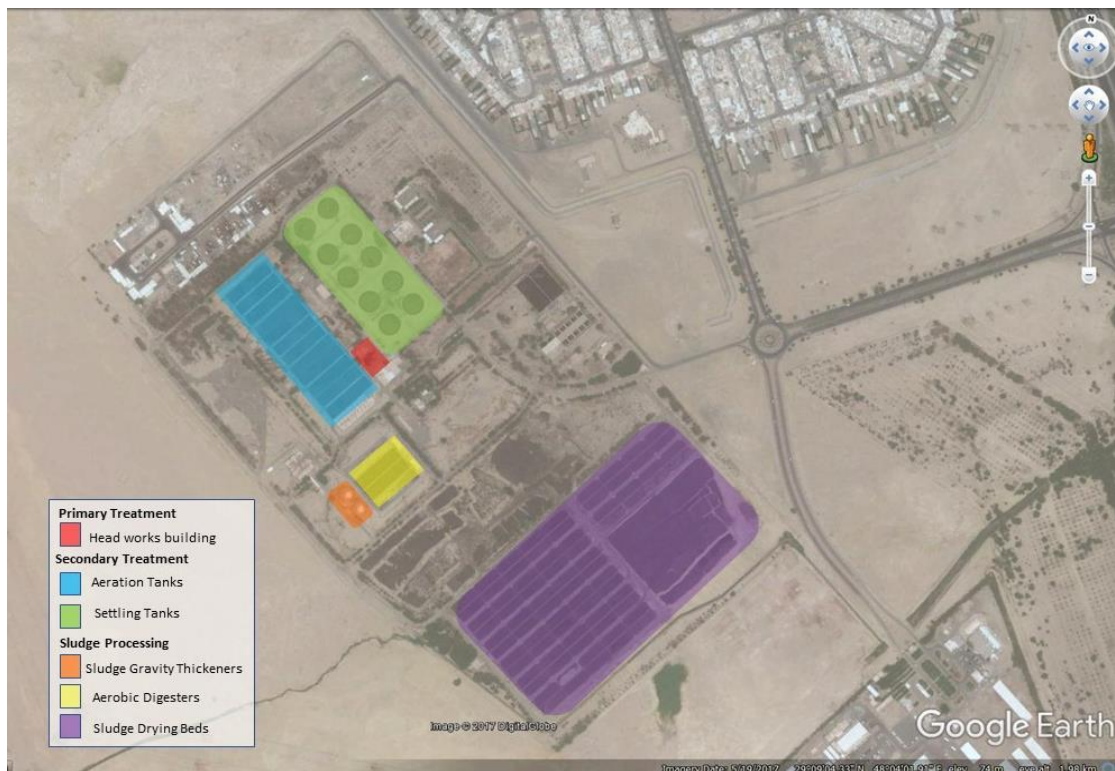
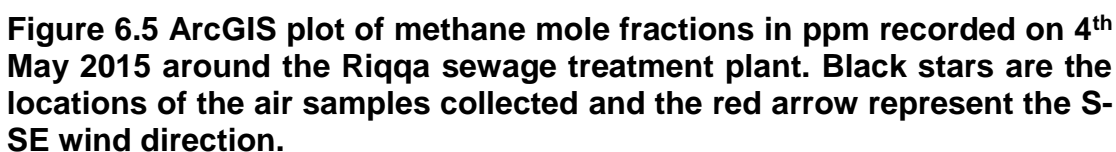


Figure 6.4 The structures of the Riqqa Sewage Treatment Plant. Red area: represents the primary treatment. Blue and green: secondary treatment, yellow and purple: sludge processing. More detail in the legend

6.2.1 4th May 2015

Riqqa wastewater treatment plant was surveyed by Picarro (G1301 CRDS) on 4th May 2015. The survey was carried out on the public road around the outside of the plant by trying to intersect the downwind methane plume. Methane emissions were intercepted while driving on the NE side of Riqqa sewage treatment plant with a maximum methane mole fraction of 2.7 ppm. Figure 6.5 shows methane mole fractions measurements for this site. Four air samples were collected along the road outside the plant and one sample inside the plant.



143

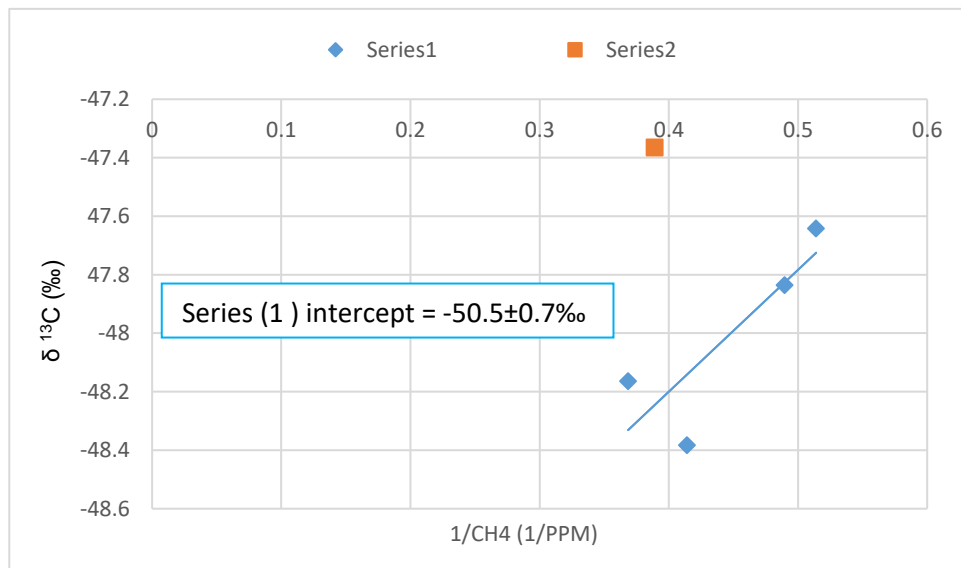


Figure 6.6 Keeling Plot based on the air samples collected on 4th May 2015 around Riqqa sewage treatment plant.



Figure 6.7 The trucks and vehicles parked next to Riqqa sewage treatment plant

6.2.2 7th January 2016

Riqqa sewage treatment plant was visited for the second time and six air samples were collected. The samples were randomly collected from different places inside the plant. Figure 6.8 shows the Keeling plot based on these six air samples of $-45.1 \pm 0.2\text{‰}$. This isotopic signature was more ^{13}C enriched and significantly different from the first visit to the same site.

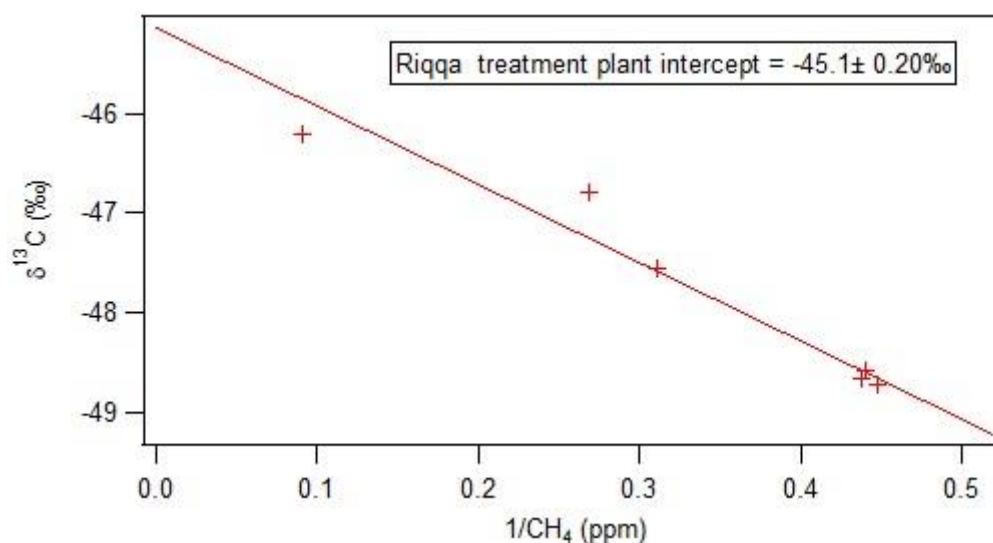


Figure 6.8 Keeling Plot based on the air samples collected on 7th January 2016 around Riqqa sewage treatment plant

6.2.3 7th March 2017

To further understand methane from the sewage treatment works in Kuwait, Riqqa was investigated for a third time. 16 air samples were collected from all processes taking place in the sewage works in order to identify the methane emitting processes. Figure 6.9 show the resulting Keeling plot that shows a wide range of $\delta^{13}\text{C}$ signatures with poor correlations.

They are interpolated to belong mostly to two different Keeling trends. This might be due to the different processes linked with the sewage treatment works. The Keeling plot for series one gives an intercept of $-50.7 \pm 0.6\text{‰}$. Series two are ^{13}C enriched relative to series one with an intercept of $-45.6 \pm 0.1\text{‰}$. Figure 6.10 shows the source signatures for the sewage work air samples. The aeration tanks show heavier $\delta^{13}\text{C}$ values that might be due to the oxidation process in this stage of waste treatment.

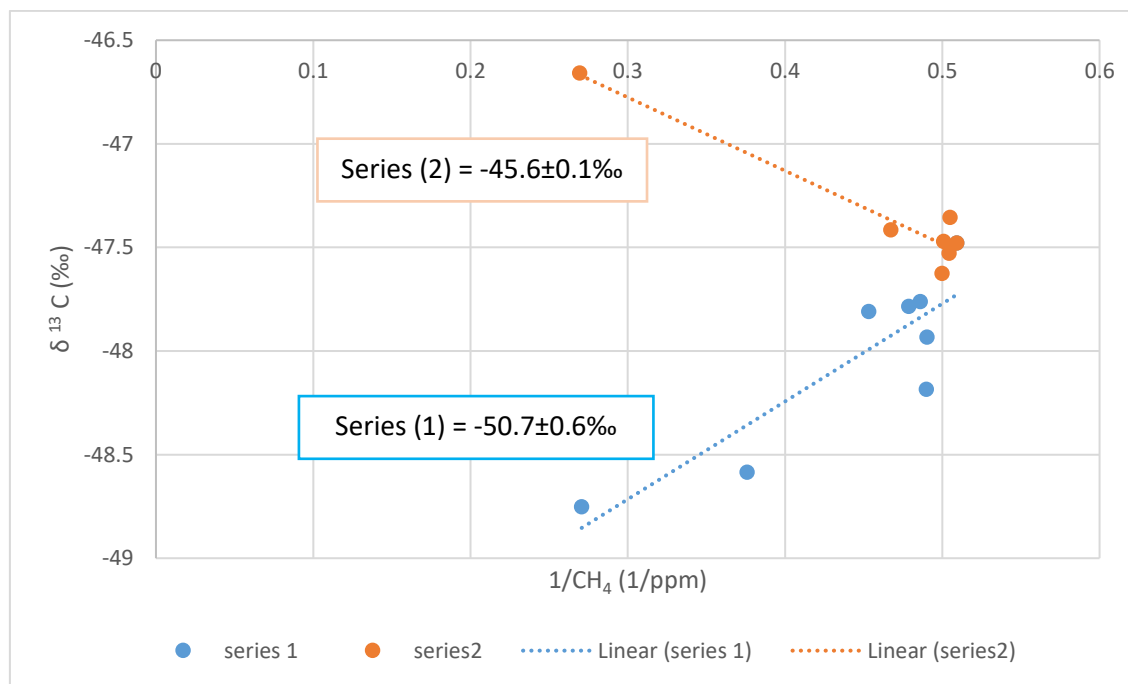


Figure 6.9 Keeling Plot based on the air samples collected on 7th March 2017 around Riqqa sewage treatment plant

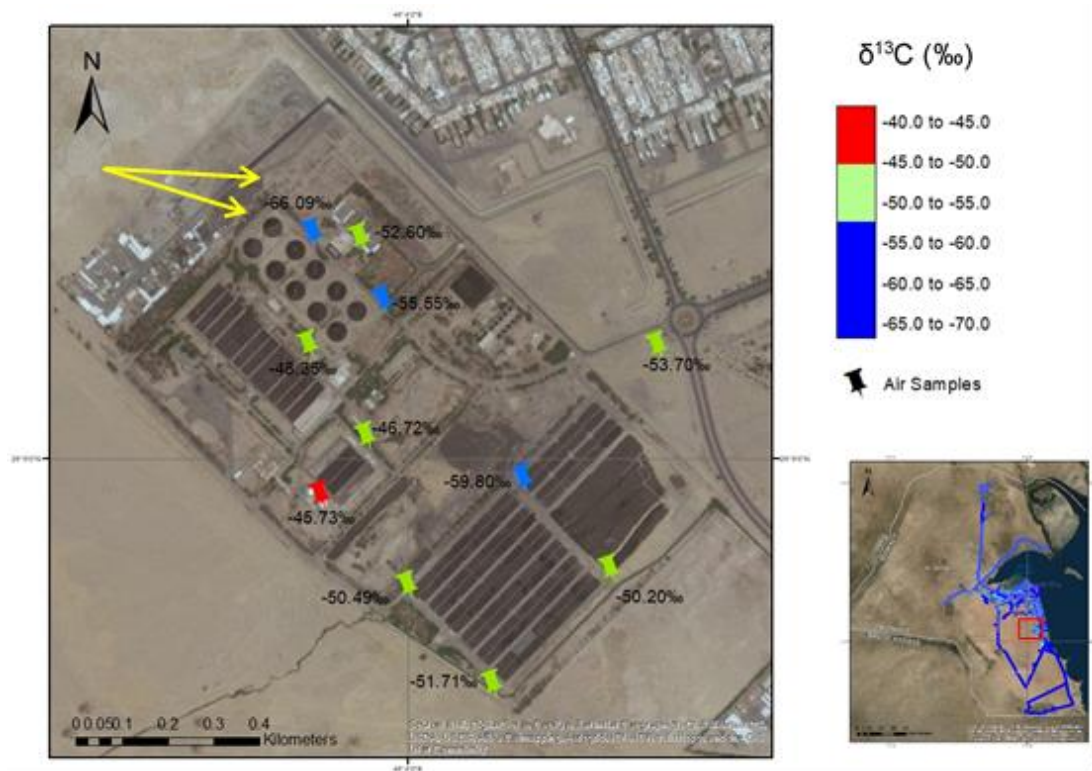


Figure 6.10 ArcGIS plot of calculated $\delta^{13}\text{C}$ source signatures (‰) for CH_4 elevations on 7th March 2017 around Riqqa sewage works. The yellow arrow represents the wind direction and the markers are the locations of the air samples collected

6.3 KM30 Industrial Wastewater Plant

This new treatment plant has the capacity to receive all kinds of industrial liquid wastes in the country. The plant currently receives 7500 cubic meters of liquid waste per day with the possibility of expanding the amount of waste received to reach 15 thousand cubic meters per day. There are three main basins to receive the industrial waste in the plant (liquid waste from the food industry, liquid waste with high content of oils and other liquid waste) as well as a site to receive industrial wastes with a higher content of trace metals. The plant contains a primary processing unit which follows the receiving stage in the three main basins where the sand, oil and chemical materials are removed from the water contained in the plant, ensuring that the water is converted to a level conforming to the sanitary effluents in preparation for biological treatment. Biological treatment,

which is the third stage of treatment, will allow about 20 thousand cubic meters of water per day to be treated to meet the criteria approved by the regulatory authorities (Ministry of Public Works and Environment Public Authority).

6.3.1 5th May 2015

The sewage works KM30 is located south of Kuwait City. The ArcGIS map in Figure 6.11 shows the methane emissions from this sewage works that were intercepted while driving in the plant by the Picarro mobile system on 6th of May 2015. Figure 6.12 shows the Keeling plot based on the four samples that were collected in this plant. These give a signature of $-46.2 \pm 0.1\text{‰}$.

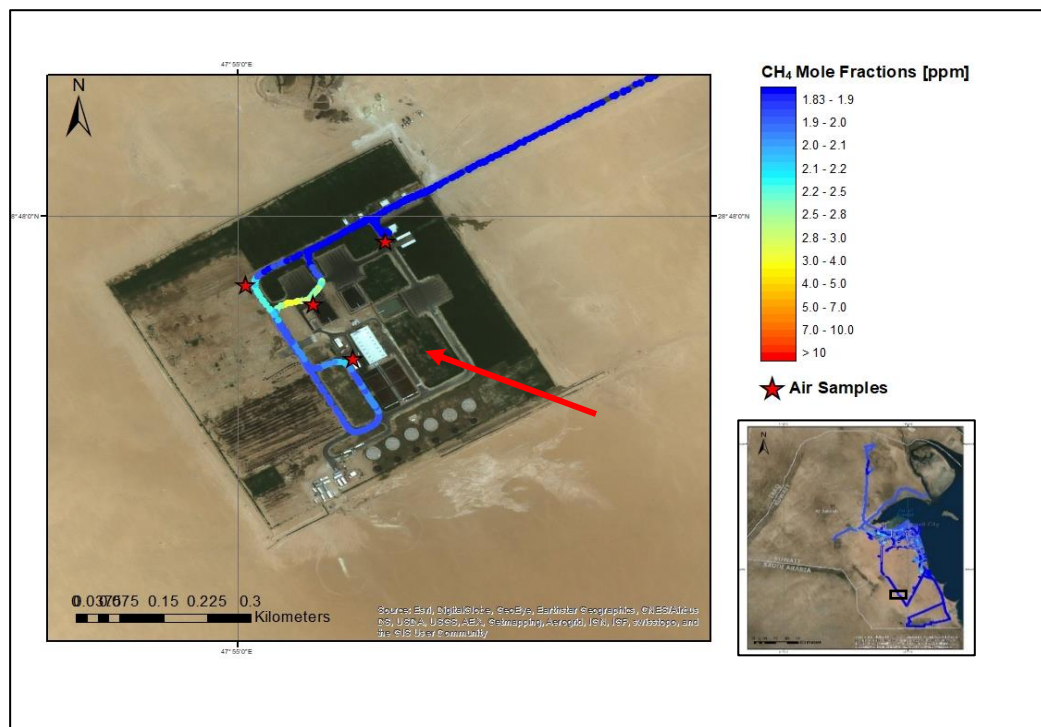


Figure 6.11 ArcGIS plot of methane mole fractions in ppm recorded on 5th May 2015 around KM30 sewage works. The red stars are the locations of the air samples collected and the red arrow represents wind direction.

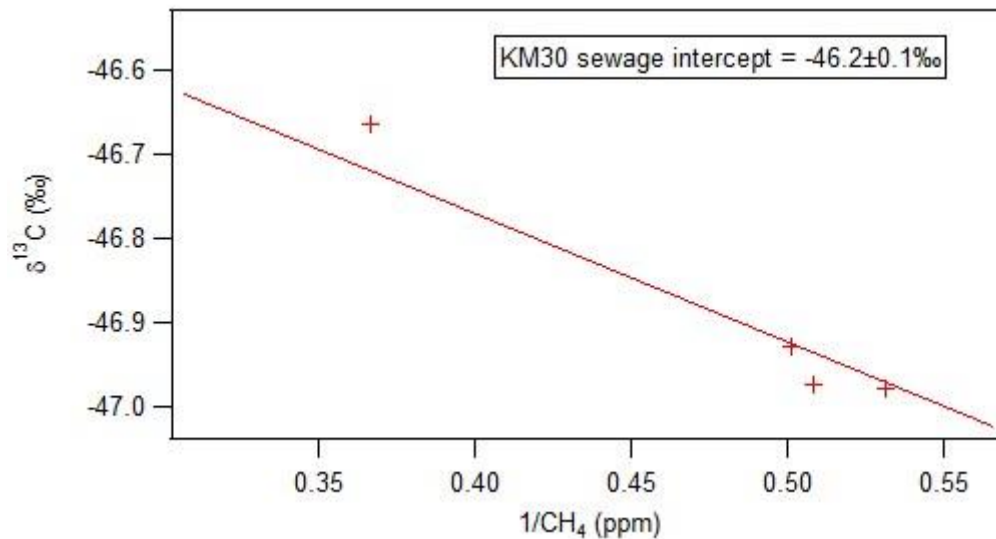


Figure 6.12 Keeling Plot based on the air samples collected on 5th May 2015 around KM30 sewage treatment plant

6.4 Umm Al-Hyman sewage Treatment Plant

This plant was started in May 2001 and designed for treatment of 2700 m³/day and delivering good quality reclaimed water for irrigation purposes. This municipal wastewater treatment plant is located 61 km south of Kuwait City and it serves the township Ali Subah Al-Salem and adjoining areas and from the nearby military camps and coastal chalets. Figure 6.13 summarises all the biological processes that take place at the Umm AL-Hyman plant, which is almost the same as at the Riqqa plant discussed previously.

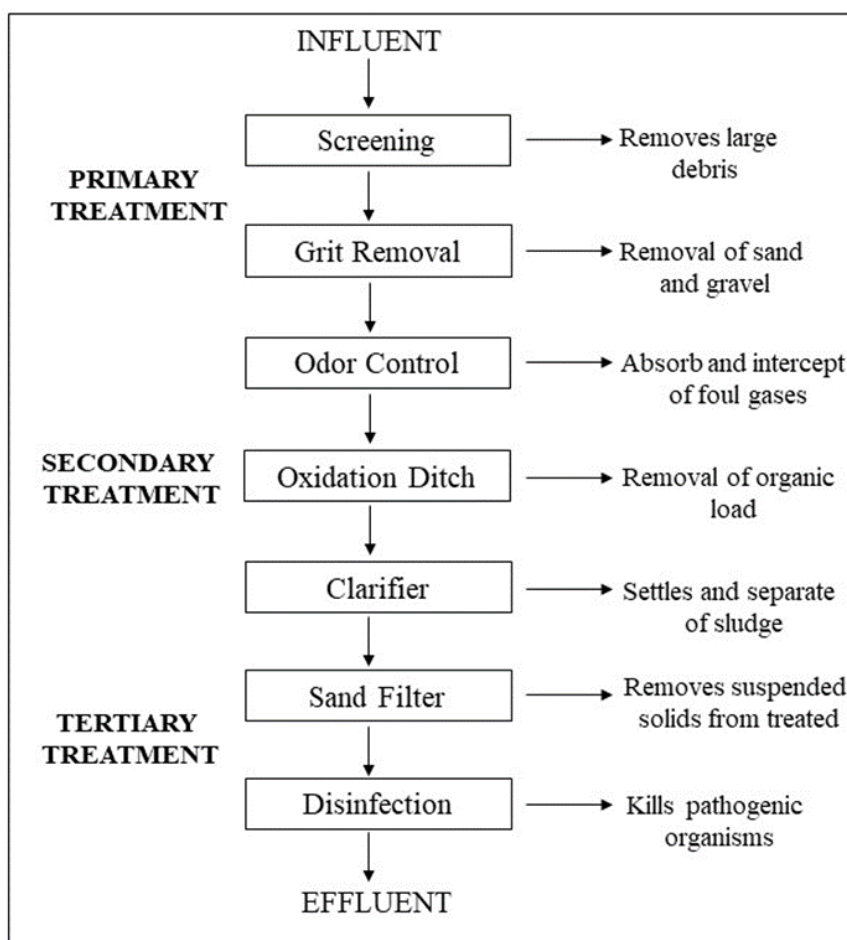


Figure 6.13 Treatment processes in the Umm Al-Hayman sewage treatment plant

6.4.1 17th March 2017

The Umm Al-Hayman sewage treatment plant was investigated in order to identify the isotopic signature of the sewage works in Kuwait. The wind direction was ENE with wind speeds of 14 to 17 k/h and the temperature around 21°C. 15 air samples were collected: 12 were collected inside the sewage treatment plant and 3 air samples were collected outside the treatment plant. Figure 6.14 shows the Keeling plot based on 12 air samples that were collected inside this plant given $\delta^{13}\text{C} -59.2 \pm 0.9\text{‰}$. Figure 6.15 show the Keeling plot based on the three samples that had been collected outside the treatment plant. Methane emitted from these 3 air samples show slight ^{13}C enrichment at $-46.8 \pm 0.04\text{‰}$, This might be due to the large domestic and industrial liquid waste pit with a large number of trucks delivering the waste as shown in Figure 6.16. Figure 6.17 show the samples location with the methane mole fraction and the source signatures in this plant.

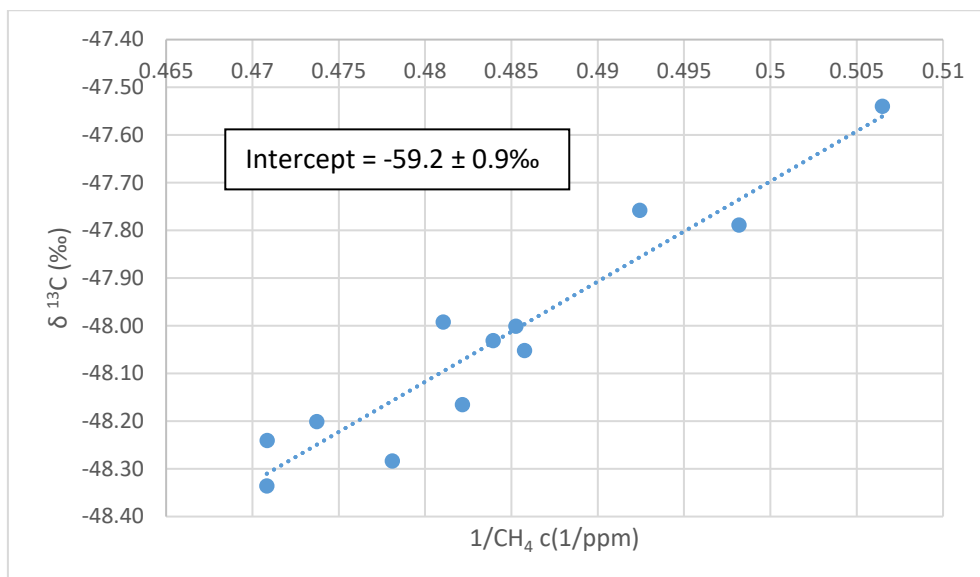


Figure 6.14 Keeling plot for the 12 air samples that were collected in Umm Al-Hayman wastewater treatment plant on 17th March 2017.

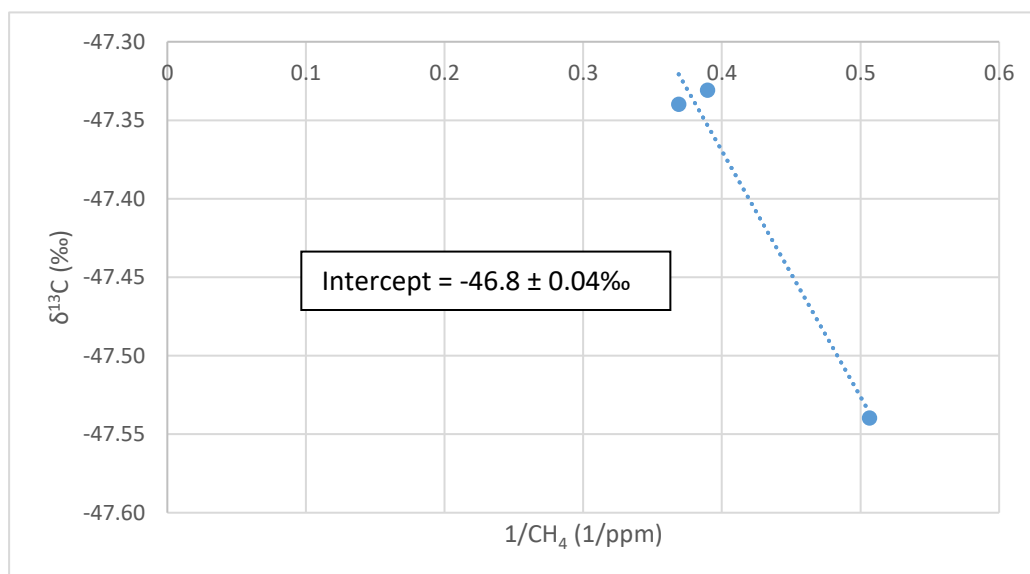
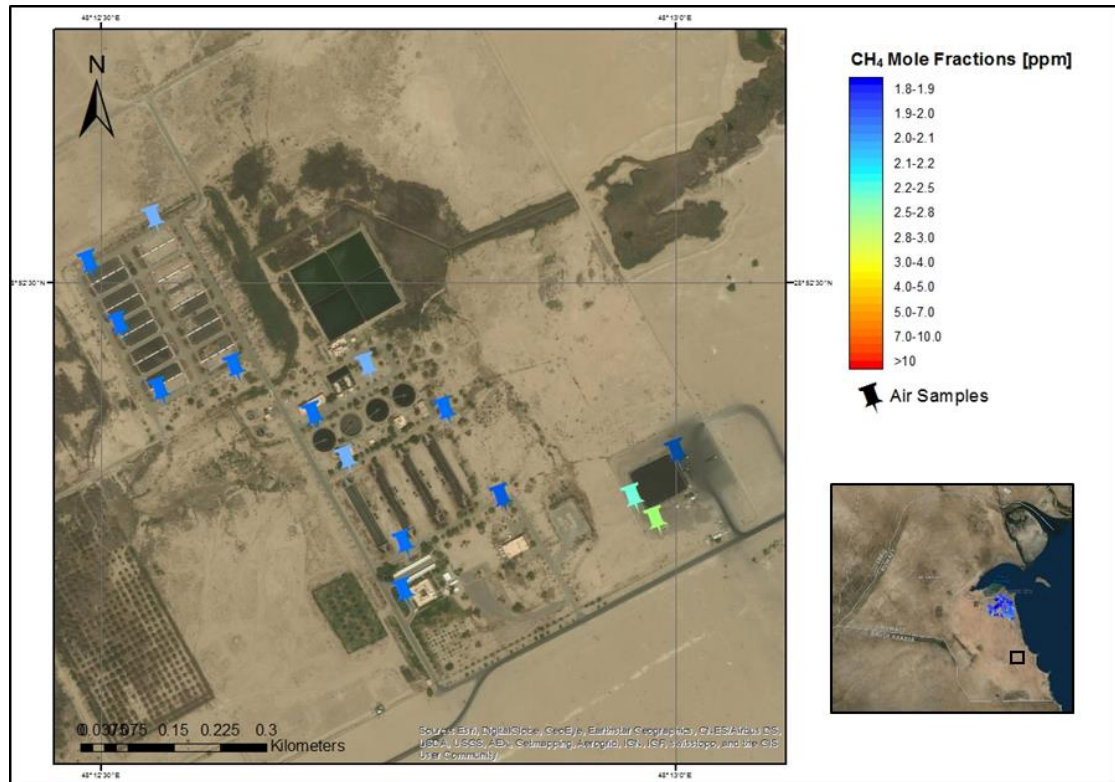


Figure 6.15 Keeling plot for the 3 air samples that were collected outside the Umm Al-Hayman wastewater treatment plant on 17th March 2017 in Kuwait



Figure 6.16 Industrial liquid waste pit located NE of Umm Al-Hayman sewage treatment plant. Three samples were collected next to this pit.

A)



B)

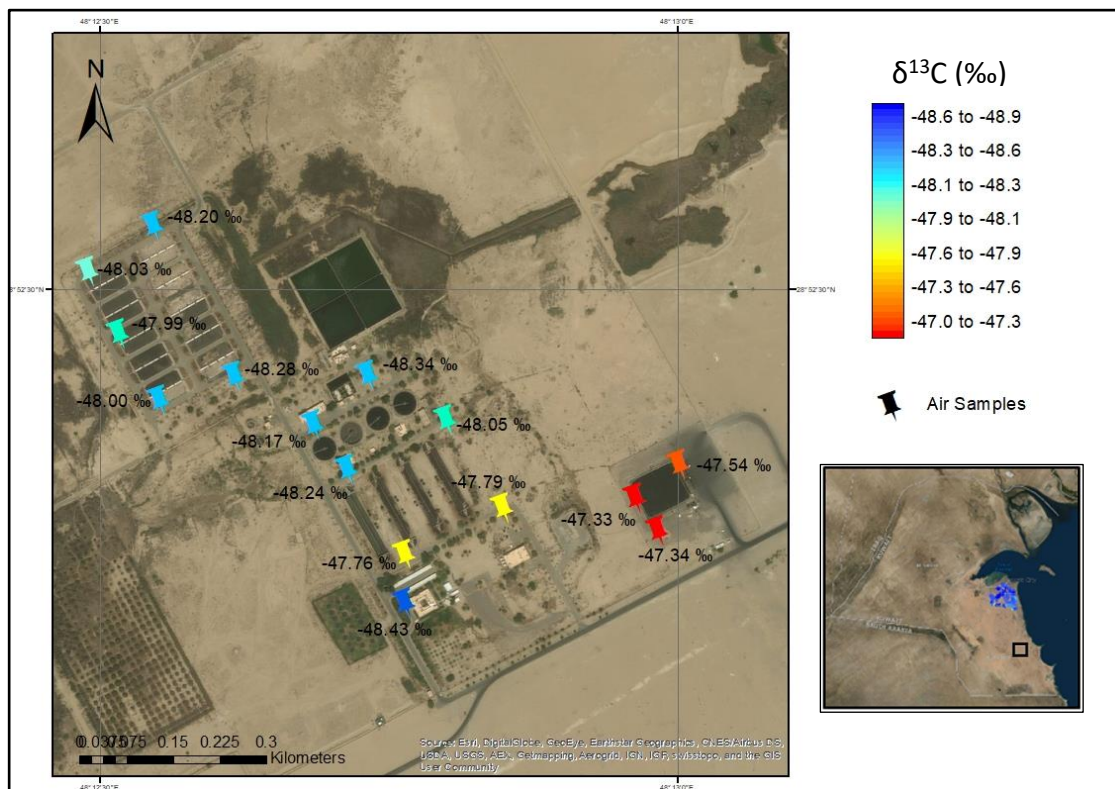


Figure 6.17 Google earth map for the locations of the 15 air samples collected at Umm Al-Hayman wastewater treatment, A) methane mole fraction (ppm), B) methane isotopic measured for all 15 samples on the 7th of March 2017 with ENE wind direction.

6.5 Discussion

Wastewater treatment plants are potential sources of methane emissions to the atmosphere (Toyoda *et al.* 2011). A few studies have examined the $\delta^{13}\text{C}$ -CH₄ isotopic values characterizing the wastewater treatment, such as the Zazzeri, (2015) case study on Methane Emissions in UK: This shows that sewage works are a complicated source and it is difficult to identify a distinct sewage $\delta^{13}\text{C}$ signature due to emissions from several processes during the sewage treatment, such as biological treatment of wastewater and anaerobic digesters. This means that the $\delta^{13}\text{C}$ signature of the downwind plume is changes depending on the different biological processes. Methane is emitted from the sewage treatment either by influent of the wastewater that contains dissolved methane, or it forms in the sewer system in the plant itself. The few previous studies revealed that methane can form in the sewer system, the sludge tanks, anaerobic zones and storage tanks with low oxygen conditions (Toyoda *et al.* 2011; Townsend-Small *et al.* 2012; Zazzeri 2015). Zazzreri (2015) studied Mogden sewage works in London and identified the two main methane sources in the sewage works process as the anaerobic digesters process with an isotopic signature of $-50.7 \pm 1.1\text{‰}$ and $-59.2 \pm 1.2\text{‰}$ for the secondary treatment.

Townsend-Small *et al.* (2012) used $\delta^{13}\text{C}$ to investigate sewage works in Los Angeles finding $\delta^{13}\text{C}$ -CH₄ isotopic values of -47.0‰ and -46.3‰ for Los Angeles County and Orange County, respectively. Toyoda *et al.* (2011) studied a municipal wastewater treatment plant located in the northern area of Tokyo called “Anaerobic water treatment system” in Japan. Toyoda *et al.* (2011) found the air samples collected over an oxic (Aeration) tank between -46.9 and -47.2‰ . Methane isotopic signatures were calculated for each process giving -45.5‰ for aeration (oxic tank) process and -51.7‰ in secondary settling process. There is suggestion in this study in particular in the measurement from Riqqa wastewater treatment plant that methane emissions from the aeration tanks are more enriched in ^{13}C than the emissions from other stages (Figure 6.9). Overall sewage treatment methane emissions may be less depleted in ^{13}C than in other countries where anaerobic treatment is more common because Kuwait’s wastewater treatment uses aerobic treatment.

A recent study by Fries *et al.* (2018) measured $\delta^{13}\text{C}-\text{CH}_4$ for sewer pipelines leakage in Cincinnati, Ohio. Fries *et al.* (2018) found variations in the methane isotopic signatures from -53.3‰ to $-48.5 \pm 0.6\text{‰}$. They related this variation in the isotopic signature to the mixing with plumes of natural gas leakage that were close to the investigated sewer pipelines.

6.6 Summary

Table 6.1 shows the $\delta^{13}\text{C}$ signature of methane emissions from Kuwait sewage works. Methane isotopic signatures for the wastewater treatment vary based on the technology employed in the treatment. There was some variation depending on the age of the treatment plant and those employing old (Aerobic biological reactors system) and new technology. On site monitoring of methane in these treatment plants would help to understand the emissions processes. Generally there is good agreement with previous studies with 2 main source signature populations around -46 and -51‰, and a smaller population with minor emissions from some secondary processes close to -59‰.

<i>Methane source</i>	<i>plant</i>	<i>Sampling Day</i>	$\delta^{13}\text{C} (\text{‰})$
<i>Wastewater treatment plant</i>	Riqqa	4 th May 2015	-50.5 ± 0.7
	Riqqa	4 th May 2015	-46.6 ± 0.03
	Riqqa	7 th January 2016	-45.1 ± 0.2
	Riqqa	7 th March 2017	-50.7 ± 0.6
	Riqqa	7 th March 2017	-45.6 ± 0.1
	KM30	5 th May 2015	-46.2 ± 0.1
	Umm Al-Hayman	17 th March 2017	-59.2 ± 0.9
	Umm Al-Hayman	17 th March 2017	-46.8 ± 0.04

Table 6.1 Methane isotopic signatures in the wastewater treatment plants in Kuwait

C_{CHAPTER 7}

R_{UMINANTS}

7. Ruminants

Ruminants are one of the primary sources of methane emissions that originate from microbial metabolism. Ruminant emissions have increased rapidly in recent decades (Lassey 2007). $\delta^{13}\text{C}$ signatures of ruminants emissions range between -75‰ to -45‰ and are highly controlled by the diet (Levin *et al.* 1993).

This chapter introduces all the surveys carried out in order to identify and isotopically characterise methane plumes from ruminant sources in Kuwait during May 2015.

Livestock in Kuwait State, according to the annual statistical bulletin 2015-2016 of the Public Authority of Agriculture and Fish Resources, were 29263, 588618 and 7718 of cows, sheep, and camels, respectively. Table 7.1 and figure 7.1 show the distribution of the livestock in the state of Kuwait during 2015-2016.

<i>District</i>	<i>Cows</i>	<i>Sheep</i>	<i>Camels</i>
<i>Al-Wafra</i>	2357	141449	3826
<i>Al-Abdalli</i>	2547	206920	2973
<i>Al-Sulabiya</i>	23542	12888	357
<i>Um-Al-Shgaya</i>	30	608	0
<i>Kabed</i>	685	206504	197
<i>Wafra Road</i>	102	18890	365
<i>Other</i>	0	1359	0
<i>Total</i>	29263	588618	7718

Table 7.1 Annual statistical bulletin of the livestock in state of the Kuwait during 2015-2016. Source: The Public Authority of Agriculture and Fish Resources/ Statistics Department 2015-2016.

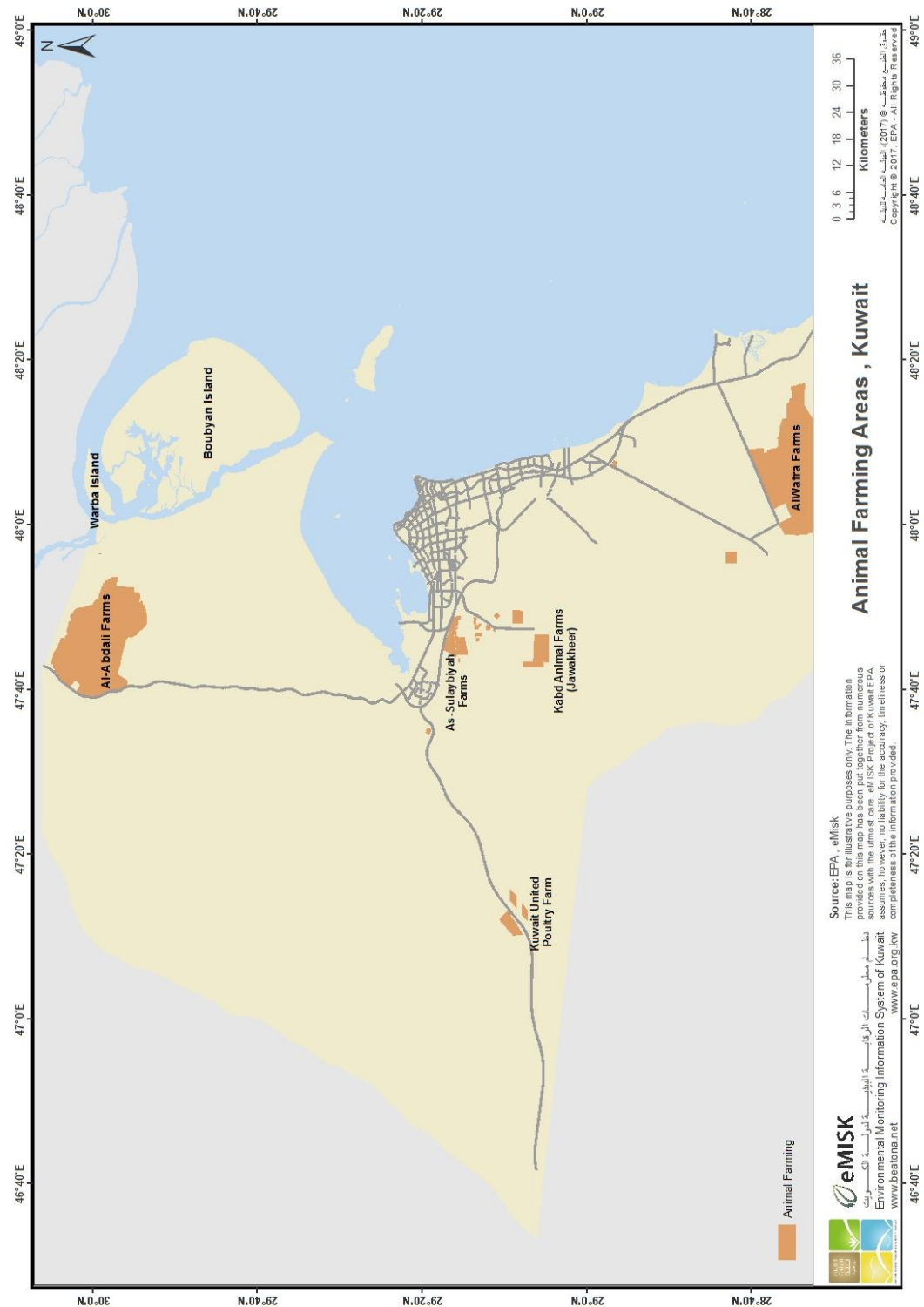


Figure 7.1 Animal farming areas in Kuwait State. Source: Emisk, Jun 2018

The Picarro mobile system was used to identify methane plumes from cows, sheep and camels and bag samples were collected for $\delta^{13}\text{C}$ analysis so that source signatures could be identified. The diet of the ruminants in Kuwait is a mixture of C3 plants and C4 plants with vitamins.

7.1 Cows

On the 3rd of May 2015, a survey was carried out with the Picarro mobile system around the animal farming area of Al-Sulabiya that is located to the west of Kuwait City in order to identify methane emissions from cows. Figure 7.2 shows the route of the survey driving around farming areas and the measured methane mole fraction.

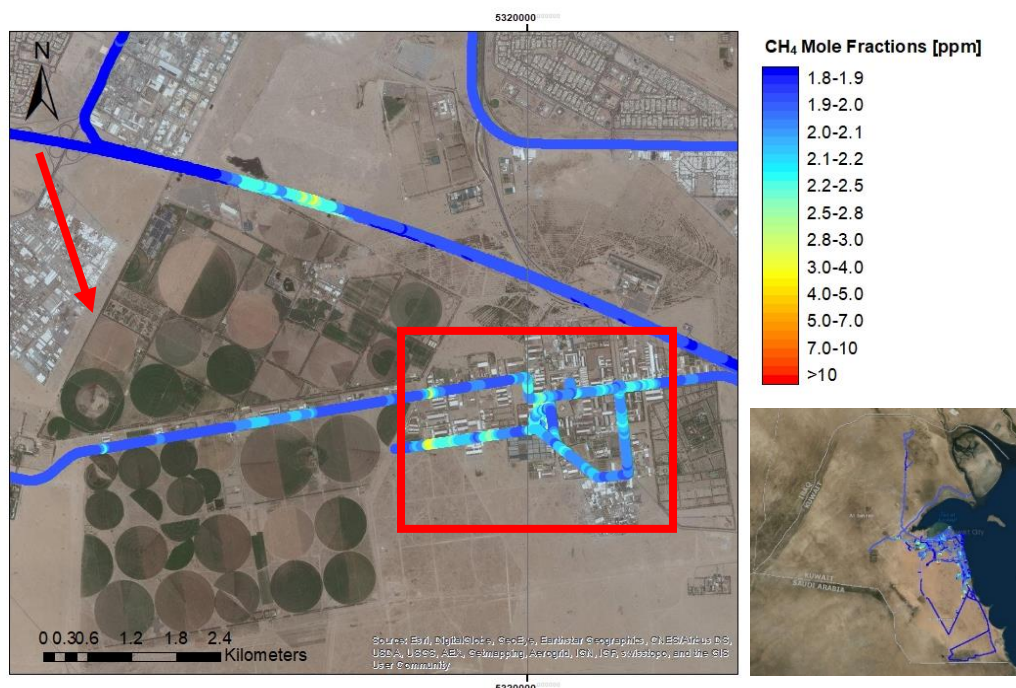


Figure 7.2 ArcGIS plot of methane mole fractions in ppm recorded on the 3rd of May 2015 around the Al-Sulabiya area. The red arrow represents NNW wind direction, the red square highlights the area of cow farms at Al-Sulabiya

The maximum methane mole fractions were recorded inside one of the cow-farms reaching 19.24 ppm. The farm hosted 1050 Kuwait, Dutch, and German cows with a total area of 110.5 m². This farm has 6 sheds of area of 20 x 30 m² and each shed hosts around 60 Holstein Friesian cows (Figure 7.3). Cows were fed on green trefoil (C3), Ca in water with vitamins, malt (C3), corn with brown flour, silage, rape seed and soya beans. The diet was a mixture of C3 and C4 with additional vitamins. Figure 7.4 shows the route of the survey inside this farm. Eight samples were collected upwind and downwind of the farm. A source of $\delta^{13}\text{C}$ signature of $-62.37 \pm 0.37\text{‰}$ resulted from the collected samples Figure 7.5.



Figure 7.3 Shows the Holstein Friesians cows inside a shed in one of the Al-Sulabiya farm.

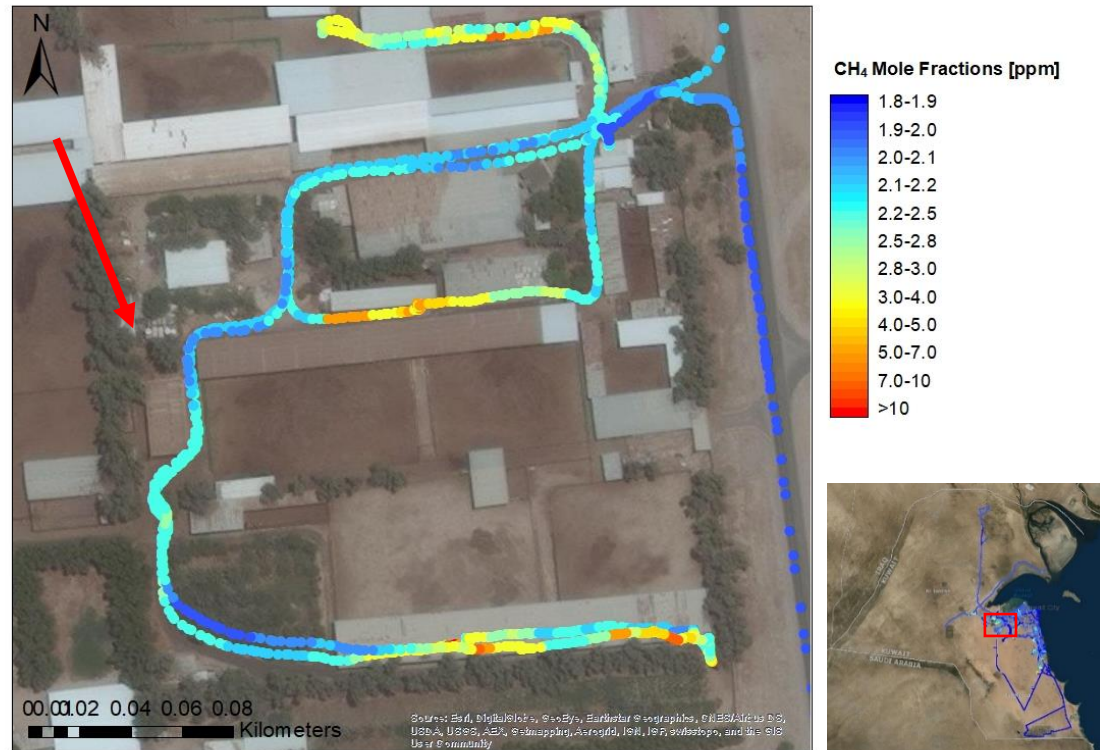


Figure 7.4 ArcGIS plot of methane mole fractions in ppm recorded on 3rd of May 2015 in a cow farm in the Al-Sulibiya area. Red arrow represents the wind direction from NNW.

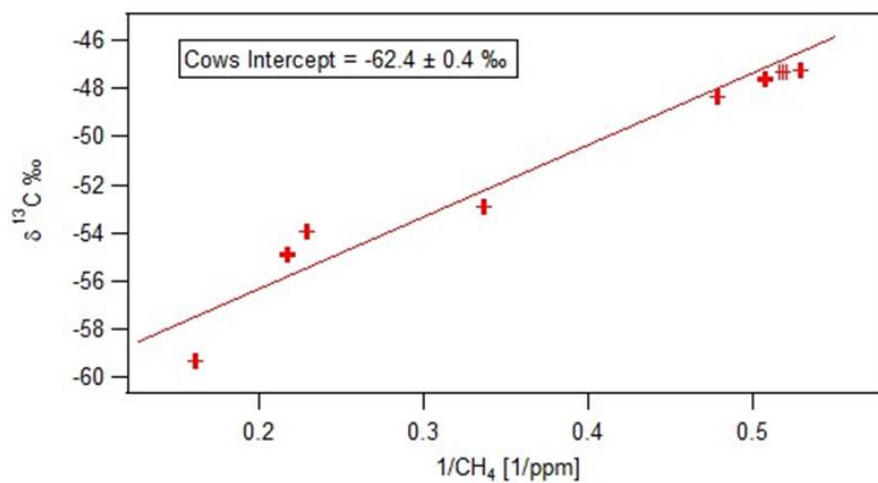


Figure 7.5 Keeling plot based on samples collected in a cow farm in the Al-Sulibiya area on 3rd of May 2015.

7.2 Sheep

The May 7th 2015 survey passed along the north side of Al-Mawashi Farm, one of the biggest Kuwait livestock farms, trying to intersect the downwind plume from the farm to the public road as there was no access inside this farm. With a S-SSE wind direction the methane plumes were detected during driving along the road (Figure 7.6), where a maximum methane mole fraction of 2.3 ppm was recorded. Two plumes and one background (1.87 ppm) air sample were collected downwind of the sheep farm and the resulting Keeling plot showed an intercept of $-63.63 \pm 0.03\text{‰}$ (Figure 7.7).



7.6 Google Earth view of methane mole fraction columns measured along the transect downwind of the sheep farm (Al-Mawashi) located in the Kabd area on 7th of May 2015. Yellow markers represent sample collections location and the yellow arrow the wind direction (S-SSE).

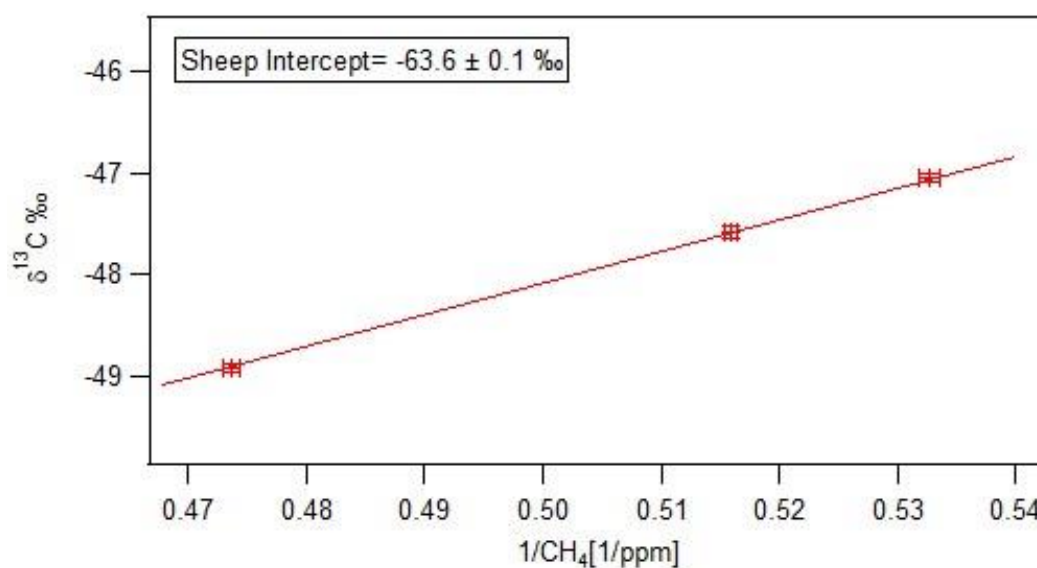


Figure 7.7 Keeling plot based on air samples collected downwind of the sheep farm (Al-Mawashi) on 7th May 2015.

7.3 Camels

On the 2nd of May 2015 methane emissions from camels were intercepted while driving on the Northern side of Kuwait City. A group of 200 camels was found next to the public road (Figure 7.8). Camels in Kuwait are fed a mix of both C3 and C4 plants, such as hay, barley, bran, and grass.

Camels emissions were detected downwind along the public road with 2.16 ppm maximum methane mole fraction. Three samples were collected, and the resulting Keeling plot showed an intercept of $-60.0 \pm 0.5\text{‰}$ (Figure 7.9).

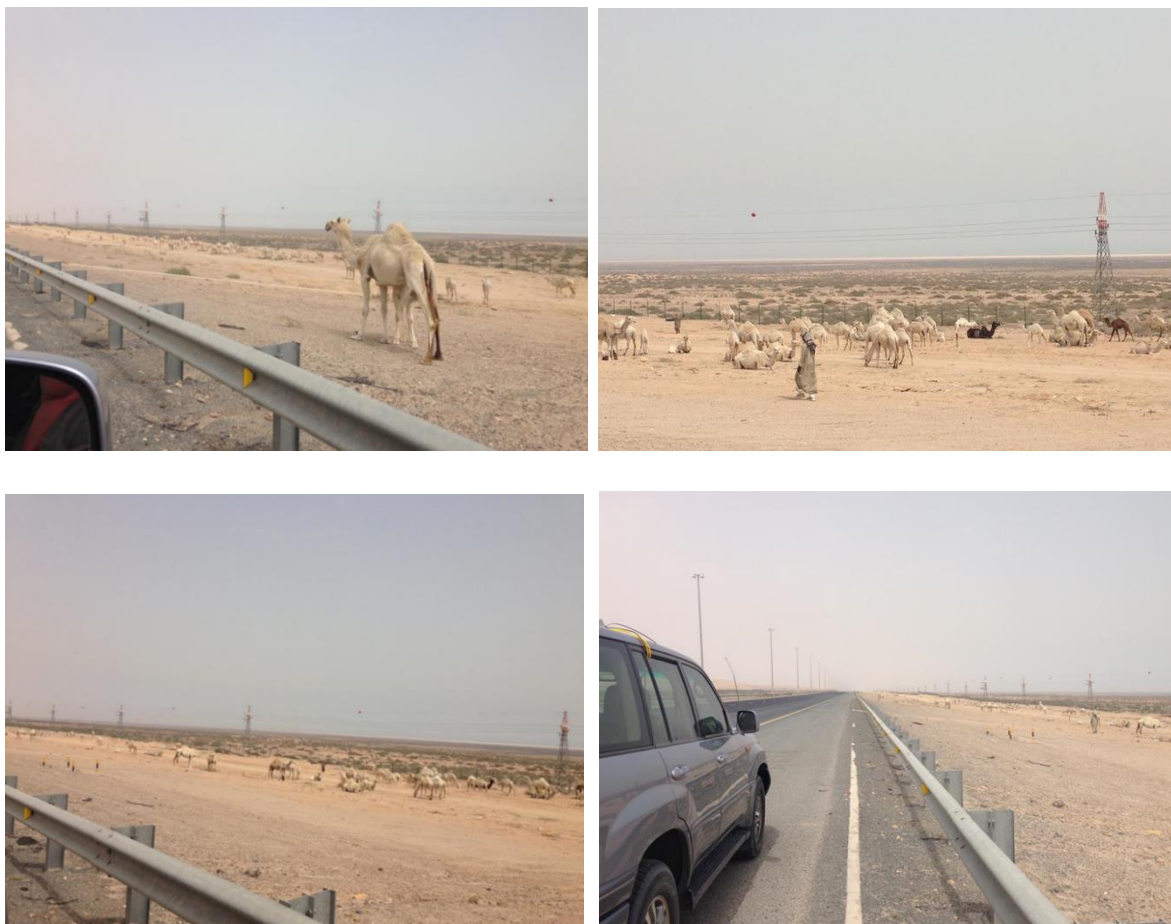


Figure 7.8 Group of 200 camels, next to the public road in the Al-Sabya desert area North of Kuwait City

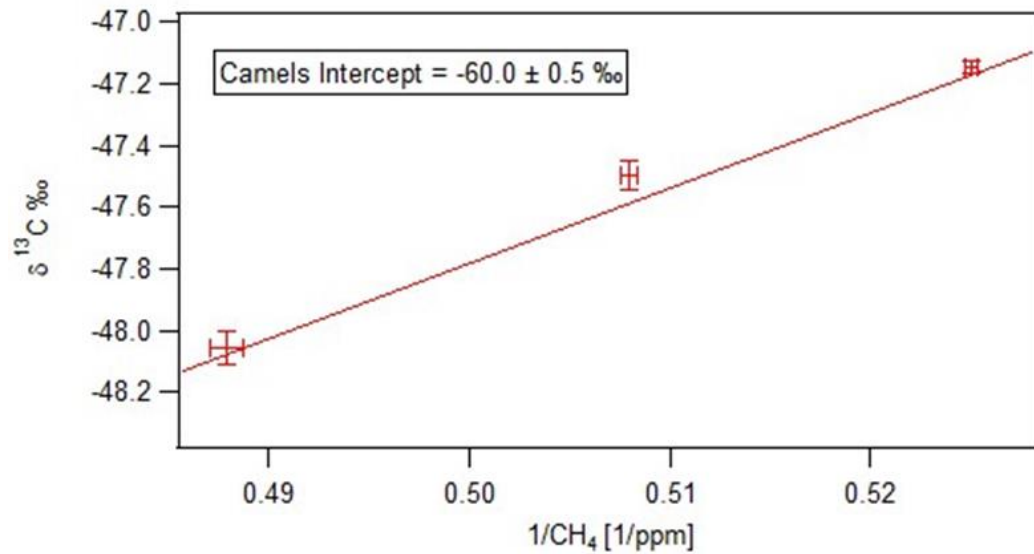


Figure 7.9 Keeling plot based on the samples collected near a group of camels in the desert on 2nd May 2015

7.4 Discussions of ruminant emissions

Globally methane emissions from ruminants are dominated by cattle which contribute 70% of ruminant emission and the remainder coming from sheep, goats, camels, and horses (Crutzen *et al.* 1986; Johnson *et al.* 1994). There are many factors that affect the production rate of methane from ruminants such as the quantity and quality of feed, level of feed intake, type of carbohydrate in the diet, presence of ionophores or lipids in the diet, digest passage rate, energy intake, enteric ecology, ambient temperature, energy expenditure of the animals and body weight, age, and exercise (Lerner & Matthews 1988; McAllister *et al.* 1996).

7.4.1 Ruminants eructation

Bilek et al.(2001) found that the diet type of cattle does not change the amount of CH₄ emitted but plays a substantial role in the $\delta^{13}\text{C}$ value of emitted CH₄.The type of feed controls the isotopic signature of methane eructed. There are two main groups of plants with different $\delta^{13}\text{C}$ -CH₄ values due to their photosynthetic pathways. The emissions from ruminants eating a C3 plants diet , such as temperate, grasses, produce methane with more depleted $\delta^{13}\text{C}$ values of $-67.0 \pm 4.5\text{‰}$ than those eating C4 plants diet which is dominated by savanna grasses and maize that produces more enriched methane with $\delta^{13}\text{C}$ values of $-52.3 \pm 5.5\text{‰}$ (Vigano *et al.* 2009). A compilation by Dlugokencky *et al.* (2011) showed, the $\delta^{13}\text{C}$ values for ruminants digesting C3 plants are -65 to -60‰ and those eating C4 plants are -55 to -50‰. The carbon in C4 plants is ~14‰ enriched in ¹³C compared with C3 (Bilek *et al.* 2001). Klevenhusen *et al.* (2009) found about a 13.5 ‰ difference in $\delta^{13}\text{C}$ between the cattle diets consisting either of C3 or C4 plants. This is similar to the sheep diet difference (14‰) between C3 and C4 diet (Rust 1981).

7.4.2 Ruminants rumen

Rust, (1981) showed that the differences in the isotopic ratios of the feed plants are reflected in the carbon isotopic ratios of both the rumen CH₄ and the eructed CH₄. Isotopic values of rumen methane have a wide range from -80‰ to -50‰. This is associated with feed composition and sampling techniques (Schulze *et al.* 1998). A study on cows, camels, and sheep under identical feed conditions and sampling the rumen gases found $\delta^{13}\text{C}$ methane -69.5 to -66.9‰, -76.8 to -72.0‰ and -76.5 to 70.5‰ for cows, sheep and camels, respectively (Schulze *et al.* 1998) .

7.4.3 Sampling technique

Sampling technique plays a significant role in determining the $\delta^{13}\text{C}$ -CH₄ from ruminants (Schulze et al. 1998). There are different methods to collecting samples from the ruminants. Many techniques exist to quantify methane emissions from individuals or groups of animals. The SF6 tracer technique was developed for cattle

by Johnson *et al.* (1994). This technique called the ERUCT technique (Emissions from Ruminants Using Calibrated Tracer) to measure the methane production from the animals using sulfur hexafluoride (SF_6), an inert gas tracer, placed in the rumen of each participating animal and the “breath” of the animals while grazing (Figure 7.10). This method is widely adopted in many countries such as USA , Canada, Australia and Ireland (Lassey 2007), For further details see Johnson *et al.* (1994); Johnson & Johnson (1995) ; Ulyatt *et al.* (1999) ; Lassey *et al.* 2001 and Lassey (2007).

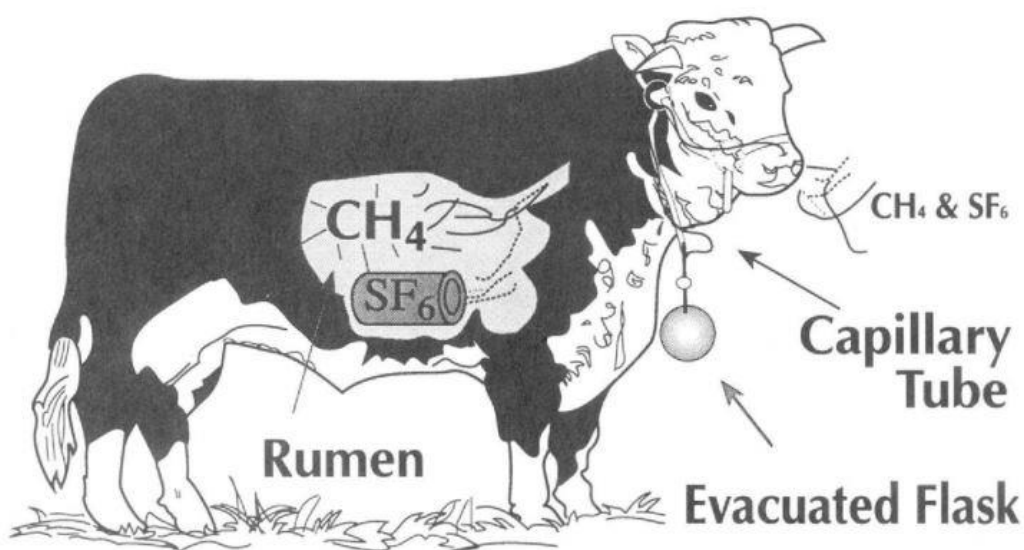


Figure 7.10 Illustration of tracer methodology by (Johnson *et al.* 1994)

Ulyatt *et al.* (1999) studied alternative methods for measuring methane emissions on fields. Each of these methods has strengths and weaknesses. The method used by Judd *et al.* (1999) measures methane fluxes on the downwind side from a tower site (4 to 1.2 meters above the ground). Denmead (1994) collected gas samples from many ports on a framework up to 3.5 m high surrounding the enclosure, dubbed the Enclosure Technique (Judd *et al.* 1999). Both these techniques agree well with the SF_6 technique.

All the discussed methods were designed to measure the methane emissions from animals. In this study, air samples were collected to measure methane emissions in order to analyse the $\delta^{13}\text{C}\text{-CH}_4$ source signatures by using the Picarro mobile system driving along public roads in (Al-Sulibiya). This is one of the biggest farming areas in Kuwait. Large methane plumes were detected as shown in Figure 7.2. Air samples were collected upwind and downwind of the plume from a cow farm. Additional samples were collected inside the farm as shown in Figure 7.4. These samples represent a mixed manure and eructation signature as the plumes are from individual barns and the farm as a whole.

Table 7.2 Summarises several studies of the $\delta^{13}\text{C}$ values from ruminants with the type of diet and sampling technique.

<i>Study / Location</i>	<i>Animals</i>	<i>Sampling technique</i>	<i>Diet</i>	$\delta^{13}\text{C} \text{ ‰}$	<i>Authors</i>
<i>Range of sources</i>	Dairy cow Dairy cow sheep	Eructate Rumen rumen	C3 C3 C3	-61.6 -52.5 to -47.4 -70.2 to -67	(Rust 1981)
<i>New York</i>	Dairy cow	rumen	forage	-71.3 \pm 4.1	(Wahline <i>et al.</i> 1989)
<i>Washington</i>	Dairy cow	rumen		-63	(Lansdown. 1992)
<i>Germany</i>	Dairy cow sheep	Eructate Eructate Eructate	C3 (100%) C4 (60-80%) C3	-65.1 \pm 1.7 -55.6 \pm 1.4 -70.6	(Levin <i>et al.</i> 1993)
<i>Germany</i>	Cow Sheep camels	rumen rumen rumen	Hay and concentrates	-69.5 to -66.9 -76.8 to -72.0 -76.5 to -70.5	(Schulze <i>et al.</i> 1998)
<i>Japan</i>	Dairy cows	Animal chamber	C3 and C4	-70.6 \pm 4.9	(Bilek <i>et al.</i> 2001)
<i>Los Angeles</i>	cow Cow	Breath manure		-65 to -60.2 -62.1 to -59.1	(Townsend-Small <i>et al.</i> 2012)

Table 7.2 Literature Isotopic value of ruminants from a range of previous studies

7.5 Summary

The methane isotopic signature of ruminants in Kuwait from three main sources were identified as shown in Table 7.3

<i>Methane Source</i>	<i>$\delta^{13}\text{C}$ isotopic signature (‰)</i>
<i>Cow</i>	-62.4± 0.4
<i>Sheep</i>	-63.6 ± 0.1
<i>Camels</i>	-60.0 ± 0.5

Table 7. 3 Isotopic signatures of methane from ruminants in Kuwait State (this study).

The $\delta^{13}\text{C}$ signature of methane emissions from animals is more ^{13}C depleted relative to the isotopic signatures of other biogenic sources, such as landfill and waste water treatment. Methane emissions from cattle globally show a large variation in $\delta^{13}\text{C}$ signatures from -75 to - 45‰. Several studies mentioned earlier investigate the relationship between cattle diet and sampling technique for the methane emissions by using the measurement of $\delta^{13}\text{C}$. The main difference in the isotopic signature of methane emissions comes from diets of C3 and C4 plants, with cow breath focused around -70 ± 4 ‰ for C3 diets and -49 ± 4 ‰ for C4 diets (Dlugokencky *et al.* 2011). This is complicated by: a) mixed diets containing C3 and C4 plants, and b) cow barns that contain mixtures of cow breath emissions, and cow waste manure emissions, which have different isotopic signatures (Dlugokencky *et al.* 2011).

***C**CHAPTER 8*

***A**MBIENT METHANE*

MEASUREMENTS IN KUWAIT: LONG TERM STUDY

8. Ambient Methane Measurements in Kuwait: Long-Term Study

Stable carbon isotopic analysis coupled with methane mole fraction measurements allow determination of the mean $\delta^{13}\text{C-CH}_4$ source signature of a region and estimation of the proportion of methane sources in a source mix. For example, for better understanding of urban methane sources, analysis of the source mix directly in the city centre can allow validation of methane inventories (Zazzeri *et al.* 2015). During the period 2015 to 2016 air samples were collected weekly from three different sites in Kuwait. This long-term monitoring study aimed to use the methane mole fraction measurements combined with the stable carbon isotopic composition to identify the most important methane sources in Kuwait State. The technique of attribution of sources according to the isotopic source mix has been used in other urban areas such as London (Zazzeri *et al.* 2017) and Denver (Townsend-Small *et al.* 2016).



Figure 8.1 Google Earth map showing the three sites for collection of air samples (green pushpins) in Kuwait during 2015 and 2016.

8.1 Long-Term Methane Measurements.

1948 was the turning point in the economic life of Kuwait when the first shipment of oil was sent to the international market. In the early 1950s, the population grew rapidly and urban areas expanded (Abu-Ayyash 1980). According to the Central Statistical Bureau of Kuwait state, the population estimate at the beginning of 2018 was 4,226,920 people. There are many potential sources of greenhouse gases in and around Kuwait City such as landfills, sewage treatment plants, ruminant farms, refineries and around 2,001,940 vehicles (www.csb.gov.kw : 30 of June 2018).

The long-term study of methane emissions from Kuwait City was run for two years. To decide the best locations for regular air sampling, meteorology and air trajectory analysis must be understood. Kuwait occupies 17,818 km² with 195 kilometers of coastline. Summer months (June, July, August, and September) are mostly dry and hot, with a temperature range in summer of 42°C to 48°C. The highest temperature recorded on the 21st of July 2016 in Mitribah was 54°C (http://www.met.gov.kw/Climate/climate_hist.php?lang=eng). Dramatic dust storms occur mainly in June and July when northwesterly wind covers the city in sand (Al-Hamad and Khan, 2008). In winter, the temperature can drop to -2 °C in the desert and the average temperature is around 18°C from December to February. Generally clear sky, high temperature and airborne dust are the feature of the summer season whereas mild to relatively cold with light rain is the feature of the winter season (Al-Hamad and Khan, 2008). Al-Nassar et al.(2005) analysed wind speed and direction over 46 years based on hourly mean values from Kuwait International Airport and showed clearly that the main prevailing wind in Kuwait is the northwesterly wind with an average wind speed of 5.5 m/s. Another study (Al-Rashidi *et al.* 2005) shows that the prevailing wind direction is from the north west. Al-Azmi *et al.* (2009) found that in 2001 60% of the wind in Kuwait was from a north west direction and in 2004, about 46% of the wind comes from the NW sector. Backward trajectory modelling shows the most dominant winds coming from the NW sector between Northern Africa, the eastern Mediterranean, Middle-East, Southern Russia, and Iran (see next section 8.2).

8.2 Backward Trajectories

To assess the continental provenance of air masses, the Hybrid Single-Particle Lagrangian Integrated Trajectory model (HYSPLIT) has been used to compute air trajectories arriving at 100 meters to 1000 meters above ground. This web-based system was initially developed in 1997 by the National Oceanic and Atmospheric Administration's (NOAA) Air Resources Laboratory (ARL) and named the Real-time Environmental Applications and Display (READY, [http:// www.ready.noaa.gov](http://www.ready.noaa.gov)) (Rolph *et al.* 2017). The HYSPLIT model shows that the provenance of air masses arriving in Kuwait is very difficult to define on some days, with air at different heights having different sources (Figure 8.2).

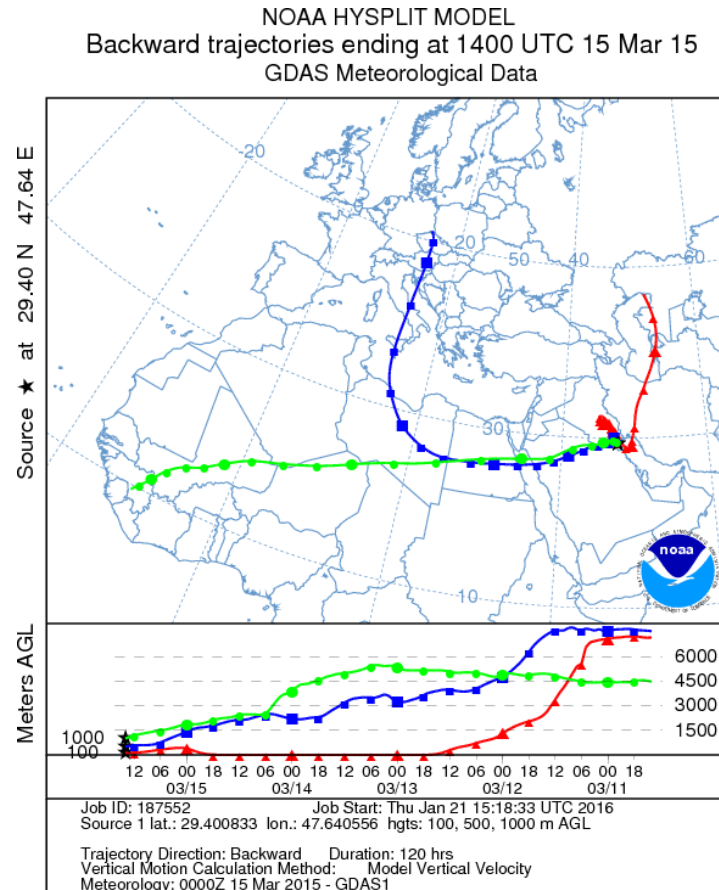


Figure 8.2 Backward trajectory model for Kuwait, calculated for a duration of 120 hrs air movement. The red line represents the air trajectories arriving at 100m, blue 500m and green line 1000m above the ground.

The air movement for 120 hours prior to arrival in Kuwait was computed with the NOAA HYSPLIT backward trajectory model for the period 2015 and 2016. The most common provenance of air masses was from Iraq after passing through many countries to reach Kuwait. Most of the remaining air masses passed over either Saudi Arabia, the Arabian Gulf or Iran. Figures 8.3 and 8.4 show an example of each of these trajectory clusters.

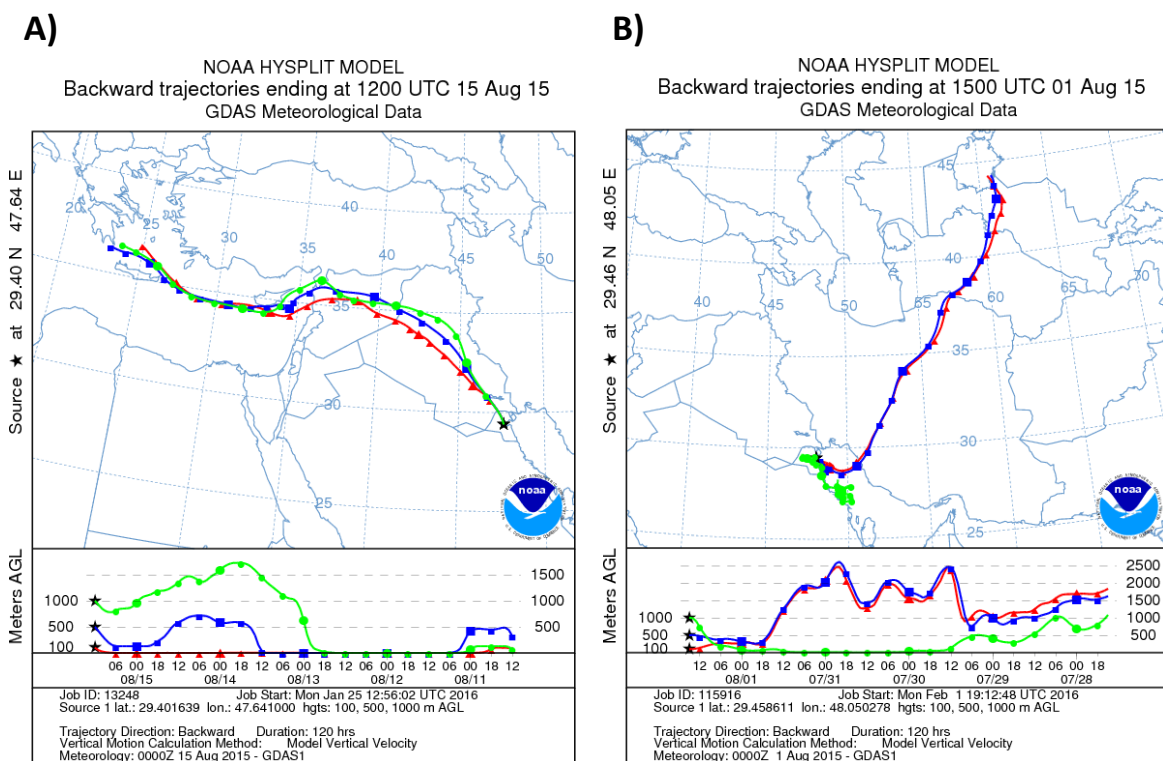


Figure 8.3 Backward trajectory model for air arriving at Kuwait City, calculated for a duration of 120 hrs of air movement. (A) the air mass is coming from Iraq and Syria, (B) coming from Iran. The red line represents the air trajectories arriving at 100m, blue 500m and green line 1000m above the ground.

B)

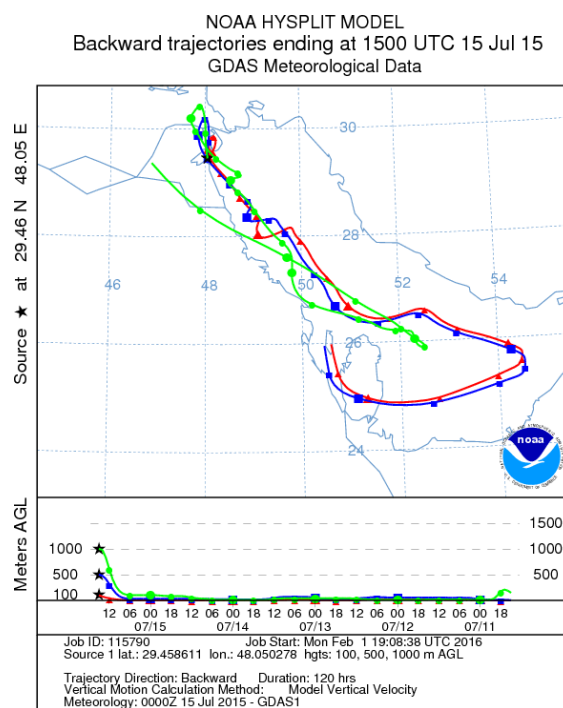


Figure 8.4 Backward trajectory model for air arriving at Kuwait City, calculated for a duration of 120 hrs air movement. (A) coming from Saudi Arabia and (B) from the Arabian Gulf. The red line represents the air trajectories arriving at 100m, blue 500m and green line 1000m above the ground.

The calculation of the air movement during 2015 and 2016 for each sampling day shows that 66% of the air masses are coming from a NW direction passing through Jordan, Syria and Iraq. Some of these air masses pass over Cyprus and the eastern Mediterranean region as shown in figure 8.3A. Additionally, 20% of the air masses come from Saudi Arabia (Figure 8.4A), 8% from the Arabian Gulf and 6% from Iran.

8.3 Air Sampling Sites

To understand and identify methane emissions locally and regionally, three sites were selected to collect air samples weekly, Al-Mutla (upwind), Khaldiya (central city) and Fahaheel (downwind) (Figure 8.1).

Al-Mutla is a desert area around 33 km North West of Kuwait City with coordinates 29°24'05.9" N and 47°38'27.6 " E. According to the most common wind directions influencing Al-Mutla, samples were collected from a site usually upwind of the Al-Mutla area. This site was chosen to isotopically characterise air coming from the eastern Mediterranean, Syria, and Iraq. Figure 8.5 shows the Al-Mutla location. There are no methane sources close to the site. The main building in this area is Al-Mutla police station 100 m south of the collection site.

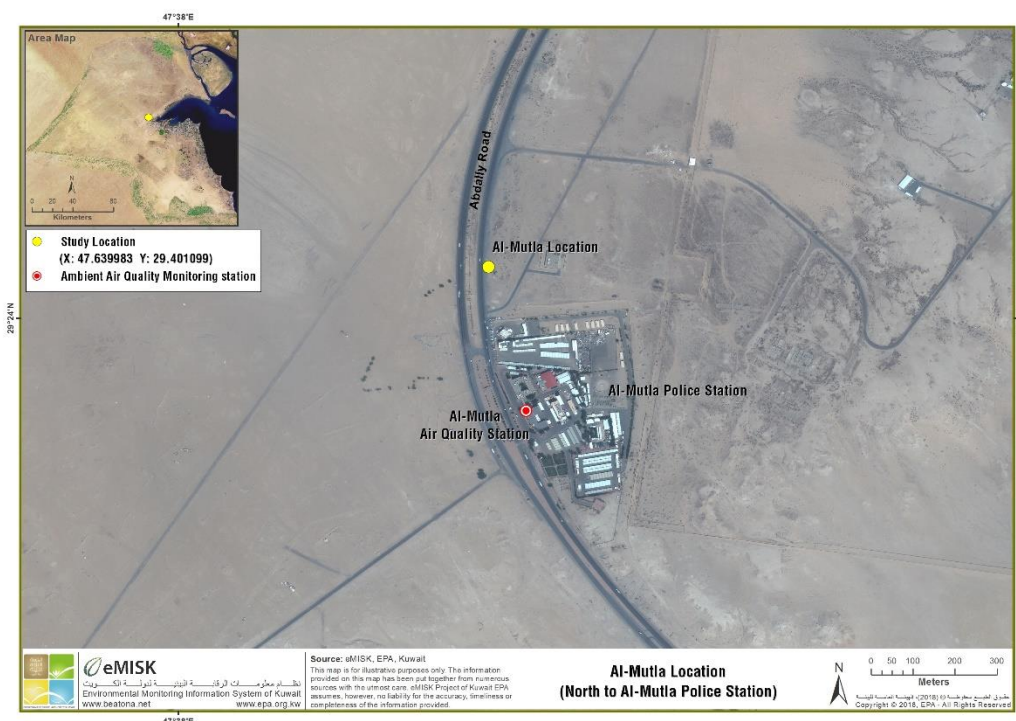


Figure 8.5 Al-Mutla, where samples were collected for the period of 2015-2016 (Source: eMISK, 2018)

A second sampling site was in the city with coordinates 29°19'51.1"N and 47°58'30.1"E on the roof of the Department of Earth and Environmental Sciences at Kuwait University, College of Science in the Khaldiya area. This site was located in the center of Kuwait City to allow better understanding of urban CH₄ sources. This site is influenced by many potential methane sources such as landfills and a sewage works (Figure 8.6). There are four landfills located near this site. The closest one 2 km away is called Al-Yarmouk landfill. The Jleeb Al-Shuyoukh landfill (with an area of 6 km², the largest in Kuwait), is located around 8 km south-west of the site (see chapter 4.3.7), and the North and South Ring Road landfills (see chapter 4.3.2) may also be an influence. As shown in Figure 8.4 this site is in Kuwait University next to the main student car parking.

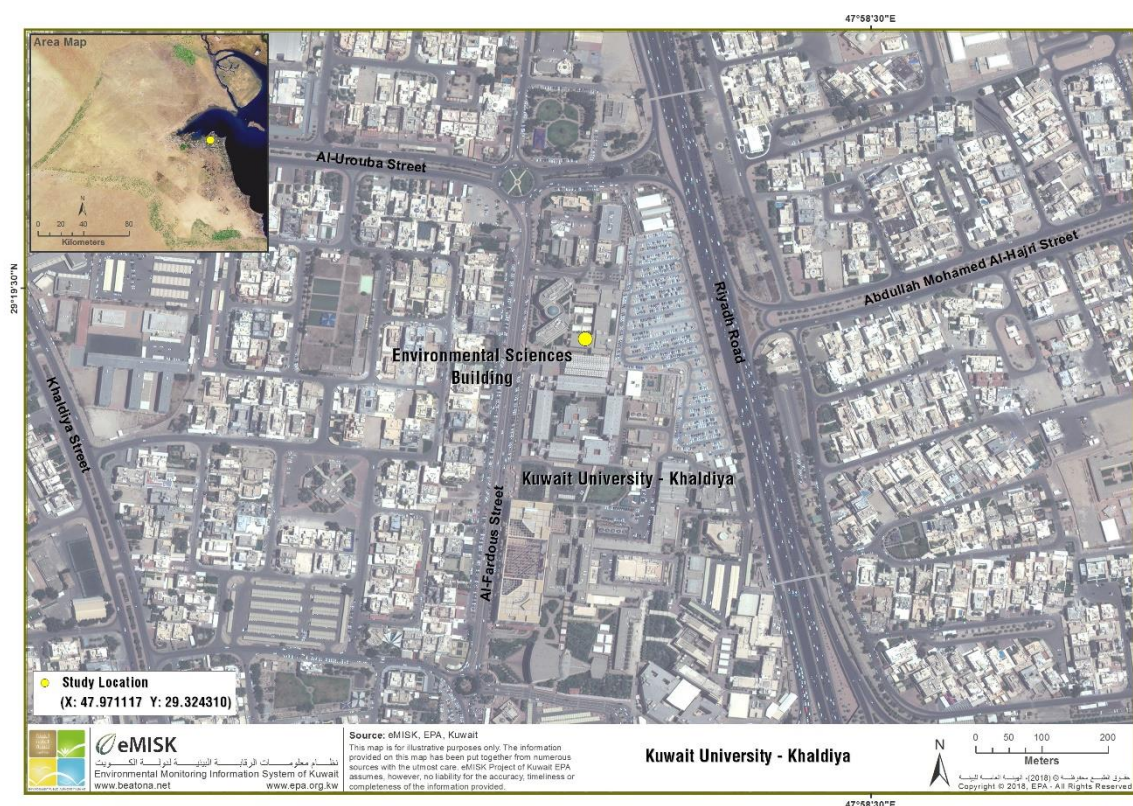


Figure 8.6 Khaldiya site in the Kuwait University, College of Science. (Source: eMISK, 2018).

The third site is downwind located 35 km South East of Kuwait City and two km west of the coastline. The coordinate for this is 29°04'80.9"N and 48°06'99.1'E. This site is surrounded by potential methane sources such as refineries around 1.5 km away in the sector to the ESE to S, oil fields around 5 km SW, oil tanks 1 km away and a sewage treatment plant 8 km NW (Figure 8.7).



Figure 8.7 The location of the Fahaheel site (Source: eMISK, 2018)

During the two-year period January 2015 to December 2016 samples were collected weekly from the three sites approximately at the same time. Air samples were collected by pumping air into 3 L Tedlar bags and were analysed at RHUL for methane mole fraction and $\delta^{13}\text{C-CH}_4$. Figure 8.5 shows the methane mole fractions of the three sites for the two years of sampling, 2015 and 2016. Seasonal changes in the methane mixing ratio are observed. A significant difference is observed between summer and winter methane mole fractions. The meteorological conditions also play an important role in pollutant distribution affecting the ground level concentrations in the residential areas (Al-Azmi *et al.* 2009). Increased wind turbulence and a high inversion layer affect dispersion leading to a low methane mole fraction in summer in Kuwait. The reaction with hydroxyl radicals (OH) is the main sink of methane and is enhanced in summer. This exerts a fractionation effect on methane $\delta^{13}\text{C}$ (Nisbet *et al.* 2014; Zazzeri *et al.* 2017). Methane mole fractions reached the minimum values in summer and build-up in winter (November and December) (Zhou *et al.* 2004). This is partly due to the boundary layer height. In autumn and winter. This tends to be is much lower than in summer (Worthy *et al.* 1998; Levin *et al.* 1999; Zhou *et al.* 2004; Al-Azmi *et al.* 2009; Zazzeri *et al.* 2015). The lower values in summer are highlighted in Figure 8.8 by the shaded yellow zone. In winter, the meteorological conditions are calmer and are accompanied by a low inversion layer (Al-Azmi *et al.* 2009). Methane mole fraction tends to rise due to low dispersion as shown in the blue shaded zone in Figure 8.8. For the period 2015 and 2016, mean winter time methane mixing ratios are around 90 ppb higher than the summer values.

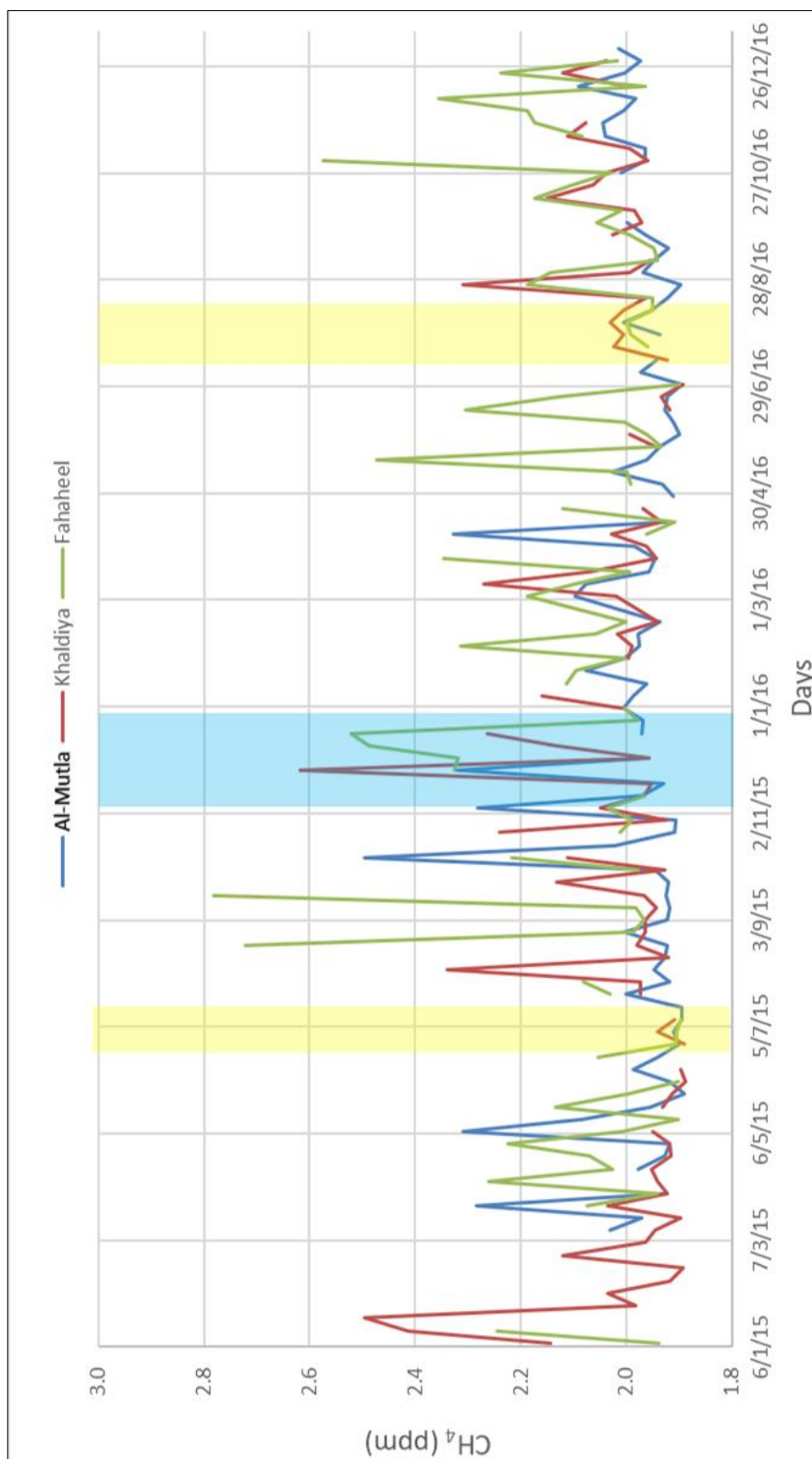


Figure 8.8 Methane mole fraction for the period 2015 and 2016 for three sites in Kuwait. The minimum period is highlighted by the yellow shaded area in summer and the maximum by the blue shade area in winter.

Long term measurements of methane mole fraction combined with stable carbon isotopic composition are used to determine mean $\delta^{13}\text{C-CH}_4$ source signature characterising a region and hence allow estimation of the proportion of the main CH_4 sources in a source mix. Figure 8.9 shows measured $\delta^{13}\text{C}$ in 2015 and 2016 for the three sites. Seasonal variations were observed in $\delta^{13}\text{C-CH}_4$ with mean amplitude of $\pm 0.4\text{‰}$ with more depleted values down to -49.94‰ associated with maximum methane mole fractions, indicating that most CH_4 emissions in the region are isotopically lighter than background atmospheric CH_4 (Yamada *et al.* 2005). The methane cycle is strongly modulated by the changing stability of the atmospheric boundary layer (Worthy *et al.* 1998; Levin *et al.* 1999; Zhou *et al.* 2004; Fisher *et al.* 2011). There were two outliers in 2015 and one in 2016 from the Fahaheel sites. These outliers have a high methane mole fraction and different $\delta^{13}\text{C}$. This might be due to improperly flushed bags but could be a local source near to the site. The histogram charts in Figure 8.10 show the basic statistics and distribution of $\delta^{13}\text{C}$ values and methane mole fractions of each site individually for 2015 and 2016. For the Al-Mutla and Khaldiya sites, the distribution is not very different. At Fahaheel site, the distribution was mildly different because of the effect of the outliers.

A summary of the $\delta^{13}\text{C-CH}_4$ values and methane mole fraction measurements that have been measured in this study are shown in Table 8.1.

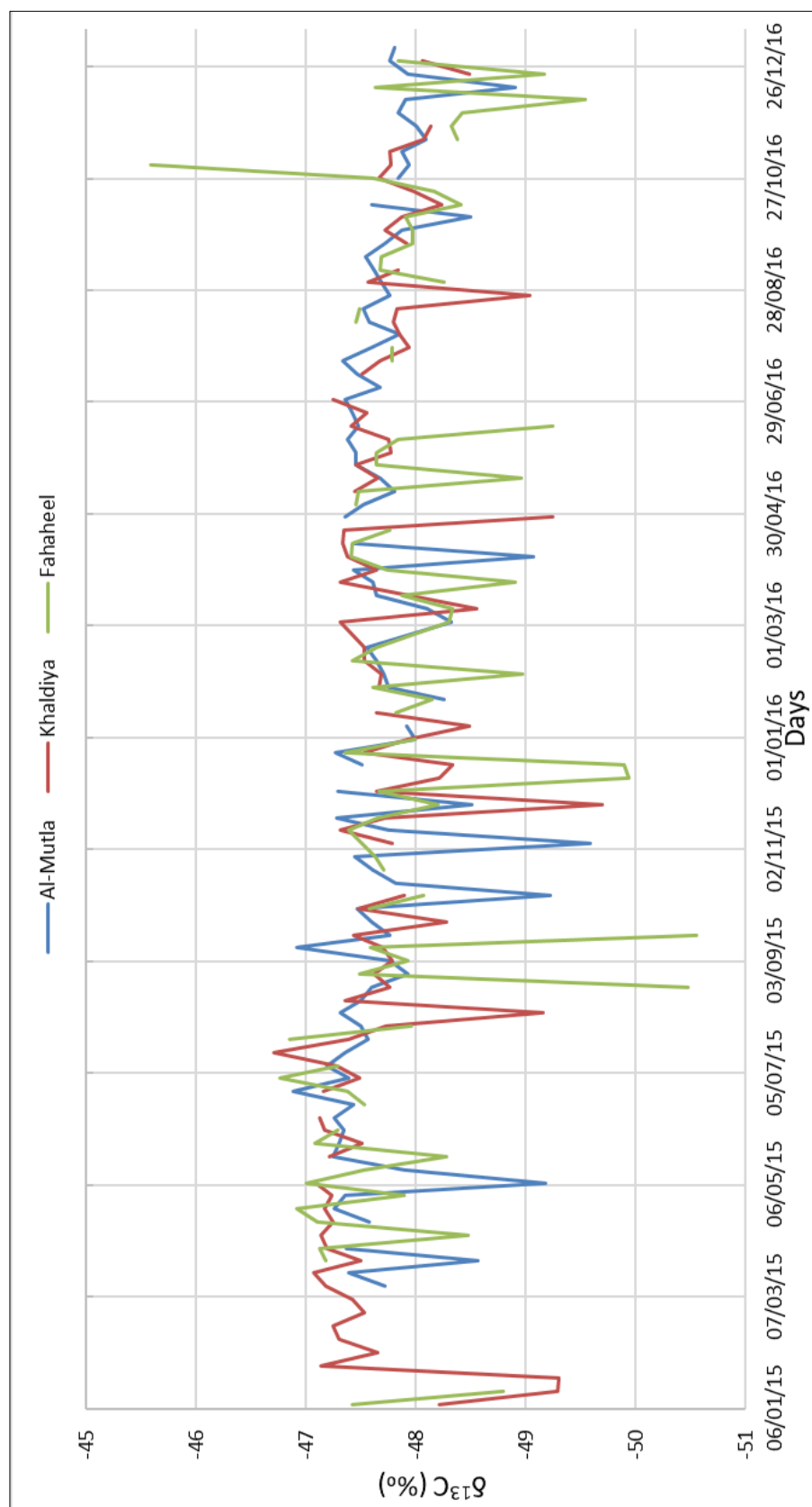


Figure 8.9 Methane isotopic signatures values for period 2015 and 2016 for three sites in Kuwait.

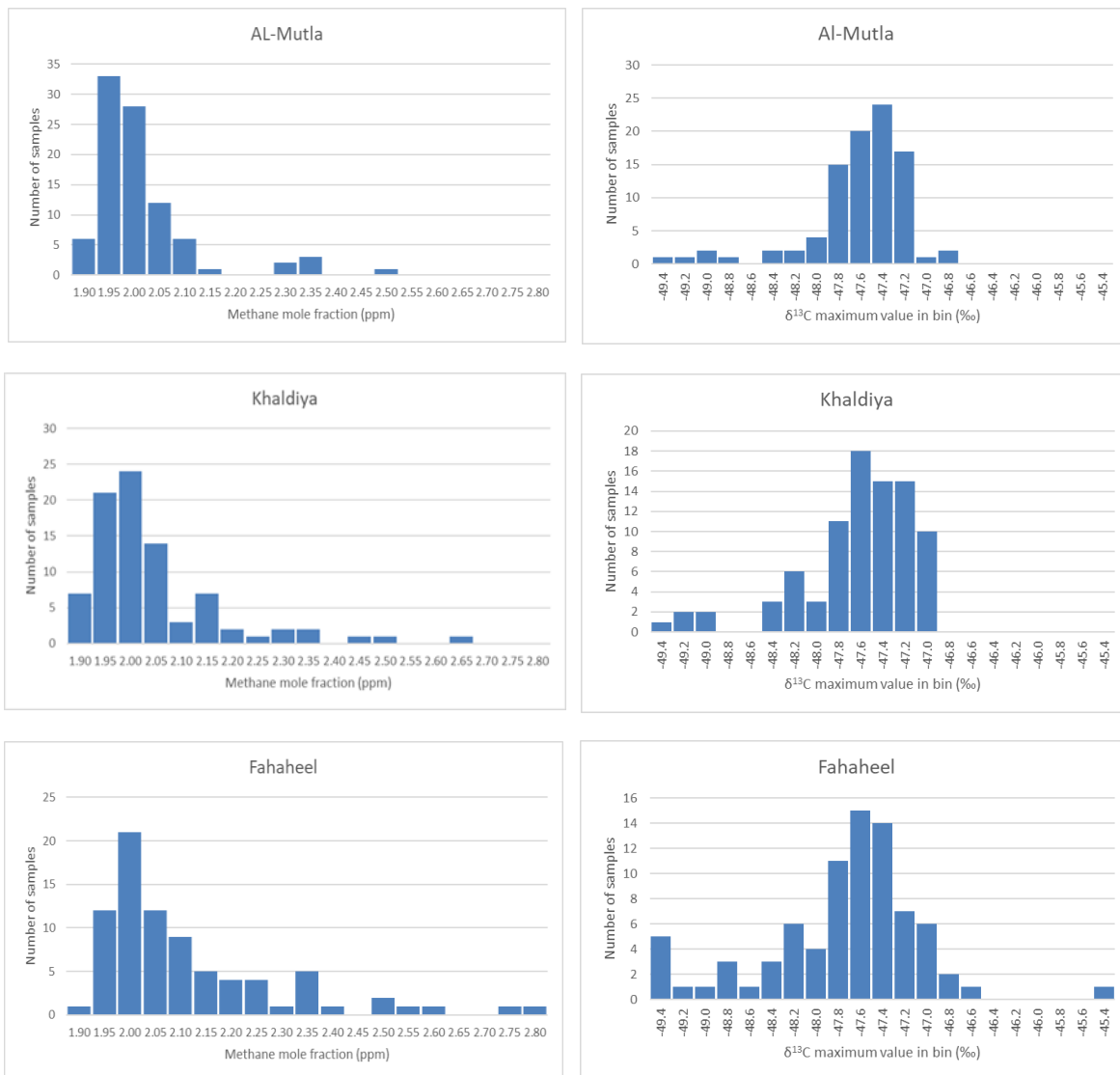


Figure 8.10 $\delta^{13}\text{C}$ -CH₄ values and methane mole fractions measurements for the air samples collected in 2015 and 2016 from three sites (Al-Mutla, Khaldiya and Fahaheel)

Year	Measurements	Sites		
		Al-Mutla	Khaldiya	Fahaheel
2015	Mean CH ₄ (ppm)	1.995	2.015	2.092
	Sd (ppm)	0.13	0.164	0.217
	Median (ppm)	1.951	1.963	2.005
	Max (ppm)	2.495	2.619	2.782
	Min (ppm)	1.890	1.888	1.896
	Mean $\delta^{13}\text{C}$ (‰)	-47.66	-47.66	-47.81
	Sd (‰)	0.56	0.63	0.91
	Number of samples	44	48	40
2016	Mean CH ₄ (ppm)	1.979	2.015	2.087
	Sd (ppm)	0.071	0.088	0.151
	Median (ppm)	1.967	1.996	2.028
	Max (ppm)	2.328	2.309	2.575
	Min (ppm)	1.890	1.891	1.900
	Mean $\delta^{13}\text{C}$ (‰)	-47.77	-47.81	-47.97
	Sd (‰)	0.36	0.43	0.67
	Number of samples	48	44	44
Both 2015 and 2016	Mean CH ₄ (ppm)	1.986	2.02	2.089
	Sd (ppm)	0.105	0.135	0.184
	Median (ppm)	1.962	1.973	2.012
	Max (ppm)	2.495	2.619	2.782
	Min (ppm)	1.890	1.888	1.896
	Mean $\delta^{13}\text{C}$ (‰)	-47.72	-47.73	-47.89
	Sd (‰)	0.56	0.55	0.80
	Number of samples	92	92	84

Table 8.1 Summary of measurements for samples collected at the 3 sites (2015-2016)

To comprehend methane emissions better, polar plots were used to plot methane mole fraction measured $\delta^{13}\text{C}$ and calculated isotopic source signature for each site. For source isotopic signatures, the plots were made by only considering samples with methane mole fractions 50 ppb higher than the background for the long-term methane measurements in Kuwait for 2015 and 2016, otherwise the source calculations would have a very large error. The plots show calculated $\delta^{13}\text{C}$ -CH₄ source signatures by wind direction ranging from -67 to -42 ‰.

8.3.1 Al-Mutla site

Ninety-two air samples were collected in Al-Mutla. The polar plot in Figure 8.11 shows the mean methane mole fractions (ppm) by wind speed and wind direction for the period of 2015-2016. The plot indicates northwest as the most common wind direction and is usually associated with background levels of CH₄. The highest methane mole fraction was observed in the southern sector with a maximum value of 2.5 ppm.

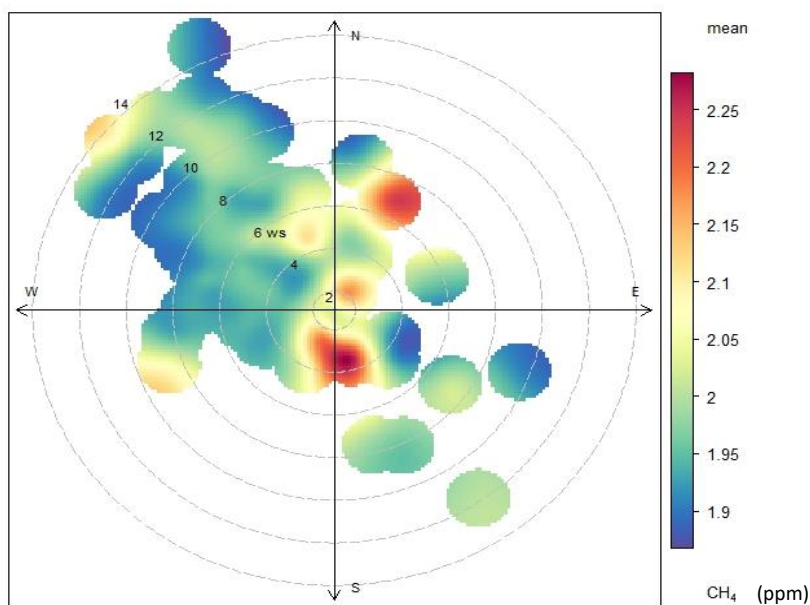
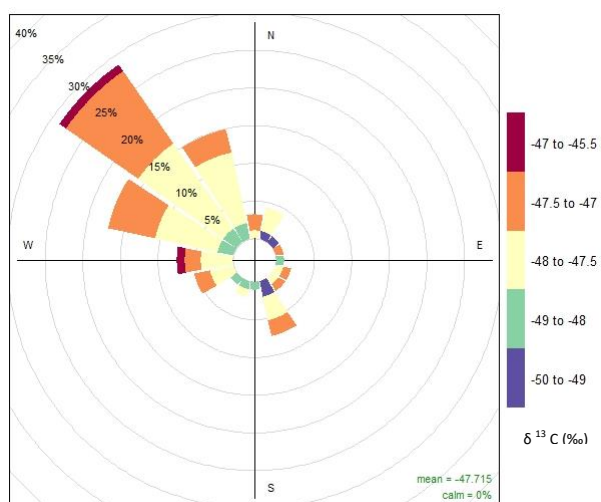


Figure 8.11 Polar plot of methane mole fractions (ppm) recorded for 2015 and 2016 in Al-Mutla site, Kuwait

Possible sources are car parking in the police station less than 100 m away or the active (Al-Jahra) landfill located approximately 6 km south of the sampling site. Figure 8.12A shows, the high CH_4 mole fractions in the SSE sector are associated with the most ^{13}C depleted value of -49.22‰ , which would suggest a biogenic source such as landfill rather than vehicles. $\delta^{13}\text{C}\text{-CH}_4$ measurements were plotted against wind direction (Figure 8.12B). Most of the source signatures ranged from -60 to -50‰ . NOAA back trajectories show that the local wind system in Kuwait is dominated airflow from the north to northwest sector. These air masses pass through different regions (Iraq, Syria, Jordan and other countries) before reaching Kuwait. Concentrations were low in this sector so probably not usually reflecting large emissions from these countries.

A)



B)

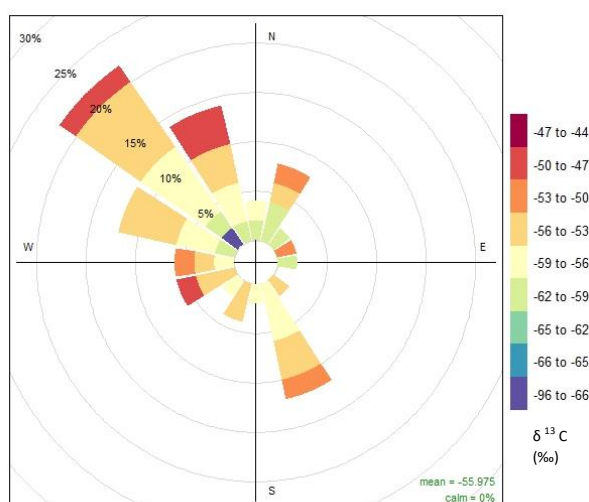


Figure 8.12 A) Measured $\delta^{13}\text{C}$ values, B) Calculated $\delta^{13}\text{C}$ source signatures split by wind direction for 2015 and 2016

8.3.2 Khaldiya site

A total of 92 samples were collected from this site. The highest methane mole fraction recorded from this site was 2.6 ppm. Slow wind and calm conditions can give rise to a buildup of high concentration in the immediate vicinity of the sources (Al-Azmi *et al.* 2009). This site was associated with low wind speed, constantly below 3 m/s (Figure 8.13). Most high methane values come from the south to southwest sector. Four landfills are located to the Southwest, one sewage treatment plant to the West and Kuwait airport is 3 km in a southerly direction.

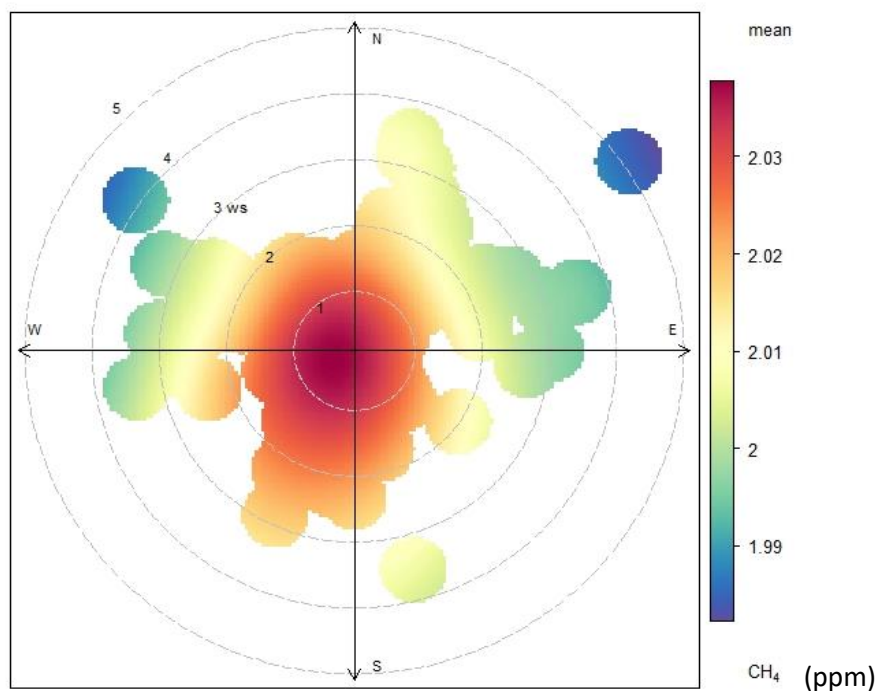
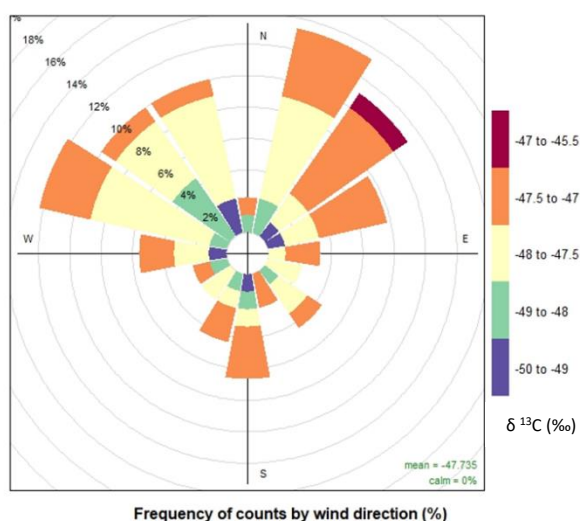


Figure 8.13 Polar plot of methane mole fraction (ppm) recorded for 2015 and 2016 in Khaldiya

Figure 8.14A, shows the measured $\delta^{13}\text{C}$ values for this site. Figure 8.14B, shows the calculated the $\delta^{13}\text{C}$ source signatures. This site is located next to the largest car park in the Sciences college of Kuwait University.

A)



B)

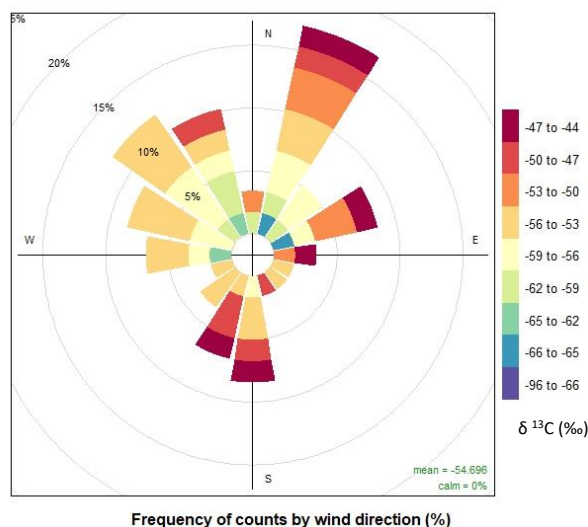


Figure 8.14 A) Measured $\delta^{13}\text{C}$ values, B) Calculated $\delta^{13}\text{C}$ source signatures split by wind direction for 2015 and 2016 at Khaldiya.

8.3.3 Fahaheel site

A total of 84 air samples were collected from this site. The maximum value of methane mole fraction recorded in this site was 2.8 ppm which is the highest value for all three sites. The air masses often cross the city with methane added by city emissions en route to the sampling site (Figure 8.15). The polar plot clearly demonstrates a sea air mass influence from the East sector with lower values of methane mole fraction whilst the SW to WNW direction is characterised by highest values of methane mole fraction.

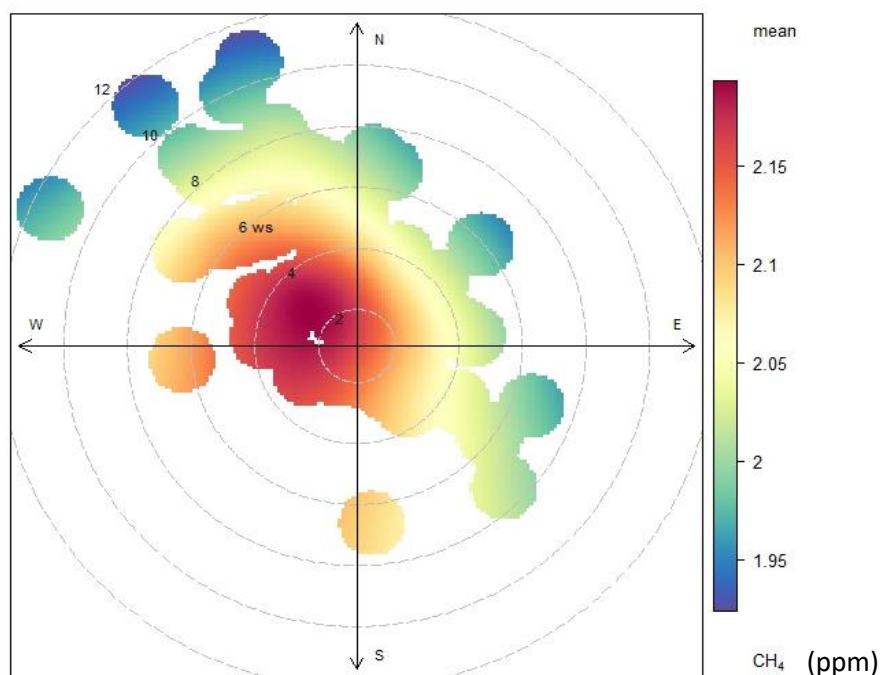
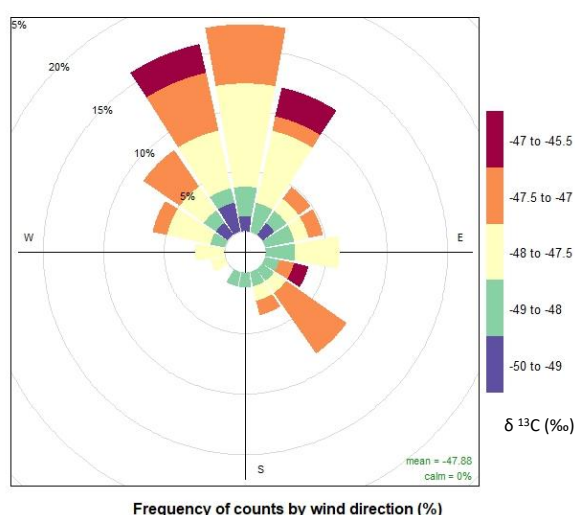


Figure 8.15 Polar plot of methane mole fraction (ppm) recorded for 2015 and 2016 in Fahaheel site, Kuwait

Figure 8.16A, shows the isotopic measurements of methane at this site for 2015 and 2016. When the wind is from the W to NNW, the air masses have passed through different regions and Kuwait City and been loaded by methane emissions from different sources. According to the back-trajectory studies of Kuwait the dominant wind direction is from the northwest sector but also there are frequent winds from the south to southeast coming from Saudi Arabia and the Arabian Gulf and this is apparent at the Fahaheel site.

A)



B)

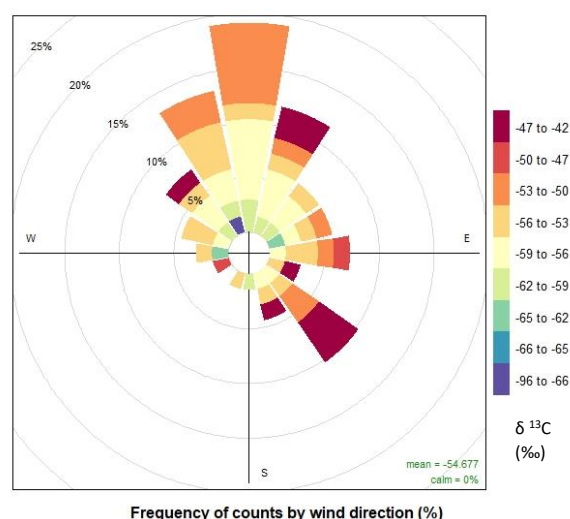


Figure 8.16 A) Measured $\delta^{13}\text{C}$ values, B) Calculated $\delta^{13}\text{C}$ source signatures split by wind direction for 2015 and 2016 at Fahaheel.

Figure 8.16B, show that the N and NNW sectors were dominated by $\delta^{13}\text{C}$ depleted signatures ranging from -60.5 to -50‰, which might have been related to the sewage treatment plant and landfill. The East to South sector has more $\delta^{13}\text{C}$ -enriched signatures, which could be due to the oil refineries that are located in this direction 1 to 2 km away

8.4 Miller -Tans Plots

The Miller-Tans approach can be used for calculating isotopic signatures of a source mix from atmospheric measurements of $\delta^{13}\text{C}$. This is similar to the two end-member mixing model of Keeling (Keeling, 1961) but allows for a time-varying background of $\delta^{13}\text{C}$ and for evaluating time series where background is changing (Miller & Tans, 2003). This model is discussed in detail in chapter 3. This approach is preferable to use when either or both the background concentration or isotopic ratio of CH_4 is changing over time. The “Keeling plot” approach assumes a constant background concentration and $\delta^{13}\text{C}$ of CH_4 , which is violated when analyzing a time-series. (Miller & Tans, 2003). The isotopic signature of the source mix was calculated for all three sites combined during 2015 and 2016 and a background value for each season for all three sites in Kuwait was calculated. Figure 8.17 shows the source signature calculated using a Miller-Tans plot and the overall $\delta^{13}\text{C}$ source mix for Kuwait is $-55.9 \pm 0.7\text{‰}$. Figure 8.18 shows individual plots for the three sites.

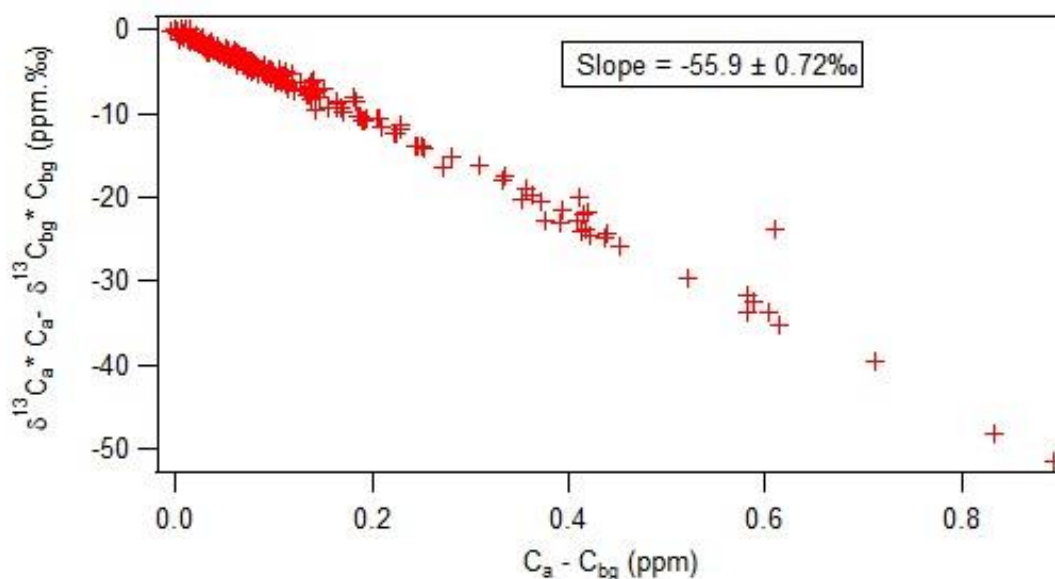
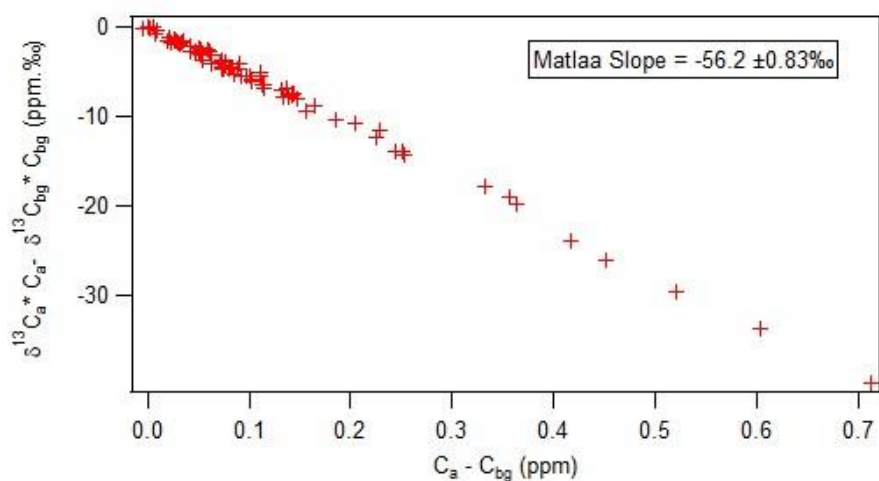
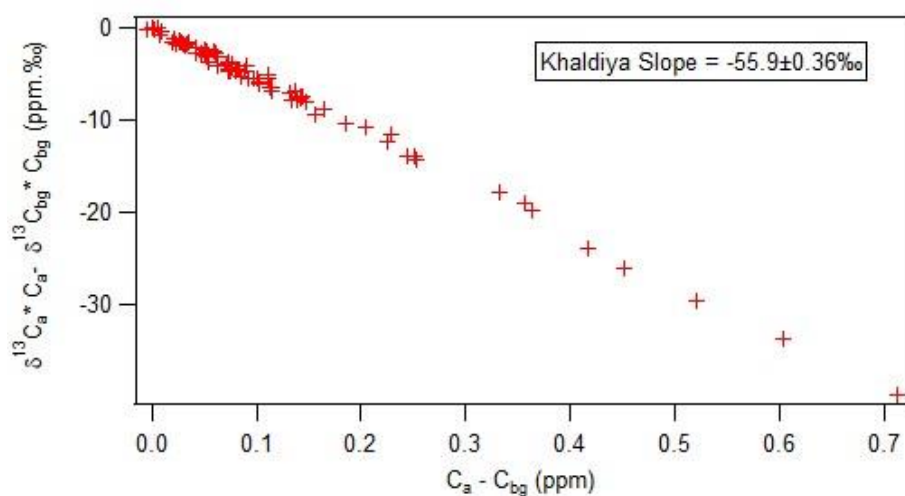


Figure 8.17 Miller-Tans plot based on all the isotopic values measured and the background values for each season.

a)



b)



c)

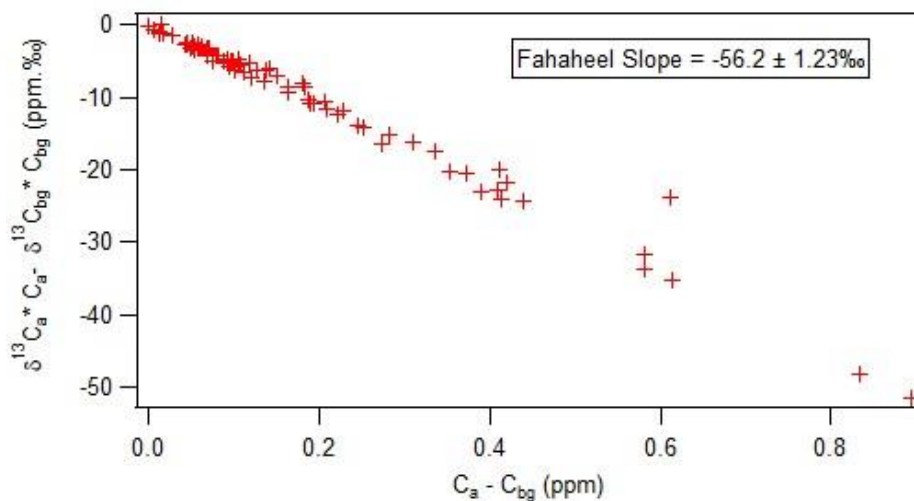


Figure 8.18 Miller-Tans plots for each site a) Al-Mutla, b) Khaldiya and c) Fahaheel for 2015 and 2016 in Kuwait.

8.5 Diurnal Measurements in Al-Rabya

Several diurnal studies were carried out during 2016 from the Al-Rabya urban area in Kuwait City in order to understand methane local sources by determining the isotopic signature of overnight build-up profiles.

Detailed weather forecasts were studied before choosing the sampling periods. Clear skies and low wind speed were preferred. Air samples were collected in 3L Tedler bags every 2 hours at 6-meter height on a terrace of the house. All the air samples were shipped to Royal Holloway University of London to measure with a Picarro G1301 CRDS analyser. The carbon isotope ratio ($\delta^{13}\text{C}$) was measured in triplicate to high precision ($\pm 0.05\text{‰}$) by GC-IRMS (see chapter 3).

Figure 8.19 shows the location of the Al-Rabya residential area and the major sources of air emissions in Kuwait State. The aim of this study was to use atmospheric trace gas concentration and isotopic measurements to identify major local methane emitters and regional build-up in the course of the diurnal cycle. Under strong nighttime inversion situations, the trace gas concentration increases and the $\delta^{13}\text{C}\text{-CH}_4$ changes if the ground level sources are characterized by different isotopic ratio (Levin *et al.* 1999; Al-Azmi *et al.* 2009).

The 5-day HySplit back trajectories show air masses from different regions (Figures 8.2, 8.3, 8.4).

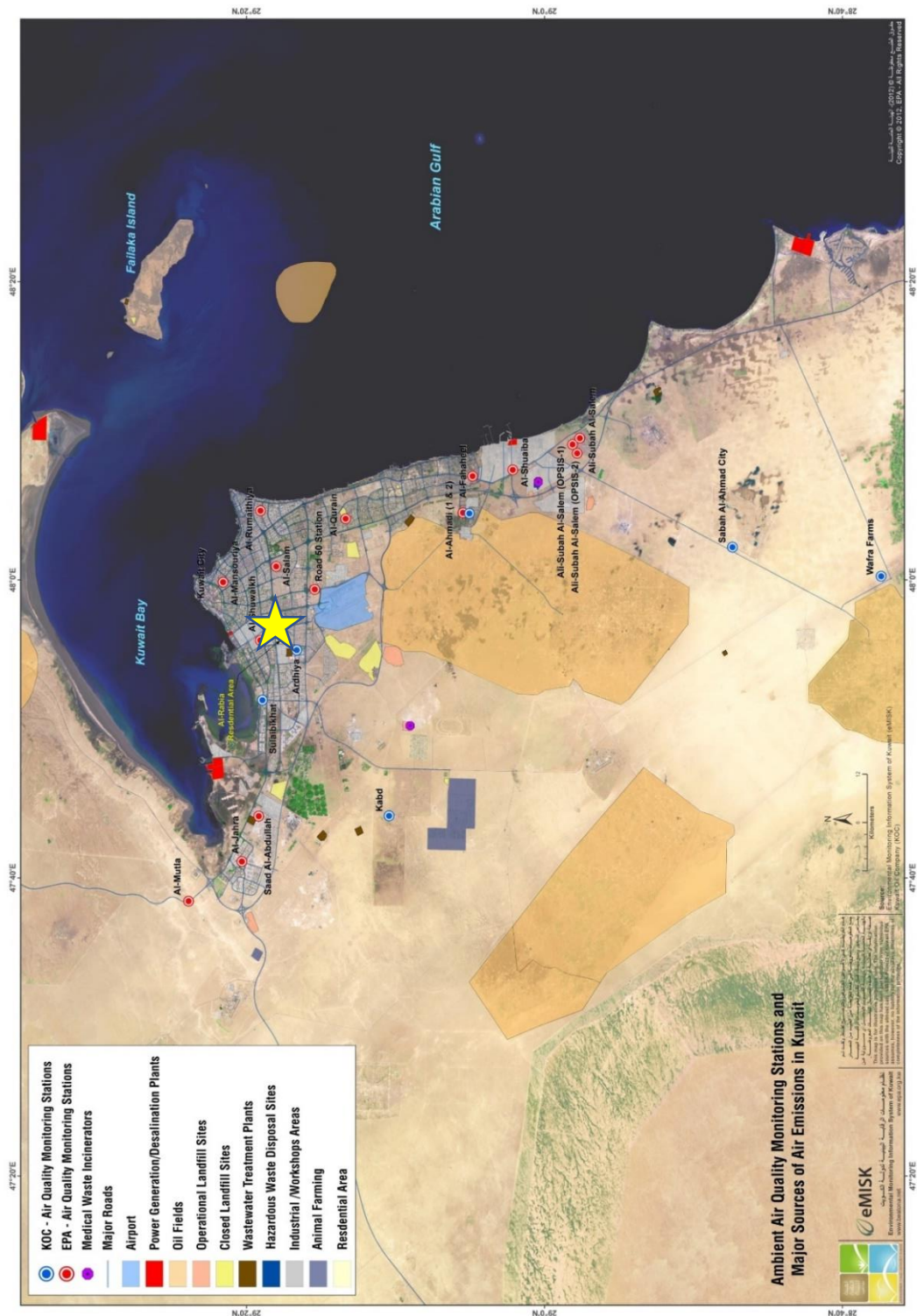


Figure 8.19 Location of Al-Rabya Residential Area (yellow star) and the major sources of air emissions in Kuwait (Source: eMISK, 2017)

8.5.1 5th – 6th January 2016

The first diurnal study was in winter 2016 and ten air samples were collected every 2 hours over 24 hours in the Al-Rabya urban area with coordinates 29°17'80.2'N and 47°56'19.4'E. In winter, the boundary layer height is much lower than summer allowing methane build-up overnight (Levin *et al.* 1999; Zazzeri *et al.* 2015). The Keeling plot in Figure 8.20 shows an intercept of $-56.1 \pm 0.9\text{‰}$ based on the collected air samples. The isotopic signature suggests a dominance of methane from biogenic emission such as landfills. The backward trajectories for 72 hrs in figure 8.21 show an air mass coming across Saudi Arabia. This southerly wind crossed the southern part of Kuwait that included most of methane sources such as landfills and refineries. Figure 8.22 shows the build-up of methane overnight with a maximum mole fraction of 5.7 ppm at midnight and dissipation in the morning as the air is mixed. This might be according to the drop of the wind speed from 1.7 m/h to 0.7 m/h (www.met.gov.kw).

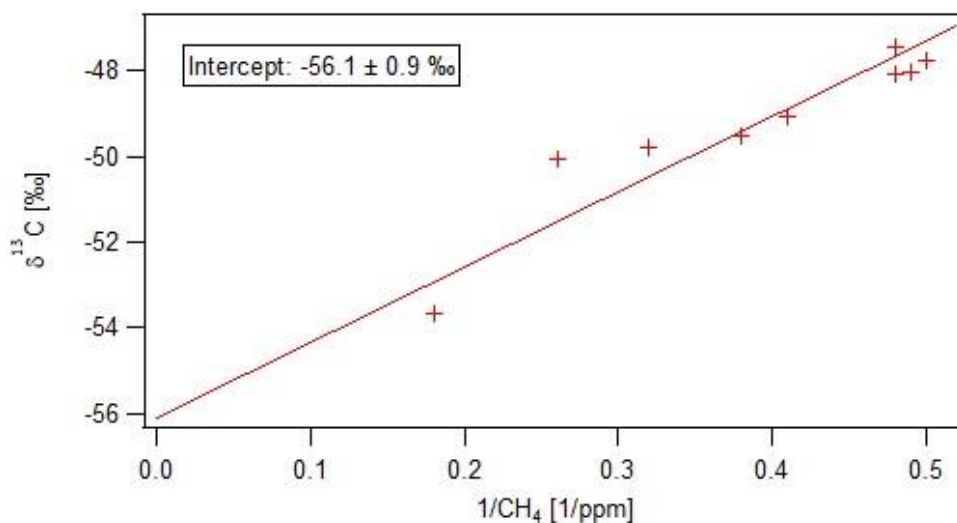


Figure 8.20 Keeling plot based on samples collected in Al-Rabya area on 5th – 6th January 2016.

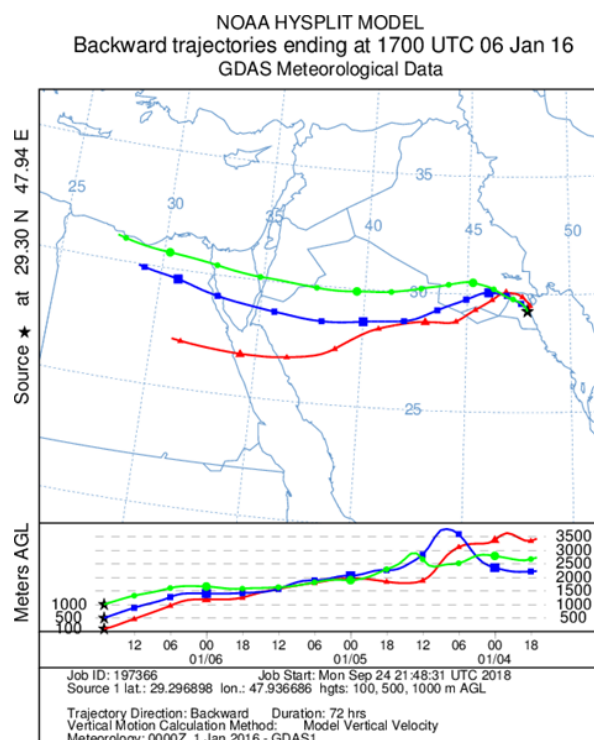


Figure 8.21 Backward trajectory model for Al-Rabya for air moving on 6th January 2016 calculated for a duration of 72 hrs air movement.

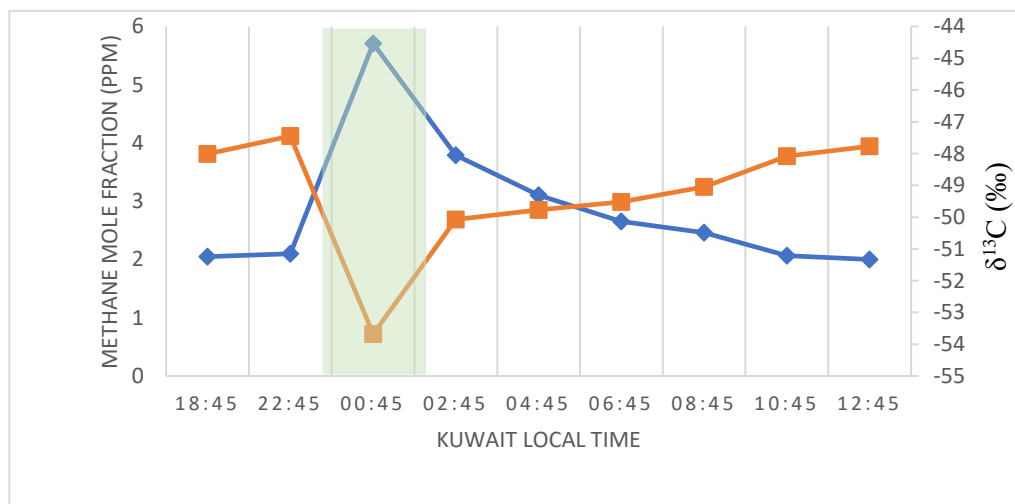


Figure 8.22 Methane mole fractions and $\delta^{13}\text{C}$ for air collected in Al-Rabya on 5th to 6th January 2016, blue line represents methane mole fractions, orange line is $\delta^{13}\text{C}$ and green shaded zone shows that the highest CH_4 mole fraction sample has ^{13}C -depleted signature.

8.5.2 18th –19 July 2016

The second diurnal sampling took place on 18th – 19th July 2016. Twelve air samples were collected every 2 hours. The sampling started at 3 pm with an easterly wind direction which changed later to a southerly wind in early morning with maximum methane mole fraction 4.8 ppm and lowest $\delta^{13}\text{C}$ of $-54.1 \pm 0.04\text{‰}$ (Figure 8.23). This may be due to the largest landfill in Kuwait (Jleeb Al-Shuyoukh) that is located south of Al-Rabya area. Figure 8.24 shows the intercept of Keeling plot of $-58.2 \pm 0.4 \text{‰}$ that is indicative of a biogenic source. According to the backward trajectories shown in Figure 8.25 based on the previous 72 hrs, air masses were coming from Syria and crossing Iraq.

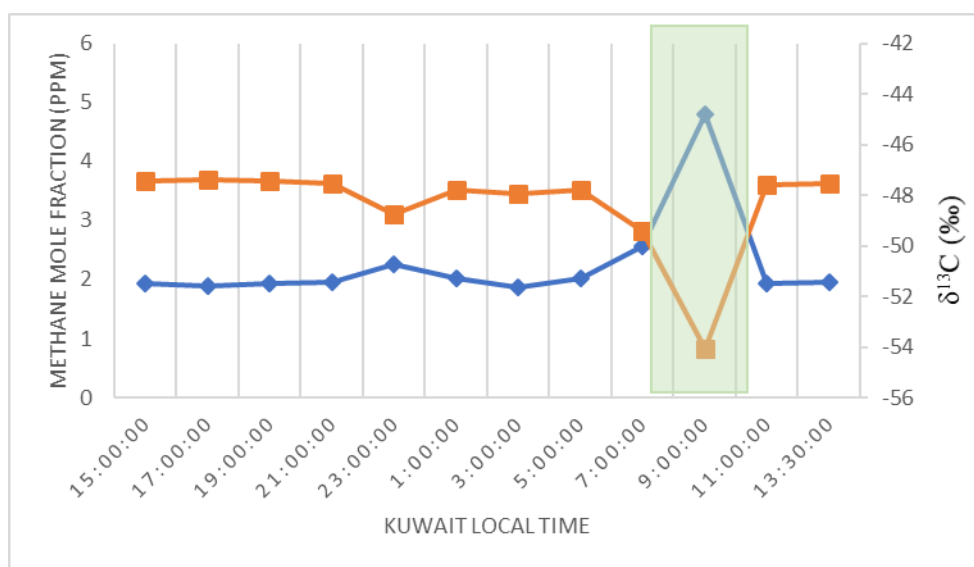


Figure 8.23 Methane mole fractions and $\delta^{13}\text{C}$ on 18th to 19th July 2016 at Al-Rabya, blue line represents methane mole fractions, orange line is $\delta^{13}\text{C}$ and green shaded zone shows that the highest CH_4 mole fraction sample has ^{13}C -depleted signature.

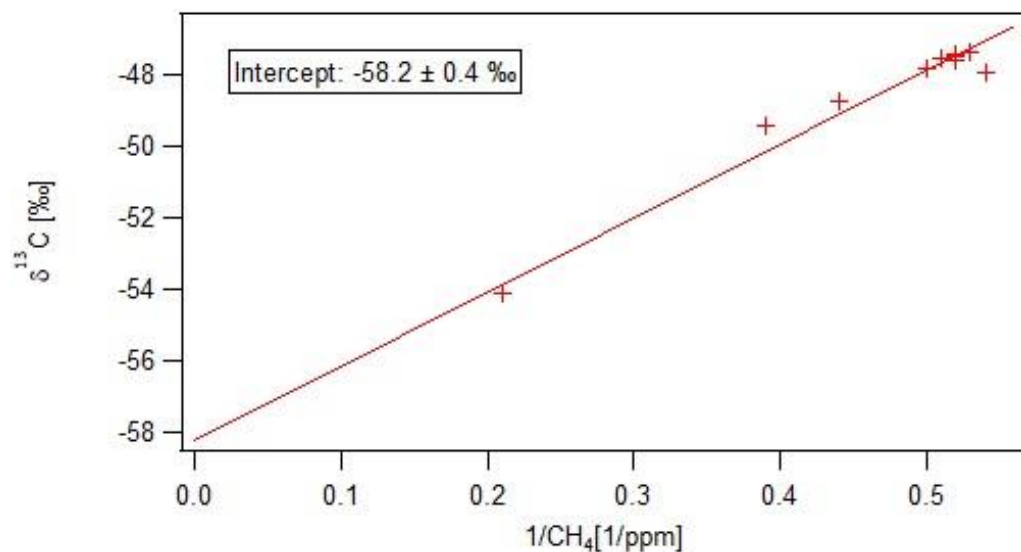


Figure 8.24 Keeling plot based on samples collected in Al-Rabya area on 18th – 19th July 206

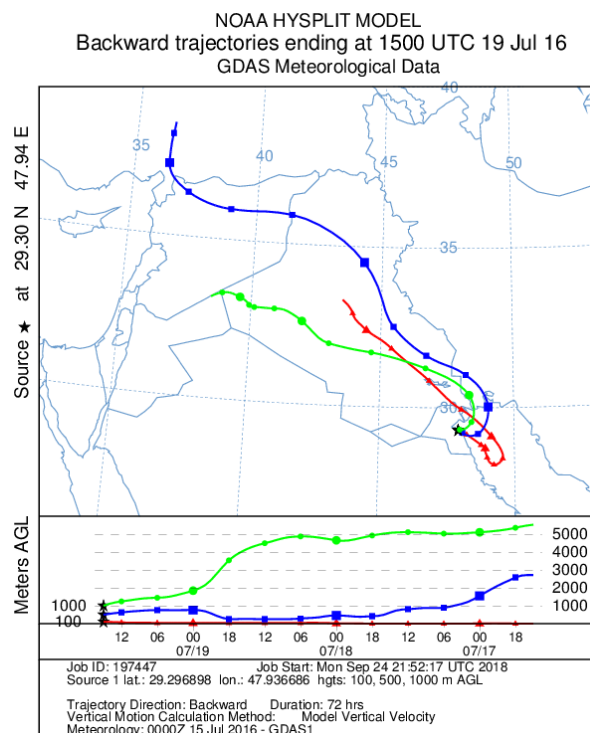


Figure 8.25 Backward trajectory model for air a moving at Al-Rabya on 19th July, calculated for a duration of 72 hrs air movement.

8.5.3 17th – 18th October 2016

The last diurnal study was carried out in autumn 2016. Twelve air samples were collected every 2 hours for 24 hours. Figure 8.26 shows the Keeling plot based on the samples giving a signature of $-59.3 \pm 0.3\text{‰}$, which is more ^{13}C -depleted relative to the previous diurnal studies in the same year 2016. The study was started at 3 pm when the wind direction was N to NW for the first four hours then it turned to a southerly wind direction. HySplit backward trajectories for 72 hrs show in Figure 8.27 that the air mass was coming from a south direction. This southerly air mass during late to early morning of the next day contained methane highly depleted in ^{13}C . The nocturnal temperature inversion led to accumulation of methane overnight to reach the maximum values of 6.9 ppm, but the methane dissipated in the late morning. Figure 8.28 shows the diurnal methane mole fraction and $\delta^{13}\text{C}$ values recorded on 17th and 18th of October 2016, which can be attributed to a prevalent biogenic component in methane emissions such as landfills.

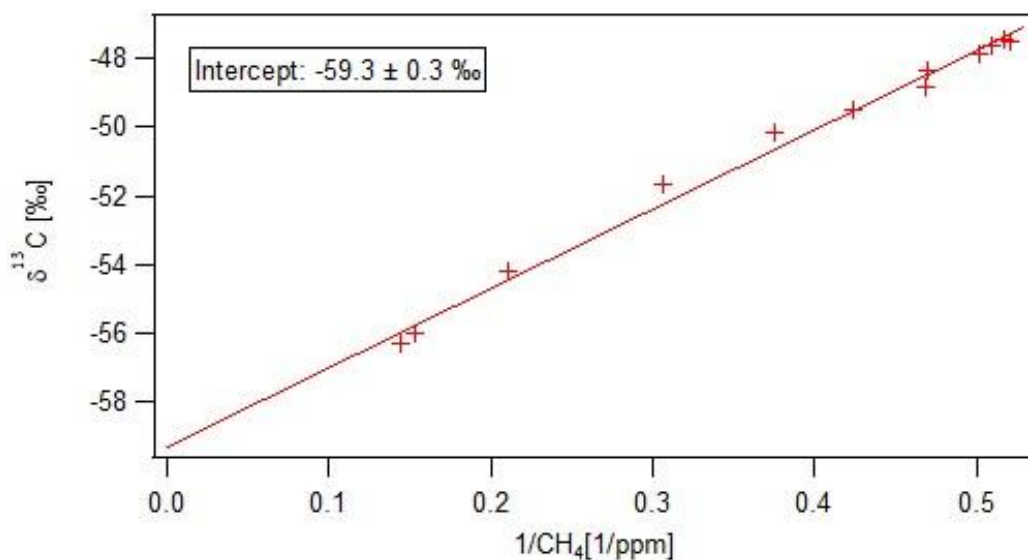


Figure 8.26 Keeling plot based on samples collected in Al-Rabya area on 17th – 18th October 2016

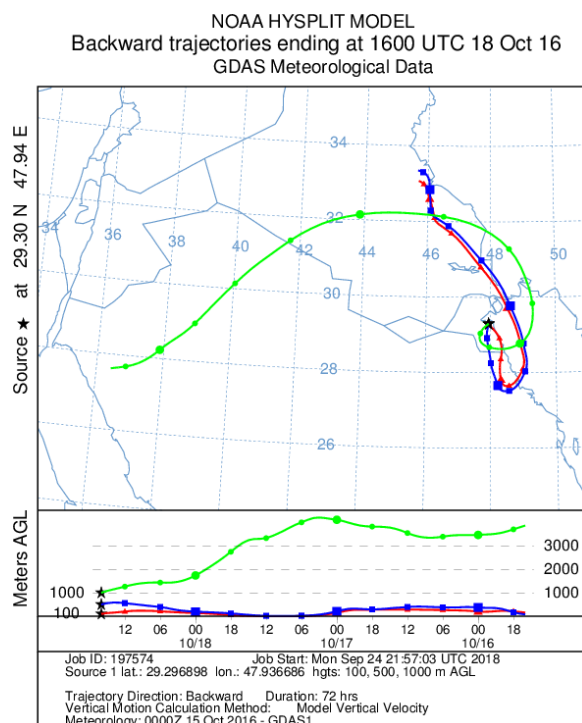


Figure 8.27 Backward trajectory model for Al-Rabya calculated for 72 hrs air movement.

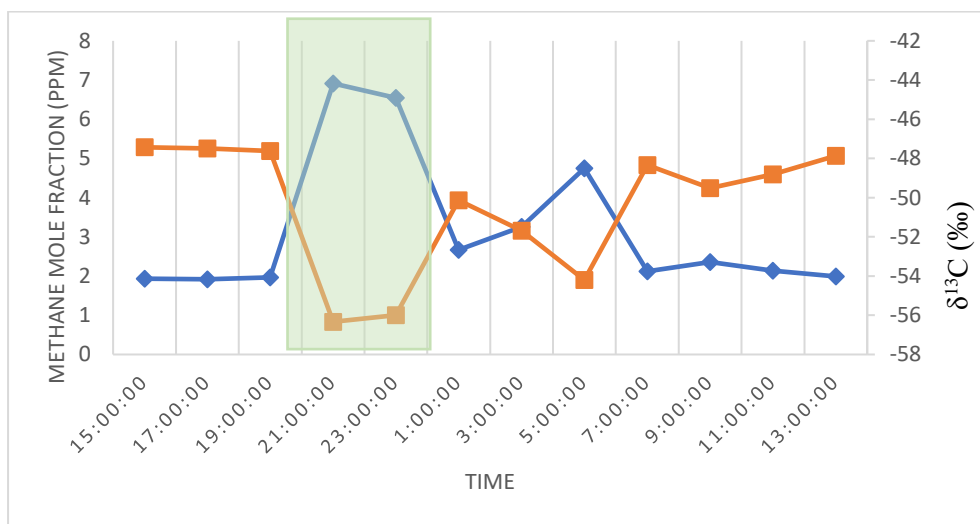


Figure 8.28 Methane mole fractions and $\delta^{13}\text{C}$ measured in Al-Rabya 17th – 18th October 2016, blue line presented methane mole fractions, orange line is $\delta^{13}\text{C}$ and green shaded zone shows that the highest CH_4 mole fraction sample has a ^{13}C -depleted signature.

8.6 Summary

The aim of this chapter is to study the weekly and diurnal measurements of methane in Kuwait to identify major local methane emitters and regional buildup. By calculating the air movement during 2015 and 2016, this study found the air masses are coming mostly from the NW sector which passing through Jordan, Syria and Iraq. Three diurnal studies in Al-Rabya residential area were carried out during 2016. These diurnal measurements showed that methane mole fraction built up overnight and after dawn the inversion breaks up and mixing occurs. This is similar to other studies, e.g. in London where Fisher *et al.* (2006) and (Zazzeri 2015) showed the methane mole fraction built-up over night for a period 22:00 until 06:00. Generally, the high methane mole fractions correspond to depletion in ^{13}C and are associated with a southerly wind direction in this study. Table 8.2 summarises all the diurnal studied in Al-Rabya area.

<i>days</i>	$\delta^{13}\text{C}$ (‰)	<i>Maximum CH₄ (ppm)</i>
-------------	---------------------------	-------------------------------------

<i>5th – 6th January 2016</i>	-56.1±0.9	5.7
---	-----------	-----

<i>18th -19th July 2016</i>	-58.2±0.4	4.8
---	-----------	-----

<i>17th–19th October 2016</i>	-59.3±0.3	6.9
---	-----------	-----

Table 8.2 $\delta^{13}\text{C}$ and methane mole fraction values for the diurnal studies that were carried out in Kuwait State during 2016.

Diurnal measurements of methane $\delta^{13}\text{C}$ have been studied by many authors (Lowry *et al.* 2001; Fisher *et al.* 2006; Townsend-Small *et al.* 2012; Zazzeri *et al.* 2017). In central London recent studies have shown the isotopic composition of the methane is $-45.7 \pm 0.5\text{‰}$ (Zazzeri *et al.* 2017). Zazzeri *et al.* (2017) confirmed that this source mix is due to the dominance of fossil methane emissions in the methane budget in central London.

Townsend-Small *et al.* (2012) studied the isotopic measurements of methane in Los Angeles and found that the isotopic composition of the source mix is -41.5‰ . This study concluded that the major source of CH_4 in Los Angeles is leakage of fossil fuels such as geologic formations, natural gas pipelines and oil refining. Similar results were shown by Moriizumi *et al.* (1998). Moriizumi *et al.* (1998) found that $\delta^{13}\text{C}$ -40.8‰ for Nagoya, Japan. They also related this ^{13}C -enrichment to natural gas sources.

The results of this study are completely different. The results of this long-term study show a depleted ^{13}C source signature for Kuwait State of -55.9‰ . This study was carried out for two years 2015 and 2016 and confirms that the prevalence of biogenic methane emissions such as landfills in the overall methane budget in the State of Kuwait.

C_{CHAPTER 9}

D_{ISCUSSION}

9. Discussion

This chapter will give an overview of an international inventory of anthropogenic methane emissions, the Emissions Database for Global Atmospheric Research (EDGAR) and a local inventory of Kuwait's initial national communications under the United Nations Framework Convention on Climate Change (UNFCCC). Methane emissions estimations in both inventories comply with the Intergovernmental Panel on Climate Change (IPCC) Guidelines for National Greenhouse Gas Inventories (2006 Guidelines). Methane mole fraction in Kuwait is compared with data from the National Oceanic and Atmospheric Administration (NOAA) Global Monitoring Divisions (GMD) which measures the atmospheric distribution and trends of the three main long-term drivers of climate change, carbon dioxide (CO_2), methane (CH_4), and nitrous oxide (N_2O), as well as carbon monoxide (CO). GMD produce a regional and global-scale, long-term measurement record with high-accuracy calibrated measurements. In this study, methane measurements are compared to flask measurements from a surface observation site (NOAA), and to XCH_4 retrievals from the Greenhouse gases Observation SATellite (GOSAT) and (SCIAMACHY).

9.1 Kuwait Methane Measurements Compared to NOAA Baseline Observatories

The NOAA measurement program includes around the clock measurements at 4 baseline observatories and 8 tall towers as well as greenhouse gas measurements in air samples collected from 204 sites in 45 countries. Unfortunately, there is a big gap for greenhouse gases measurements in the Middle East region as shown in Figure 9.1A. In this study, the closest NOAA/ESRL/GMD station that measures greenhouse gases is used to identify long-term trends and seasonal variability of methane emissions. Figure 9.1B shows the location of this site at 29.9646°N and 35.0605°E . Air samples are collected weekly from this site in flasks from 151 metres above sea level (2 samples). Methane mole fractions have been measured since 27th of November 1995 at this station. The long-term measurements of methane mole fraction in this study for 2015 and 2016 were compared to this

NOAA/ESRL/GMD/CCGG station. Figure 9.2 show the long-term measurements of methane mole fraction (ppm) from the three sites in Kuwait and the NOAA site for the similar period 2015 and 2016.

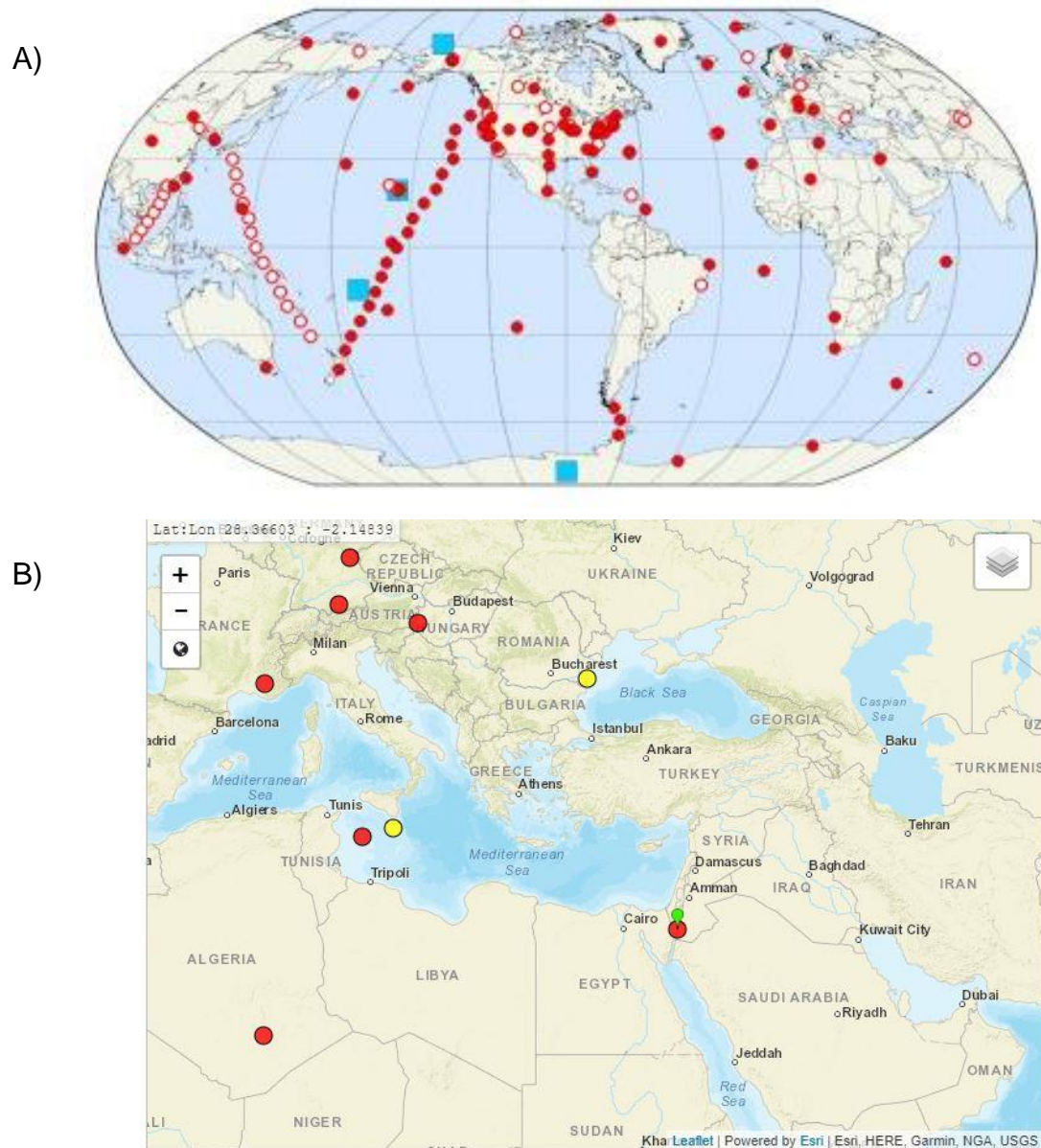


Figure 9.1 A) NOAA greenhouse gas reference network sites, B) NOAA/ESRL/GMD station location, that is the only station in the Middle East and the closet to Kuwait State. Blue squares represent NOAA in situ observatories, hollow red circles are terminated and red circles current flasks collection. Source: NOAA.gov

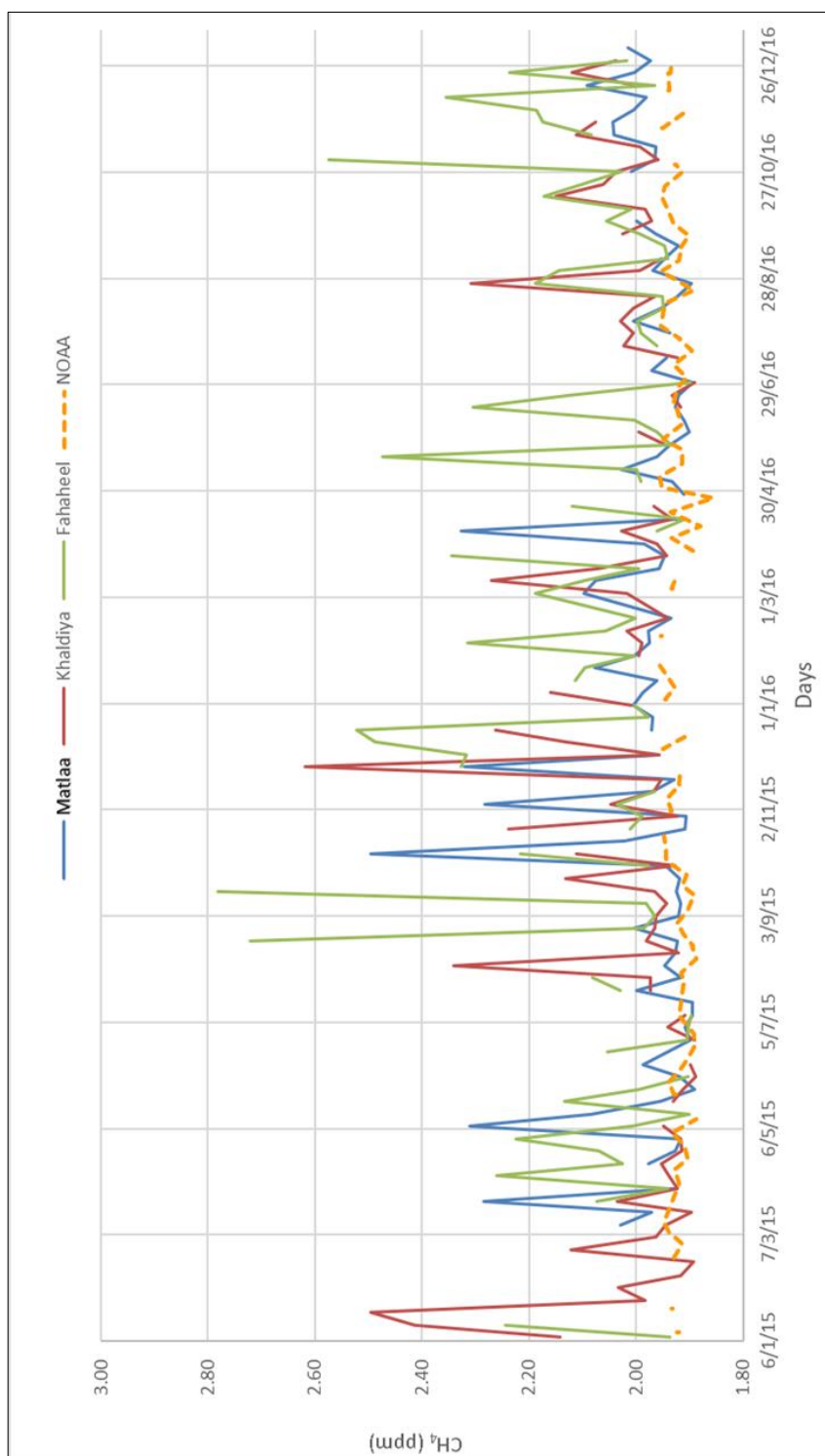


Figure 9.2 Comparison of long-term measurements of three sites in Kuwait and the closest NOAA site.

The average background methane mole fraction for the NOAA site is 1.89 ppm, which is similar to the Kuwait background 1.90 ppm for the period 2015 and 2016. Figure 9.2 shows the trend of methane mole fraction and the seasonal variation for all sites. Continuous measurements of these gases provide great detail in their long-term trends, seasonal and short-term variations, and diurnal cycles. In summer, the Kuwait sites and the NOAA site show the minimum readings in May and June and build-up in winter (November) as is shown in Figure 9.2. In this study there is a good agreement between the background measurements in 2015 and 2016 at all 3 Kuwait sites and the atmospheric observations of NOAA over the same period.

9.2 Satellite Observation of Atmospheric Methane

Emission inventories use “bottom-up” estimates of activity rates and emission factors for individual methane sources which are generally much larger than the “Top-down” observations that are from direct measurements of air (Nisbet *et al.* 2014). SCIAMACHY was the first satellite instrument that measured the greenhouse gases (CH₄ and CO₂). SCIAMACHY aimed to understand the variations of methane in time and space. This imaging spectrometer's primary mission objective was to perform global measurements of trace gases in the troposphere and in the stratosphere.

Figure 9.3 shows the global maps of atmospheric methane for the period 2003 to 2005. The major methane source regions are shown, such as wetlands (e.g. tropics) and rice fields (e.g. China). It clearly shows that the Southern Hemisphere is lower in methane mole fraction than the Northern Hemisphere (Rigby *et al.* 2008).

Methane SCIAMACHY/ENVISAT

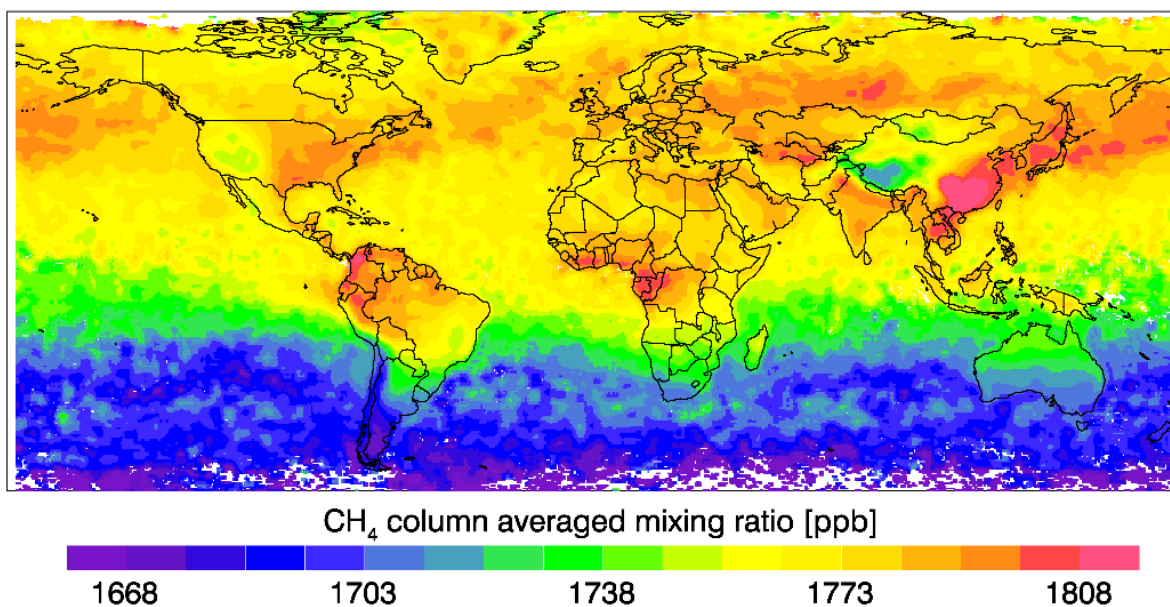
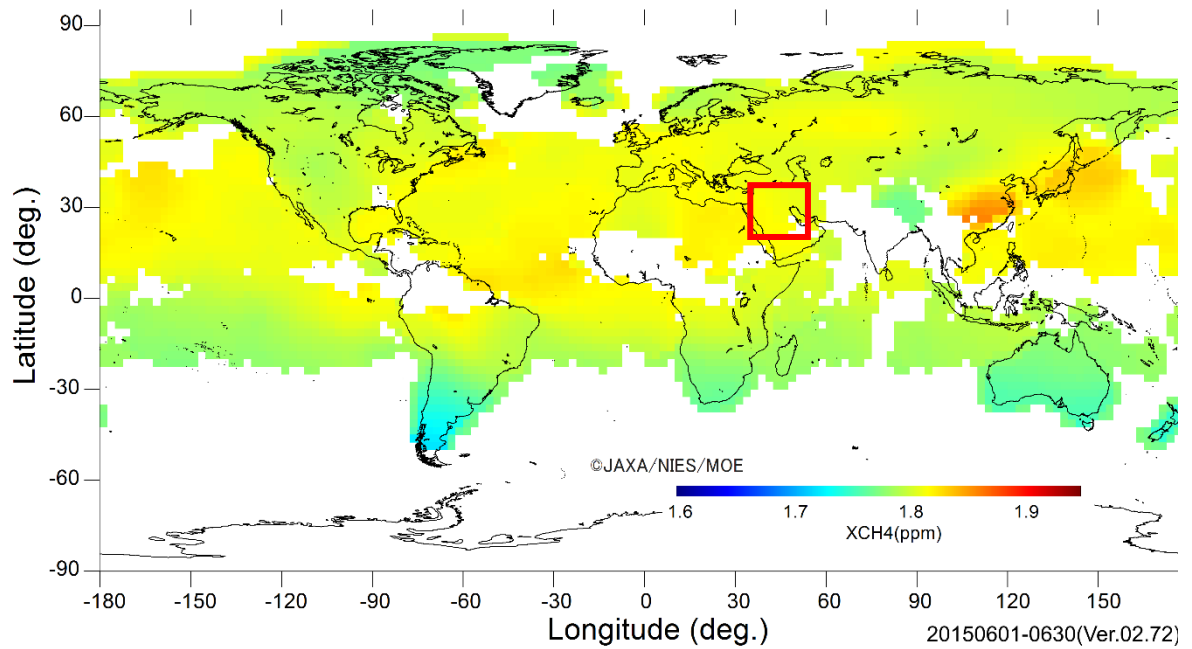


Figure 9.3 Global methane for the period 2003 to 2005. Reference: IUP.uni-bremen.de.

Another satellite observation of atmospheric methane is GOSAT (Greenhouse gases Observing Satellite). GOSAT is a JAXA (Japan Aerospace Exploration Agency) mission within the GCOM (Global Change Observation Mission) programme of Japan. The purpose of the GOSAT Project is to estimate emissions and absorptions of the greenhouse gases such as carbon dioxide (CO₂) and methane (CH₄) on a subcontinental scale and accumulate new knowledge on the global distribution and temporal variation of the greenhouse gases. According to GOSAT, methane growth over the past year (August 2018- August 2017) was 9.9 ppb/yr. Figures 9.4 and 9.5 show the seasonal maps of atmospheric methane for the period 2015 and 2016. Figure 9.4 A and B show methane total column mole fraction (XCH₄) in summer and Figure 9.5 A and B show XCH₄ in the winter season. The region centred on Kuwait does not stand out as a major emissions region, unlike SE China.

A)



B)

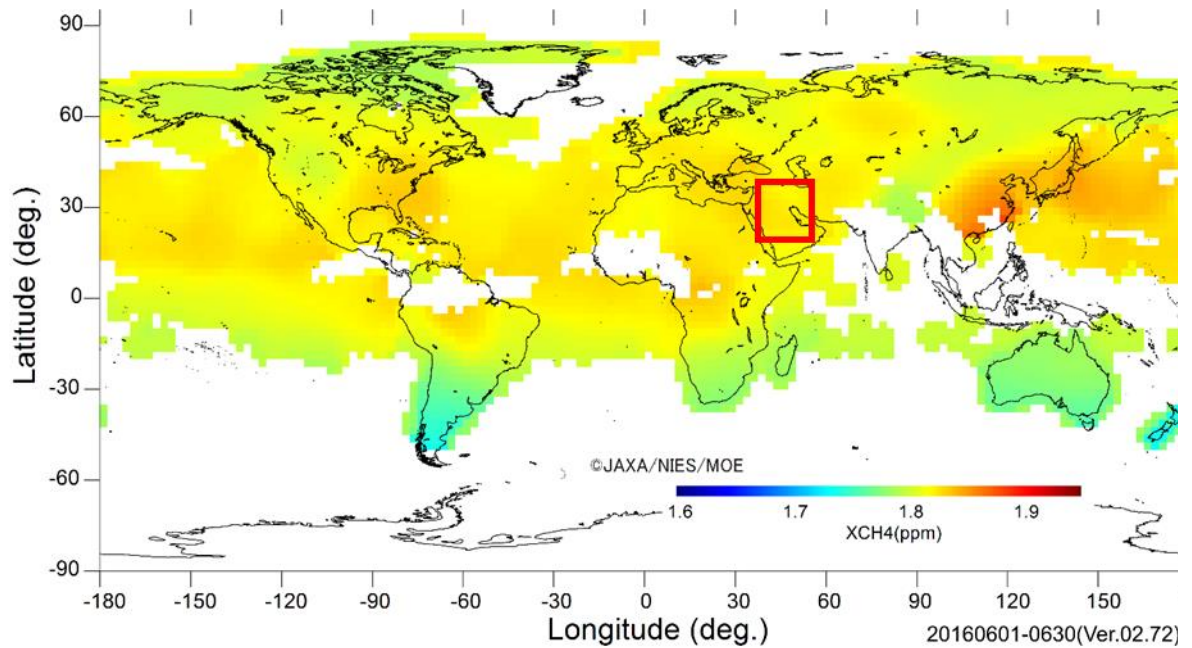
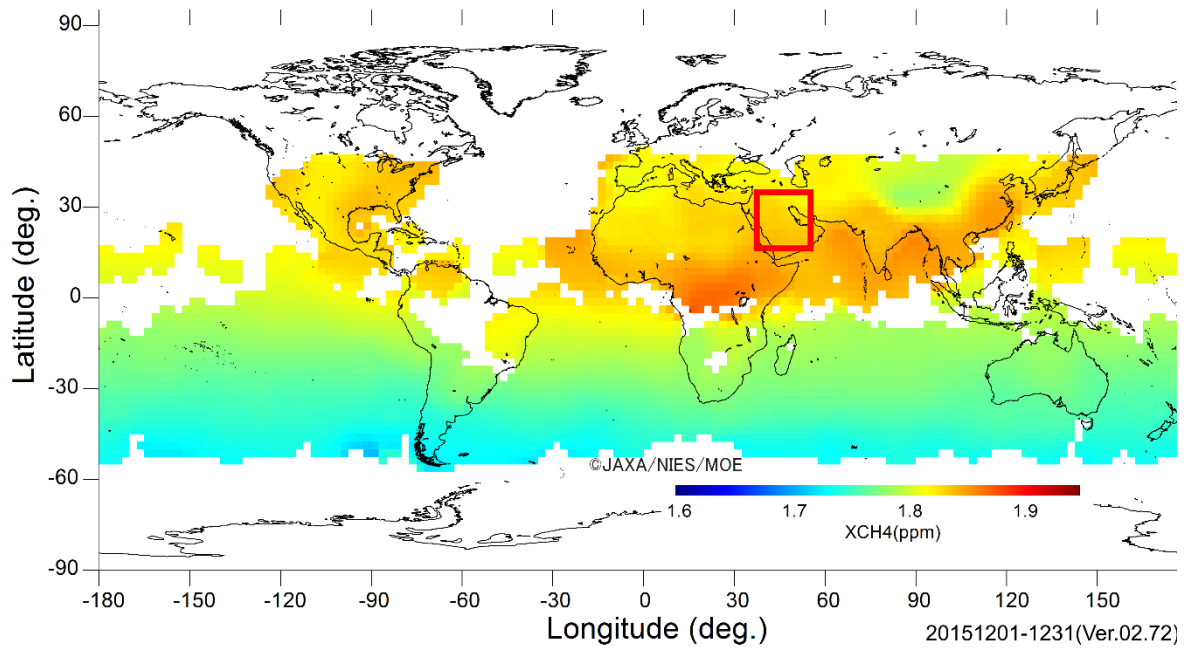


Figure 9.4 GOSAT satellite observation of atmospheric methane For A) Jun, 2015 and B) Jun, 2016. The red box represents Kuwait location
Sources:GOSAT.nise.go.jp

A)



B)

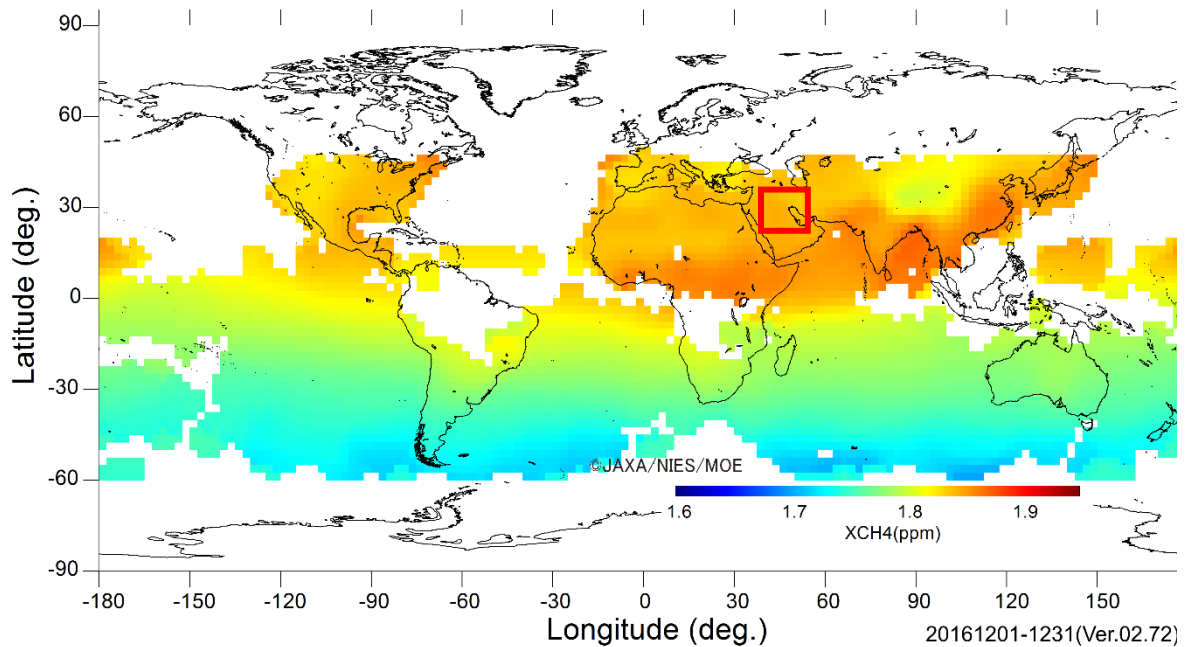


Figure 9.5 GOSAT satellite observation of atmospheric methane For A) DEcember, 2015 and B) DEcember, 2016. The red box represents Kuwait location Sources:GOSAT.nise.go.jp

GOSAT maps show minimum methane mole fractions in early to mid-summer (May-July) and maximum in late autumn to winter (November to February). Both NOAA and GOSAT data show similar seasonal changes, though these are slightly different from one another. GOSAT methane column concentrations are slightly lower than the NOAA observation data and the measurements of this study for the period of 2015 and 2016. GOSAT measurements show smaller values by 40 ppb than those based on methane measurements at the surface level such as NOAA, not surprising as the satellites are measuring total column methane. Concentrations become lower with altitude as it is dispersed in the air (GOsat.nise.go.jp). Figure 9.6 shows GOSAT measurements for methane atmosphere concentrations over 10 years.

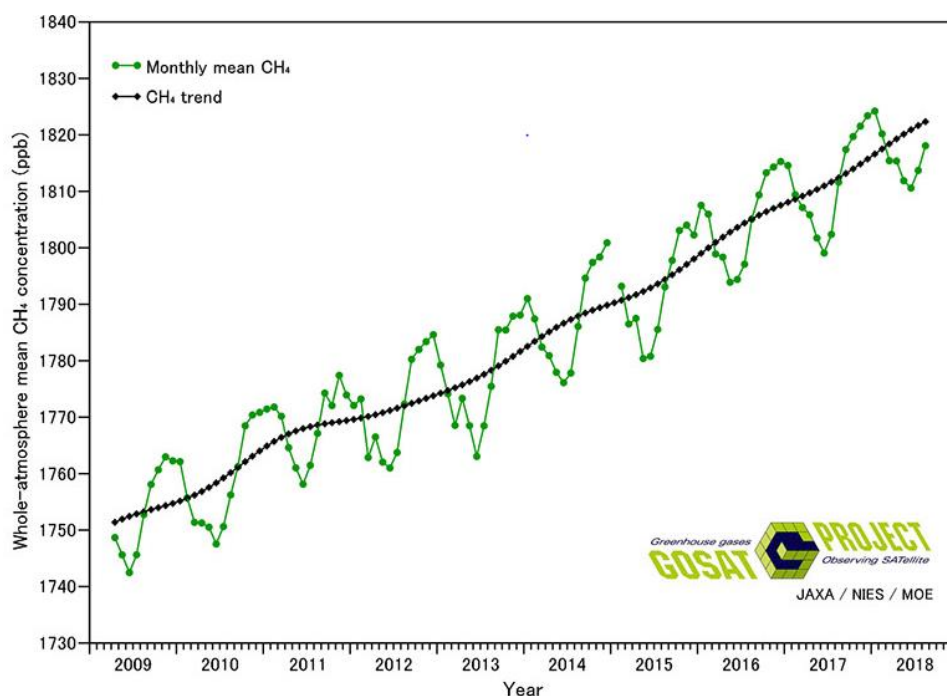


Figure 9.6 Methane concentration measurements data from GOSAT.
Sources: GOSAT.nise.go.jp

9.3 Evaluation of the EDGAR Emissions Database for Kuwait

This section describes anthropogenic emissions in the Emissions Database for Global Atmospheric Research (EDGAR). EDGAR report the major sources of anthropogenic methane emission sources such as: fossil fuel, livestock and solid waste. EDGAR was started in 1993 in order to provide a time-series of global anthropogenic emissions of GHG and short-lived atmospheric pollutants from 1970 to 2008. EDGARv4.3.2 is a comprehensive database of an anthropogenic emission time series from 1970 until 2016 for CO₂ and until 2012 for the other GHGs that use the IPCC sectoral classification. The data are represented per source category and both at country/region levels, as well as on grid basis. The purpose of this database is to serve as a reference database for policy applications to assess potential for emission reductions, and also for scientific studies by providing gridded emissions as input for atmospheric models. The activity data were mostly taken from international statistical sources and the emission factors for greenhouse gases of this data were mostly from the 2006 IPCC Guidelines for National Greenhouse Gas Inventories (IPCC, 2006).

The uncertainty in the EDGAR dataset at a national level might be significant, especially for methane and nitrous oxide (www.EDGAR.jrc.europa.eu). This uncertainty is due to the limited accuracy of international activity data used and of emission factors selected for calculating emissions on a country level. The new version of EGDAR v4.3.2 is used in this study. This version compiles gaseous emissions from the anthropogenic sectors during the time period (1970–2012). This version uses international activity, principally energy balance statistics of IEA (2014) and agricultural statistics of FAO (2014).

Figure 9.7 shows EDGAR estimated methane emissions for Kuwait for all source categories following the IPCC description. Clearly the dominant source of methane emission is fugitive emissions from oil and gas, making up 90% to 96% of the total methane emissions of Kuwait.

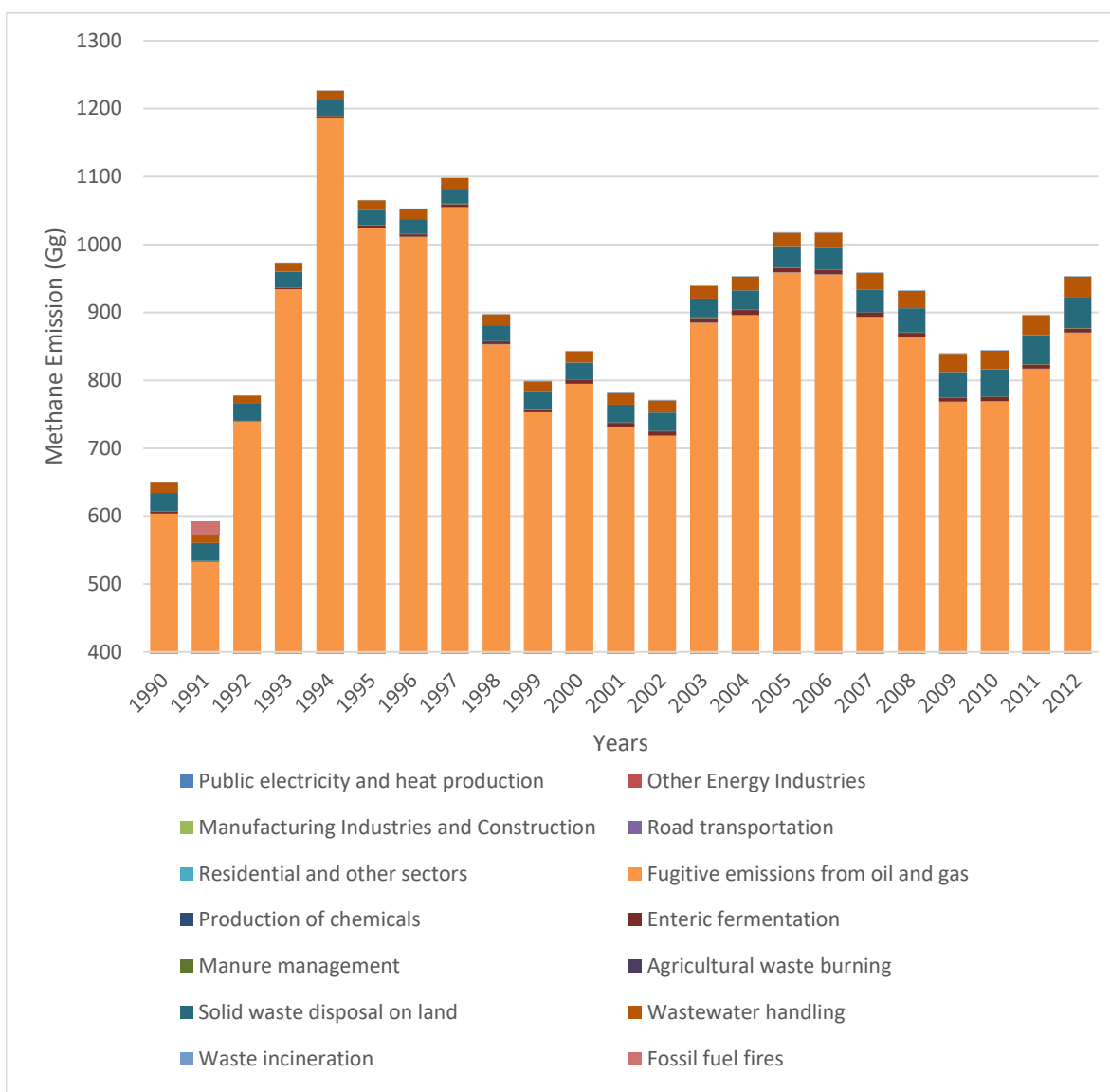


Figure 9.7 EDGAR data for Kuwait methane emissions for all sectors from 1990 to 2012. Source: www.edgar.jrc.europa.eu, 2016.

Figure 9.8 shows the EDGAR estimated total methane emissions for all source categories in Kuwait and other countries in the region such as Saudi Arabia, Qatar and Iran for the period 1970 to 2012. The EDGAR database shows that 70% to 96% of methane emissions for these countries are derived from fugitive emissions from oil and gas sources. All countries had a strong drop of methane emissions for this sector in the years prior to 1984, with an associated decrease in crude oil production of up to 46%, but since then there is no obvious decrease, despite some increase in crude oil production. Figure 9.9 shows the crude oil production for the same countries for the period 1970 to 2017.

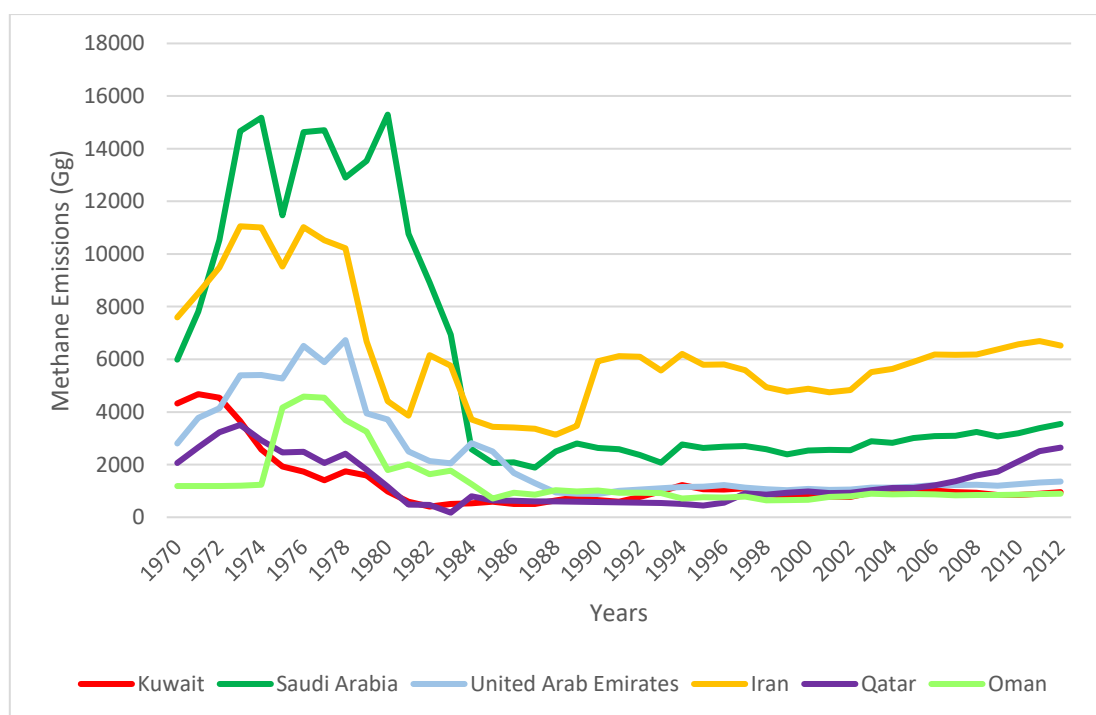


Figure 9.8 EDGAR data for all source categories for Kuwait (in red) and other countries in the same region. Source: www.edgar.jrc.europa.eu, 2016

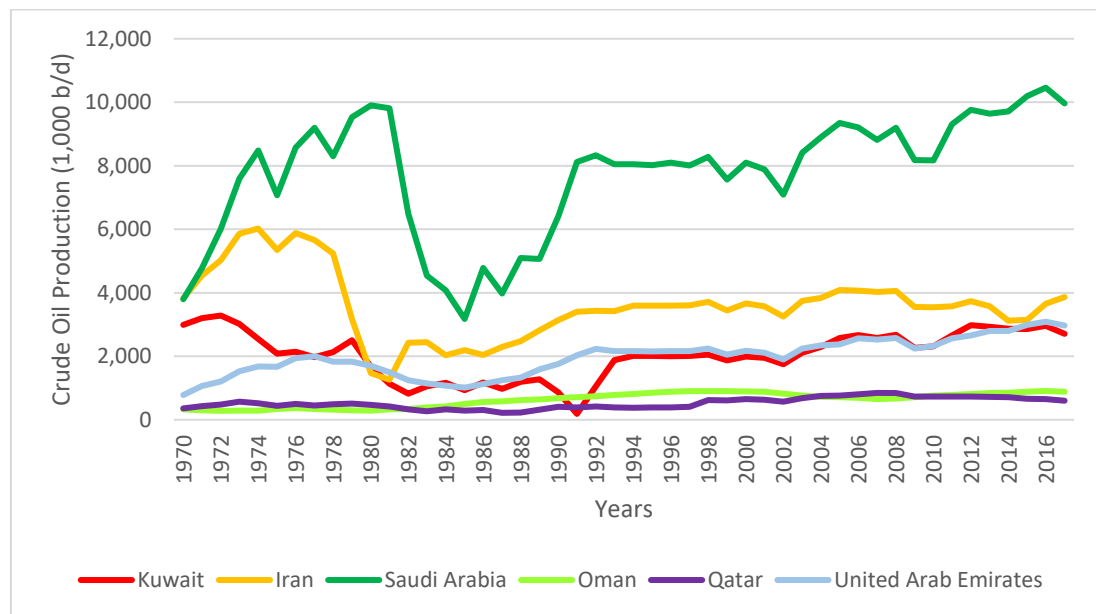


Figure 9.9 Crude oil production for Kuwait and other countries for the period 1970 to 2017. Source: OPEC,2018

Figure 9.10 shows the EDGAR global methane emissions map for 2012 for all source categories. The map shows Kuwait and clearly the high methane emission in red is associated with the refineries and oilfields to the north and south of Kuwait City. Höglund-Isaksson, (2017) found a 73% higher emission in his study of the global bottom-up inventory of methane for oil and gas system compared to EDGAR for the same time period. Höglund-Isaksson (2017) relates this difference to the country-specific circumstances in the generation and management of associated gas.

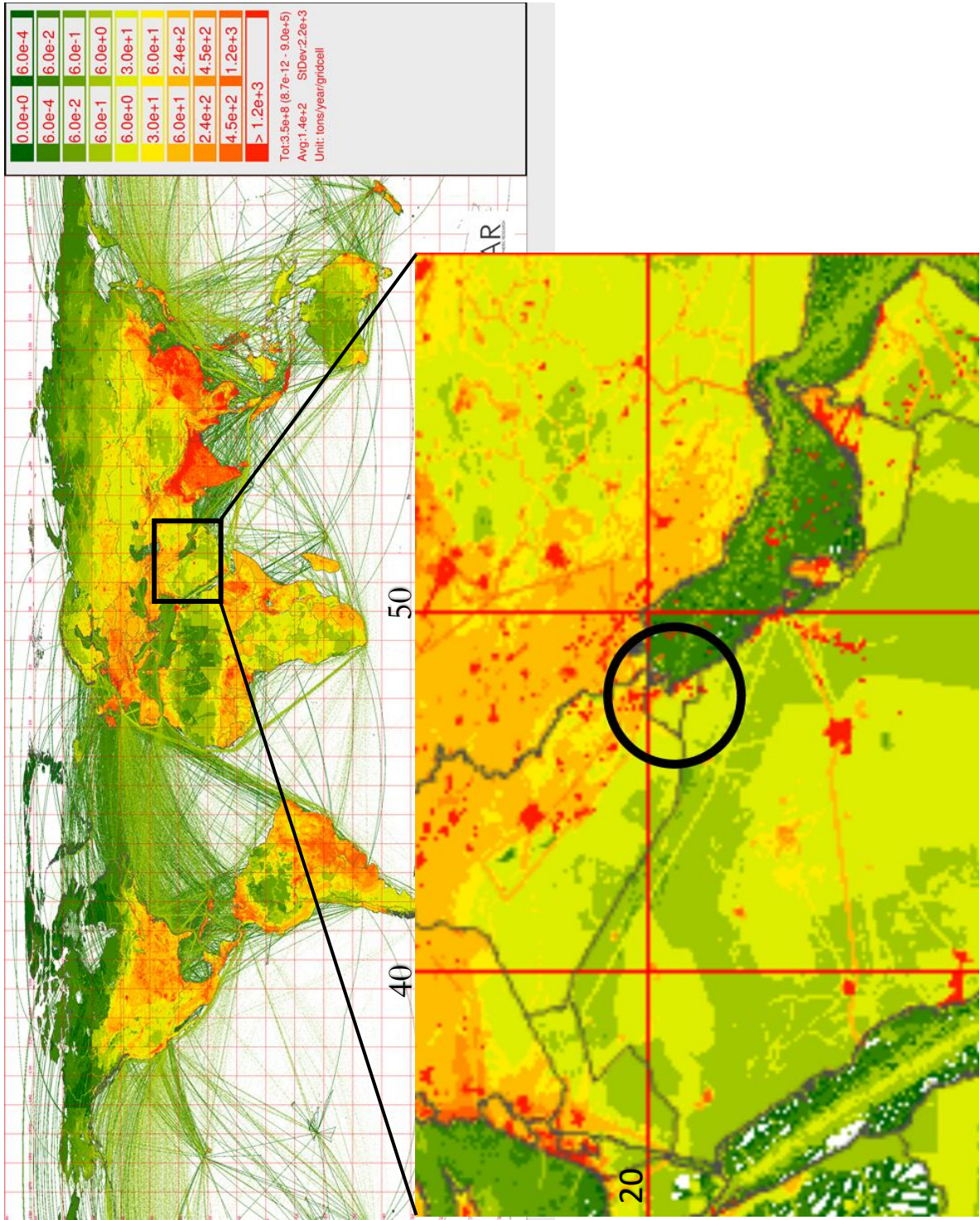


Figure 9. 10 EDGAR 2012 data for global methane emissions for all sectors.
Source: www.edgar.jrc.europa.eu,2016

The bottom-up estimation by EDGAR that is based on statistics multiplied by specific emission factors is likely to overestimate the methane emissions derived from the oil and gas sector in Kuwait compared with results from the surveys. As was shown in chapter 4, there was no evidence that significant methane emissions were coming from the oil fields during the surveys with the Picarro mobile system while driving on the public road between the Burgan oil fields in 2015, or from the more recent air samples collected in the northern area oil fields.

These over-estimations in the EDGAR database could also apply to other major oil and gas producing countries in the Middle East. This suggests that a revision of the source distribution given by the emission inventories is needed.

9.4 Kuwait Inventory by Kuwait EPA

Kuwait's Initial National Communications (INC) under the United Nations Framework Convention on Climate Change (UNFCCC) is the first greenhouse gas emission inventory for Kuwait that focuses on emission level. This inventory followed the IPCC 1996 guidelines in development and used the year 1994 as a base year.

Table 1.1 in Chapter 1 shows the greenhouse gas sources in Kuwait based on this inventory. The inventory estimated 70.4% of Kuwait methane emissions to be derived from fugitive emissions from fuels, 26.2% from waste and 2.1% from agriculture. All of the waste sector methane emission is classed as from landfill with no wastewater emissions from the perceived aerobic processes.

The uncertainties of the UNFCCC report associated with estimating GHG emissions and removals in Kuwait are due to data gaps, quality issues, and inconsistencies across different sources. The uncertainty of results includes differing interpretations of source/sink categories, use of average emission factors instead of Kuwait specific factors, and an incomplete scientific understanding of the GHG emission and removal processes. Additionally, there were serious data gaps and quality issues for the year 1994

9.5 Verification of Inventories

This research is the first in Kuwait to identify the isotopic signatures of the methane sources. The results in Table 9.1 summarise all the isotopic signatures that have been measured in this research for all the methane sources in Kuwait, which will be used to calculate a single average value for each source category in order to verify the inventory.

<i>Methane source</i>	<i>Site</i>	$\delta^{13}\text{C}$ (‰)
<i>Landfills</i>	ALJahra Landfill (Active)	-59.4 ± 1.4
	South Seven Ring Road (Active)	-58.5 ± 0.5
	Mina Abdullah (Active)	-59.5 ± 1.0
	AL-Sulaibiyah (Closed)	-51.9 ± 0.2
	AL-Qurain (Closed)	-54.3 ± 1.9
	Jleeb AL-Shuyoukh (Closed)	-56.4 ± 1.9
<i>Natural Gas</i>	Al-Ahmadi Town (gas leakage)	-50.0 ± 0.2
	Refineries	-51.6 ± 0.5
	Ahmadi oil field (Greater Burgan)	-49.9 ± 0.2
<i>Ruminants</i>	Cow	-62.4 ± 0.4
	Sheep	-63.6 ± 0.1
	Camels	-60.0 ± 0.5
<i>Wastewater treatment plant</i>	Al-Reqqa	-45.1 ± 0.2
	Al-Reqqa	-50.5 ± 0.7
	Al-Reqqa	-50.7 ± 0.6
	Al-Reqqa	-45.6 ± 0.1
	Kilo 30	-46.2 ± 0.1
<i>Car Exhaust</i>	Um-Al-Himan	-59.2 ± 0.9
	Um-Al-Himan	-46.8 ± 0.04
		-13.1 ± 1.0

Table 9.1 Methane isotopic signatures for difference sources in Kuwait.

To calculate the average value for landfill in Kuwait, the maximum peak (mole fraction) of methane that was measured on each site by the Picarro mobile system during the Kuwait campaign was identified, and the background atmospheric methane component removed (table 9.2). Using these values and the average isotopic signature for each landfill an estimated emission weighted landfill signature can be calculated using the equation below. The overall mean methane source signature for the landfill category using this method is -58.1‰ for Kuwait.

$$\frac{\sum \delta^{13}\text{C source} * \text{CH}_4 \text{ excess}}{\sum \text{CH}_4 \text{ excess}}$$

Kuwait Landfill Sites	$\delta^{13}\text{C}$ (‰)	Excess CH_4 (ppm)
Al-Jahra	-59.4	9.34
7th Ring Road	-58.5	36.7
Mina Abdullah	-59.1	21.8
AL-Sulaibiyah	-51.9	1.6
AL-Qurain	-54.3	9.45
Jleeb Al-Shuyoukh	-56.4	3.2
Sum		82.09
Average value isotopic signature		-58.1

Table 9.2 Estimated landfill signature in Kuwait.

For the natural gas category, the average of the three sources of the natural gas that were measured and shown in table 9.2 was estimated as -50‰. A single source was measured in this study for the combustion category in Kuwait -13.1‰ as is shown in the same table 9.1. This is a very small source in the inventory and so this isotopic value has little influence on the subsequent calculations.

Globally, methane emissions from cattle are 74 % of all livestock emissions compared with sheep and buffalo which together account for 9% (Lassey 2007). Aljaloud *et al.* (2011) studied the emissions from livestock in Saudi Arabia in 2007 and found that the cattle and sheep were the biggest CH₄ producers, followed by camels and goats. The IPCC emissions factors from the Aljaloud *et al.* (2011) study are used to calculate the average emissions from the livestock in Kuwait. There are almost 20 times more sheep in Kuwait than cows, so although emission per sheep is only 10% of a cow the total sheep emission from Kuwait is still twice that from cows. The overall mean methane source signature for the livestock in Kuwait is -63‰

For the wastewater treatment source category, the mean value from all isotopic signatures that are shown in table 9.1 is estimated as -49‰.

Table 9.3 shows the methane emissions from inventories and the isotopic signatures of the source mix calculated for each inventory based on the % of each source in the inventory. Use of mass balance was attempted to calculate an appropriate source mix for Kuwait based on the average of Miller-Tans plots of -55.9‰, which is likely to represent the actual source mix for Kuwait methane (more details in chapter 8).

According to the EDGAR inventory for the years 1994 and 2012, the overall regional source mix from Kuwait would be -50.3 and -50.5 ‰ respectively. The EDGAR database estimates that around 90 to 96 % of methane emissions in Kuwait are resulting from the gas and oil sector and 3 to 10 % derived from the landfill and sewage waste treatment sector. These estimates for methane emissions from Kuwait lead to an overall ¹³C-enriched source mix. This is close to the KEPA estimates for methane emissions in Kuwait in 1994. KEPA estimated that the main sources of methane were the gas sector at 70%, with 26% from landfills, which gives -52 ‰ for the overall regional source mix for Kuwait. Both inventories give an enriched mix of $\delta^{13}\text{C}$ -52‰ to -50.3‰, compared to the -55.9‰ based on the long-term records for the three atmospheric measurement sites. A newly updated KEPA 2016 inventory will soon be available for Kuwait. Based on provisional % source

calculations for this and the isotopic data two new estimates of percentage source emissions that represent two end members have been calculated (Table 9.3).

<i>Inventory</i>	Fossil Fuel (%)	Landfills (%)	Sewage (%)	Animals (%)	Combustion (%)	Total (%)	Isotopic signature of Source mix (‰)
<i>KEPA, 1994</i>	70.4	26.2		2.1	1.3	100	-52
<i>EDGAR, 1994</i>	96.45	1.81	1.16	0.23	0.15	99.99	-50.3
<i>EDGAR, 2012</i>	90.9	4.7	2.23	0.69	0.13	99.99	-50.5
<i>KEPA, 2018</i>	11.5	81.6		6.9		100	-57.4
<i>$\delta^{13}\text{CH}_4$ (‰) based on measurement</i>	-50	-58	-49	-63	-13	Miller-Tans -55.9	
<i>Isotopic Estimate (A) of (%) source for this study</i>	6.72	77.76	4	7.68	3.84	100	-55.9
<i>Isotopic Estimate (B) of (%) source for this study</i>	7	81	0	8	4	100	-56.2

Table 9.3 Methane emissions from inventories and verification. (A) and (B) are an isotopic estimate of (%) source for this study.

The overall regional source mix from Kuwait based on the long-term measurements for two years in this study is more ^{13}C depleted than the inventories. By using Miller-Tans plots, the mix of sources for methane emissions of Kuwait were calculated as discussed in chapter 8 at -55.9‰ for the years 2015 and 2016. This suggests that the majority of the methane source in Kuwait is derived from biogenic sources such as landfills. This is supported by the Kuwait mobile campaign observations that aimed to identify the main sources of methane emissions in Kuwait and found that landfills are the main source for methane emissions with the average value of isotopic signature of -58.1‰ .

The new inventory by Kuwait EPA 2018, (personal communication/unpublished data) is in better agreement with this research results. In this inventory, KEPA estimate that 11.5% of methane emissions are derived from the gas sector and 81.6% from the waste sector. KEPA 2018 agree that the main source of methane emissions in Kuwait is the biogenic source resulting from waste sector. As shown in Table 9.3 the KEPA, 2018 balance is in closer agreement with the -55.9‰ identified by Miller-Tans plots. The Kuwait EPA inventory 2018 estimated methane emissions suggest -57.4‰ for the Kuwait source mix, again presuming that the waste emission is all from landfill. While the new inventory agrees with the finding of this thesis that the largest source of methane from Kuwait is biogenic and, predominantly from waste sources, the isotopic mass balance suggests that either up to 17.5% of methane from sewage treatment is missing from the inventory (Estimate A), or alternatively that the fossil emissions are still up to 29% of the emissions (Estimate B). Given the observation from the surveys the answer is likely somewhere between these 2 estimates.

C***HAPTER 10***

C***ONCLUSIONS***

10. Conclusions

This research demonstrates for the first time in Kuwait that continuous mobile measurements for plume identification coupled with high-precision isotopic analysis using CF-GC-IRMS (Continuous Flow Gas Chromatography-Isotope Ratio Mass Spectrometry) is an effective and precise way of understanding methane emissions and identifying sources. The research has identified high methane mole fractions from anthropogenic sources such as the fossil fuel industry, landfill sites, sewage (wastewater) treatment and ruminants. High precision isotopic analysis allowed verification of these sources in Kuwait. The results of this research will contribute to understanding the methane budget of this poorly understood region.

10.1 Key Findings

Six days of mobile measurements were carried out in Kuwait between May 1 and May 7, 2015. These covered most of the country between the northern border with Iraq and the southern border with Saudi Arabia.

- The campaigns identified landfill sites as the main source of methane in Kuwait
- The expected high emissions from oil production were not seen, however there were emissions from oil refineries, and from Ahmadi Town, the only area of Kuwait with a gas distribution network.
- There were very few and only small peaks within Kuwait City because there is no gas distribution network.

A two-year time series of methane mole fraction measurements and $\delta^{13}\text{C}$ were made in bags filled weekly at three sites that represent upwind, downwind and city center for the main two wind directions NW and SE.

- This is compared with the closest NOAA station to Kuwait and a good agreement was seen with upwind site background measurements.
- Elevated mole fractions have a consistent isotopic signature of -55.9‰ which suggests biogenic sources dominate the local source mix in Kuwait.

The isotopic signatures for all of the methane sources in Kuwait have been characterised by collecting air samples close to sources and in downwind emission plumes.

- Most of the methane sources in Kuwait are depleted in ^{13}C relative to the background signature. This makes it harder to distinguish between sources compared to countries that have more thermogenic fossil fuel and combustion sources that are enriched in ^{13}C relative to atmospheric background.
- Signatures from landfills and ruminants are similar to those measured in other countries averaging -58‰ and -63‰ respectively.
- Sewage and fossil fuel have very similar average isotopic signatures of -49‰ and -50‰ respectively, but the fossil fuel sources show very little variability whereas the sewage has a wide range depending on the amount of aeration of the waste product.

Inventories suggest that $> 70\%$ of methane emissions are from the oil and gas sector and most of the rest from the landfills.

- Isotopic mass balance suggests that the opposite is true and fossil fuel sources account for less than 30% of Kuwait methane emissions.
- KEPA inventories have sewage methane emissions as zero, but the survey shows that there are emissions from all sites visited. If a sewage emission is included, then the isotopic mass balance requires that the fossil fuel component reduces further below 30% .

10.2 Recommendations for Future Studies and Mitigation of Methane Emissions in the Middle East

- Long term high precision measurement of methane mole fraction and $\delta^{13}\text{C}$ in Kuwait should continue to be able to evaluate future changes in the sources and to assess the effect of mitigation strategies.
- A further mobile survey should be carried out with additional ethane measurements as this would be another way of distinguishing thermogenic fossil fuel sources.
- Collection of gas from landfills (waste to energy) in other countries has proved to be very successful and an important source of income for the waste companies. Implementation of similar technology in Kuwait would greatly reduce emissions.
- The isotopic mass balance and KOC reports of greatly reduced flaring suggest that there have been big reductions in emissions from fossil sources in recent years, but this is not transferred to the EDGAR database. Improvements in national inventories in this region should be taken into account when producing future versions of global inventories.
- This study has the potential to be extended to other countries in the region that follow similar landfill and fossil fuel extraction and distribution practices but may not have verification of inventories.

***R**EFERENCES*

References

- Aali, J., Rahimpour-Bonab, H. & Kamali, M.R. 2006. Geochemistry and origin of the world's largest gas field from Persian Gulf, Iran. *Journal of Petroleum Science and Engineering*, 50, 161–175,
<https://doi.org/10.1016/j.petrol.2005.12.004>.
- Abdullah, M.A., 2010. Determination of optimum location for Municipal Solid Waste Landfill Sites in Kuwait using Geographical Information Systems (GIS). Unpublished MS.c. dissertation, Arabian Gulf University, Bahrain
- Abichou, T., Chanton, J., Powelson, D., Fleiger, J., Escoriaza, S., Lei, Y. & Stern, J. 2006. Methane flux and oxidation at two types of intermediate landfill covers. *Waste Management*, 26, 1305–1312,
<https://doi.org/10.1016/j.wasman.2005.11.016>.
- Abu-Ayyash, A.-I. 1980. Urban development and planning strategies in Kuwait.,
<https://doi.org/10.1111/j.1468-2427.1980.tb00373.x>.
- Agustine, I., Yulinawati, H., Suswantoro, E. & Gunawan, D. 2017. Application of open air model (R package) to analyse air pollution. *Indonesian Journal of Urban and Environmental Technology*, 1, 94–108.
- Akritas, M. G. & Bershady, M. A. 1996. Linear regression for astronomical data with measurement errors and intrinsic scatter. *The astrophysical journal*, 470, 706–714.
- Al-Azmi, B.N., Nassehi, V. & Khan, A.R. 2009. SO₂ and NO_x Emissions from Kuwait Power Stations in Years 2001 and 2004 and Evaluation of the Impact of These Emissions on Air Quality Using Industrial Sources Complex Short-Term (ISCST) Model. *Water, Air, and Soil Pollution*, 203, 169–178,

<https://doi.org/10.1007/s11270-009-0001-4>.

- Al-Faraj, M.S. 2005. Landfill sites in the State of Kuwait and their impact on the residential areas - An Analytical Geographical Study. Refereed Journal, Geography Dept. and Kuwaiti Geographical Society, Vol. 302, 79p. [In Arabic]
- Al-Hamad, K.K., Nassehi, V. & Khan, A.. 2008a. Impact of Green House Gases (GHG) Emissions from Oil Production Facilities at Northern Kuwait Oilfields : Simulated Results Department of Chemical Engineering Loughborough University , Coastal and Air Pollution Division , Kuwait Institute for Scientific. 4, 491–501.
- Al-Hamad, K.K., Nassehi, V. & Khan, A.R. 2008b. Methane and Other Hydrocarbon Gas Emissions Resulting from Flaring in Kuwait Oilfields. International Journal of Civil and Environmental Engineering, 2, 144–152.
- Al-Hamad, K.K., Nassehi, V. & Khan, A.. 2009. Methane and Other Hydrocarbon Gas Emissions Resulting from Flaring in Kuwait Oilfields. Recent Advance in Technologies, 601–618.
- Al-Hamad, K.K. & Khan, A.R. 2008. Total emissions from flaring in Kuwait oilfields. American Journal of Environmental Sciences, 4, 31–38, <https://doi.org/10.3844/ajessp.2008.31.38>.
- Al-Ahmad, M. (2012). Optimization of the Assessment and Rehabilitation of Old Landfill in Kuwait. Unpublished doctoral Thesis. Rostock University, Germany
- Al-Ahmad, M., Dimashki, M., Nassour, A. & Nekkes, M. 2012. Characterization , Concentrations and Emission Rates of Volatile Organic Compounds from Two Major Landfill Sites in Kuwait. Journal, American Sciences, Environmental Publications, Science, 8, 56–63.

- Al-Meshan M. & Mahrous, F. 1999. Principles of Solid Waste Management in the State of Kuwait. The Public Authority for Applied Education and Training, Kuwait
- Al-Meshan, M. and Mahrous, F., 2002. Management of municipal solid waste landfills in the State of Kuwait". Proceedings of the 2nd Asian Pacific Landfill Symposium. September, 25-28. Seoul, Korea.
- Al-Nassar, W., Alhajraf, S., Al-Enizi, A. & Al-Awadhi, L. 2005. Potential wind power generation in the State of Kuwait. Renewable Energy, 30, 2149–2161, <https://doi.org/10.1016/j.renene.2005.01.002>.
- Al-Rashed, A. 2014. Detection of Natural gas leakage in Al-Ahmadi area, South of Kuwait: A preliminary study. Nature and Science, 12, 87–93.
- Al-Rashidi, M.S., Nassehi, V. & Wakeman, R.J. 2005. Investigation of the efficiency of existing air pollution monitoring sites in the state of Kuwait. Environmental Pollution, 138, 219–229, <https://doi.org/10.1016/j.envpol.2005.04.006>.
- Al-Rashidi, M.S., Yassin, M.F., Alhajeri, N.S. & Malek, M.J. 2018. Gaseous air pollution background estimation in urban, suburban, and rural environments. Arabian Journal of Geosciences, 11, <https://doi.org/10.1007/s12517-017-3369-2>.
- Al-Saffae, A. & Al-Sarawi, M. 2018. Geo-visualization of the distribution and properties of landfill gases at Al-Qurain Landfill , Kuwait. Kuwait journal of Science, 45, 93–104.
- Al-Tahw, G. 2006. Application of Vulnerability of Groundwater to Pollution Produced from Activities in the State of Kuwait, Geographical Information Systems. Unpublished MS.C. dissertation. Program of Technological Management, University of Arabian Gulf, Bahrain, 87p. [In Arabic].

- Al-Yaqout, A.F., Hamoda, M.F. 2000. Operating characteristics of municipal solid waste landfills in Kuwait. In: The 16th International Conference on Solid Waste Technology and management, Philadelphia, December 10–13.
- Al-Yaqout, A.F. & Hamoda, M.F. 2002. Report: Management problems of solid waste landfills in Kuwait. *Waste Management and Research*, 20, 328–331, <https://doi.org/10.1177/0734247X0202000403>.
- Al-Yaqout, A.F. & Hamoda, M.F. 2007. Movement of unlined landfill under preloading surcharge. *Waste management*, 27, 448–458, <https://doi.org/10.1016/j.wasman.2006.02.006>.
- Al-Yaqout, A.F., Koushki, P.A. & Hamoda, M.F. 2002. Public opinion and siting solid waste landfills in kuwait. *Resources, Conservation and Recycling*, 35, 215–227.
- Al-Yaqout, A.F., Hamoda, M.F. & Zafar, M. 2005. Characteristics of Wastes, Leachate, and Gas at Landfills Operated in Arid Climate. *Practice Periodical of Hazardous, Toxic, and Radioactive Waste Management*, 9, 97–102, [https://doi.org/10.1061/\(ASCE\)1090-025X\(2005\)9:2\(97\)](https://doi.org/10.1061/(ASCE)1090-025X(2005)9:2(97)).
- Aljaloud, A.A., Yan, T. & Abdukader, A.M. 2011. Development of a national methane emission inventory for domestic livestock in Saudi Arabia. *Animal Feed Science and Technology*, 166–167, 619–627, <https://doi.org/10.1016/j.anifeedsci.2011.04.044>.
- Alkhaledi, K., Alrushaid, S., Almansouri, J. & Alrashed, A. 2015. Using fault tree analysis in the Al-Ahmadi town gas leak incidents. *Safety Science*, 79, 184–192, <https://doi.org/10.1016/j.ssci.2015.05.015>.

- Allan, W., Lowe, D.C. & Gomez, A.J. 2005. Interannual variation of ^{13}C in tropospheric methane : Implications for a possible atomic chlorine sink in the marine boundary layer. *Journal of Geophysical Research: Atmosphere*, 110, 1–8, <https://doi.org/10.1029/2004JD005650>.
- Alsharhan, A.S. & Nairn, A.E.M. 1997. Hydrocarbon Habitat of the Greater Arabian Basin. In: *Sedimentary Basins and Petroleum Geology of the Middle East*. Elsevier Ltd, 525–649., <https://doi.org/http://dx.doi.org/10.1016/B978-044482465-3/50012-7>.
- Arata, C., Rahn, T. & Dubey, M.K. 2016. Methane Isotope Instrument Validation and Source Identification at Four Corners, New Mexico, United States. *Journal of Physical Chemistry A*, 120, 1488–1494, <https://doi.org/10.1021/acs.jpca.5b12737>.
- Arouri, K.R., Van Laer, P.J., Prudden, M.H., Jenden, P.D., Carrigan, W.J. & Al-Hajji, A.A. 2010. Controls on hydrocarbon properties in a Paleozoic petroleum system in Saudi Arabia: Exploration and development implications. *AAPG Bulletin*, 94, 163–188, <https://doi.org/10.1306/07060908133>.
- Badr, O., Probert, S.D. & Callaghan, P.W.O. 1991. Atmospheric Methane : Its Contribution to Global Warming. *Applied Energy*, 40, 273–313.
- Bergamaschi, P., Lubina, C., Königstedt, R. & Fischer, H. 1998. Stable isotopic signatures ($\delta^{13}\text{C}$, δ^{D}) of methane from European landfill sites. *Journal of Geophysical Research*, 103, 8251–8265.
- Bergamaschi, P., Corazza, M., Karstens U., Athanassiadou M., Thompson R. L., Pison I., Manning A. J., Bousquet P., Segers A., Vermeulen A. T., Janssens-Maenhout G., Schmidt M., Ramonet M., Meinhardt F., Aalto T., Haszpra L., Moncrieff J., Popa M. E., Lowry D., Steinbacher M., Jordan A., S. O'Doherty S., Piacentino S., and Dlugokencky E. 2015. Top-down estimates of European

- CH₄ and N₂O emissions based on four different inverse models. *Atmospheric Chemistry and Physics*, 15, 715–736, <https://doi.org/10.5194/acp-15-715-2015>.
- Bernard, B.B., Brooks, J.M. & Sackett, W.M. 1978. Light Hydrocarbons in Recent Texas Continental Shelf and Slope Sediments. *Journal of Geophysical Research*, 83, 4053–4061, <https://doi.org/10.1029/JC083iC08p04053>.
- Berner, U. & Faber, E. 1996. Empirical carbon isotope/maturity relationships for gases from algal kerogens and terrigenous organic matter, based on dry, open-system pyrolysis. *Organic Geochemistry*, 24, 947–955, [https://doi.org/10.1016/S0146-6380\(96\)00090-3](https://doi.org/10.1016/S0146-6380(96)00090-3).
- Bilek, R.S., Tyler, S.C., Kurihara, M. & Yagi, K. 2001. Investigation of cattle methane production and emission over a 24-hour period using measurements of $\delta^{13}\text{C}$ and δD of emitted CH₄ and rumen water. *Journal of Geophysical Research Atmospheres*, 106, 15405–15413, <https://doi.org/10.1029/2001JD900177>.
- Bloom, A.A., Palmer, P. I., Fraser, A., Reay, D.S. & Frankenberg, C. 2010. Large-Scale Controls of Methanogenesis Inferred from Methane and Gravity Spaceborne Data. *Nature Chemistry*, 2, 61–65, <https://doi.org/10.1038/nchem.467>.
- Bogner, J. & Matthews, E. 2003. Global methane emissions from landfills : New methodology and annual estimates 1980 – 1996. *Global biogeochemical cycles* i, 17, <https://doi.org/10.1029/2002GB001913>.
- Börjesson, G., Chanton, J. & Svensson, B.H. 2001. Methane Oxidation Two Swedish Landfill Cover Measured with Carbon-13 to Carbon-12 Isotope Ratios. *journal of Environmental quality*, 30, 369–376, <https://doi.org/10.1016/B978-1-4377-0721-2.00005-2>.

- Bousquet, P., Ciais, P., Miller, J. B., Dlugokencky, E. J., Hauglustaine, D. A., Prigent, C., Van der Werf, G. R., Peylin, P., Brunke, E.-G., Carouge, C., Langenfelds, R. L., Lathière, J., Papa, F., Ramonet, M., Schmidt, M., Steele, L. P., Tyler, S. C. and White, J. 2006. Contribution of anthropogenic and natural sources to atmospheric methane variability. *Nature*, 443, 439–443, <https://doi.org/10.1038/nature05132>
- Bousquet, P., Ringeval, B., Pison, I., Dlugokencky, E. J., Brunke, E.-G., Carouge, C., Chevallier, F., Fortems-Cheiney, A., Frankenberg, C., Hauglustaine, D. A., Krummel, P. B., Langenfelds, R. L., Ramonet, M., Schmidt, M., Steele, L. P., Szopa, S., Yver, C., Viovy, N., and Ciais, P. 2011. Source attribution of the changes in atmospheric methane for 2006-2008. *Atmospheric Chemistry and Physics*, 11, 3689–3700, <https://doi.org/10.5194/acp-11-3689-2011>.
- Bridgman, S., Cadillo-Quiroz, H., Keller, J.K. & Q., Z. 2013. Methane emissions from wetlands : biogeochemical , microbial , and modeling perspectives from local to global scales. *Global change biology*, 19, 1325–1346, <https://doi.org/10.1111/gcb.12131>.
- Carman, G.J. 1996. Structural elements of onshore Kuwait. *GeoArabia*, 1, 239–266.
- Carslaw, D.C. 2015. The Openair Manual Open-source Tools for Analysing Air Pollution Data. King's College London, 287, <https://doi.org/10.1094/PDIS-92-6-0980B>.
- Carslaw, D.C. & Beevers, S.D. 2013. Characterising and understanding emission sources using bivariate polar plots and k-means clustering. *Environmental Modelling and Software*, 40, 325–329, <https://doi.org/10.1016/j.envsoft.2012.09.005>.

- Carslaw, D.C. & Ropkins, K. 2012. Openair - An r package for air quality data analysis. *Environmental Modelling and Software*, 27–28, 52–61, <https://doi.org/10.1016/j.envsoft.2011.09.008>.
- Central Statistical Bureau. [Online]. Available at: www.csb.gov.kw. [Accessed: March 2018]
- Chanton, J. & Liptay, K. 2000. Seasonal variation in methane oxidation in a landfill cover soil as determined by an in situ stable isotope technique. *Global Biogeochemical Cycles*, 14, 51–60, <https://doi.org/10.1029/1999GB900087>.
- Chanton, J., Abichou, T., Jeffrey Chanton a, , Tarek Abichou b, Langford, C., Spokas, K., Hater, G., Green, R., Goldsmith, D., Barlaz, M.A. 2011. Observations on the methane oxidation capacity of landfill soils. *Waste Management*, 31, 914–925, <https://doi.org/10.1016/j.wasman.2010.08.028>.
- Chanton, J.P., Rutkowski, C.M. & Mosher, B. 1999. Quantifying methane oxidation from landfills using stable isotope analysis of downwind plumes. *Environmental Science and Technology*, 33, 3755–3760, <https://doi.org/10.1021/es9904033>.
- Chanton, J.P., Rutkowski, M., Schwartz, C., Ward, D.E., Boring, L. & Jones, W. 2000. Factors influencing the stable carbon isotopic signature of methane from combustion and biomass burning. *Journal of Geophysical Research*, 105, 1867–1877.
- Chen, Y.H. & Prinn, R.G. 2006. Estimation of atmospheric methane emissions between 1996 and 2001 using a three-dimensional global chemical transport model. *Journal of Geophysical Research Atmospheres*, 111, <https://doi.org/10.1029/2005JD006058>.
- Christensen, T.R., Ekberg, A., Stro, L., Mastepanov, M. & Panikov, N. 2003.

- Factors controlling large scale variations in methane emissions from wetlands. *Geophysical Research Letters*, 30, 10–13, <https://doi.org/10.1029/2002GL016848>.
- Christensen, T.H., 2011. *Solid Waste Technology and Management* (1st ed.). Wiley-Blackwell, Chichester, West Sussex, UK.
- Ciais, P., C. Sabine, G. Bala, L. Bopp, V. Brovkin, J. Canadell, A. Chhabra, R. DeFries, J. Galloway, M. Heimann, C. Jones, C. Le Quéré, R.B. Myneni, S. Piao and P. Thornton, 2013: Carbon and Other Biogeochemical Cycles. In: *Climate Change 2013: The Physical Science Basis. Contribution of Working Group I to the Fifth Assessment Report of the Intergovernmental Panel on Climate Change* [Stocker, Qin T.F., Plattner D. G.-K., Tignor M., Allen S.K., Boschung, J. Nauels, A. Xia Y., Bex V. and Midgley P.M. (eds.)]. Cambridge University Press, Cambridge, United Kingdom and New York, NY, USA.
- Crippa, M., Guizzardi, D., Muntean, M., Schaaf, E., Dentener, F., van Aardenne, J. A., Monni, S., Doering, U., Olivier, J.G. J., Pagliari, V., and Greet Janssens-Maenhout, G., 2018. Gridded emissions of air pollutants for the period 1970–2012 within EDGAR v4.3.2. *Earth System Science Data*, 10, 1987–2013, <https://doi.org/10.5194/essd-10-1987-2018>.
- Crosson, E.R. 2008. A cavity ring-down analyzer for measuring atmospheric levels of methane, carbon dioxide, and water vapor. *Applied Physics B: Lasers and Optics*, 92, 403–408, <https://doi.org/10.1007/s00340-008-3135-y>.
- Crutzen, P.J., Aselmann, I. & Seiler, W. 1986. Methane production by domestic animals, wild ruminants, other herbivorous fauna, and humans. *Tellus B*, 38 B, 271–284, <https://doi.org/10.1111/j.1600-0889.1986.tb00193.x>.

- Czepiel, P., Crill, P. & Harriss, R. 1993. Methane Emissions from Municipal Wastewater Treatment Processes. *Environmental Science and Technology*, 27, 2472–2477, <https://doi.org/10.1021/es00009a030>.
- Denman, K.L., G. Brasseur, A. Chidthaisong, P. Ciais, P.M. Cox, R.E. Dickinson, D. Hauglustaine, C. Heinze, E. Holland, D. Jacob, U. Lohmann, S. Ramachandran, P.L. da Silva Dias, S.C. Wofsy and X. Zhang, 2007: Couplings Between Changes in the Climate System and Biogeochemistry. In: *Climate Change 2007: The Physical Science Basis. Contribution of Working Group I to the Fourth Assessment Report of the Intergovernmental Panel on Climate Change* [Solomon, S., D. Qin, M. Manning, Z. Chen, M. Marquis, K.B. Averyt, M. Tignor and H.L. Miller (eds.)]. Cambridge University Press, Cambridge, United Kingdom and New York, NY, USA.
- Denmead, O.T. 1994. Measuring fluxes of CH₄ and NO between agricultural systems and the atmosphere. In: Minami, K., Mosier, A and Sass, R (eds.). *Proceedings of an International Workshop: Methane and Nitrous Oxide Emission from Natural and Anthropogenic Sources and their Reduction Research Plan* (Tsukuba, Japan: March 25-26, 1992). NIAES Series 2; 1994. pp.209-234
- De Visscher A., Boeckx P. & Van Cleemput O. 2007. Artificial Methane Sinks. In Reay, D. S., Hewitt, C. N., Smith, K. A. & Grace J., *Greenhouse Gas Sinks*. Athenaeum Press Ltd, Gateshead
- Dlugokencky, E.J., Steele, L.P., Lang, P.M. & Masarie, K.A. 1994. The growth rate and distribution of atmospheric methane. *Journal of Geophysical Research*, 99, 17021–17043.
- Dlugokencky, E.J., Masarie, K.A., Lang, P.M. & Tans, P.P. 1998. Continuing decline in the growth rate of the atmospheric methane burden.

Letters to Nature, 58, 1200–1203.

- Dlugokencky, E.J., Walter, K.A., Masarie, P.M., Lang, P.M. & Kasischke, E.S. 2001. Measurements of an anomalous global methane increase during 1998. *Journal of Geophysical Research*, 28, 499–502.
- Dlugokencky, E. J., Myers, R. C., Lang, P. M., Masarie, K. A., Crotwell, A. M., Thoning, K. W., Hall, B. D., Elkins, J. W., & Steele, L. P. 2005. Conversion of NOAA atmospheric dry air CH₄ mole fractions to a gravimetrically prepared standard scale. *Journal of Geophysical Research D: Atmospheres*, 110, 1–8, <https://doi.org/10.1029/2005JD006035>.
- Dlugokencky, E.J., Bruhwiler, L., White, J. W. C., Emmons, L. K. , Novelli, P. C., Montzka, S. A., Masarie, K. A., Lang, P. M., Crotwell, A. M., Miller, J. B. and Gatti, L. V. 2009. Observational constraints on recent increases in the atmospheric CH₄ burden. *Geophysical Research Letters*, 36, <https://doi.org/10.1029/2009GL039780>.
- Dlugokencky, E.J., Nisbet, E.G., Fisher, R. & Lowry, D. 2011. Global atmospheric methane: budget, changes and dangers. *Philosophical Transactions of the Royal Society A: Mathematical, Physical and Engineering Sciences*, 369, 2058–2072, <https://doi.org/10.1098/rsta.2010.0341>.
- Dunfield P. F. 2007. The Soil Methane Sink. In R Reay, D. S., Hewitt, C. N., Smith, K. A. & Grace J., 2007. *Greenhouse Gas Sinks*. Athenaeum Press Ltd, Gateshead
- Dutaur, L. & Verchot, L. V. 2007. A global inventory of the soil CH₄ sink. *Global biogeochemical cycles*, 21, 1–9, <https://doi.org/10.1029/2006GB002734>.
- Doorn M, Hobson J, Senhaji F. 1999. Methane and nitrous oxide emissions from wastewater handling. Background paper for the IPCC expert meeting on Good

Practice in national inventory preparation. Sao Paolo, Brazil.

- Doorn M., Liles D., Thorneloe S. 2000. Quantification of methane emissions from latrines, septic tanks, and stagnant, open sewers in the world. In: van Ham J., Baede A.P.M., Meyer L.A., Ybema R. (eds) *Non-CO2 Greenhouse Gases: Scientific Understanding, Control and Implementation*. P. 83-88. Springer, Dordrecht
- Ehhalt, B.D.H. 1974. The atmospheric cycle of methane. *Tellus*, 26, 58–70, <https://doi.org/https://doi.org/10.1111/j.2153-3490.1974.tb01952.x>.
- Einola, J.M., Kettunen, R.H. & Rintala, J.A. 2007. Responses of methane oxidation to temperature and water content in cover soil of a boreal landfill. *Soil Biology & Biochemistry*, 39, 1156–1164, <https://doi.org/10.1016/j.soilbio.2006.12.022>.
- El-Fadel, M. & Massoud, M. 2001. Methane emissions from wastewater management. *Environmental Pollution*, 114, 177–185, [https://doi.org/10.1016/S0269-7491\(00\)00222-0](https://doi.org/10.1016/S0269-7491(00)00222-0).
- eMISK (2018). Environmental Monitoring Information System of Kuwait. [Online]. Available at: <http://www.emisk.org/emisk/>.
- eMISK/KEPA, 2011. Environmental Monitoring Information System of Kuwait (eMISK) Kuwait Environment Public Authority (KEPA)
- Engeln, R., Berden, G., Peeters, R. & Meijer, G. 1998. Cavity enhanced absorption and cavity enhanced magnetic rotation spectroscopy. *Review of Scientific Instruments*, 69, 3763–3769, <https://doi.org/10.1063/1.1149176>.
- Environment Public Authority (KEPA). 2012. Kuwait's Initial National Communications under the United Nations Framework Convention on Climate Change. Kuwait.

- Etiope, G., Fridriksson, T., Italiano, F., Winiwarter, W. & Theloke, J. 2007. Natural emissions of methane from geothermal and volcanic sources in Europe. *Journal of Volcanology and Geothermal Research*, 165, 76–86, <https://doi.org/10.1016/j.jvolgeores.2007.04.014>.
- Etiope, G., Lassey, K.R., Klusman, R.W. & Boschi, E. 2008. Reappraisal of the fossil methane budget and related emission from geologic sources. *Geophysical Research Letters*, 35, <https://doi.org/10.1029/2008GL033623>.
- European Commission, Joint Research Centre (EC-JRC)/Netherlands Environmental Assessment Agency (PBL). Emissions Database for Global Atmospheric Research (EDGAR), release EDGAR v4.3.2 (1970 - 2012) of March 2016, <http://edgar.jrc.ec.europa.eu>, 2016.
- Fairley, D. & Fischer, M.L. 2015. Top-down methane emissions estimates for the San Francisco Bay Area from 1990 to 2012. *Atmospheric Environment*, 107, 9–15, <https://doi.org/10.1016/j.atmosenv.2015.01.065>.
- Fisher, R., Lowry, D., Wilkin, O., Sriskantharajah, S. & Nisbet, E.G. 2006. High-precision, automated stable isotope analysis of atmospheric methane and carbon dioxide using continuous-flow isotope-ratio mass spectrometry. *Rapid Communications in Mass Spectrometry*, 20, 200–208, <https://doi.org/10.1002/rcm.2300>.
- Fisher, R. E., Sriskantharajah, S., Lowry, D., Lanoisellé, M., Fowler, C. M. R., James, R. H., Hermansen, O., Lund Myhre, C., Stohl, A., Greinert, J., Nisbet-Jones, P. B. R., Mienert, J. and Nisbet, E. G. 2011. Arctic methane sources: Isotopic evidence for atmospheric inputs. *Geophysical Research Letters*, 38, 3–8, <https://doi.org/10.1029/2011GL049319>.

- Fisher, R. E., France, J. L., Lowry, D., Lanoisellé, M., Brownlow, R., Pyle, J. A., Cain, M., Warwick, N., Skiba, U. M., Drewer, J., Dinsmore, K. J., Leeson, S. R., Bauguitte, S. J. B., Wellpott, A., O'Shea, S. J., Allen, G., Gallagher, M. W., Pitt, J., Percival, C. J., Bower, K., George, C., Hayman, G. D., Aalto, T., Lohila, A., Aurela, M., Laurila, T., Crill, P. M., McCalley, C. K., & Nisbet, E. G. 2017. Measurement of the ^{13}C isotopic signature of methane emissions from northern European wetlands. *Global Biogeochemical Cycles*, 31, 605–623, <https://doi.org/10.1002/2016GB005504>.
- France, J. L., Cain, M., Fisher, R. E., Lowry, D., Allen, G., O'Shea, S. J., Illingworth, S., Pyle, J., Warwick, N., Jones, B. T., Gallagher, M. W., Bower, K., Breton, M., Percival, C., Muller, J., Welpott, A., Bauguitte, S., George, C., Hayman, G. D., Manning, A. J., Myhre, C. L., Lanoisellé, M., & Nisbet, E. G. Measurements of $\delta^{13}\text{C}$ in CH_4 and using particle dispersion modeling to characterize sources of arctic methane within an air mass. *Journal of Geophysical Research*, 121, 14,257–14,270, <https://doi.org/10.1002/2016JD026006>.
- Frankenberg, C., Bergamaschi, P., Butz, A., Houweling, S., Meirink, JF, Notholt, J., Petersen, AK, Schrijver, H, Warneke, T, Aben, I. 2008. Tropical methane emissions : A revised view from SCIAMACHY onboard ENVISAT. *Geophysical Research Letters*, 35, 1–5, <https://doi.org/10.1029/2008GL034300>.
- Frankenberg, C., Aben, I., Bergamaschi, P., Dlugokenckv, E. J., Hees, R., Houweling, S., Meer, P., Snel, R., & Tol, P. 2011. Global column - averaged methane mixing ratios from 2003 to 2009 as derived from SCIAMACHY : Trends and variability. *Journal of Geophysical Research*, 116, 1–12, <https://doi.org/10.1029/2010JD014849>.

- Fries, A.E., Schiffman, L.A., Shuster, W.D. & Townsend-Small, A. 2018. Street-level emissions of methane and nitrous oxide from the wastewater collection system in Cincinnati, Ohio. *Environmental Pollution*, 236, 247–256, <https://doi.org/10.1016/j.envpol.2018.01.076>.
- Galimov, E.M. & Rabbani, A.R. 2001. Geochemical Characteristics and Origin of Natural Gas in Southern Iran. *Geochemistry International*, 39, 780–792.
- Grainger, C., Clarke, T., McGinn, S.M., Auldist, M. J., Beauchemin, K. A., Hannah, M. C., Waghorn, G. C., Clark, H. and Eckard, R. J. 2007. Methane Emissions from Dairy Cows Measured Using the Sulfur Hexafluoride (SF₆) Tracer and Chamber Techniques. *Journal of Dairy Science*, 90, 2755–2766, <https://doi.org/10.3168/jds.2006-697>.
- Guisasola, A., de Haas, D., Keller, J. & Yuan, Z. 2008. Methane formation in sewer systems. *Water Research*, 42, 1421–1430, <https://doi.org/10.1016/j.watres.2007.10.014>.
- Höglund-Isaksson, L. 2017. Bottom-up simulations of methane and ethane emissions from global oil and gas systems 1980 to 2012. *Environmental Research Letters*, 12, <https://doi.org/10.1088/1748-9326/aa583e>.
- Houweling, S., Bergamaschi, P., Chevallier, F., Heimann, M., Kaminski, T., Krol, M., Michalak, A. M., and Patra, P. 2017. Global inverse modeling of CH₄ sources and sinks : an overview of methods. *Atmospheric Chemistry and Physics*, 17, 235–256, <https://doi.org/10.5194/acp-17-235-2017>.
- Hsu, Y-K., VanCuren T. Park S. Jakober C. Herner J. Gibbon M. F., Blake D. R., Parrish D. P., 2010. Methane emissions inventory verification in southern California. *Atmospheric Environment*, 44, 1–7, <https://doi.org/10.1016/j.atmosenv.2009.10.002>.

- Hwang, K.L., Bang, C.H. & Zoh, K.D. 2016. Characteristics of methane and nitrous oxide emissions from the wastewater treatment plant. *Bioresource Technology*, 214, 881–884, <https://doi.org/10.1016/j.biortech.2016.05.047>.
- Ibrahim A. I. 2015. Air Emissions Management in Kuwait Oil Company. [Online]. Available at: <https://www.epa.gov/sites/production/files/2016-04/documents/tue4emissionmanagementinkoc.pdf>
- IPCC (2006a). 2006 IPCC Guidelines for National Greenhouse Gas Inventories, Prepared by the National Greenhouse Gas Inventories Programme, Eggleston H.S., Buendia L., Miwa K., Ngara T. and Tanabe K. (eds). Published: IGES, Japan.
- IPCC (2006b) 'Fugitive Emissions', Oil and natural gas in Picard.D. Azhari A. F. M., Gjerald E., Nordrum S., and Yesserkepova I. (eds) 2006 IPCC Guidelines for National Greenhouse Gas Inventories, Institute for Global Environmental Strategies, Kanagawa, Japan, pp3.1–3.40.
- IPCC (2006c) 'Solid waste disposal', in J. Wagener Silva Alves, Q. Gao, C. Lopez Cabrera, K. Mareckova, H. Oonk, E. Scheehle, C. Sharma, A. Smith and M. Yamada (eds) 2006 IPCC Guidelines for National Greenhouse Gas Inventories, Institute for Global Environmental Strategies, Kanagawa, Japan, pp3.1–3.40.
- IPCC (2006d) 'Wastewater treatment and discharge', in M. R. J. Doorn, S. Towprayoon, S. M. Manso, W. Irving, C. Palmer, R. Pipatti and C. Wang (eds) 2006 IPCC Guidelines for National Greenhouse Gas Inventories. Institute for Global Environmental Strategies, Kanagawa, Japan, pp6.1–6.28.
- IPCC (2006e) 'Emissions from livestock and manure management', in Picard.D. Azhari A. F. M., Gjerald E., Nordrum S., and Yesserkepova I. (eds) 2006 IPCC Guidelines for National Greenhouse Gas Inventories, Institute for Global

Environmental Strategies, Kanagawa, Japan, pp3.1–3.40 – VOL 4 CH10

- IPCC, 2007 Climate Change 2007: Synthesis Report. Contribution of Working Groups I, II and III to the Fourth Assessment Report of the Intergovernmental Panel on Climate Change [Core Writing Team, Pachauri, R.K and Reisinger, A. (eds.)]. IPCC, Geneva, Switzerland, 104 pp.
- IPCC, 2013: Climate Change 2013: The Physical Science Basis. Contribution of Working Group I to the Fifth Assessment Report of the Intergovernmental Panel on Climate Change [Stocker, T.F., D. Qin, G.-K. Plattner, M. Tignor, S.K. Allen, J. Boschung, A. Nauels, Y. Xia, V. Bex and P.M. Midgley (eds.)]. Cambridge University Press, Cambridge, United Kingdom and New York, NY, USA, 1535 pp.
- IPCC AR5, 2014: Climate Change 2014: Synthesis Report. Contribution of Working Groups I, II and III to the Fifth Assessment Report of the Intergovernmental Panel on Climate Change [Core Writing Team, R.K. Pachauri and L.A. Meyer (eds.)]. IPCC, Geneva, Switzerland, 151 pp.
- IPCC, 2018: Summary for Policymakers. In: Global warming of 1.5°C. An IPCC Special Report on the impacts of global warming of 1.5°C above pre-industrial levels and related global greenhouse gas emission pathways, in the context of strengthening the global response to the threat of climate change, sustainable development, and efforts to eradicate poverty [V. Masson-Delmotte, P. Zhai, H. O. Pörtner, D. Roberts, J. Skea, P. R. Shukla, A. Pirani, W. Moufouma-Okia, C. Péan, R. Pidcock, S. Connors, J. B. R. Matthews, Y. Chen, X. Zhou, M. I. Gomis, E. Lonnoy, T. Maycock, M. Tignor, T. Waterfield (eds.)]. World Meteorological Organization, Geneva, Switzerland, 32 pp

- Janssens-Maenhout, G., Crippa, M., Guizzardi, D., Muntean, M., Schaaf, E., Dentener, F., Bergamaschi, P., Pagliari, V., Olivier, J. G. J., Peters, J. A. H. W., van Aardenne, J. A., Monni, S., Doering, U., and Petrescu, A. M. R. 2017. EDGAR v4.3.2 Global Atlas of the three major Greenhouse Gas Emissions for the period 1970--2012. *Earth System Science Data Discussions*, 1–55, <https://doi.org/10.5194/essd-2017-79>.
- Jenden, P.D., Titley, P.A. & Worden, R.H. 2015. Enrichment of nitrogen and ^{13}C of methane in natural gases from the Khuff Formation, Saudi Arabia, caused by thermochemical sulfate reduction. *Organic Geochemistry*, 82, 54–68, <https://doi.org/10.1016/j.orggeochem.2015.02.008>.
- Ji, E.S. & Park, K. 2012. Methane and Nitrous Oxide Emissions from Livestock Agriculture in 16 Local Administrative Districts of Korea. *Asian-Aust. J. Anim. Sci.*, 25, 1768–1774.
- Johnson, K.A. & Johnson, D.E. 1995. Methane emissions from cattle. *Journal of animal science*, 73, 2483–2492, <https://doi.org/10.2527/1995.7382483x>.
- Johnson, K.A., Huyler, M.T., Westburg, H.H., Lamb, B.K. & Zimmerman, P. 1994. Johnson, K. A.; Huyler, M. T.; Westburg, H. H.; Lamb, B. K.; Zimmerman, P. Measurement of methane emissions from ruminant livestock using a SF₆ tracer technique. *Environmental Science and Technology*, 28, 359–362.
- Johnson, K.A., Kincaid, R.L., Westberg, H.H., Gaskins, C.T., Lamb, B.K. & Cronrath, J.D. 2002. The Effect of Oilseeds in Diets of Lactating Cows on Milk Production and Methane Emissions 1. *Journal of Dairy Science*, 85, 1509–1515, [https://doi.org/10.3168/jds.S0022-0302\(02\)74220-3](https://doi.org/10.3168/jds.S0022-0302(02)74220-3).
- Judd, M.J., Kellier, F.M., Ulyatt, M.J., Lassey, K.R., Tate, K.R., Shelton, D., Harvey, M.J., Walker, C.F. 1999. Net methane emissions from grazing sheep. *Global Change Biology*, 5, 647–657, <https://doi.org/10.1046/j.1365->

2486.1999.00264.x.

- Judd A.G. (2000) Geological Sources of Methane. In: Khalil M.A.K. (eds) Atmospheric Methane. Springer, Berlin, Heidelberg
- Karion, A., Sweeney, C., Pétron, G., Frost, G., Hardesty, R. M., Kofler, J., Miller, B. R., Newberger, T., Wolter, S., Banta, R., Brewer, A., Dlugokencky, E., Lang, P., Montzk, S. A., Schnell, R., Tans, P., Trainer, M., Zamora, R., & Conley, S. 2013. Methane emissions estimate from airborne measurements over a western United States natural gas field. *Geophysical Research Letters*, 40, 4393–4397, <https://doi.org/10.1002/grl.50811>.
- Kasischke, E.S. & Bruhwiler, L.P. 2003. Emissions of carbon dioxide , carbon monoxide , and methane from boreal forest fires in 1998. *Journal of Geophysical Research*, 108, <https://doi.org/10.1029/2001JD000461>.
- Keeling, C.D. 1958. The concentration and isotopic abundances of carbon dioxide in the atmosphere. *Geochimica et Cosmochimica Acta*, 13, 322–334.
- Keeling, C.D. 1961. The concentration and isotopic abundances of carbon dioxide in rural and marine air. *Geochimica et Cosmochimica Acta*, 24, 277–298.
- Kelliher FM, Clark H. 2010. Ruminants. In: Reay D, Smith P, van Amstel A, editors. Methane and climate change. London: Earthscan. p. 136–150.
- Kennett, J. P., K. G. Cannariato, I. L. Hendy, and R. J. Behl (2003), Methane Hydrates in Quaternary Climate Change: The Clathrate Gun Hypothesis, AGU, Washington, D. C.
- Keppler, F., Hamilton, J.T.G., Braß, M. & Röckmann, T. 2006. Methane emissions from terrestrial plants under aerobic conditions. *Nature*, 439, 187–191, <https://doi.org/10.1038/nature04420>.

- Keppler, F., Boros, H.M., Frankenberg, C., Lelieveld, J., McLeod, A., Pirttilä, A. M., Röckmann, T., Schnitzler, J-P. 2009. Methane formation in aerobic environments. CSIRO Publishing, 6, 459–465, <https://doi.org/10.1071/EN09137>.
- King, S.L., Quay, P.D. & Lansdown, J., M. 1989. The $^{13}\text{C}/^{12}\text{C}$ Kinetic Isotope Effect for Soil Oxidation of Methane increase. *Journal of Geophysical Research*, 94, 273–277.
- Kirschke, S., Bousquet, P., Ciais, P., Saunois, M., Canadell, J. G., Dlugokencky, E. J., Bergamaschi, P., Bergmann, D., Blake, D. R., Bruhwiler, L., Cameron-Smith, P., Castaldi, S., Chevallier, F., Feng, L., Fraser, A., Heimann, M., Hodson, E. L., Houweling, S., Josse, B., Fraser, P. J., Krummel, P. B., Lamarque, J. F., Langenfelds, R. L., Quéré, C., Naik, V., O'Doherty, S., Palmer, P. I., Pison, I., Plummer, D., Poulter, B., Prinn, R. G., Rigby, M., Ringeval, B., Santini, M., Schmidt, M., Shindell, D. T., Simpson, I. J., Spahni, R., Steele, L. P., Storde, S. A., Sudo, K., Szopa, S., Werf, G. R., Voulgarakis, A., Weele, M., Weiss, R. F., Williams, J. E., & Zeng, G. 2013. Three decades of global methane sources and sinks. *Nature Geoscience*, 6, 813–823, <https://doi.org/10.1038/ngeo1955>.
- Klevenhusen, F., Bernasconi, S.M., Hofstetter, T.B., Bolotin, J., Kunz, C. & Soliva, C.R. 2009. Efficiency of monolaurin in mitigating ruminal methanogenesis and modifying C-isotope fractionation when incubating diets composed of either C3 or C4 plants in a rumen simulation technique (Rusitec) system. *British Journal of Nutrition*, 102, 1308–1317, <https://doi.org/10.1017/S0007114509990262>.
- Kuwait Oil Company. 2016. Annual Report, Kuwait Oil Company.

- Kuwait Meteorological Centre, Directorate General of Civil Aviation, Climate history. [Online]. Available at:
http://www.met.gov.kw/Climate/climate_hist.php?lang=engwww.met.gov.kw.
 [April 2015]
- Lansdown, 1992. J.M., The carbon and hydrogen stable isotope composition of methane released from wetlands and ruminants, Unpublished Ph.D. dissertation, University of Washington Seattle, 1992.: The Public Authority of Agriculture and Fish Resources/ Statistics Department 2015-2016
- Lakshmi, P., Rao, S., Rasheed, M.A., Hasan, S.Z., Rao, P.H. & Harinarayana, T. 2014. Role of Geochemistry in Coalbed Methane -A Review. *Geosciences*, 4, 29–32, <https://doi.org/10.5923/j.geo.20140402.01>.
- Lassey, K.R. 2007. Livestock methane emission: From the individual grazing animal through national inventories to the global methane cycle. *Agricultural and Forest Meteorology*, 142, 120–132, <https://doi.org/10.1016/j.agrformet.2006.03.028>.
- Lassey, K.R., Walker, C.F., McMillan, A.M.S. & Ulyatt, M.J. 2001. On the performance of SF₆ permeation tubes used in determining methane emission from grazing livestock. *Chemosphere - Global Change Science*, 3, 367–376, [https://doi.org/10.1016/S1465-9972\(01\)00017-4](https://doi.org/10.1016/S1465-9972(01)00017-4).
- Leng, L., Zhang, T., Kleinman, L. & Zhu, W. 2007. Ordinary least square regression, orthogonal regression, geometric mean regression and their applications in aerosol science. *Journal of Physics: Conference Series*, 78, <https://doi.org/10.1088/1742-6596/78/1/012084>.
- Lerner, J. & Matthews, E. 1988. Methane Emission from animals: A global high-resolution data base. *Global Biogeochemical Cycles*, 2, 139–156.

- Levin, I., Bergamaschi, P., Dorr, H. & Trapp, D. 1993. Stable Isotopic Signature of Methane From Major sources in Germany . *Chemosphere*, 26, 161–177.
- Levin, I., Glatzel-Mattheier, H., Marik, T., Cuntz, M., Schmidt, M. & Worthy, D.E. 1999. Verification of German methane emission inventories and their recent changes based on atmospheric observations. *Journal of Geophysical Research*, 104, 3447–3456, <https://doi.org/10.1029/1998JD100064>.
- Levine J. 2010. Biomass burning. In: Reay D, Smith P, van Amstel A, editors. Methane and climate change. Earthscan. p. 97–114.
- Liptay, K., Chanton, J., Czepiel, P. & Mosher, B. 1998. Use of stable isotopes to determine methane oxidation in landfill cover soils. *Journal of Geophysical Research*, 1.3, 8243–8250.
- Liu, J., Chen, H., Zhu, Q., Shen, Y., Wang, X. & Wang, M. 2015. Review article A novel pathway of direct methane production and emission by eukaryotes including plants , animals and fungi : An overview. *Atmospheric Environment*, 115, 26–35, <https://doi.org/10.1016/j.atmosenv.2015.05.019>.
- Loulergue, L., Schilt, A., Spahni, R., Masson-Delmotte, V., Blunier, T., Lemieux, B., Barnola, J-M., Raynaud, D., Stocker, T.F. and Chappellaz, J . 2008. Orbital and millennial-scale features of atmospheric CH₄ over the past 800,000 years. *Nature*, 453, 383.
- Lowe, D.C., Brenninkmeijer, C.A.M., Brailsford, G.W., Lassey, K.R., Gomez, A.J. & Nisbet, E.G. 1994. Concentration and ¹³C records of atmospheric methane in New Zealand and Antarctica: Evidence for changes in methane sources. *Journal of Geophysical Research*, 99, 16913, <https://doi.org/10.1029/94JD00908>.

- Lowry, D., Holmes, C.W., Rata, N.D., O'Brien, P. & Nisbet, E.G. 2001. London methane emissions: Use of diurnal changes in concentration and $\delta^{13}\text{C}$ to identify urban sources and verify inventories. *Journal of Geophysical Research: Atmospheres*, 106, 7427–7448, <https://doi.org/10.1029/2000JD900601>.
- Marchese, A. J., Zimmerle, D., Vaughn, T. L., Martinez, D., Williams, L. L., Robinson, A. L., Mitchell, A. L., Subramanian, R., Tkacik, D. S., Roscioli, J. R., Herndon, S. C 2015. Methane Emissions from United States Natural Gas Gathering and Processing. *Environmental Science and Technology*, 49, 10718–10727, <https://doi.org/10.1021/acs.est.5b02275>.
- Masiol, M., Hopke, P.K., Felton, H.D., Frank, B.P., Rattigan, O. V., Wurth, M.J. & LaDuke, G.H. 2017. Analysis of major air pollutants and submicron particles in New York City and Long Island. *Atmospheric Environment*, 148, 203–214, <https://doi.org/10.1016/j.atmosenv.2016.10.043>.
- Maslin, M., Owen, M., Betts, R., Day, S., Jones, T.D. & Ridgwell, A. 2010. Gas hydrates: past and future geohazard? *Philosophical Transactions of the Royal Society of London A*, 368, 2369–2393, <https://doi.org/10.1098/rsta.2010.0065>.
- Matthews, E. & Fung, I. 1987. Methane emission from natural wetlands: Global distribution, area, and environmental characteristics of sources. *Global biogeochemical cycles*, 1, 61–86.
- McAllister, T.A., Cheng, K.-J., Okine, E.K. & Mathison, G.W. 1996. Dietary, environmental and microbiological aspects of methane production in ruminants. *Canadian Journal of Animal Science*, 76, 231–243, <https://doi.org/10.4141/cjas96-035>.
- McDougall, F.R., White, P.R., Franke, M., Hindle, P. 2001. *Integrated Waste Management: A Life Cycle Inventory*, second ed. Wiley-Blackwell, Oxford, UK.

- Meier-Augenstein, W. 1999. Applied gas chromatography coupled to isotope ratio mass spectrometry. *Journal of Chromatography A*, 842, 351–371, [https://doi.org/10.1016/S0021-9673\(98\)01057-7](https://doi.org/10.1016/S0021-9673(98)01057-7).
- Mikaloff Fletcher, S.E., Tans, P.P., Bruhwiler, L.M., Miller, J.B. & Heimann, M. 2004. CH₄ sources estimated from atmospheric observations of CH₄ and its ¹³C/¹²C isotopic ratios: 2. Inverse modeling of CH₄ fluxes from geographical regions. *Global Biogeochemical Cycles*, 18, 1–15, <https://doi.org/10.1029/2004GB002224>.
- Miller, J.B. & Tans, P.P. 2003. Calculating isotopic fractionation from atmospheric measurements at various scales. *Tellus, Series B: Chemical and Physical Meteorology*, 55B, 207–214, <https://doi.org/10.1034/j.1600-0889.2003.00020.x>.
- Millson, J.A., Quin, J.G., Idiz, E., Turner, P. & Al-Harthi, A. 2008. The Khazzan gas accumulation, a giant combination trap in the Cambrian Barik Sandstone Member, Sultanate of Oman: Implications for Cambrian petroleum systems and reservoirs. *AAPG Bulletin*, 92, 885–917, <https://doi.org/10.1306/02210807100>.
- Mitchell, A.L., Tkacik, D.S., Roscioli, J.R., Herndon, S.C., Yacovitch, T.I., Martinez, D.M., Vaughn, T.L., Williams, L.L., Sullivan, M.R., Floerchinger, C., Omara, M., Subramanian, R., Zimmerle, D., Marchese, A.J. and Robinson, A.L. 2015. Measurements of methane emissions from natural gas gathering facilities and processing plants: Measurement methods. *Atmospheric Measurement Techniques*, 8, 2017–2035, <https://doi.org/10.5194/amt-8-2017-2015>.
- Mønster, J.G., Samuelsson, J., Kjeldsen, P., Rella, C.W. & Scheutz, C. 2014. Quantifying methane emission from fugitive sources by combining tracer release and downwind measurements - A sensitivity analysis based on

- multiple field surveys. *Waste Management*, 34, 1416–1428, <https://doi.org/10.1016/j.wasman.2014.03.025>.
- Moriizumi, J., Nagamine, K., Iida, T. & Ikebe, Y. 1998. Carbon isotopic analysis of atmospheric methane in urban and suburban areas: Fossil and non-fossil methane from local sources. *Atmospheric Environment*, 32, 2947–2955, [https://doi.org/10.1016/S1352-2310\(98\)00014-4](https://doi.org/10.1016/S1352-2310(98)00014-4).
- Morino, I., Uchino, O., Inoue, M., Yoshida, Y., Yokota, T., Wennberg, P., Toon, G., Wunch, D., Roehl, C. M., Notholt, J., Warneke, T., Messerschmidt, J., Griffith, D. W., Deutscher, N. M., Sherlock, V., Connor, B., Robinson, J., Sussmann, R. & Rettinger, M. 2011. Preliminary validation of column-averaged volume mixing ratios of carbon dioxide and methane retrieved from GOSAT short-wavelength infrared spectra. *Atmospheric Measurement Techniques*, 4, 1061–1076, <https://doi.org/10.5194/amt-4-1061-2011>.
- Muqem, S.H. 2009. Assessment of Management Practices of Operating Municipal Solid Waste Landfill Sites in the State of Kuwait”. Unpublished MS.C. dissertation, Arabian Gulf University, Bahrain.
- Nakagawa, F., Tsunogai, U., Komatsu, D.D., Yamada, K., Yoshida, N., Moriizumi, J., Nagamine, K., (...), Ikebe, Y. 2005. Automobile exhaust as a source of ^{13}C - and D-enriched atmospheric methane in urban areas. *Organic Geochemistry*, 36, 727–738, <https://doi.org/10.1016/j.orggeochem.2005.01.003>.
- NAEI: National Atmospheric Emission Inventory 2018. UK Emission Mapping Methodology. A report of the National Atmospheric Emission Inventory-2016. Obtained from: http://naei.beis.gov.uk/reports/reports?report_id=973
- NASEM - National Academies of Sciences, Engineering, and Medicine. 2018. Improving Characterization of Anthropogenic Methane Emissions in the United States. Washington, DC: The National Academies Press. doi:

<https://doi.org/10.17226/24987>.

Neef, L., Weele, M. Van & Velthoven, P. Van. 2010. Optimal estimation of the present - day global methane budget. *Global biogeochemical cycles*, 24, 1–10, <https://doi.org/10.1029/2009GB003661>.

Nisbet, E.G., Dlugokenckt, E.J. & Bousquet, P. 2014. Methane on the Rise-Again. *science*, 343, 493–495.

Nisbet, E. G., Dlugokencky, E. J., Manning, M. R., Lowry, D., Fisher, R. E., France, J. L., Michel, S. E., Miller, J. B., White, J. W. C., Vaughn, B., Bousquet, P., Pyle, J. A., Warwick, N. J., Cain, M., Brownlow, R., Zazzeri, G., Lanoisellé, M., Manning, A. C., Gloor, E., Worthy, D. E. J., Brunke, E. G., Labuschagne, C., Wolff, E. W., & Ganesan, A. L. 2016. Rising atmospheric methane: 2007-2014 growth and isotopic shift. *Global Biogeochemical Cycles*, 30, 1356–1370, <https://doi.org/10.1002/2015GB005349>. Received.

NOAA. National Oceanic and Atmospheric Administration: available at: <http://www.esrl.noaa.gov/gmd/ccl/>. [Accessed: 2015-01-16].

OPEC ASB 'Annual Statistical Bulletin. Annual report 2018. 53rd edition. Available at <https://asb.opec.org/>

Openair. Open-source tools for air pollution data analysis. [Online]. Available at: <http://www.openair-project.org/>. [Accessed: 2017-09-06]

Page, S.E., Siegert, F., Rieley, J.O., Boehm, H. V, Jaya, A. & Limin, S. 2002. The amount of carbon released from peat and forest fires in Indonesia during 1997. *Letters to Nature*, 1999, 61–65, <https://doi.org/10.1038/nature01141.1>.

- Pallasser, R.J. 2000. Recognising biodegradation in gas / oil accumulations through the $\delta^{13}\text{C}$ compositions of gas components. *Organic Geochemistry*, 31, 1363–1373.
- Pangala, S.R., Hornibrook, E.R.C., Gowing, D.J. & Gauci, V. 2015. The contribution of trees to ecosystem methane emissions in a temperate forested wetland. *Global Change Biology*, 21, 2642–2654, <https://doi.org/10.1111/gcb.12891>.
- Pangala, S.R., Enrich-Prast, A., Basso, L.S., Peixoto, R.B., Bastviken, D., Hornibrook, E.R.C., Gatti, L.V., Marotta, H., Calazans, L.S.B., Sakuragui, C.M., Bastos, W.R., Malm, O., Gloor, E., Miller, J.B., Gauci, V. 2017. Large emissions from floodplain trees close the Amazon methane budget. *Nature*, 552, 230–234, <https://doi.org/10.1038/nature24639>.
- Pataki, DE, Ehleringer, JR, Flanagan, LB, Yakir, D, Bowling, DR, Still, CJ, Buchmann, N, Kaplan, JO, Berry, JA. 2003. The application and interpretation of Keeling plots in terrestrial carbon cycle research. *Global Biogeochemical Cycles*, 17, Issue 1. <https://doi.org/10.1029/2001GB001850>.
- Picarro, 2012. Picarro Mobile Kit User's Guide 40047 Revision B. [Online].
- Picarro. [Online]. Available at: <http://www.picarro.com>. [Accessed: 2016-02-23]
- Phillips, N.G., Ackley R., Crosson, E.R., Downd, A., Huttyra, L.R., Brondfield, M., Karr, J.D, Zhao, K., Jackson, R.P., 2013. Mapping urban pipeline leaks: Methane leaks across Boston. *Environmental Pollution*, 173, 1–4, <https://doi.org/10.1016/j.envpol.2012.11.003>.
- Rice D. D., 1992. Controls, habitat, and resource potential of ancient bacterial gas,"in *Bacterial Gas*, R. Vially, Ed., pp. 91–118, Éditions Technip, 1992

- Reay D. S. Smith K. A. & Hewitt C. N. 2007a. Methane: Importance, Sources and Sinks. In Reay, D. S., Hewitt, C. N., Smith, K. A. & Grace J., Greenhouse Gas Sinks. Athenaeum Press Ltd, Gateshead
- Reay, D. S., Hewitt, C. N., Smith, K. A. & Grace J., 2007b. Greenhouse Gas Sinks. Athenaeum Press Ltd, Gateshead
- Reay D, Smith P, van Amstel A, editors. 2010. Methane and climate change. London:
- Reay, D.S., Smith, P., Christensen, T.R., James, R.H. & Clark, H. 2018. Methane and Global Environmental Change. *Annual Review of Environmental Resources*, 43, 165–192.
- Rella, C.W., Hoffnagle, J., He, Y. & Tajima, S. 2015. Local- and regional-scale measurements of CH₄, $\delta^{13}\text{CH}_4$, and C₂H₆ in the Uintah Basin using a mobile stable isotope analyzer. *Atmospheric Measurement Techniques*, 8, 4539–4559, <https://doi.org/10.5194/amt-8-4539-2015>.
- Reeburgh, W.S. 2003. Global methane biogeochemistry. In: Holland, H. D. and Turekian K. K. eds., *Treatise on Geochemistry, The Atmosphere*, vol. 4, Elsevier-Pergamon, Oxford, 65–89.
- Rice, D.D. 1992. Controls, habitat, and resource potential of ancient bacterial gas. Bacterial gas. Proc. conference, Milan, 1989, 91–118.
- Richardson, S.J., Miles, N.L., Davis, K.J., Crosson, E.R., Rella, C.W. & Andrews, A.E. 2012. Field testing of cavity ring-down spectroscopy analyzers measuring carbon dioxide and water vapor. *Journal of Atmospheric and Oceanic Technology*, 29, 397–406, <https://doi.org/10.1175/JTECH-D-11-00063.1>.

- Rigby, M., R. G. Prinn, P. J. Fraser, P. G. Simmonds, R. L. Langenfelds, J. Huang, D. M. Cunnold, L. P. Steele, P. B. Krummel, R. F. Weiss, S. O'Doherty, P. K. Salameh, H. J. Wang, C. M. Harth, J. Muhle, and L. W. Porter. 2008. Renewed growth of atmospheric methane. *Geophysical Research Letters*, 35, <https://doi.org/10.1029/2008GL036037>.
- Rigby, M., Stephen A. Montzka, Ronald G. Prinn, James W. C. White, Dickon Younga, Simon O'Dohertya, Mark F. Lunta, Anita L. Ganesane, Alistair J. Manningf, Peter G. Simmondsa, Peter K. Salamehg, Christina M. Harthg, Jens Mühleg, Ray F. Weissg, Paul J. Fraserh, L. Paul Steeleh, Paul B. Krummelh Archie McCullocha, and Sunyoung Park, . 2017. Role of atmospheric oxidation in recent methane growth. *Proceedings of the National Academy of Sciences*, 114, 5373–5377, <https://doi.org/10.1073/pnas.1616426114>.
- Rolph, G., Stein, A. & Stunder, B. 2017. Real-time Environmental Applications and Display sYstem: READY. *Environmental Modelling and Software*, 95, 210–228, <https://doi.org/10.1016/j.envsoft.2017.06.025>.
- Rust, F. 1981. Ruminant Methane $\delta(13C/12C)$ Values: Relation to Atmospheric Methane. *American Association for the Advancement of Science*, 211, 1044–1046.
- Saadati, H., Al-Iessa, H.J., Alizadeh, B., Tarhandeh, E., Jazayeri, M.H., Bahrami, H. & Rashidi, M. 2016. Geochemical characteristics and isotopic reversal of natural gases in eastern Kopeh-Dagh, NE Iran. *Marine and Petroleum Geology*, 78, 76–87, <https://doi.org/10.1016/j.marpetgeo.2016.09.004>.
- Saberi, M.H. & Rabbani, A.R. 2015. Origin of natural gases in the Permo-Triassic reservoirs of the Coastal Fars and Iranian sector of the Persian Gulf. *Journal of Natural Gas Science and Engineering*, 26, 558–569, <https://doi.org/10.1016/j.jngse.2015.06.045>.

- Shallcross D. E., Khalil M. A. K. Khalil and Butenhoff C. L. 2007. The atmospheric methane sink. Chapter 11 in R Reay, D. S., Hewitt, C. N., Smith, K. A. & Grace J., 2007. Greenhouse Gas Sinks. Athenaeum Press Ltd, Gateshead
- Sanderson, M.G. 1996. Biomass of termites and their emissions of methane and carbon dioxide : A global database. *Global biogeochemical cycles*, 10, 543–557.
- Saunois, M., Bousquet, P., Poulter, B., Peregon, A., Ciais, P., Canadell, J. G., Dlugokencky, E. J., Etiope, G., Bastviken, D., Houweling, S., Janssens-Maenhout, G., Tubiello, F. N., Castaldi, S., Jackson, R. B., Alexe, M., Arora, V. K., Beerling, D. J., Bergamaschi, P., Blake, D. R., Brailsford, G., Brovkin, V., Bruhwiler, L., Crevoisier, C., Crill, P., Covey, K., Curry, C., Frankenberg, C., Gedney, N., Höglund-Isaksson, L., Ishizawa, M., Ito, A., Joos, F., Kim, H. S., Kleinen, T., Krummel, P., Lamarque, J. F., Langenfelds, R., Locatelli, R., Machida, T., Maksyutov, S., McDonald, K. C., Marshall, J., Melton, J. R., Morino, I., Naik, V., O'Doherty, S., Parmentier, F. J. W., Patra, P. K., Peng, C., Peng, S., Peters, G. P., Pison, I., Prigent, C., Prinn, R., Ramonet, M., Riley, W. J., Saito, M., Santini, M., Schroeder, R., Simpson, I. J., Spahni, R., Steele, P., Takizawa, A., Thornton, B. F., Tian, H., Tohjima, Y., Viovy, N., Voulgarakis, A., Weele, M., Werf, G. R., Weiss, R., Wiedinmyer, C., Wilton, D. J., Wiltshire, A., Worthy, D., Wunch, D., Xu, X., Yoshida, Y., Zhang, B., Zhang, Z., & Zhu, Q. 2016. The global methane budget 2000-2012. *Earth System Science Data*, 8, 697–751, <https://doi.org/10.5194/essd-8-697-2016>.
- Schaefer, H., Fletcher, S. E. M., Veidt, C., Lassey, K. R., Brailsford, G. W., Bromley, T. M., Dlugokencky, E. J., Michel, S. E., Miller, J. B., Levin, I., Lowe, D. C., Martin, R. J., Vaughn, B. H., & White, J. W. C. 2016. A 21st century shift from fossil-fuel to biogenic methane emissions indicated by 13 CH₄. *Science*, 2705, 1–10, <https://doi.org/10.1126/science.aad2705> (2016).

- Schulze, E., Lohmeyer, S. & Giese, W. 1998. Determination of $^{13}\text{C}/^{12}\text{C}$ -ratios in rumen produced methane and CO_2 of cows, sheep and camels. *Isotopes in Environmental and Health Studies*, 34, 75–79, <https://doi.org/10.1080/10256019708036334>.
- Schwietzke, S., Matthews, H.S. & Bruhwiler, L.M.P. 2014. Global Bottom-Up Fossil Fuel Fugitive Methane and Ethane Emissions Inventory for Atmospheric Modeling. *ACS Sustainable Chem. Eng.*, 2, 1992–2001, <https://doi.org/10.1021/sc500163h>.
- Schwietzke, S., Sherwood, O. A., Bruhwiler, L. M. P., Miller, J. B., Etiope, G., Dlugokencky, E. J., Michel, S. E., Arling, V. A., Vaughn, B. H., White, J. W. C., & Tans, P. P. 2016. Upward revision of global fossil fuel methane emissions based on isotope database. *Nature*, 538, 88–91, <https://doi.org/10.1038/nature19797>.
- Shakhova, N., Semiletov, I., Salyuk, A., Yusupov, V., Kosmach, D. & Gustafsson, O. 2010. Extensive Methane Venting to the Atmosphere from Sediments of the East Siberian Arctic Shelf. *Science*, 1246–1251.
- Sherwood, O.A., Schwietzke, S., Arling, V.A. & Etiope, G. 2017. Global Inventory of Gas Geochemistry Data from Fossil Fuel , Microbial and Burning Sources , version 2017. *Earth System Science Data*, 9, 639–656.
- Simmonds, P.G., Manning, A.J., Derwent, R.G., Ciais, P., Ramonet, M., Kazan, V. & Ryall, D. 2005. A burning question. Can recent growth rate anomalies in the greenhouse gases be attributed to large-scale biomass burning events ? *Atmospheric Environment*, 39, 2513–2517, <https://doi.org/10.1016/j.atmosenv.2005.02.018>.
- Simpson, I.J., Blake, D.R. & Rowland, F.S. 2002. Implications of the recent fluctuations in the growth rate of tropospheric methane. *Geophysical Research*

- Letters, 29, 1998–2001.
- Storm, I.M.L.D., Hellwing, A.L.F., Nielsen, N.I. & Jørgen, M. 2012. Methods for Measuring and Estimating Methane Emission from Ruminants. *Animals*, 2, 160–183, <https://doi.org/10.3390/ani2020160>.
- Sturm, P., Leuenberger, M. & Schmidt, M. 2005. Atmospheric O₂, CO₂ and $\delta^{13}\text{C}$ observations from the remote sites Jungfraujoch, Switzerland, and Puy de Dôme, France. *Geophysical Research Letters*, 32, 1–4, <https://doi.org/10.1029/2005GL023304>.
- Sussmann, R., Forster, F., Rettinger, M. & Bousquet, P. 2012. Renewed methane increase for five years (2007–2011) observed by solar FTIR spectrometry. *Atmospheric Chemistry and Physics*, 12, 4885–4891, <https://doi.org/10.5194/acp-12-4885-2012>.
- Swinehart, D.F. 1962. The Beer-Lambert Law. *Journal of Chemical Education*, 39, 333, <https://doi.org/10.1021/ed039p333>.
- Tang, Y., Perry, J.K., Jenden, P.D. & Schoell, M. 2000. Mathematical modeling of stable carbon isotope ratios in natural gases. *Geochimica et Cosmochimica Acta*, 64, 2673–2687, [https://doi.org/10.1016/s0016-7037\(00\)00377-x](https://doi.org/10.1016/s0016-7037(00)00377-x).
- Thompson, A.M. 1992. The Oxidizing Capacity of the Earth's Atmosphere : Probable Past and Future Changes. *Science*, 256, 1157–1166.
- Townsend-Small, A., Tyler, S.C., Pataki, D.E., Xu, X. & Christensen, L.E. 2012. Isotopic measurements of atmospheric methane in Los Angeles, California, USA: Influence of 'fugitive' fossil fuel emissions. *Journal of Geophysical Research Atmospheres*, 117, 1–11, <https://doi.org/10.1029/2011JD016826>.

- Townsend-Small, A., Botner, E. C., Jimenez, K. L., Schroeder, J. R., Blake, N. J., Meinardi, S., Blake, D. R., Sive, B. C., Bon, D., Crawford, J. H., Pfister, G., & Flocke, F. M. 2016. using stable isotopes of hydrogen to quantify biogenic and thermogenic atmospheric methane sources: A case study from the Colorado Front Range. *Geophysical Research Letters*, 43, 11,462-11,471, <https://doi.org/10.1002/2014GL059364>.Received.
- Toyoda, S., Suzuki, Y., Hattori, S., Yamada, K., Fujii, A., Yoshida, N., Kouno, R., Murayama, K., and Shiomi, H. 2011. Isotopomer analysis of production and consumption mechanisms of N₂O and CH₄ in an advanced wastewater treatment system. *Environmental Science and Technology*, 45, 917–922, <https://doi.org/10.1021/es102985u>.
- Tsuruta, A., Aalto, T., Backman, L., Hakkarainen, J., van der Laan-Luijkx, I. T., Krol, M. C., Spahni, R., Houweling, S., Laine, M., Dlugokencky, E., Gomez-Pelaez, A. J., van der Schoot, M., Langenfelds, R., Ellul, R., Arduini, J., Apadula, F., Gerbig, C., Feist, D. G., Kivi, R., Yoshida, Y., and Peters, W. 2016. Development of CarbonTracker Europe - CH₄ - Part 2: global methane emission estimates and their evaluation for 2000-2012. *Geoscientific Model Development Discussions*, 1–52, <https://doi.org/10.5194/gmd-2016-182>.
- Tyler, S.C., Chrill, P.M. & Brailsford G.W. 1994. ¹³C/¹²C Fractionation of methane during oxidation in temperate forested soil. *Geochimica et Cosmochimica Acta*, 58, 1625–1633.
- Ulyatt, M.J., Baker, S.K., McCrabb, G.J. & Lassey, K.R. 1999. Accuracy of SF₆ tracer technology and alternatives for field measurements. *Australian Journal of Agricultural Research*, 50, 1329–1334, <https://doi.org/10.1071/AR99003>.
- Uria-Tellaetxe, I. & Carslaw, D.C. 2014. Conditional bivariate probability function for source identification. *Environmental Modelling and Software*, 59, 1–9,

<https://doi.org/10.1016/j.envsoft.2014.05.002>.

- USEPA. U.S. Environmental Protection Agency 2012. Global Anthropogenic Non-CO₂ Greenhouse Gas Emissions: 1990-2030. EPA 430-R-12-006. Washington, DC: USEPA. Obtained from: <https://www.epa.gov/global-mitigation-non-co2-greenhouse-gases/global-anthropogenic-non-co2-greenhouse-gas-emissions>
- USEPA. U.S. Environmental Protection Agency 2013. global mitigation of non-CO₂ greenhouse gases: 2010-2030. EPA 430-R-13-011. Washington, DC: USEPA. Obtained from: https://www.epa.gov/sites/production/files/2016-06/documents/mac_report_2013.pdf
- USEPA. U.S. Environmental Protection Agency 2017. Inventory of U.S greenhouse gas emissions and sinks: 1990-2016. EPA 430-P-17-001. Washington, DC: USEPA. Obtained from: <https://www.epa.gov/ghgemissions/inventory-us-greenhouse-gas-emissions-and-sinks-1990-2015>
- Van Amstel, A. 2012. Methane . A review. *Journal of Integrative Environmental Sciences*, 9:sup1, 5–30, <https://doi.org/10.1080/1943815X.2012.694892>.
- Van Eekert M. H. A., Jan van Dooren H., Lexmond M. and Zeeman G. 2007 Wastewater and Manure. In R Reay, D. S., Hewitt, C. N., Smith, K. A. & Grace J., 2007. *Greenhouse Gas Sinks*. Athenaem Press Ltd, Gateshead
- van Eekert M. H. A., Jan van Dooren H., Lexmond M. and Zeeman G. 2010. Chapter 10: Wastewater and Manure.. In: Reay D, Smith P, van Amstel A, editors. *Methane and climate change*. Earthscan. p. 151–170.
- Vardag, S.N., Hammer, S. & Levin, I. 2016. Evaluation of 4 years of continuous $\delta^{13}\text{C}(\text{CO}_2)$ data using a moving Keeling plot method. *Biogeosciences*, 13, 4237–4251, <https://doi.org/10.5194/bg-13-4237-2016>.

- Vigano I, Roßckmann T, Holzinger R, van Dijk A, Keppler F, Greule M, Brand WA, Geilmann H, van Weelden H. 2009. The stable isotope signature of methane emitted from plant material under UV irradiation. *Atmospheric Environment*, 43, 5637–5646, <https://doi.org/10.1016/j.atmosenv.2009.07.046>.
- Voulgarakis, A., Naik, V., Lamarque, J.-F., Shindell, D. T., Young, P. J., Prather, M. J., Wild, O., Field, R. D., Bergmann, D., Cameron-Smith, P., Cionni, I., Collins, W. J., Dalsøren, S. B., Doherty, R. M., Eyring, V., Faluvegi, G., Folberth, G. A., Horowitz, L. W., Josse, B., MacKenzie, I. A., Nagashima, T., Plummer, D. A., Righi, M., Rumbold, S. T., Stevenson, D. S., Strode, S. A., Sudo, K., Szopa, S., and Zeng, G. 2013. Analysis of present day and future OH and methane lifetime in the ACCMIP simulations. *Atmospheric Chemistry and Physics*, 13, 2563–2587, <https://doi.org/10.5194/acp-13-2563-2013>.
- Wahlen, M., Tanaka, N., Henry, R., Deck, B., Zeglen, J., Vogel, J., Southon, J., Shemesh, A., Fairbanks, R. and Broecker, W. 1989. Carbon-14 in Methane Sources and Atmospheric Methane: The Contribution from Fossil Carbon. *American Association for the Advancement of Science*, 245, 286–290.
- Wang-Yao, K., Towprayoon, S., Chiemchaisri, C., Gheewala, S.H. & Nopharatana, A. 2006. Seasonal Variation of Landfill Methane Emissions from Seven Solid Waste Disposal Sites in Central Thailand. In: *The 2th Joint International Conference on ‘Sustainable Energy and Environment (SEE2006)’*.
- Wang, P., Zhou, W., Niu, Z., Cheng, P., Wu, S., Xiong, X., Lu, X., and Du, H. 2018. Emission characteristics of atmospheric carbon dioxide in Xi'an, China based on the measurements of CO₂ concentration, $\delta^{14}\text{C}$ and $\delta^{13}\text{C}$. *Science of the Total Environment*, 619–620, 1163–1169, <https://doi.org/10.1016/j.scitotenv.2017.11.125>.

- Westbrook, G. K., Thatcher, K. E., Rohling, E. J., Piotrowski, A. M., Pälike, H., Osborne, A. H., Nisbet, E. G., Minshull, T. A., Lanoisellé, M., James, R. H., Hühnerbach, V., Green, D., Fisher, R. E., Crocker, A. J., Chabert, A., Bolton, C., BeszczynskaMöller, A., Berndt, C., and Aquilina, A 2009. Escape of methane gas from the seabed along the West Spitsbergen continental margin. *Geophysical Research Letters*, 36, 1–5, <https://doi.org/10.1029/2009GL039191>.
- Whiticar, M.J. 1996. Stable isotope geochemistry of coals, humic kerogens and related natural gases. *International Journal of Coal Geology*, 32, 191–215, [https://doi.org/10.1016/S0166-5162\(96\)00042-0](https://doi.org/10.1016/S0166-5162(96)00042-0).
- Whiticar, M.J., Faber, E. & Schoell, M. 1986. Biogenic methane formation in marine and freshwater environments: CO₂ reduction vs. acetate fermentation-Isotope evidence. *Geochimica et Cosmochimica Acta*, 50, 693–709, [https://doi.org/10.1016/0016-7037\(86\)90346-7](https://doi.org/10.1016/0016-7037(86)90346-7).
- Widory, D., Proust, E., Bellenfant, G. & Bour, O. 2012. Assessing methane oxidation under landfill covers and its contribution to the above atmospheric CO₂ levels: The added value of the isotope ($\delta^{13}\text{C}$ and $\delta^{18}\text{O}$ CO₂; $\delta^{13}\text{C}$ and δD CH₄) approach. *Waste Management*, 32, 1685–1692, <https://doi.org/10.1016/j.wasman.2012.04.008>.
- Wishkerman, A., Greiner, S., Ghyczy, M., Boros, M., Rausch, T., Lenhart, K. & Keppler, F. 2011. Enhanced formation of methane in plant cell cultures by inhibition of cytochrome c oxidase. *Plant, Cell & Environment*, 34, 457–464, <https://doi.org/10.1111/j.1365-3040.2010.02255.x>.
- WMO 2018. WMO Greenhouse Gas Bulletin. No. 14. [Online]. Available at: <https://public.wmo.int/en/resources/library/wmo-greenhouse-gas-bulletin>. [Accessed: 10-12-2018]

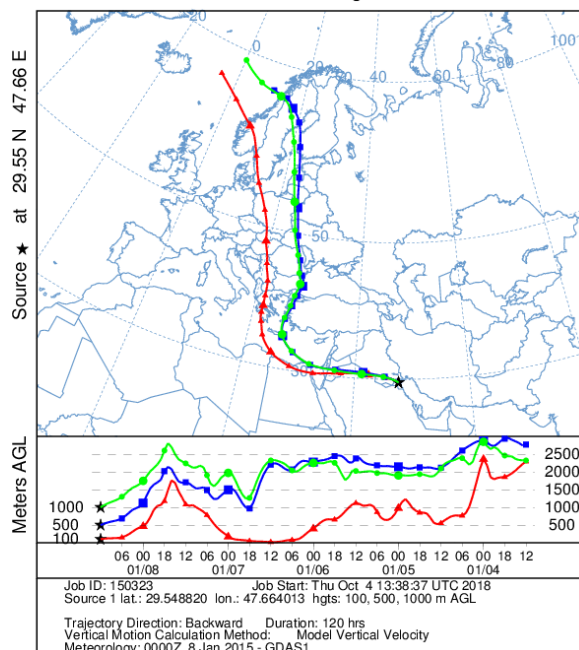
- Worden, J. R., Bloom, A. A., Pandey, S., Jiang, Z., Worden, H. M., Walker, T. W., Houweling, S., & Röckmann, T. 2017. Reduced biomass burning emissions reconcile conflicting estimates of the post-2006 atmospheric methane budget. *Nature Communications*, 8, 1–11, <https://doi.org/10.1038/s41467-017-02246-0>.
- Worden, R.H. & Smalley, P.C. 1996. H₂S-producing reactions in deep carbonate gas reservoirs: Khuff Formation, Abu Dhabi. *Chemical Geology*, 133, 157–171, [https://doi.org/10.1016/S0009-2541\(96\)00074-5](https://doi.org/10.1016/S0009-2541(96)00074-5).
- World Meteorological Organization (WMO), 2018. Kuwait Weather Information Service, available at <http://worldweather.wmo.int/en/city.html?cityId=217>
- Worthy, D.E.J., Levin, I., Trivett, N.B.A., Kuhlmann, A.J., Hopper, J.F. & Ernst, M.K. 1998. Seven years of continuous methane observations at a remote boreal site in Ontario, Canada. *Journal of Geophysical Research Atmospheres*, 103, 15995–16007, <https://doi.org/10.1029/98JD00925>.
- Wuebbles, D.J. & Hayhoe, K. 2002. Wuebbles & Hayhoe 2002-atmospheric methane.pdf. 57, 177–210.
- Yamada, K., Yoshida, N., Nakagawa, F. & Inoue, G. 2005. Source evaluation of atmospheric methane over western Siberia using double stable isotopic signatures. *Organic Geochemistry*, 36, 717–726, <https://doi.org/10.1016/j.orggeochem.2005.01.016>.
- Yan, X., Akiyama, H., Yagi, K. & Akimoto, H. 2009. Global estimations of the inventory and mitigation potential of methane emissions from rice cultivation conducted using the 2006 Intergovernmental Panel on Climate Change Guidelines. *Global biogeochemical cycles*, 23, <https://doi.org/10.1029/2008GB003299>.

- Yoshida, H., Mønster, J. & Scheutz, C. 2014. Plant-integrated measurement of greenhouse gas emissions from a municipal wastewater treatment plant. *Water Research*, 61, 108–118, <https://doi.org/10.1016/j.watres.2014.05.014>.
- Zazzeri, G. 2015. Methane Emissions in UK: Deciphering Regional Sources with Mobile Measurements and Isotopic Characterisation. Royal Holloway, University of London.
- Zazzeri, G., Lowry, D., Fisher, R.E., France, J.L., Lanoisellé, M. & Nisbet, E.G. 2015. Plume mapping and isotopic characterisation of anthropogenic methane sources. *Atmospheric Environment*, 110, 151–162, <https://doi.org/10.1016/j.atmosenv.2015.03.029>.
- Zazzeri, G., Lowry, D., Fisher, R.E., France, J.L., Lanoisellé, M., Grimmond, C.S.B. & Nisbet, E.G. 2017. Evaluating methane inventories by isotopic analysis in the London region. *Scientific Reports*, 7, 1–13, <https://doi.org/10.1038/s41598-017-04802-6>.
- Zhou, L.X., Worthy, D.E.J., Lang, P.M., Ernst, M.K., Zhang, X.C., Wen, Y.P. & Li, J.L. 2004. Ten years of atmospheric methane observations at a high elevation site in Western China. *Atmospheric Environment*, 38, 7041–7054, <https://doi.org/10.1016/j.atmosenv.2004.02.072>.
- Zimmerman, P.R., Greenberg, J.P., Wandiga, S.O. & Crutzen, P.J. 1982. Termites: A Potentially Large Source of Atmospheric Methane, Carbon Dioxide, and Molecular Hydrogen. *Science*, 218, 563–565, <https://doi.org/10.1126/science.218.4572.563>.
- Zobitz, J.M., Keener, J.P., Schnyder, H. & Bowling, D.R. 2006. Sensitivity analysis and quantification of uncertainty for isotopic mixing relationships in carbon cycle research. *Agricultural and Forest Meteorology*, 136, 56–75, <https://doi.org/10.1016/j.agrformet.2006.01.003>.

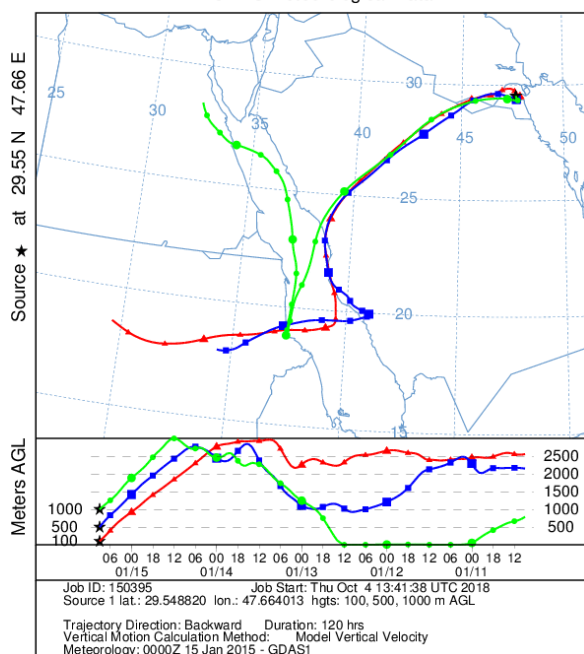
***A**PPENDICES*

Appendix 1. To assess the continental provenance of air masses, the Hybrid Single-Particle Lagrangian Integrated Trajectory model (HYSPLIT) has been used to compute air trajectories arriving at 100 meters ,500 and 1000 meters above ground. The National Oceanic and Atmospheric Administration's (NOAA) Air Resources Laboratory (ARL) and named the Real-time Environmental Applications and Display (READY, <http://www.ready.noaa.gov> web-based system is used. The HYSPLIT model shows that the provenance of air masses arriving in Kuwait is very difficult to define on some days, with air at different heights having different sources. The following maps in this appendix 1 cover the period of 2015 and 2016 for the long-term measurements of the Kuwait city site (Khaldiya) that been discussed in chapter 8.

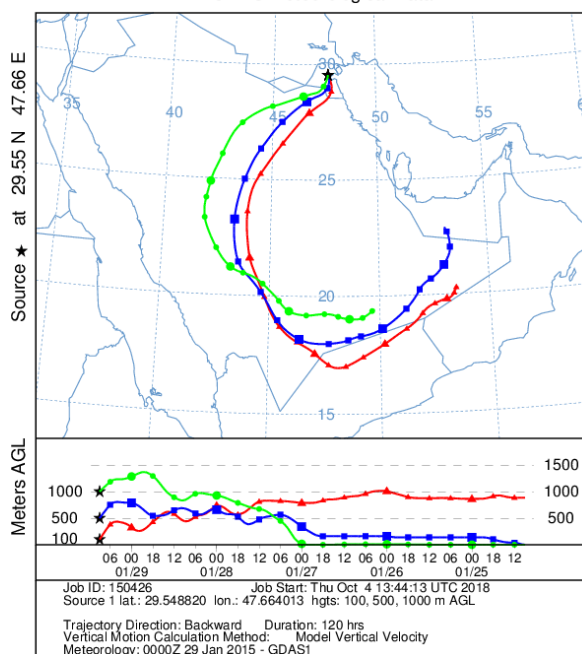
NOAA HYSPLIT MODEL
Backward trajectories ending at 1200 UTC 08 Jan 15
GDAS Meteorological Data



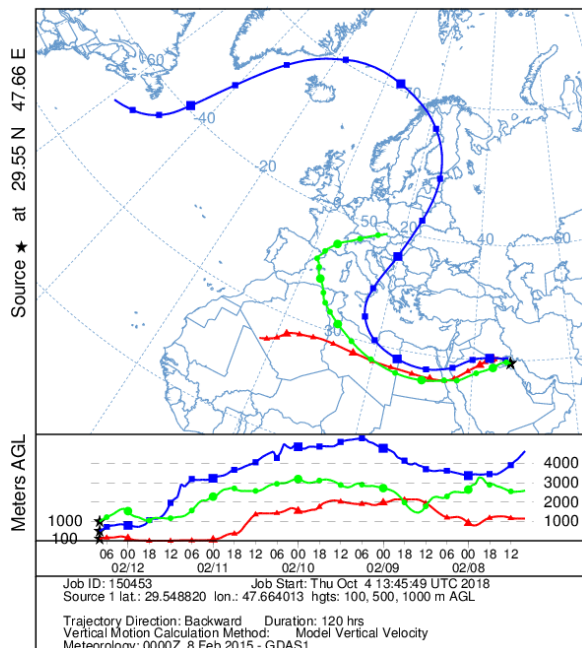
NOAA HYSPLIT MODEL
Backward trajectories ending at 0900 UTC 15 Jan 15
GDAS Meteorological Data



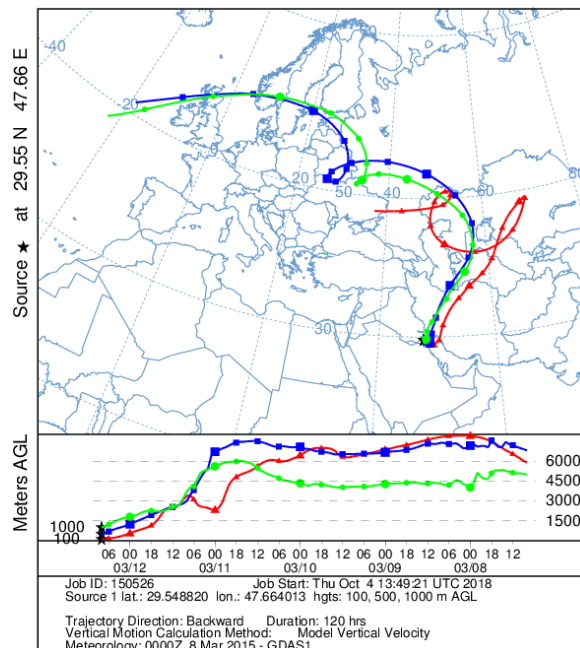
NOAA HYSPLIT MODEL
Backward trajectories ending at 0900 UTC 29 Jan 15
GDAS Meteorological Data



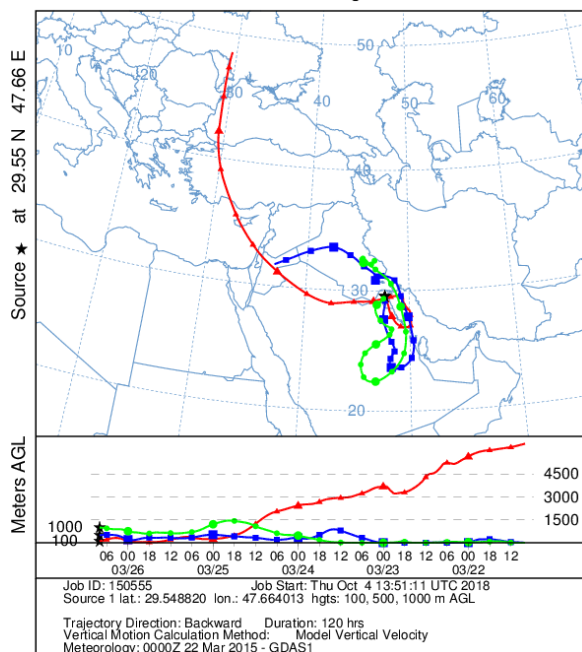
NOAA HYSPLIT MODEL
Backward trajectories ending at 0800 UTC 12 Feb 15
GDAS Meteorological Data



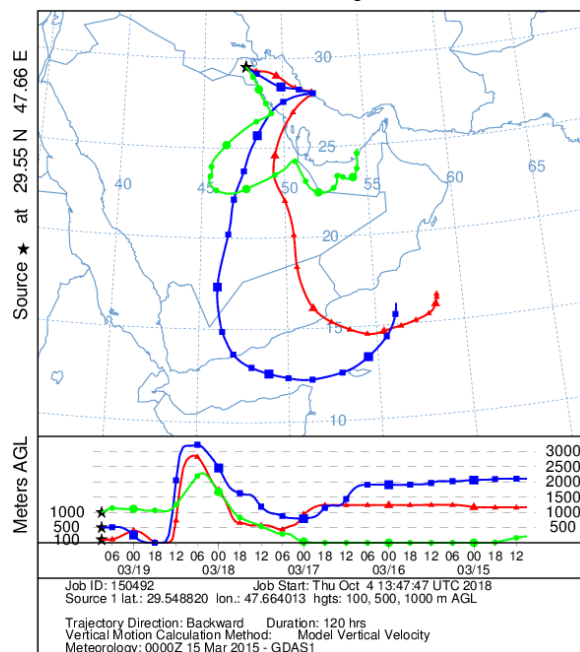
NOAA HYSPLIT MODEL
Backward trajectories ending at 0800 UTC 12 Mar 15
GDAS Meteorological Data



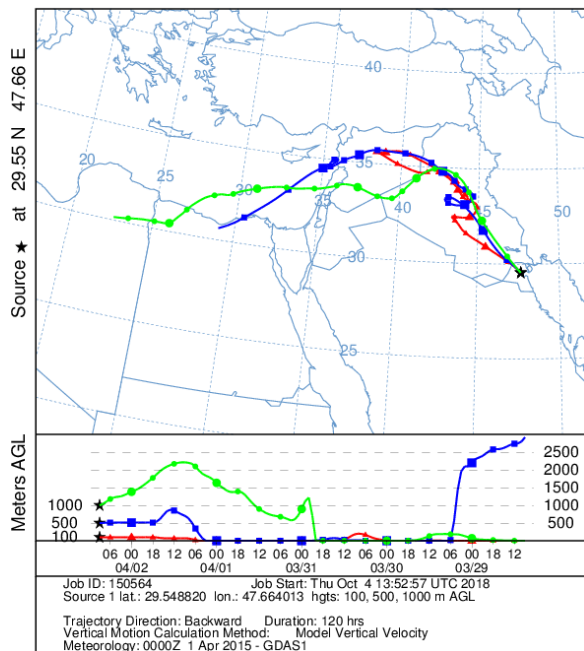
NOAA HYSPLIT MODEL
Backward trajectories ending at 0800 UTC 26 Mar 15
GDAS Meteorological Data



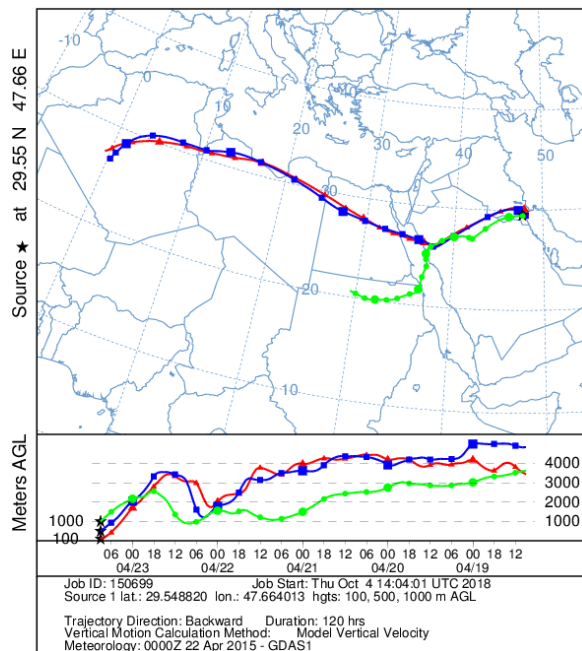
NOAA HYSPLIT MODEL
Backward trajectories ending at 0900 UTC 19 Mar 15
GDAS Meteorological Data



NOAA HYSPLIT MODEL
Backward trajectories ending at 0900 UTC 02 Apr 15
GDAS Meteorological Data

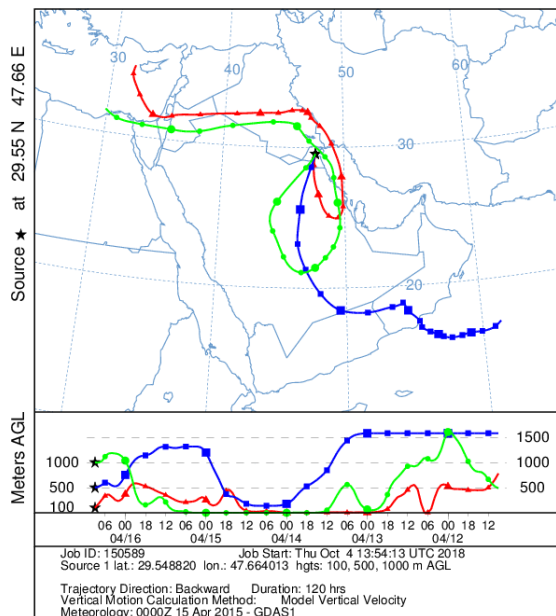


NOAA HYSPLIT MODEL
Backward trajectories ending at 0900 UTC 23 Apr 15
GDAS Meteorological Data

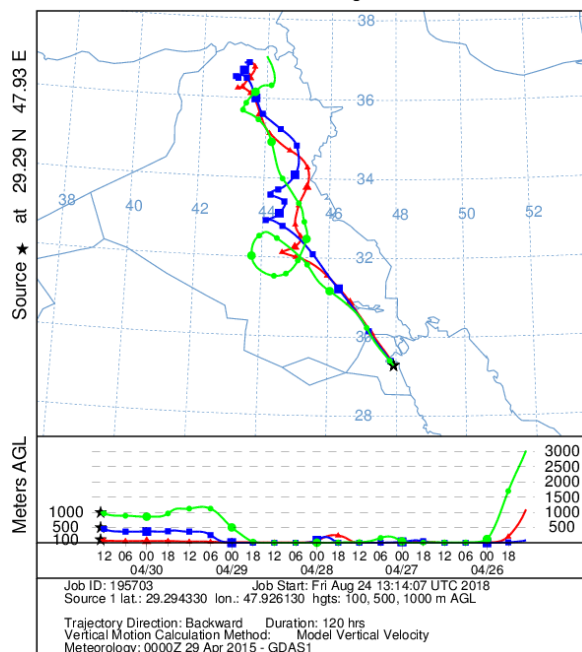


9

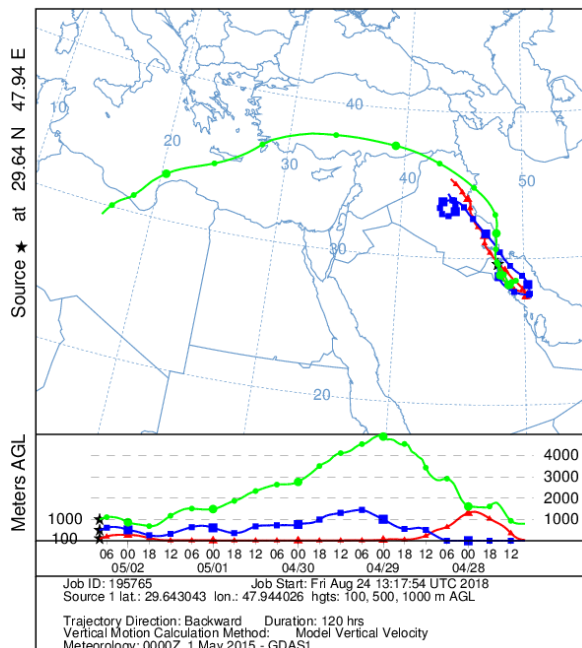
NOAA HYSPLIT MODEL
Backward trajectories ending at 0900 UTC 16 Apr 15
GDAS Meteorological Data



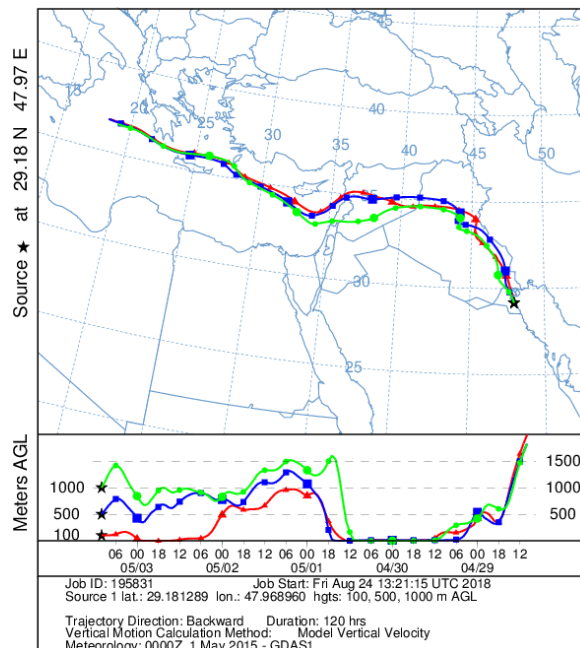
NOAA HYSPLIT MODEL
Backward trajectories ending at 1300 UTC 30 Apr 15
GDAS Meteorological Data



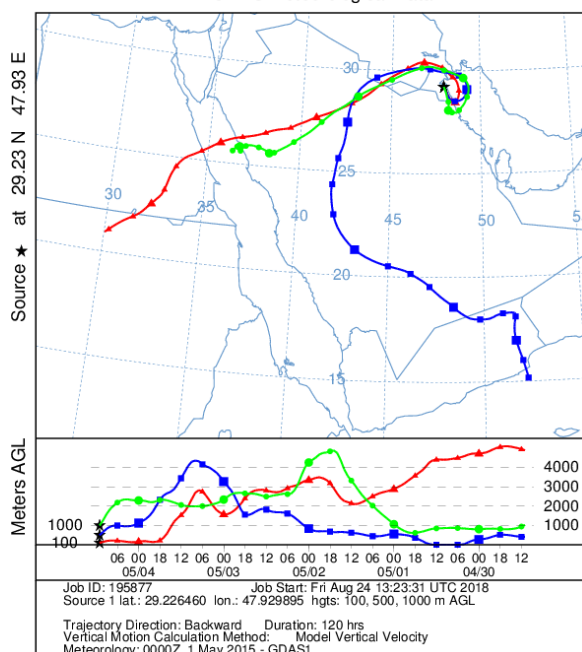
NOAA HYSPLIT MODEL
Backward trajectories ending at 0800 UTC 02 May 15
GDAS Meteorological Data



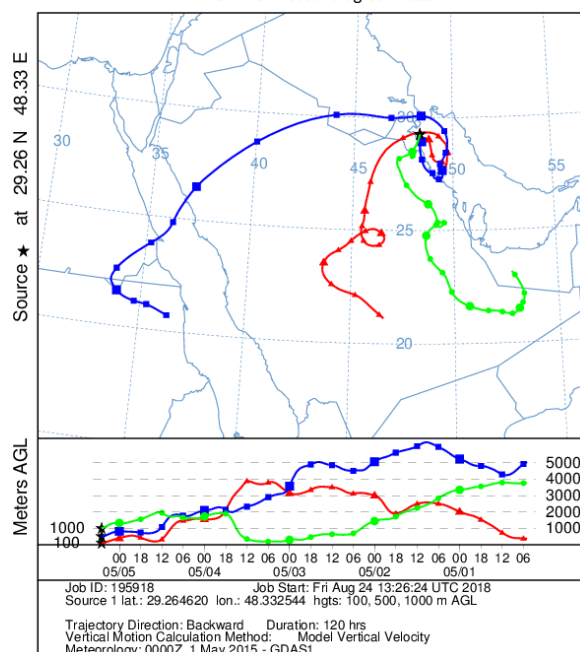
NOAA HYSPLIT MODEL
Backward trajectories ending at 1000 UTC 03 May 15
GDAS Meteorological Data



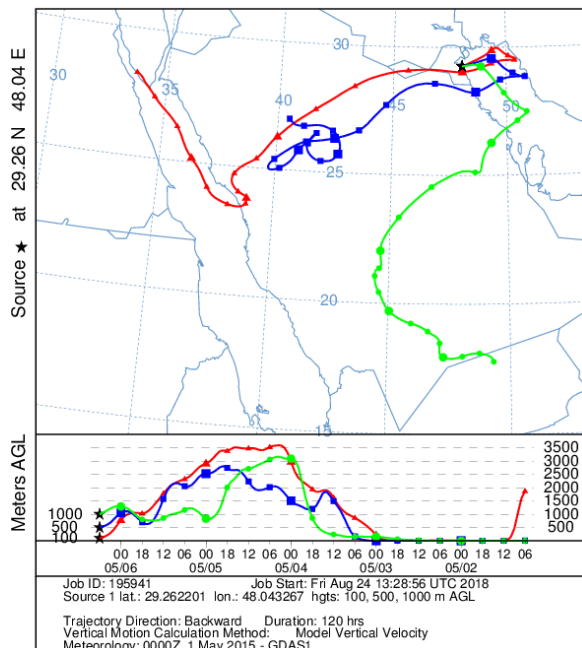
NOAA HYSPLIT MODEL
Backward trajectories ending at 1100 UTC 04 May 15
GDAS Meteorological Data



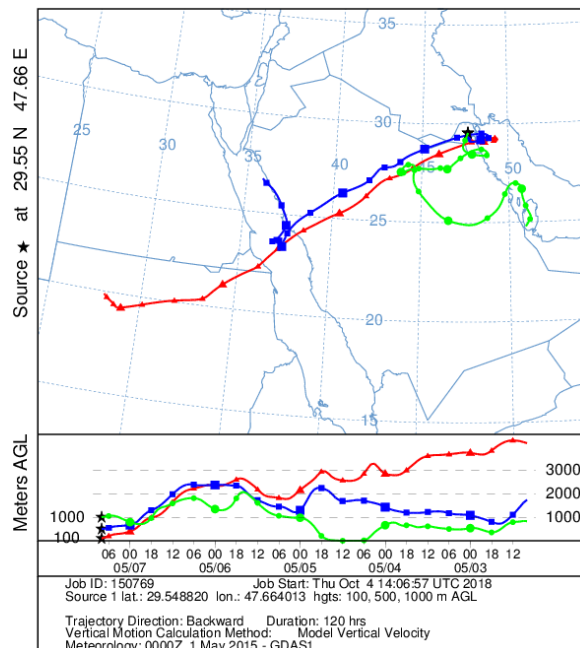
NOAA HYSPLIT MODEL
Backward trajectories ending at 0500 UTC 05 May 15
GDAS Meteorological Data



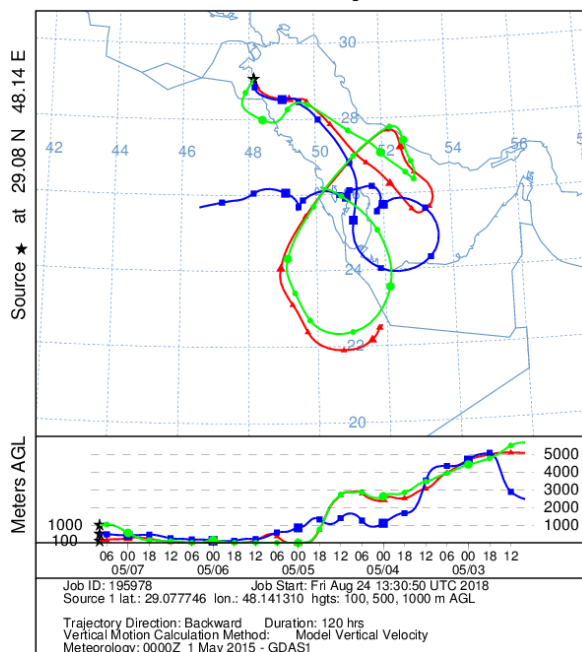
NOAA HYSPLIT MODEL
Backward trajectories ending at 0600 UTC 06 May 15
GDAS Meteorological Data



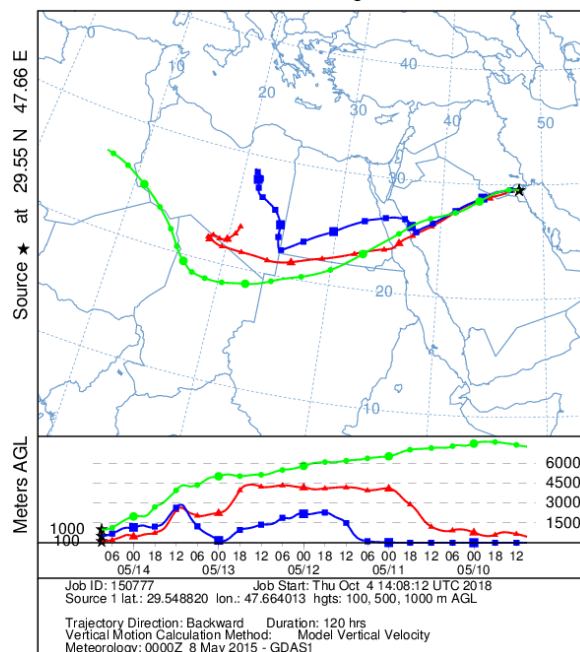
NOAA HYSPLIT MODEL
Backward trajectories ending at 0800 UTC 07 May 15
GDAS Meteorological Data



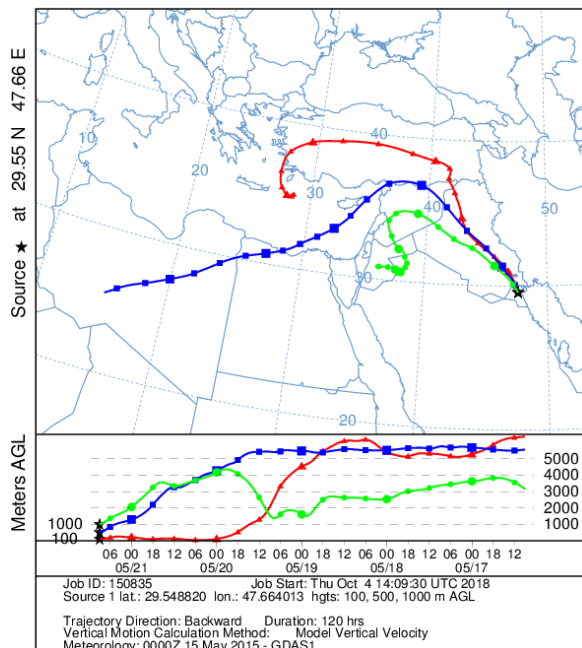
NOAA HYSPLIT MODEL
Backward trajectories ending at 0800 UTC 07 May 15
GDAS Meteorological Data



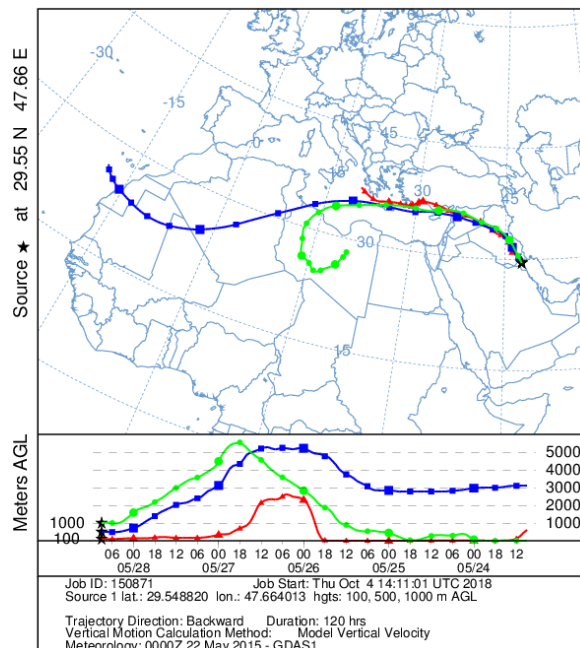
NOAA HYSPLIT MODEL
Backward trajectories ending at 0900 UTC 14 May 15
GDAS Meteorological Data



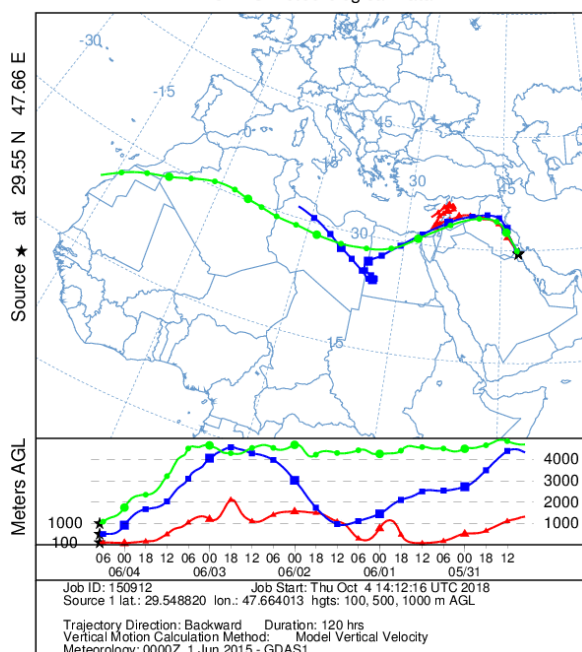
NOAA HYSPLIT MODEL
Backward trajectories ending at 0900 UTC 21 May 15
GDAS Meteorological Data



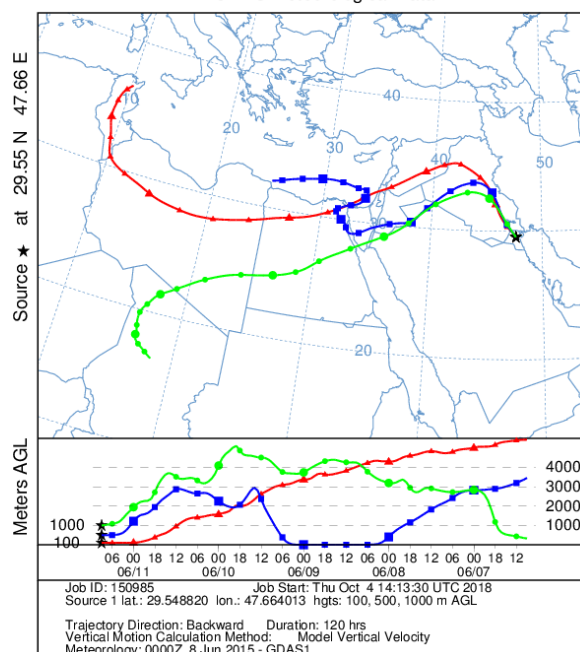
NOAA HYSPLIT MODEL
Backward trajectories ending at 0900 UTC 28 May 15
GDAS Meteorological Data



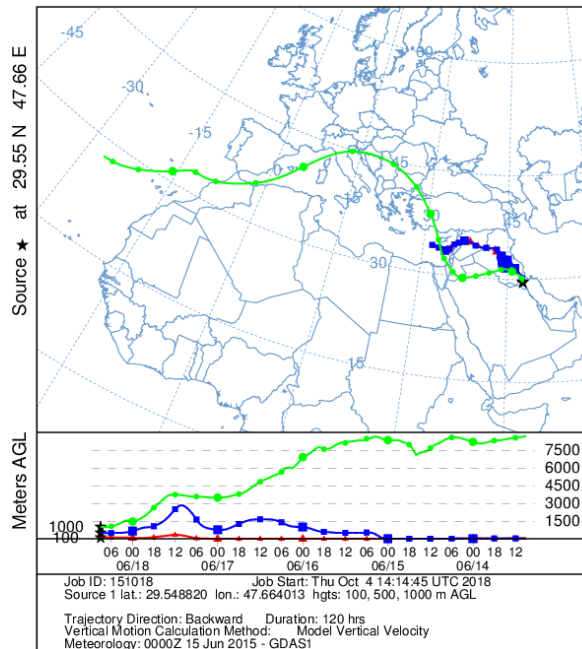
NOAA HYSPLIT MODEL
Backward trajectories ending at 0700 UTC 04 Jun 15
GDAS Meteorological Data



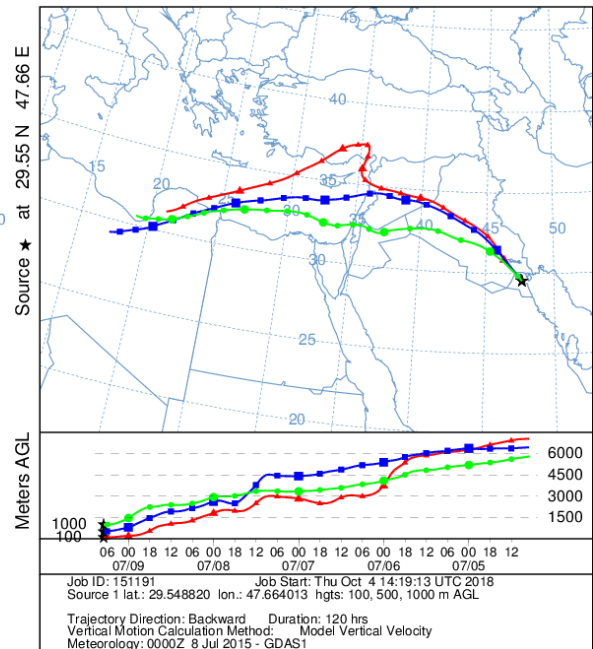
NOAA HYSPLIT MODEL
Backward trajectories ending at 0900 UTC 11 Jun 15
GDAS Meteorological Data



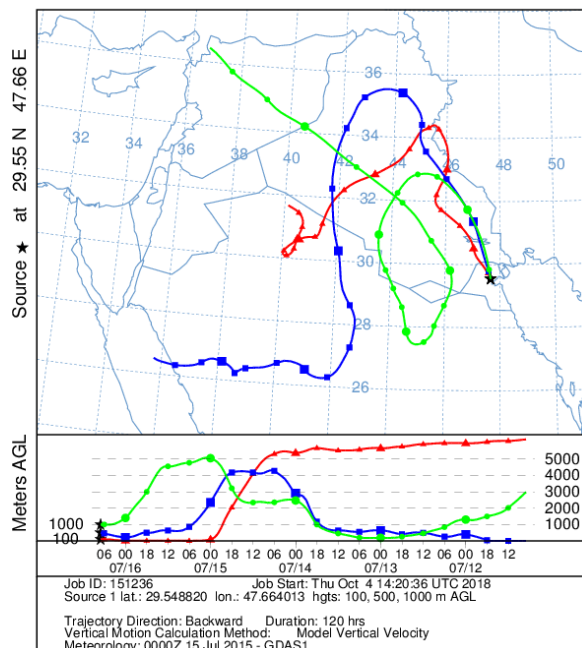
NOAA HYSPLIT MODEL
Backward trajectories ending at 0900 UTC 18 Jun 15
GDAS Meteorological Data



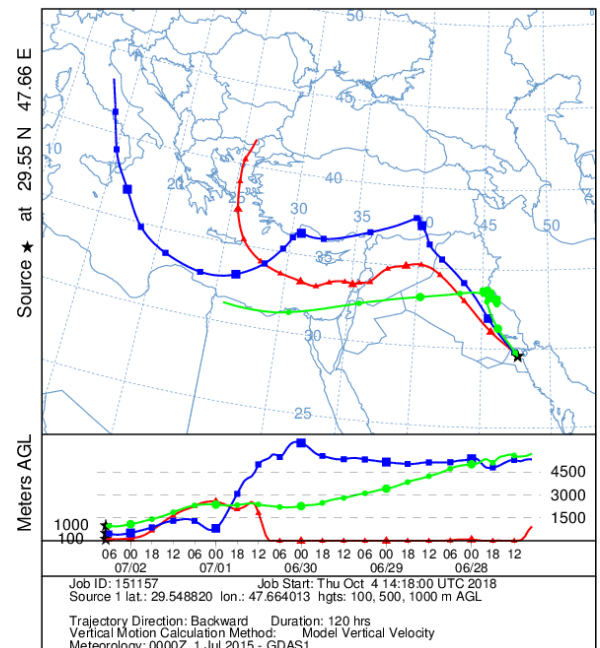
NOAA HYSPLIT MODEL
Backward trajectories ending at 0700 UTC 09 Jul 15
GDAS Meteorological Data



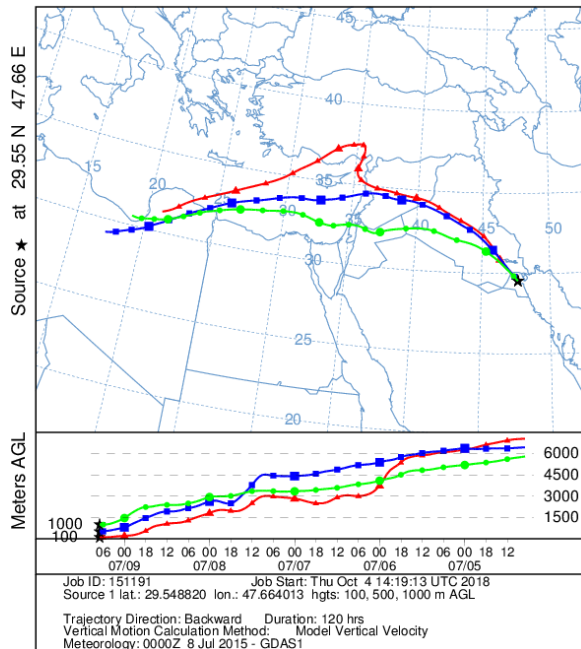
NOAA HYSPLIT MODEL
Backward trajectories ending at 0700 UTC 16 Jul 15
GDAS Meteorological Data



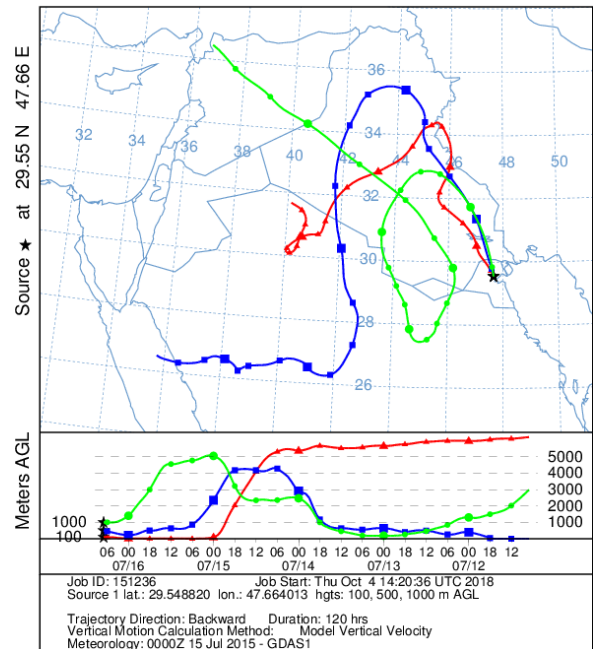
NOAA HYSPLIT MODEL
Backward trajectories ending at 0700 UTC 02 Jul 15
GDAS Meteorological Data



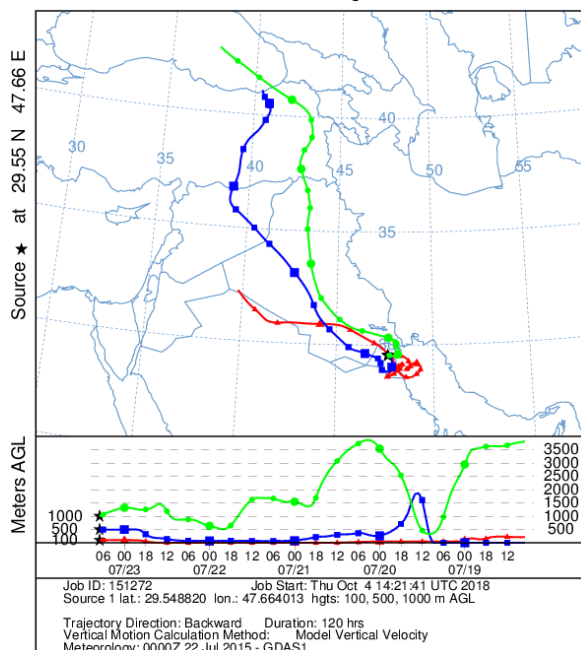
NOAA HYSPLIT MODEL
Backward trajectories ending at 0700 UTC 09 Jul 15
GDAS Meteorological Data



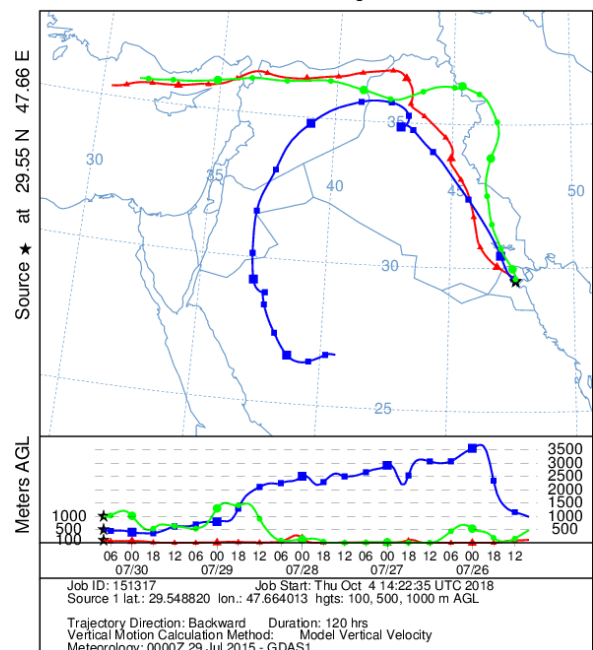
NOAA HYSPLIT MODEL
Backward trajectories ending at 0700 UTC 16 Jul 15
GDAS Meteorological Data



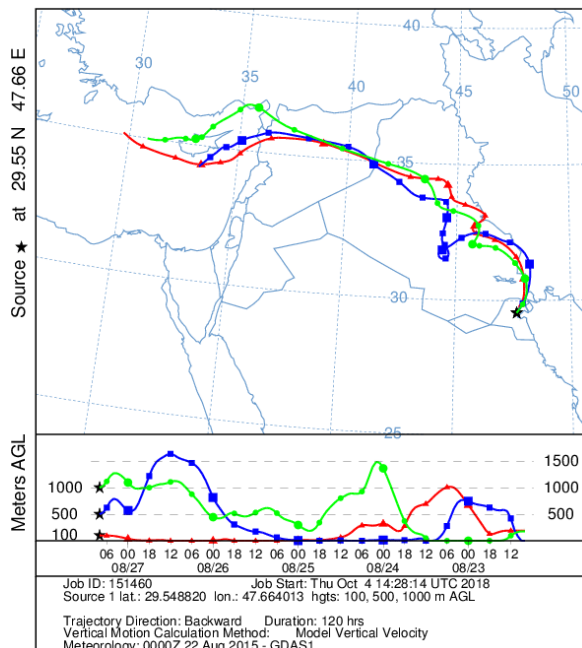
NOAA HYSPLIT MODEL
Backward trajectories ending at 0700 UTC 23 Jul 15
GDAS Meteorological Data



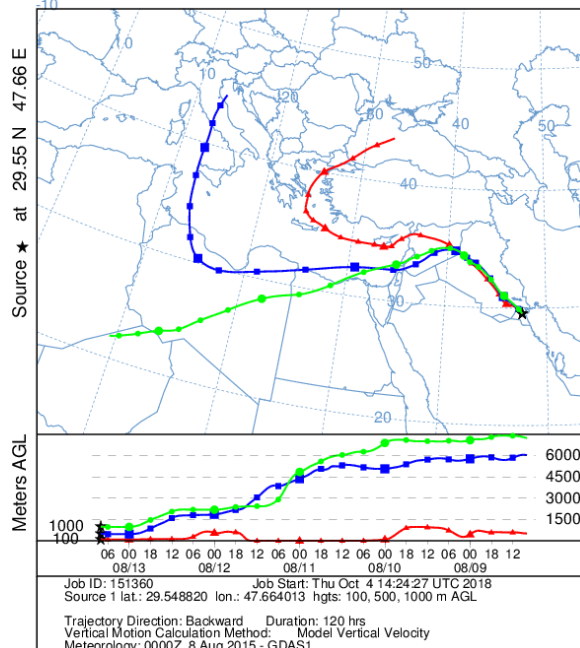
NOAA HYSPLIT MODEL
Backward trajectories ending at 0800 UTC 30 Jul 15
GDAS Meteorological Data



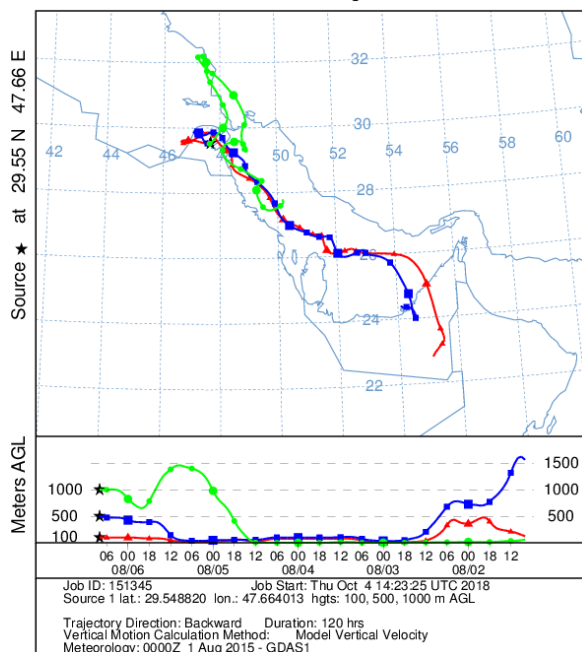
NOAA HYSPLIT MODEL
Backward trajectories ending at 0800 UTC 27 Aug 15
GDAS Meteorological Data



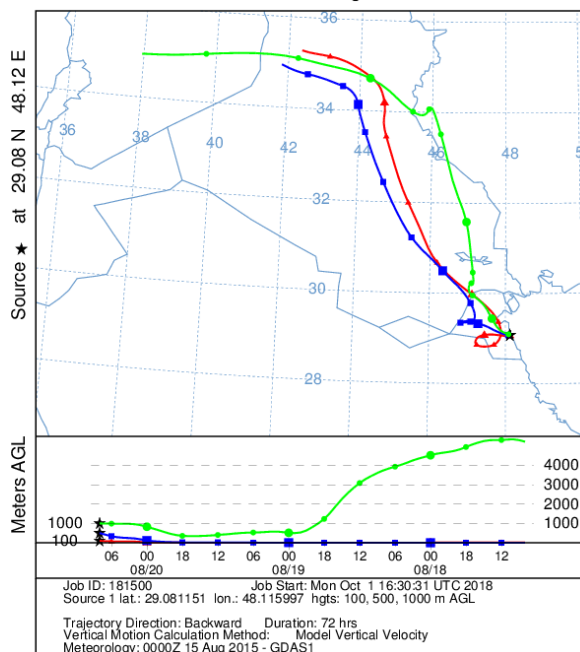
NOAA HYSPLIT MODEL
Backward trajectories ending at 0800 UTC 13 Aug 15
GDAS Meteorological Data



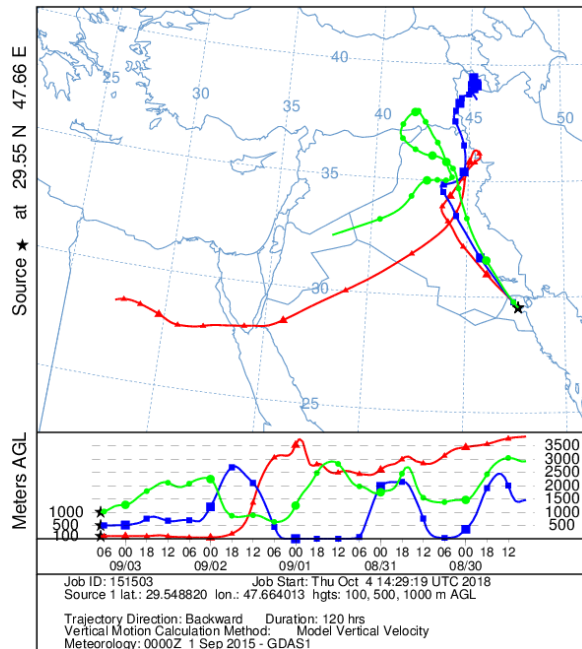
NOAA HYSPLIT MODEL
Backward trajectories ending at 0800 UTC 06 Aug 15
GDAS Meteorological Data



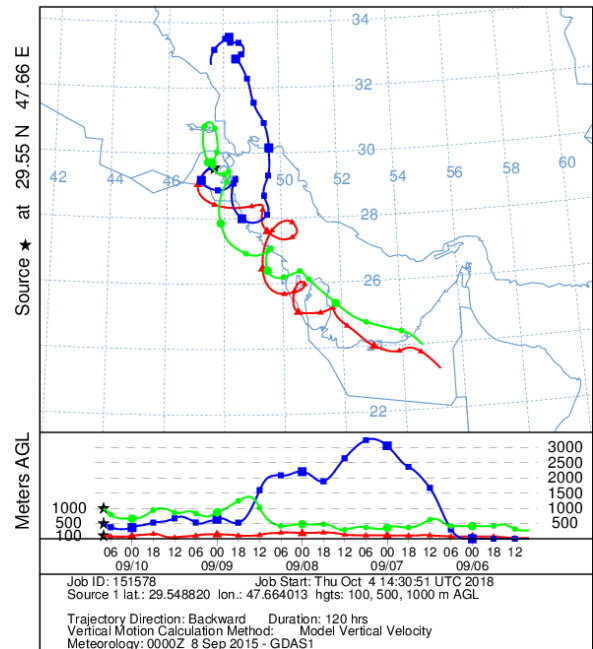
NOAA HYSPLIT MODEL
Backward trajectories ending at 0800 UTC 20 Aug 15
GDAS Meteorological Data



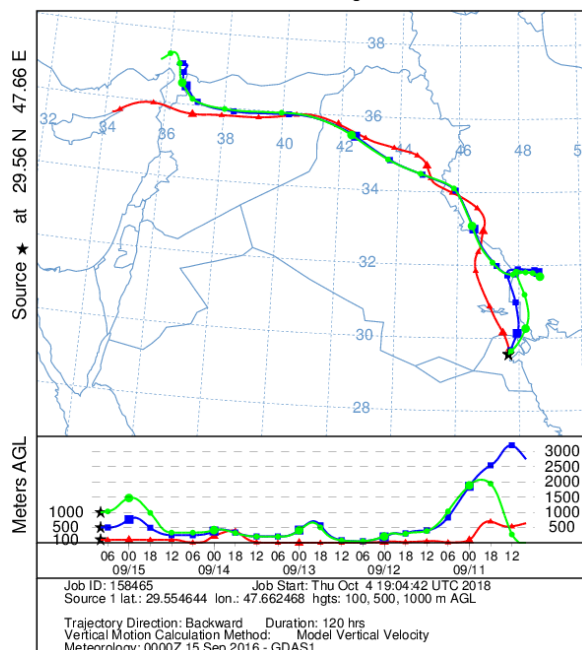
NOAA HYSPLIT MODEL
Backward trajectories ending at 0700 UTC 03 Sep 15
GDAS Meteorological Data



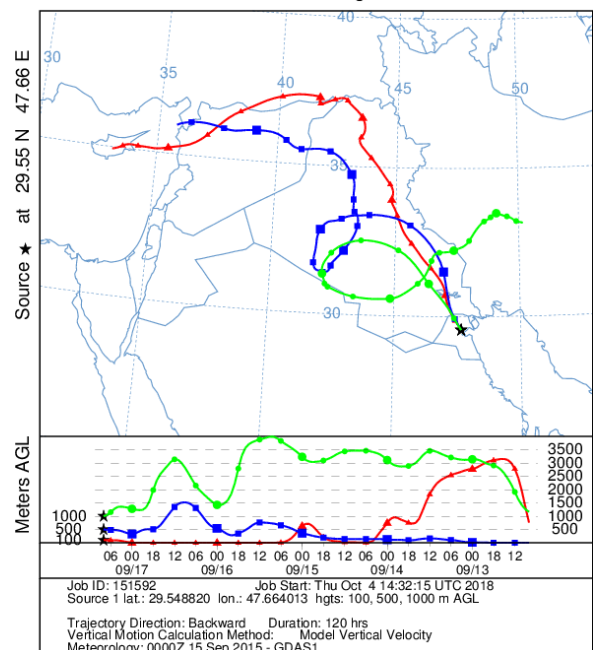
NOAA HYSPLIT MODEL
Backward trajectories ending at 0800 UTC 10 Sep 15
GDAS Meteorological Data



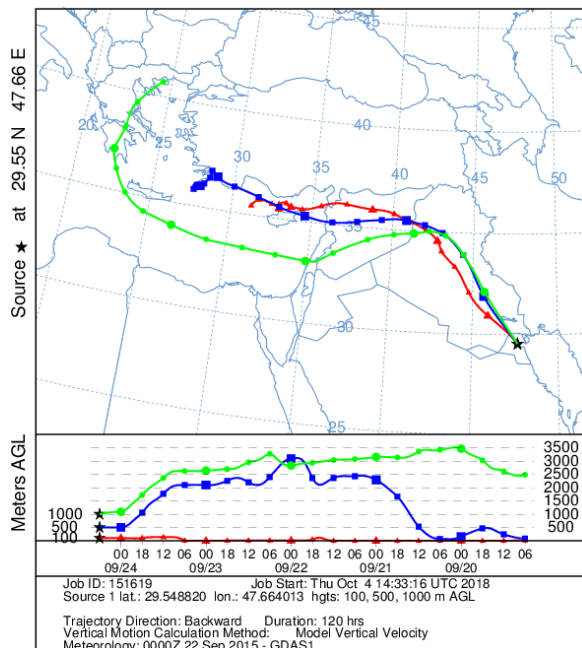
NOAA HYSPLIT MODEL
Backward trajectories ending at 0800 UTC 15 Sep 16
GDAS Meteorological Data



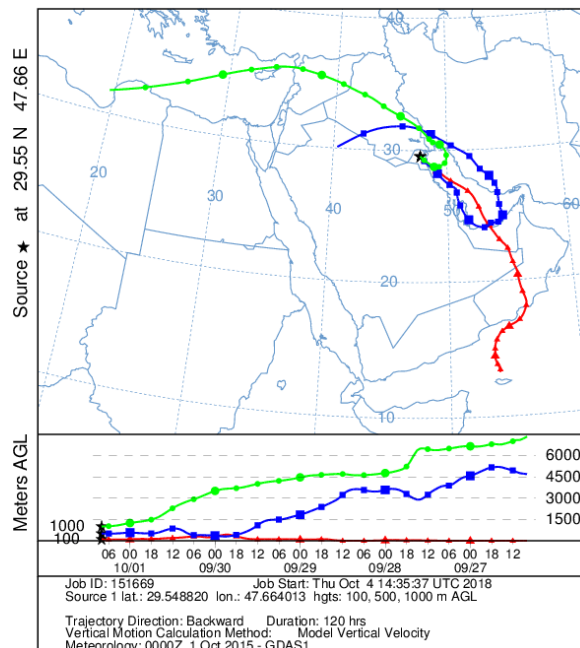
NOAA HYSPLIT MODEL
Backward trajectories ending at 0800 UTC 17 Sep 15
GDAS Meteorological Data



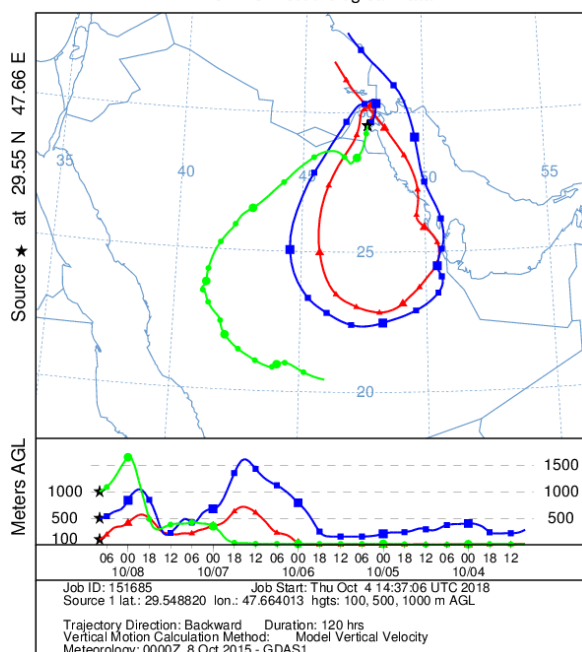
NOAA HYSPLIT MODEL
Backward trajectories ending at 0600 UTC 24 Sep 15
GDAS Meteorological Data



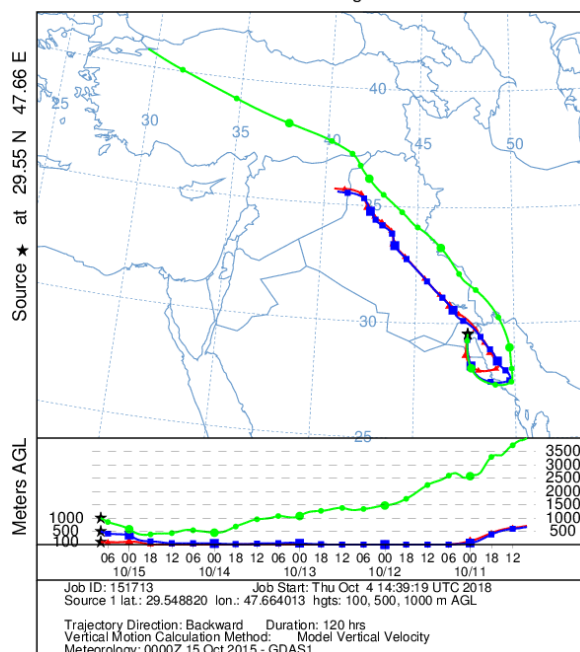
NOAA HYSPLIT MODEL
Backward trajectories ending at 0800 UTC 01 Oct 15
GDAS Meteorological Data



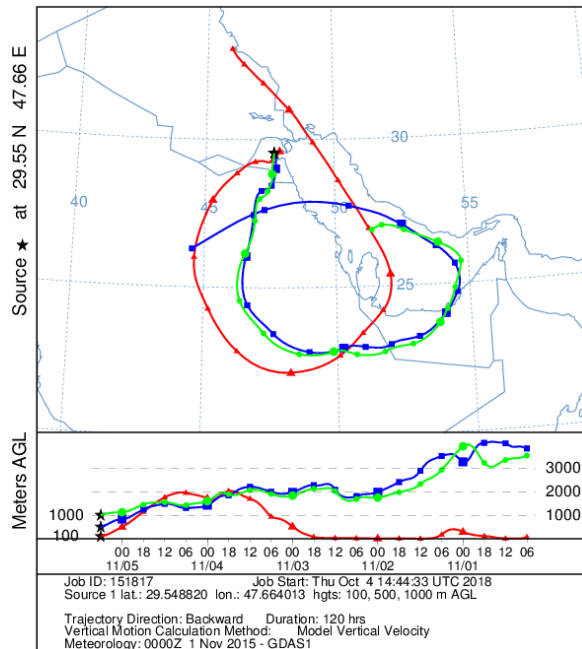
NOAA HYSPLIT MODEL
Backward trajectories ending at 0800 UTC 08 Oct 15
GDAS Meteorological Data



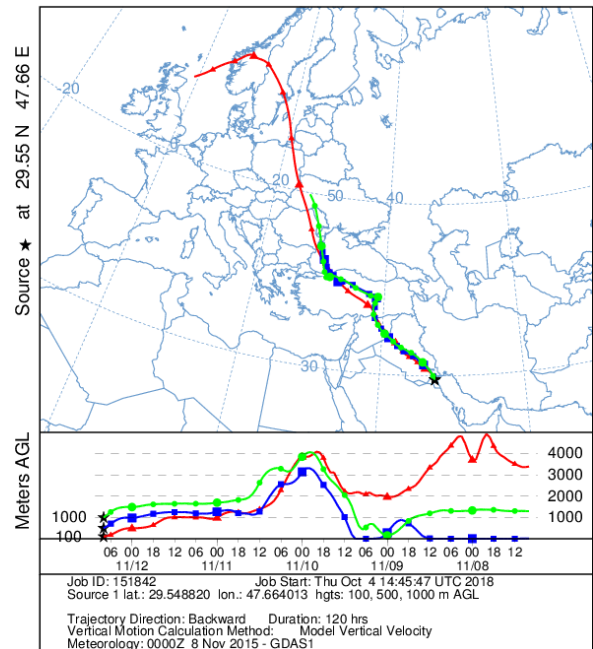
NOAA HYSPLIT MODEL
Backward trajectories ending at 0800 UTC 15 Oct 15
GDAS Meteorological Data



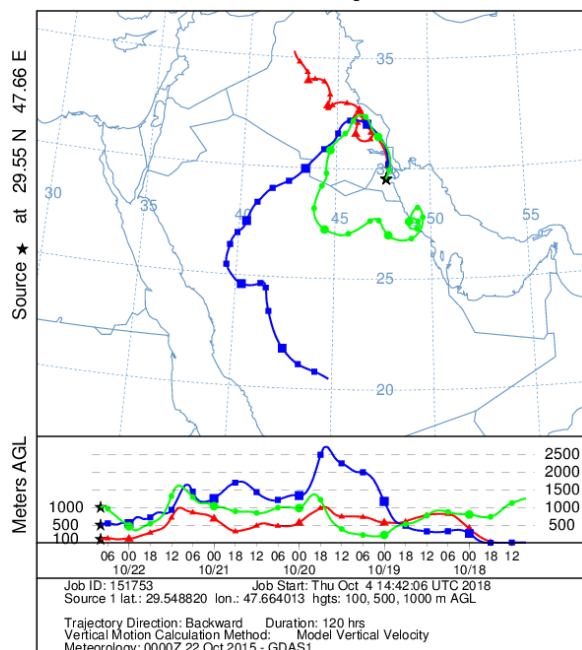
NOAA HYSPLIT MODEL
Backward trajectories ending at 0600 UTC 05 Nov 15
GDAS Meteorological Data



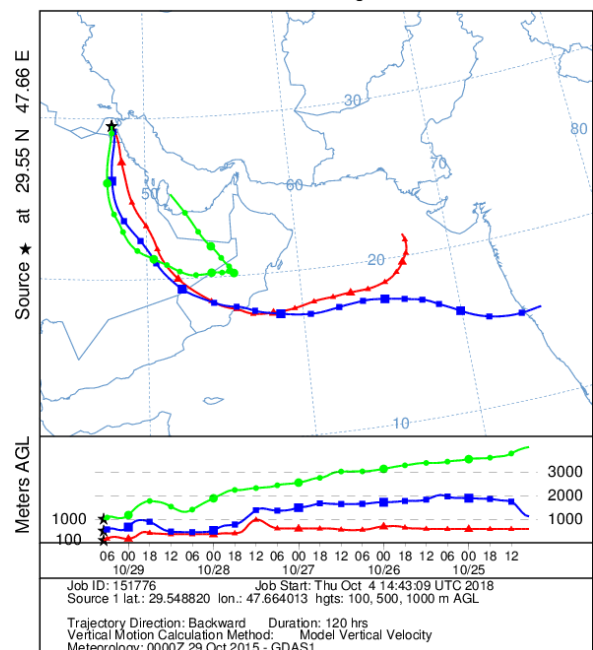
NOAA HYSPLIT MODEL
Backward trajectories ending at 0800 UTC 12 Nov 15
GDAS Meteorological Data



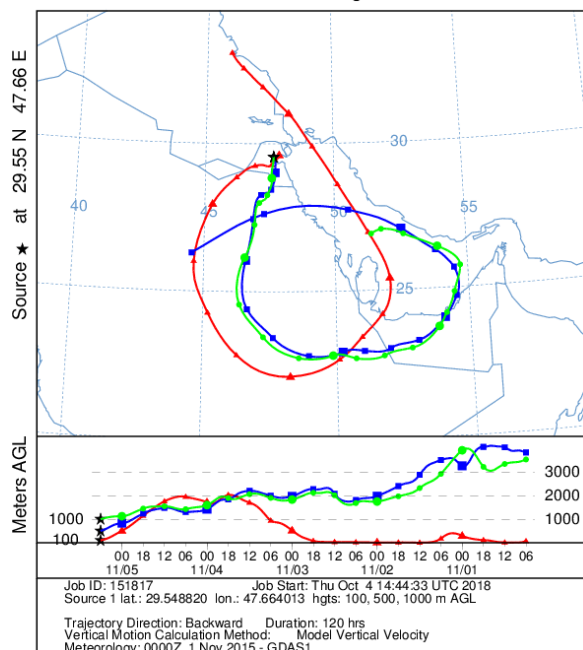
NOAA HYSPLIT MODEL
Backward trajectories ending at 0800 UTC 22 Oct 15
GDAS Meteorological Data



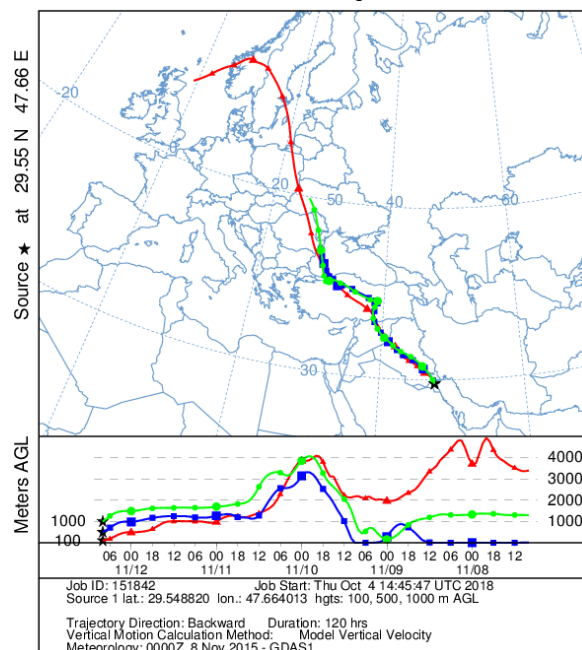
NOAA HYSPLIT MODEL
Backward trajectories ending at 0700 UTC 29 Oct 15
GDAS Meteorological Data



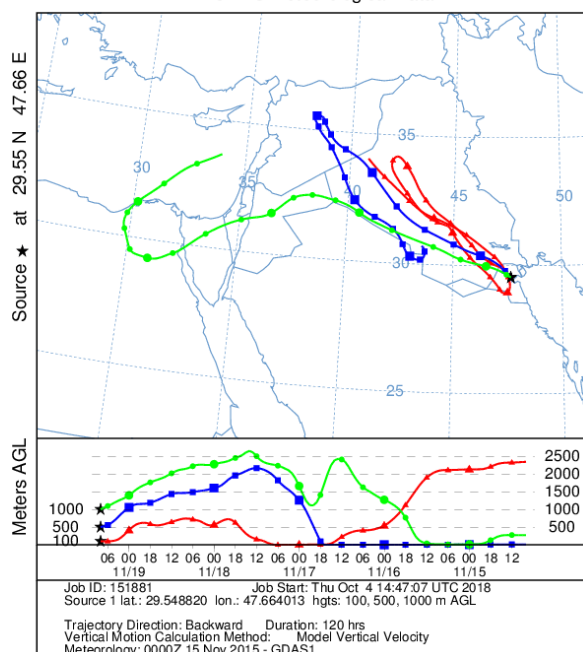
NOAA HYSPLIT MODEL
Backward trajectories ending at 0600 UTC 05 Nov 15
GDAS Meteorological Data



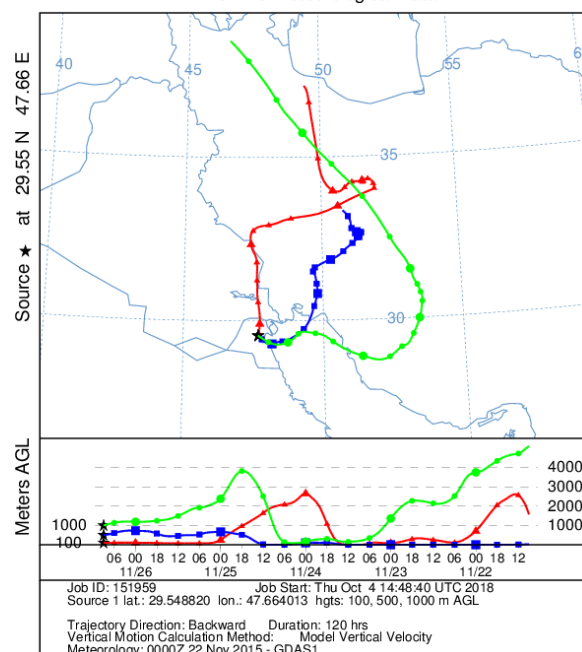
NOAA HYSPLIT MODEL
Backward trajectories ending at 0800 UTC 12 Nov 15
GDAS Meteorological Data



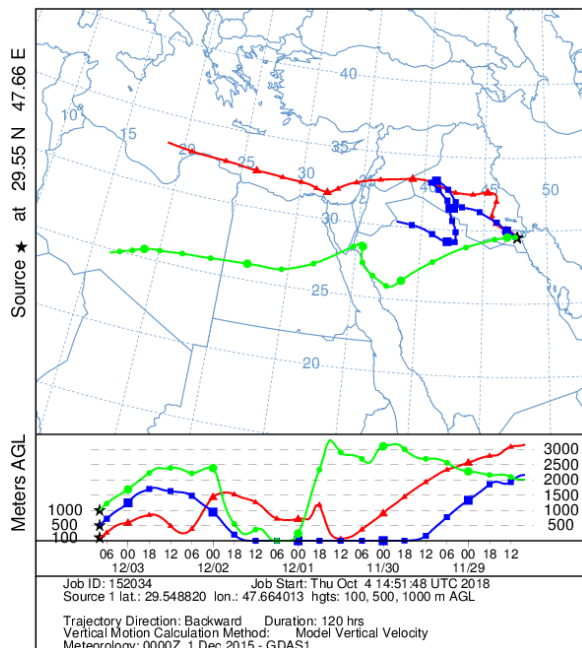
NOAA HYSPLIT MODEL
Backward trajectories ending at 0800 UTC 19 Nov 15
GDAS Meteorological Data



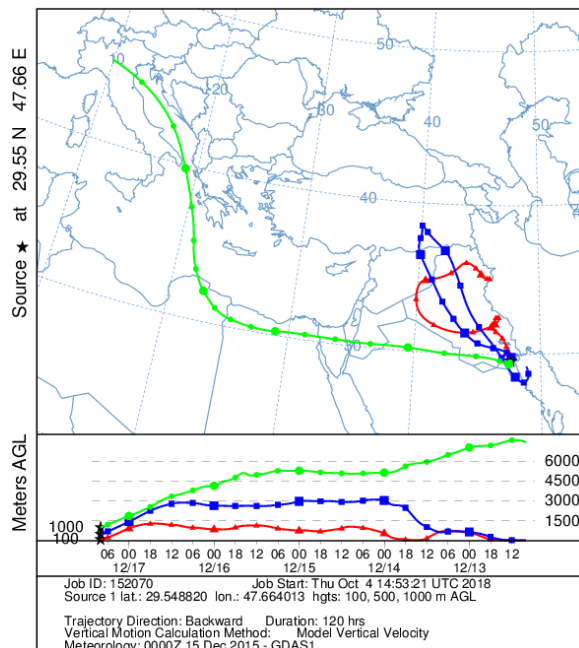
NOAA HYSPLIT MODEL
Backward trajectories ending at 0900 UTC 26 Nov 15
GDAS Meteorological Data



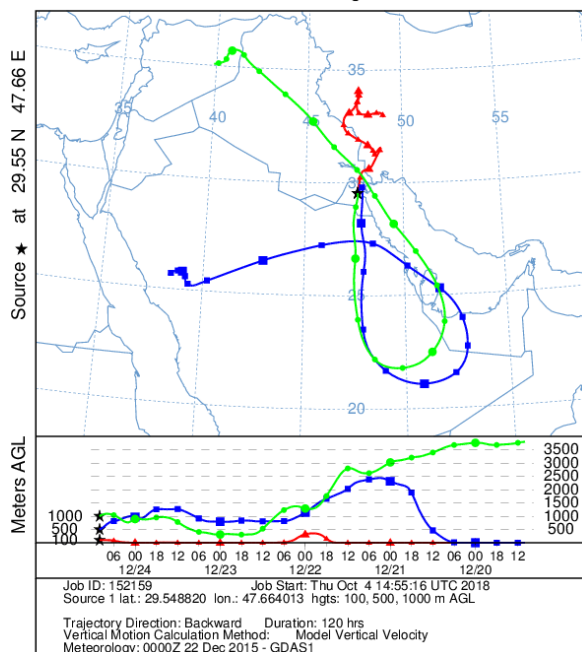
NOAA HYSPLIT MODEL
Backward trajectories ending at 0800 UTC 03 Dec 15
GDAS Meteorological Data



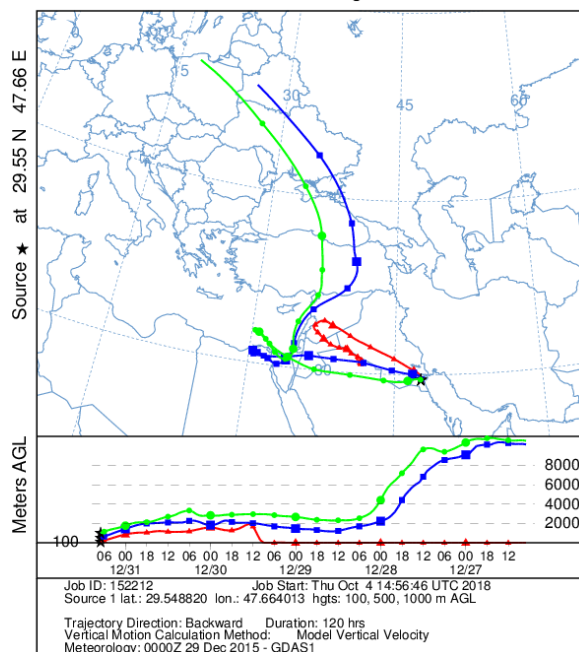
NOAA HYSPLIT MODEL
Backward trajectories ending at 0800 UTC 17 Dec 15
GDAS Meteorological Data



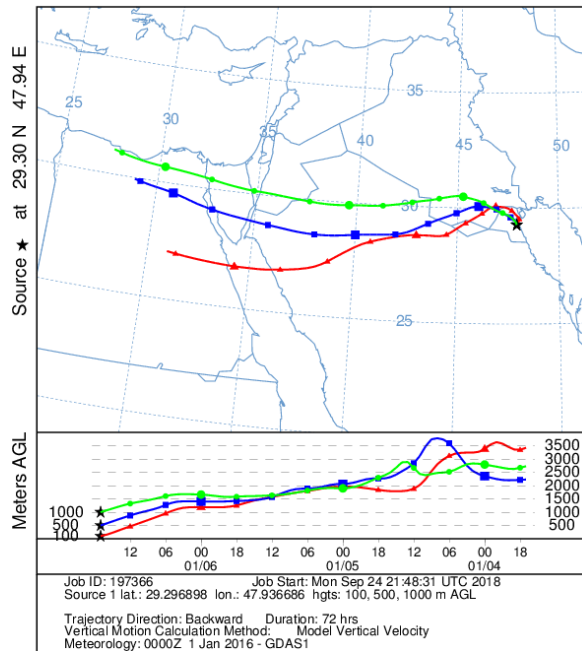
NOAA HYSPLIT MODEL
Backward trajectories ending at 1000 UTC 24 Dec 15
GDAS Meteorological Data



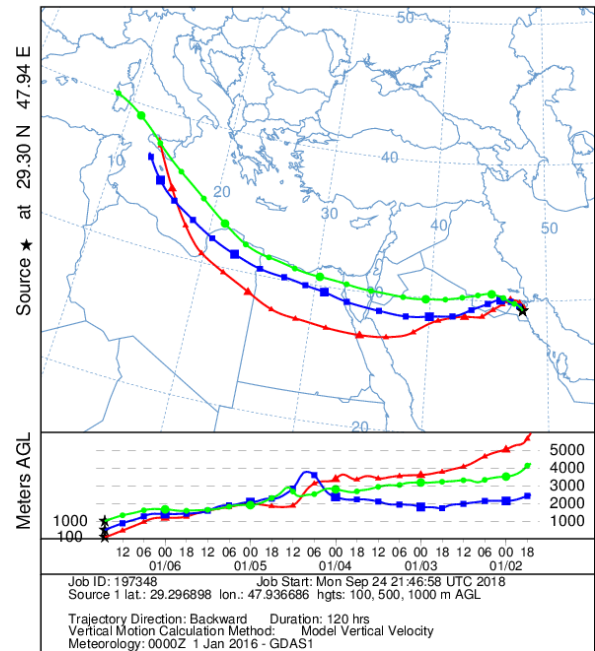
NOAA HYSPLIT MODEL
Backward trajectories ending at 0700 UTC 31 Dec 15
GDAS Meteorological Data



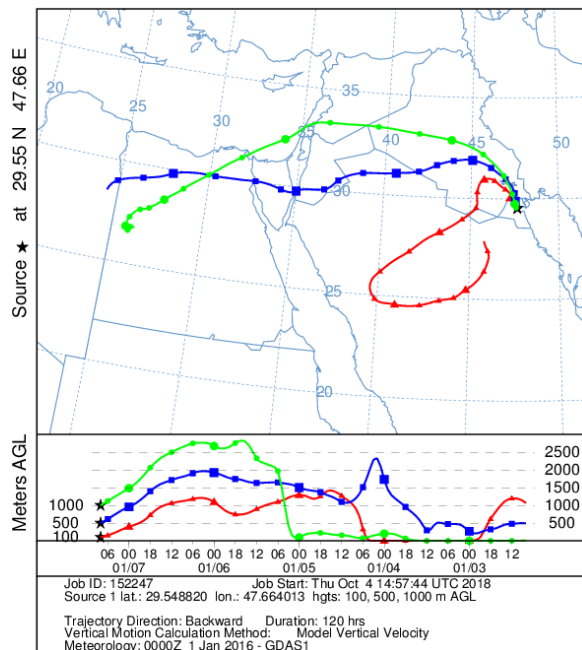
NOAA HYSPLIT MODEL
Backward trajectories ending at 1700 UTC 06 Jan 16
GDAS Meteorological Data



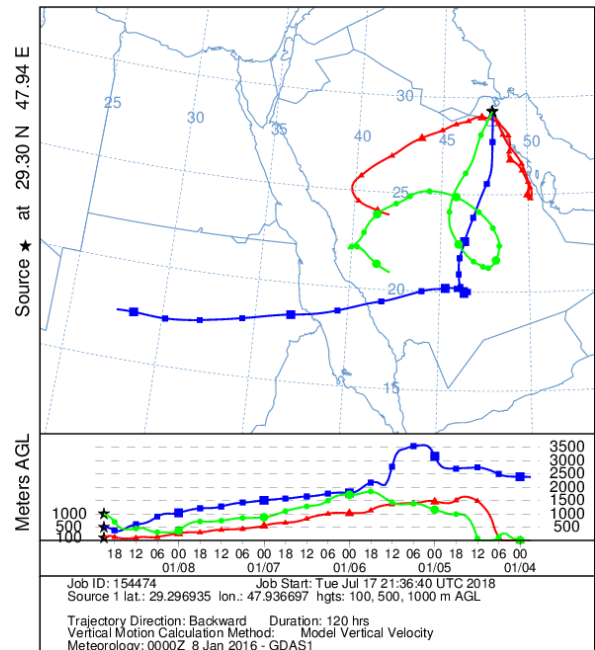
NOAA HYSPLIT MODEL
Backward trajectories ending at 1700 UTC 06 Jan 16
GDAS Meteorological Data



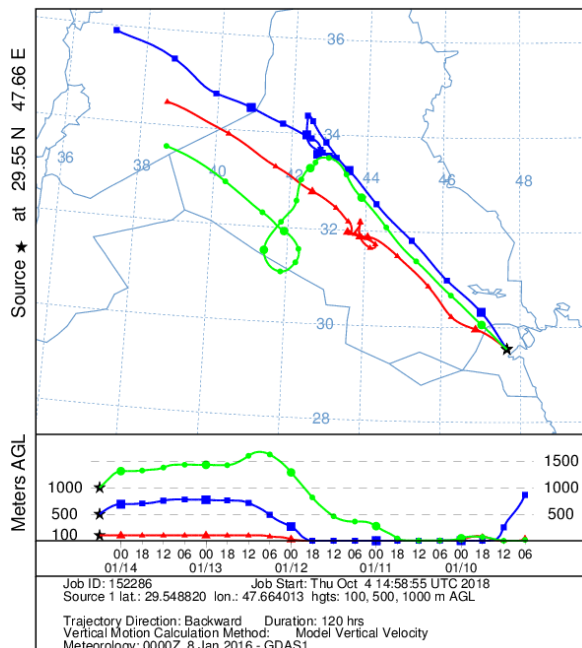
NOAA HYSPLIT MODEL
Backward trajectories ending at 0800 UTC 07 Jan 16
GDAS Meteorological Data



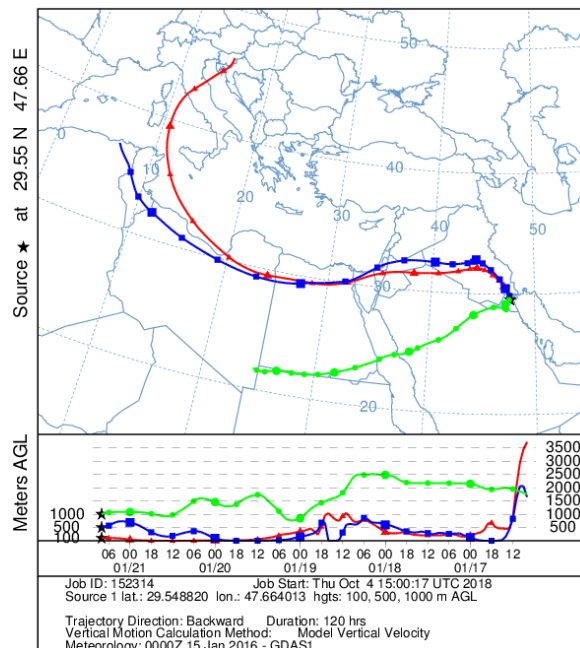
NOAA HYSPLIT MODEL
Backward trajectories ending at 2100 UTC 08 Jan 16
GDAS Meteorological Data



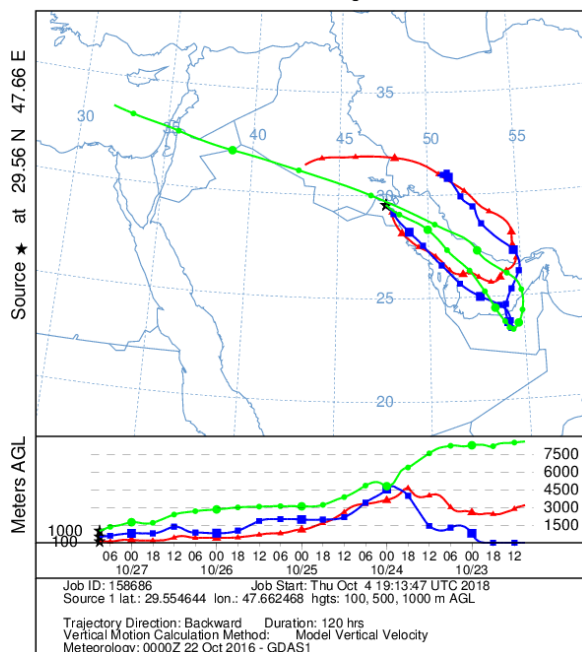
NOAA HYSPLIT MODEL
Backward trajectories ending at 0600 UTC 14 Jan 16
GDAS Meteorological Data



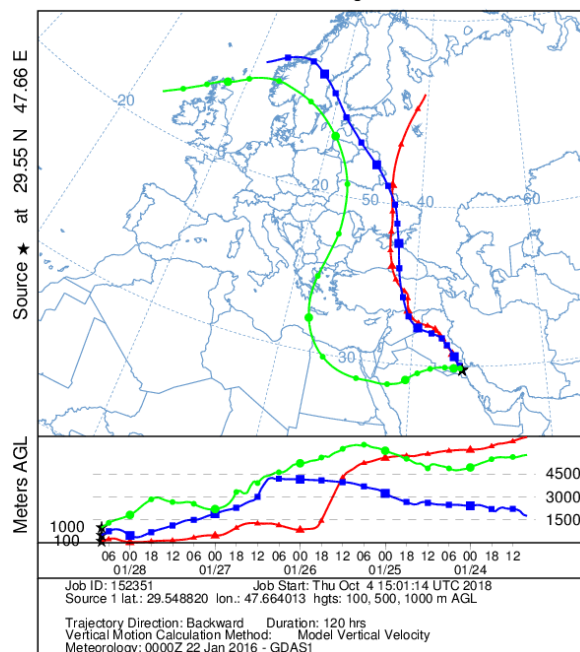
NOAA HYSPLIT MODEL
Backward trajectories ending at 0800 UTC 21 Jan 16
GDAS Meteorological Data



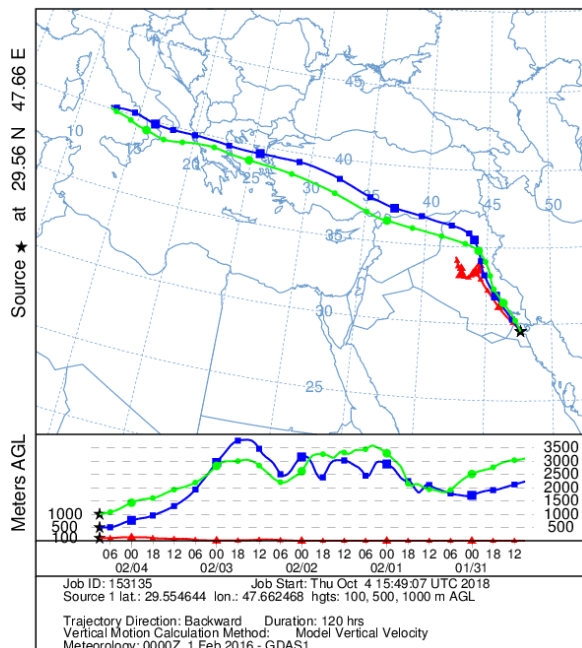
NOAA HYSPLIT MODEL
Backward trajectories ending at 0900 UTC 27 Oct 16
GDAS Meteorological Data



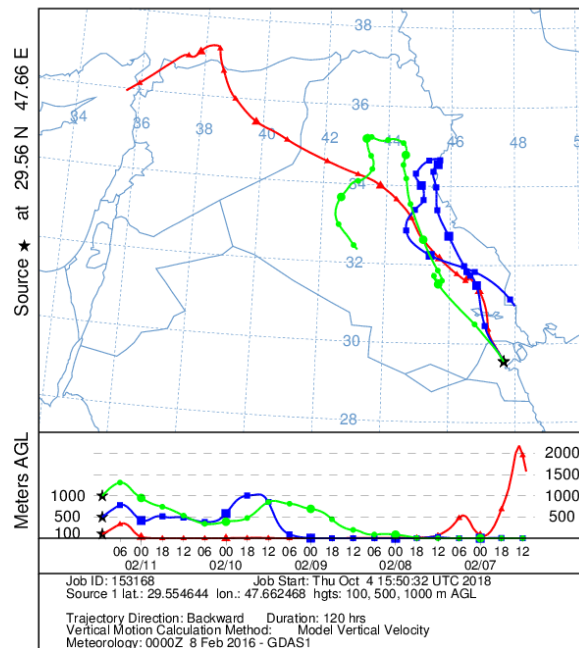
NOAA HYSPLIT MODEL
Backward trajectories ending at 0800 UTC 28 Jan 16
GDAS Meteorological Data



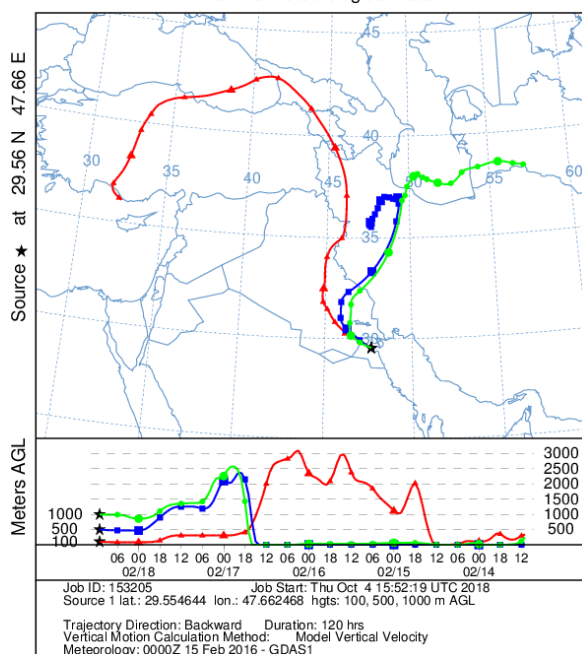
NOAA HYSPLIT MODEL
Backward trajectories ending at 0900 UTC 04 Feb 16
GDAS Meteorological Data



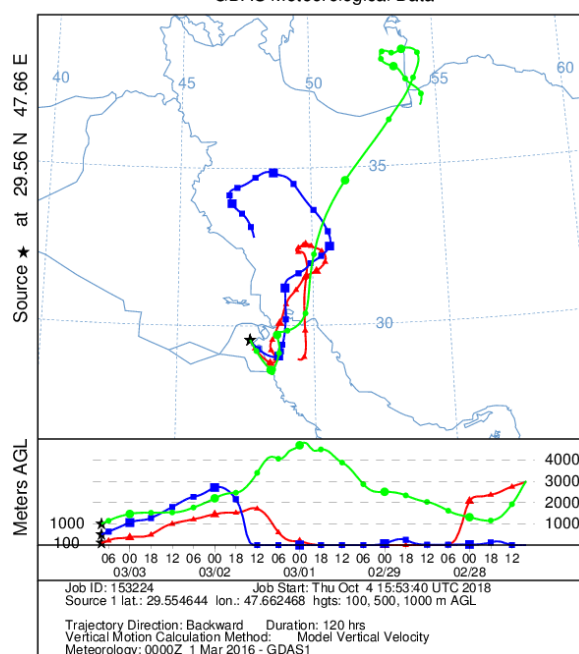
NOAA HYSPLIT MODEL
Backward trajectories ending at 1100 UTC 11 Feb 16
GDAS Meteorological Data



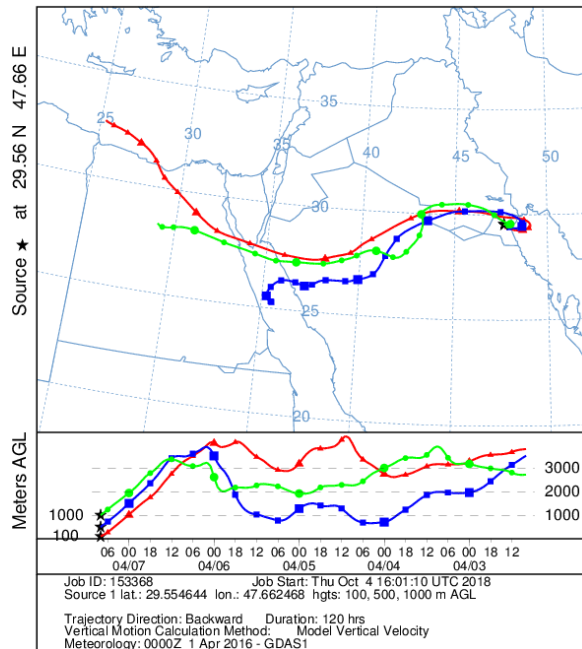
NOAA HYSPLIT MODEL
Backward trajectories ending at 1100 UTC 18 Feb 16
GDAS Meteorological Data



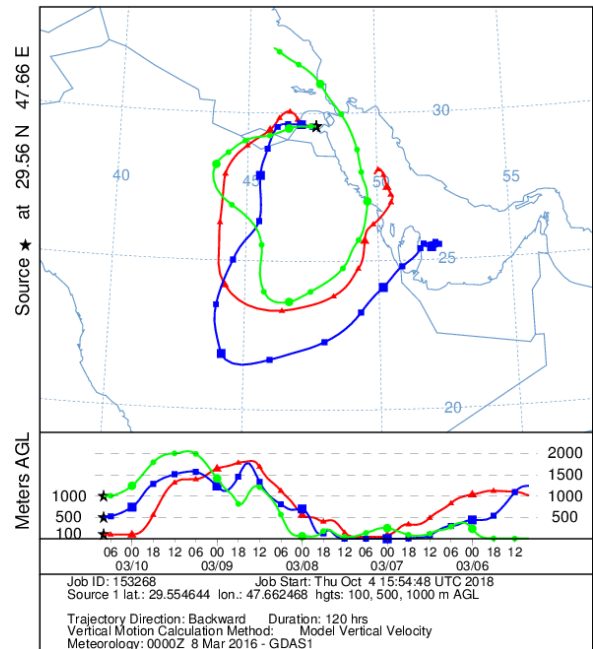
NOAA HYSPLIT MODEL
Backward trajectories ending at 0800 UTC 03 Mar 16
GDAS Meteorological Data



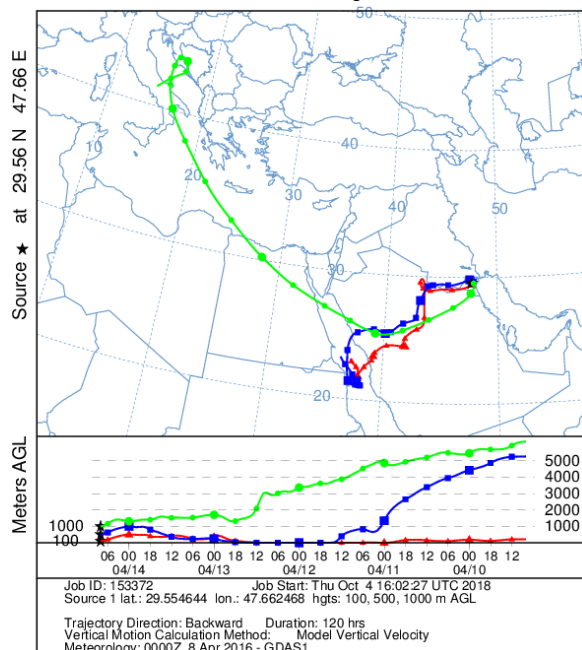
NOAA HYSPLIT MODEL
Backward trajectories ending at 0800 UTC 07 Apr 16
GDAS Meteorological Data



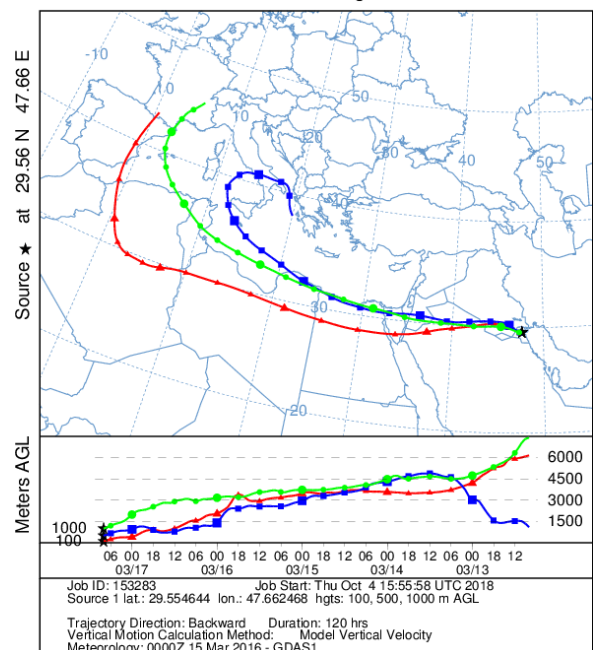
NOAA HYSPLIT MODEL
Backward trajectories ending at 0800 UTC 10 Mar 16
GDAS Meteorological Data



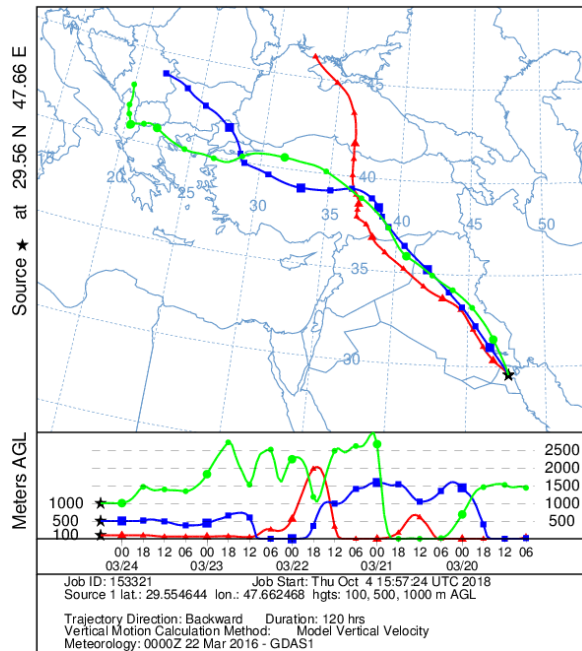
NOAA HYSPLIT MODEL
Backward trajectories ending at 0800 UTC 14 Apr 16
GDAS Meteorological Data



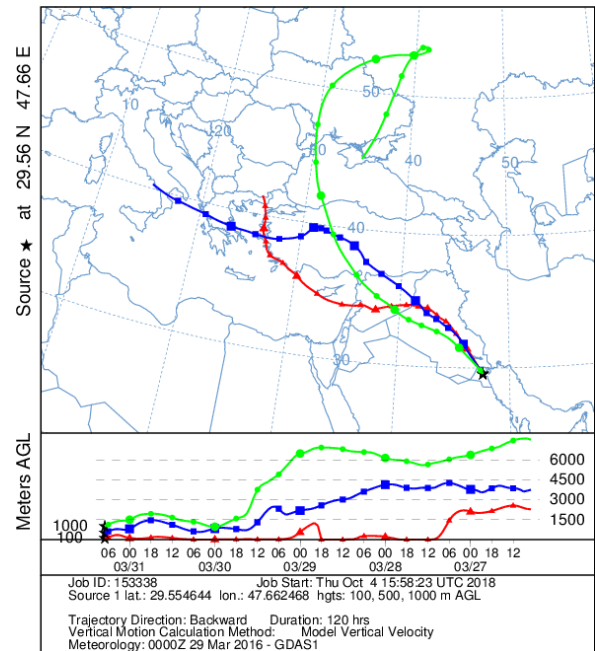
NOAA HYSPLIT MODEL
Backward trajectories ending at 0800 UTC 17 Mar 16
GDAS Meteorological Data



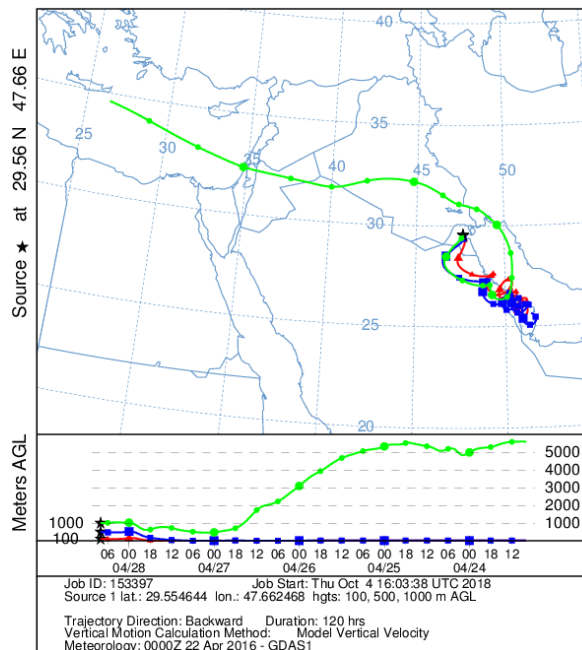
NOAA HYSPLIT MODEL
Backward trajectories ending at 0600 UTC 24 Mar 16
GDAS Meteorological Data



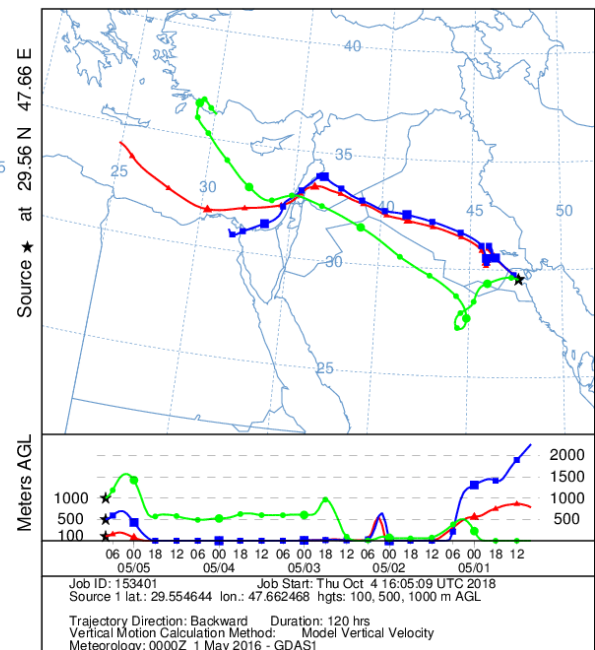
NOAA HYSPLIT MODEL
Backward trajectories ending at 0700 UTC 31 Mar 16
GDAS Meteorological Data



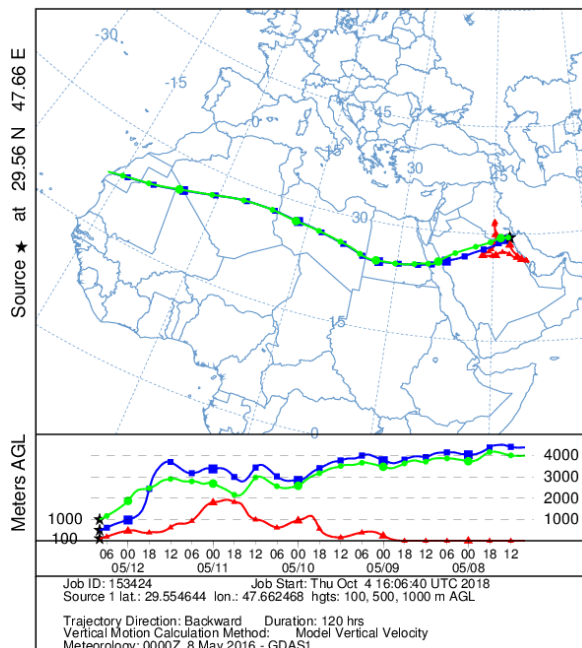
NOAA HYSPLIT MODEL
Backward trajectories ending at 0800 UTC 28 Apr 16
GDAS Meteorological Data



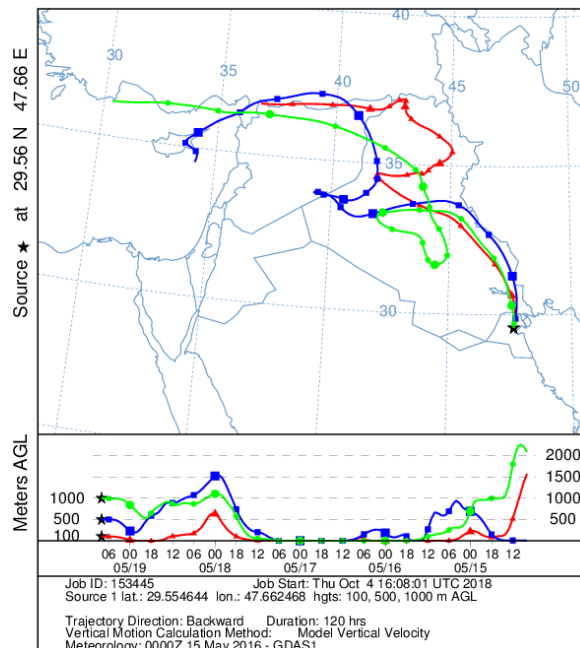
NOAA HYSPLIT MODEL
Backward trajectories ending at 0800 UTC 05 May 16
GDAS Meteorological Data



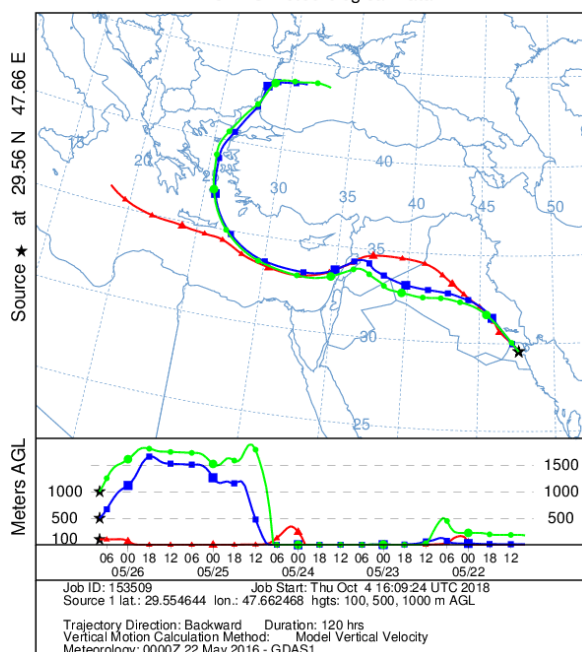
NOAA HYSPLIT MODEL
Backward trajectories ending at 0800 UTC 12 May 16
GDAS Meteorological Data



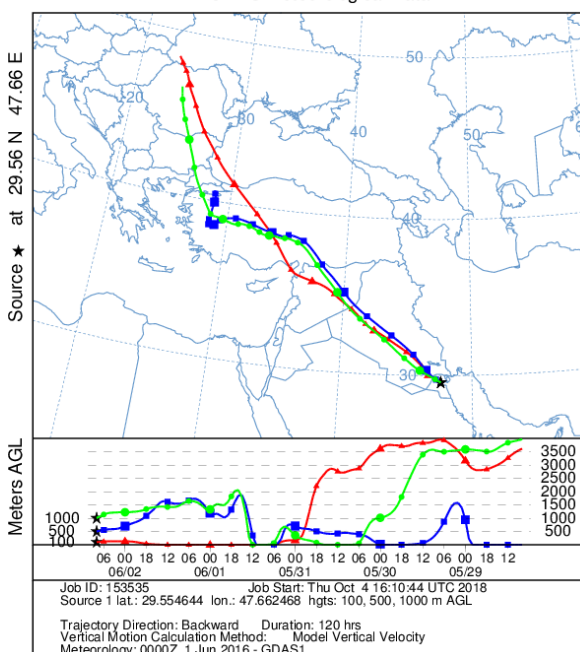
NOAA HYSPLIT MODEL
Backward trajectories ending at 0800 UTC 19 May 16
GDAS Meteorological Data



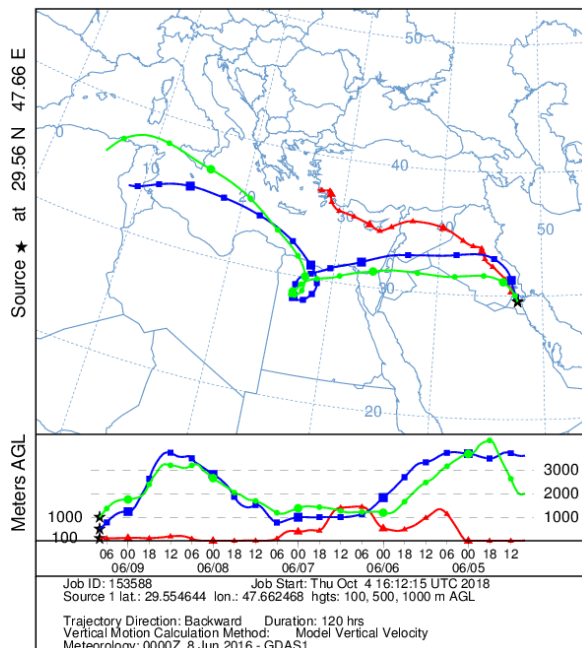
NOAA HYSPLIT MODEL
Backward trajectories ending at 0800 UTC 26 May 16
GDAS Meteorological Data



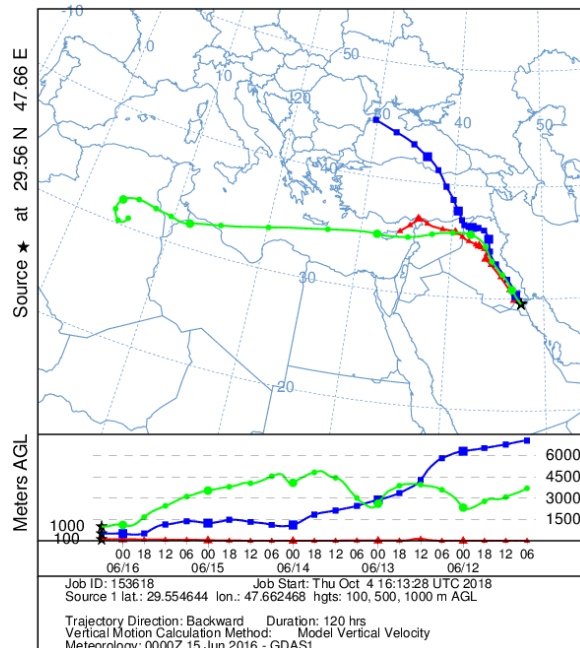
NOAA HYSPLIT MODEL
Backward trajectories ending at 0800 UTC 02 Jun 16
GDAS Meteorological Data



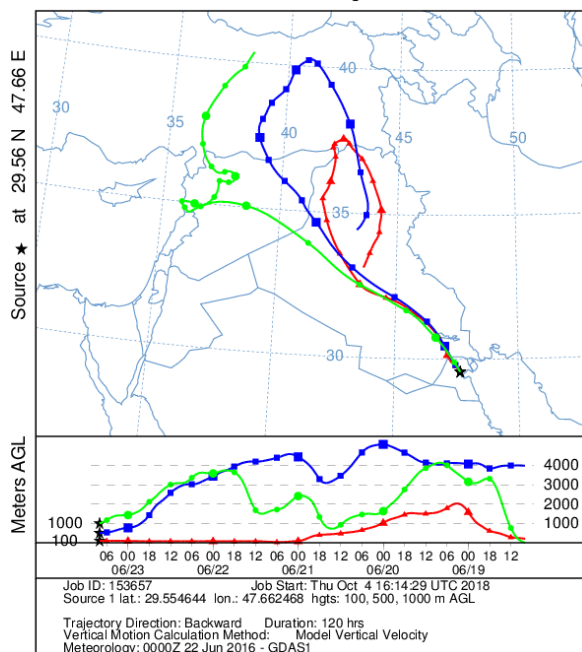
NOAA HYSPLIT MODEL
Backward trajectories ending at 0800 UTC 09 Jun 16
GDAS Meteorological Data



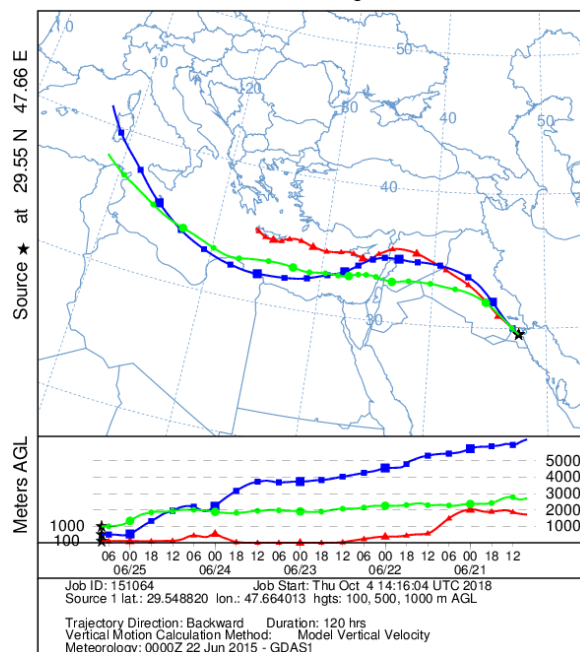
NOAA HYSPLIT MODEL
Backward trajectories ending at 0600 UTC 16 Jun 16
GDAS Meteorological Data



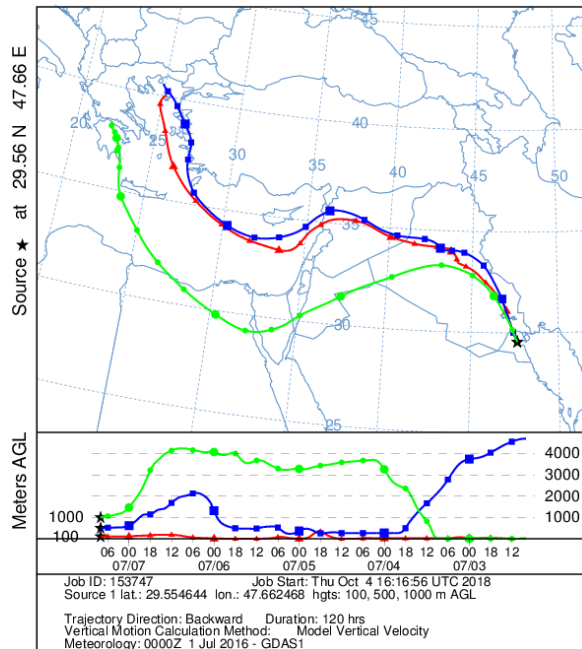
NOAA HYSPLIT MODEL
Backward trajectories ending at 0800 UTC 23 Jun 16
GDAS Meteorological Data



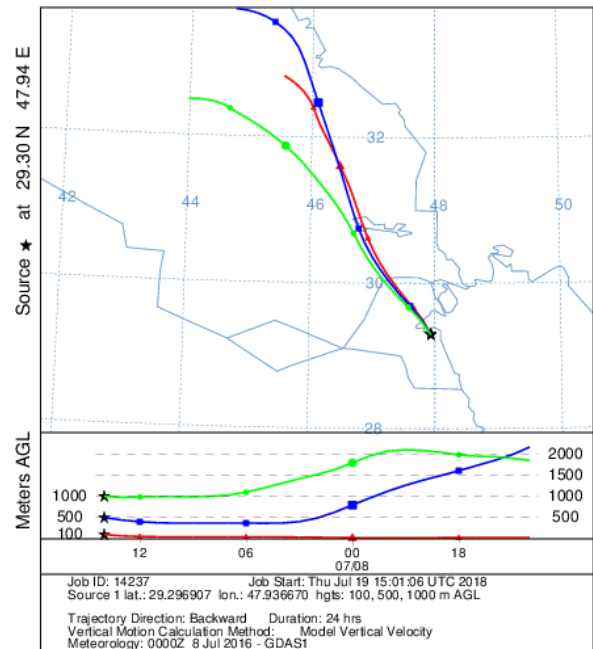
NOAA HYSPLIT MODEL
Backward trajectories ending at 0800 UTC 25 Jun 15
GDAS Meteorological Data



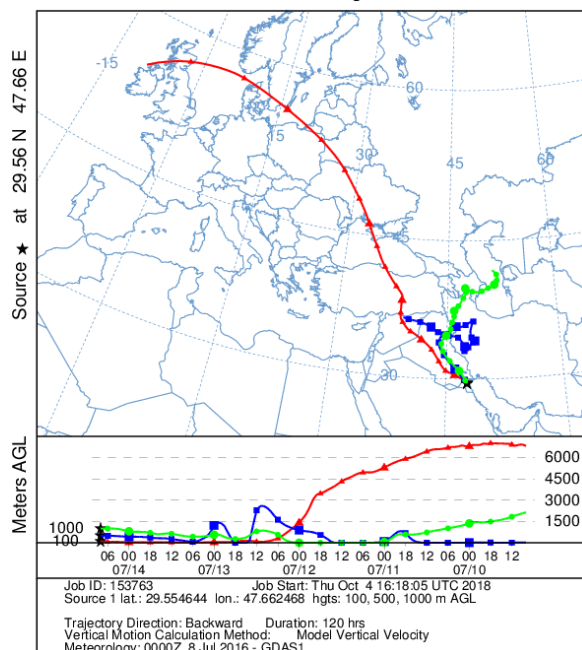
NOAA HYSPLIT MODEL
Backward trajectories ending at 0800 UTC 07 Jul 16
GDAS Meteorological Data



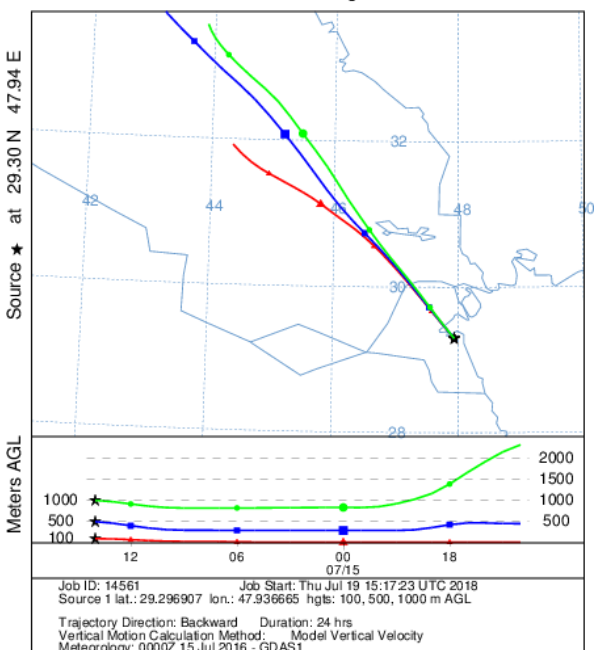
NOAA HYSPLIT MODEL
Backward trajectories ending at 1400 UTC 08 Jul 16
GDAS Meteorological Data



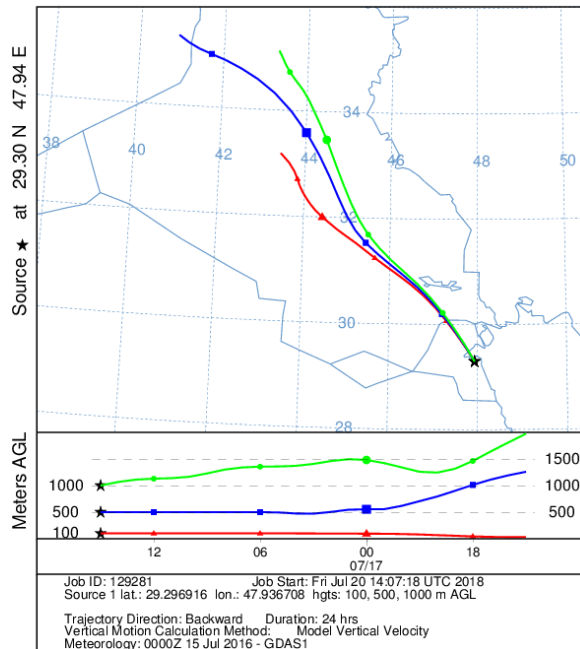
NOAA HYSPLIT MODEL
Backward trajectories ending at 0800 UTC 14 Jul 16
GDAS Meteorological Data



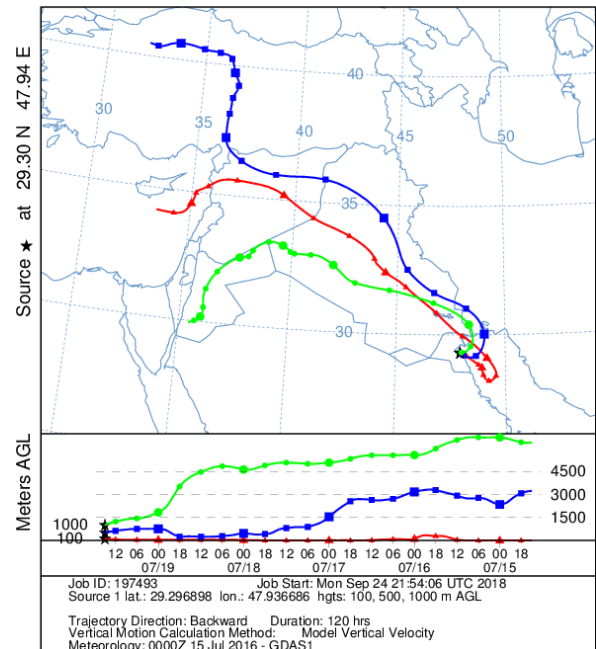
NOAA HYSPLIT MODEL
Backward trajectories ending at 1400 UTC 15 Jul 16
GDAS Meteorological Data



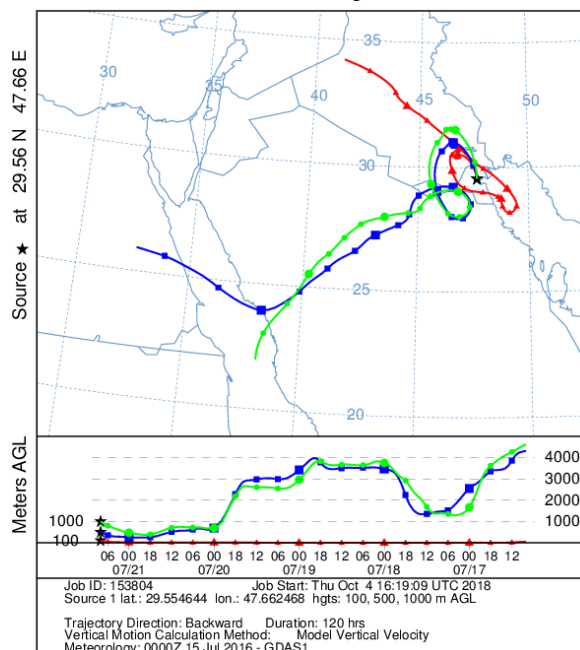
NOAA HYSPLIT MODEL
Backward trajectories ending at 1500 UTC 17 Jul 16
GDAS Meteorological Data



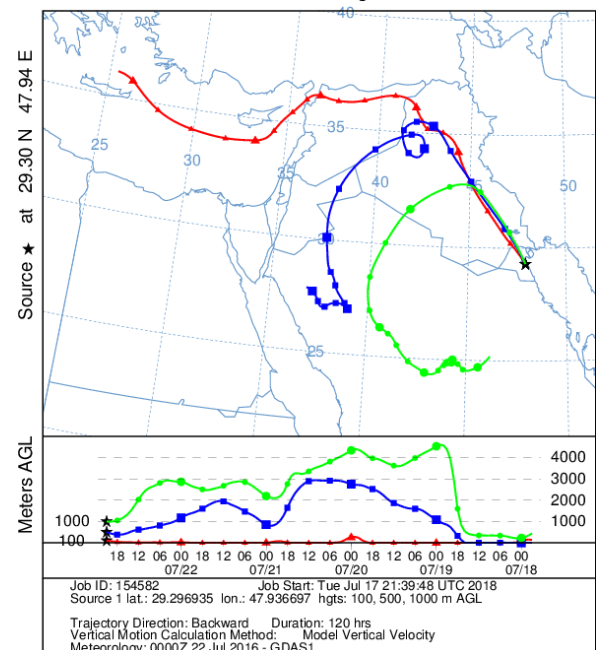
NOAA HYSPLIT MODEL
Backward trajectories ending at 1500 UTC 19 Jul 16
GDAS Meteorological Data



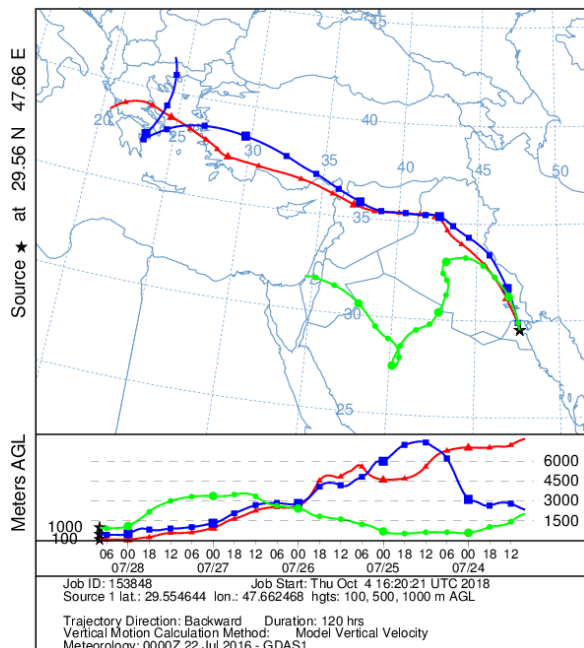
NOAA HYSPLIT MODEL
Backward trajectories ending at 0800 UTC 21 Jul 16
GDAS Meteorological Data



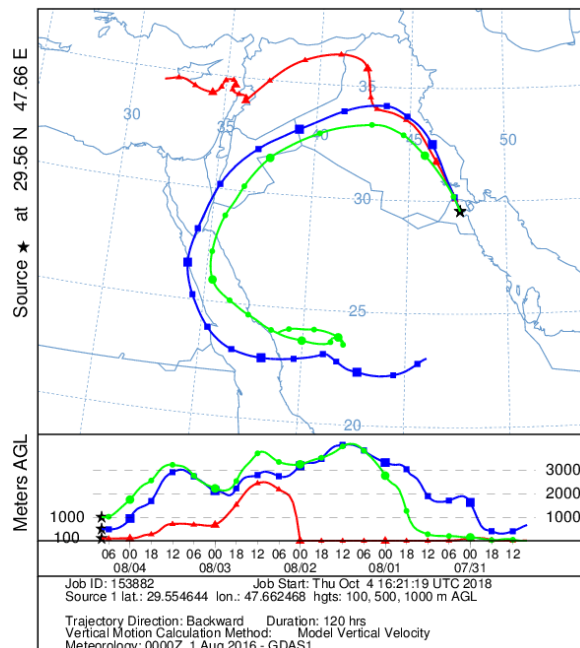
NOAA HYSPLIT MODEL
Backward trajectories ending at 2100 UTC 22 Jul 16
GDAS Meteorological Data



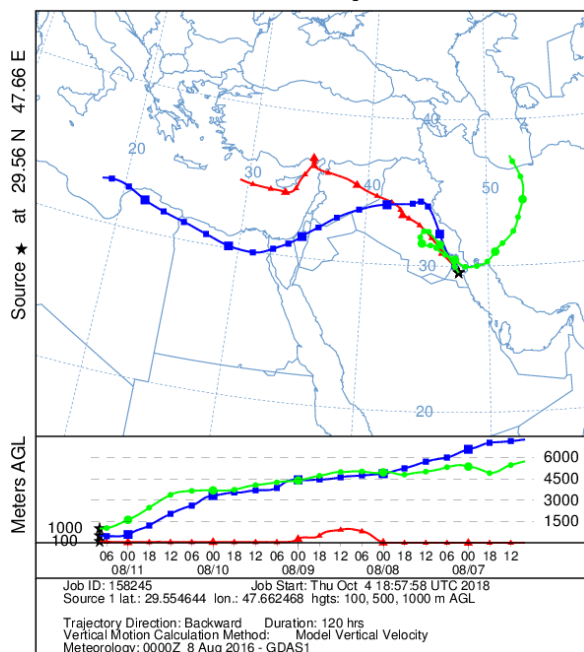
NOAA HYSPLIT MODEL
Backward trajectories ending at 0800 UTC 28 Jul 16
GDAS Meteorological Data



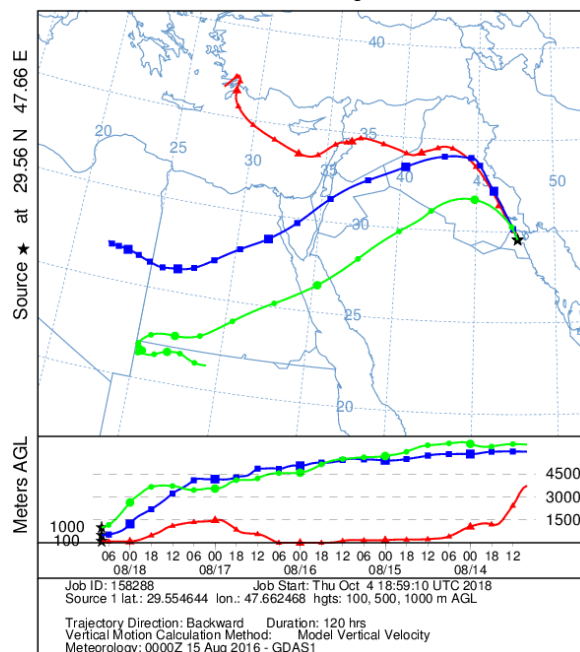
NOAA HYSPLIT MODEL
Backward trajectories ending at 0800 UTC 04 Aug 16
GDAS Meteorological Data



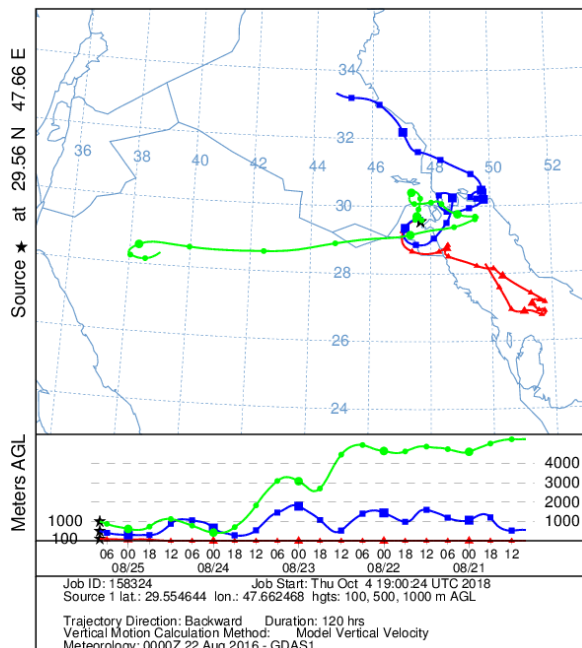
NOAA HYSPLIT MODEL
Backward trajectories ending at 0800 UTC 11 Aug 16
GDAS Meteorological Data



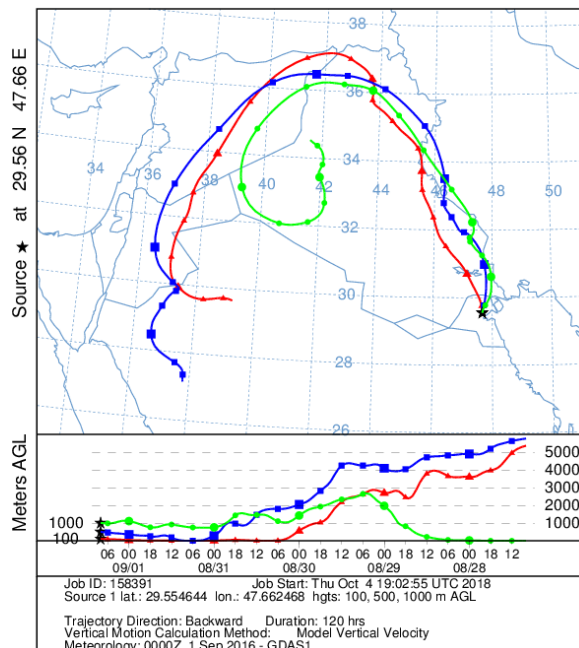
NOAA HYSPLIT MODEL
Backward trajectories ending at 0800 UTC 18 Aug 16
GDAS Meteorological Data



NOAA HYSPLIT MODEL
Backward trajectories ending at 0800 UTC 25 Aug 16
GDAS Meteorological Data

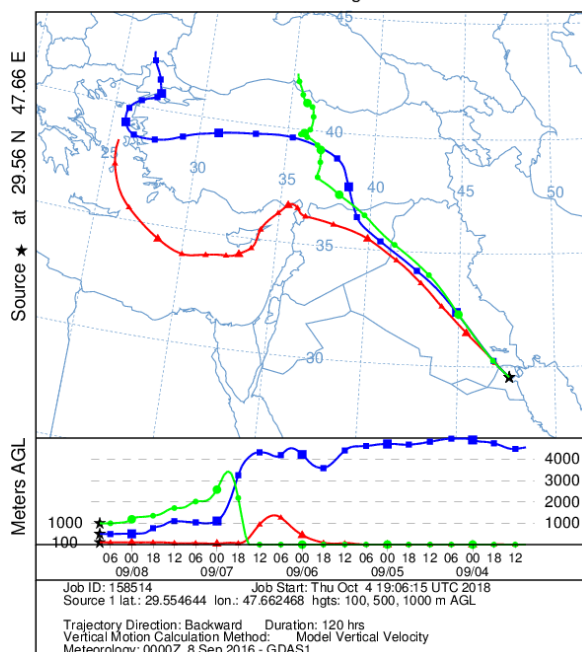


NOAA HYSPLIT MODEL
Backward trajectories ending at 0800 UTC 01 Sep 16
GDAS Meteorological Data

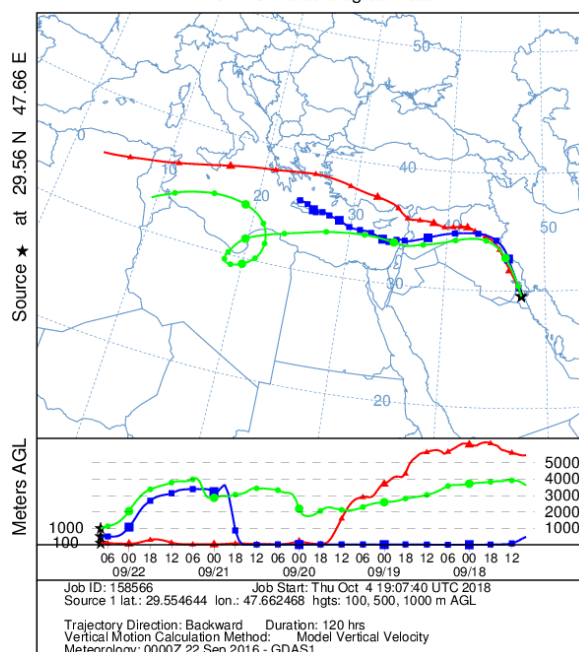


4

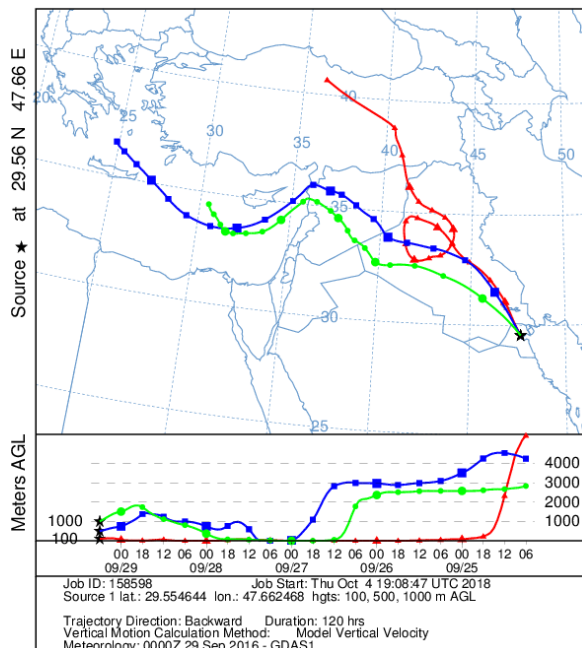
NOAA HYSPLIT MODEL
Backward trajectories ending at 0900 UTC 08 Sep 16
GDAS Meteorological Data



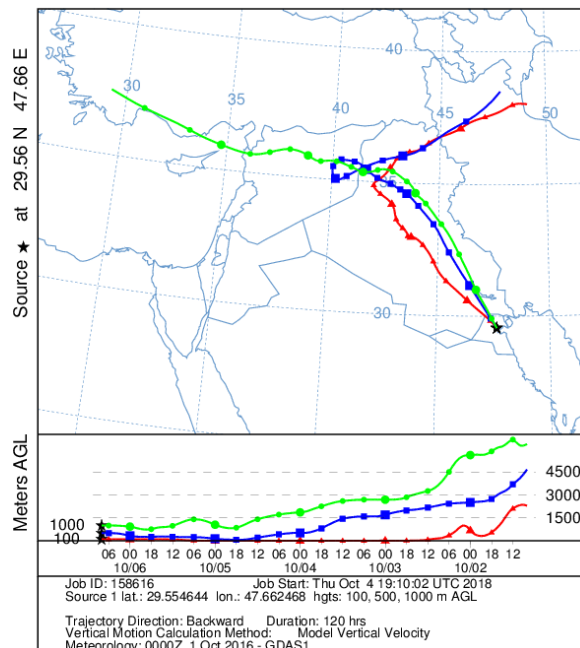
NOAA HYSPLIT MODEL
Backward trajectories ending at 0800 UTC 22 Sep 16
GDAS Meteorological Data



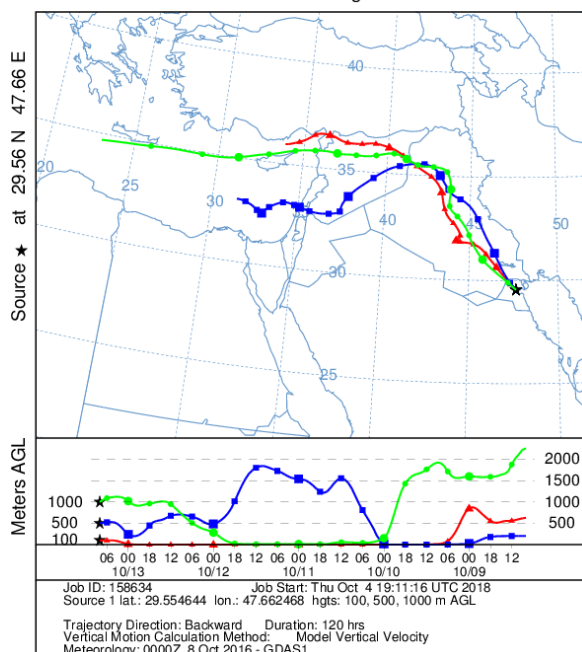
NOAA HYSPLIT MODEL
Backward trajectories ending at 0600 UTC 29 Sep 16
GDAS Meteorological Data



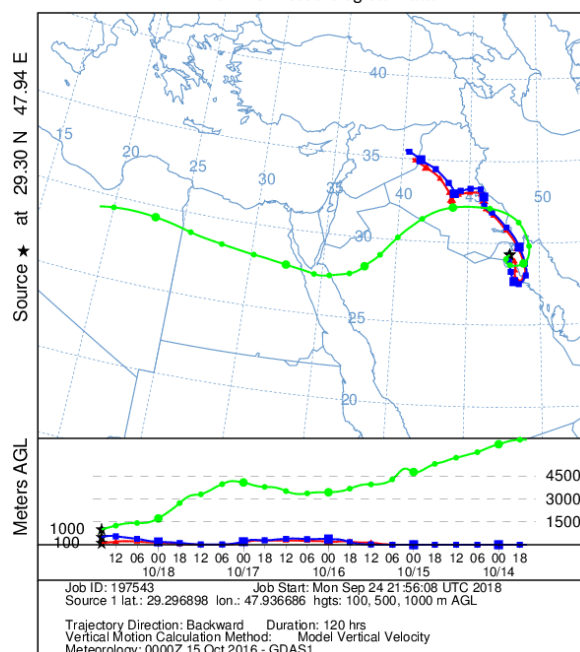
NOAA HYSPLIT MODEL
Backward trajectories ending at 0800 UTC 06 Oct 16
GDAS Meteorological Data



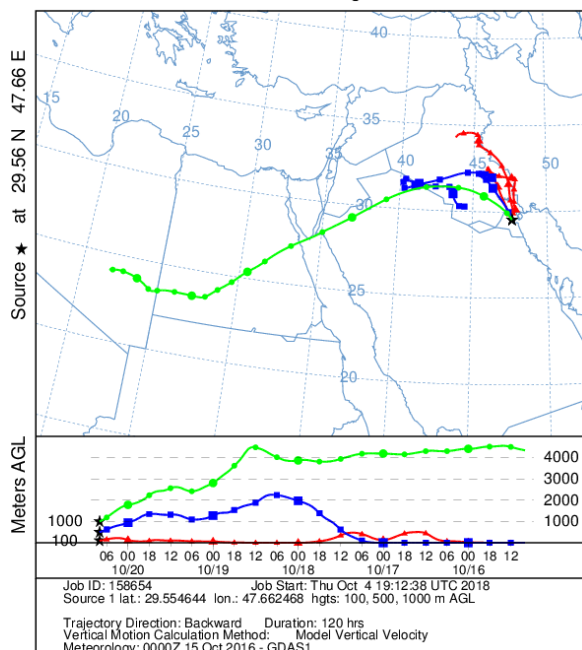
NOAA HYSPLIT MODEL
Backward trajectories ending at 0800 UTC 13 Oct 16
GDAS Meteorological Data



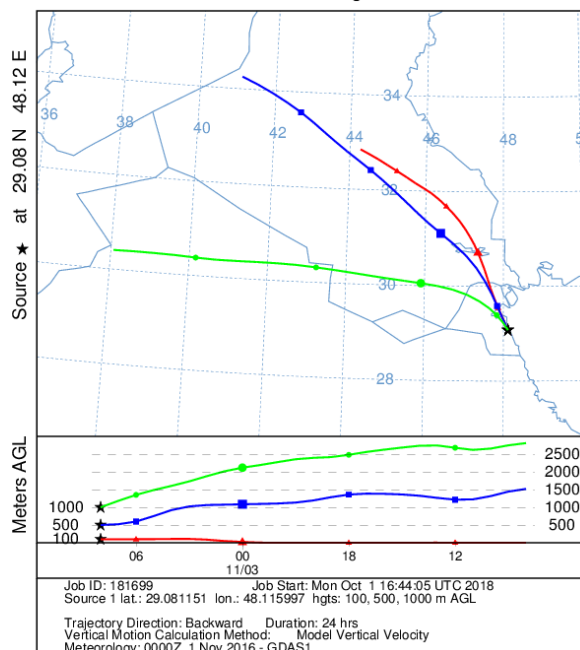
NOAA HYSPLIT MODEL
Backward trajectories ending at 1600 UTC 18 Oct 16
GDAS Meteorological Data



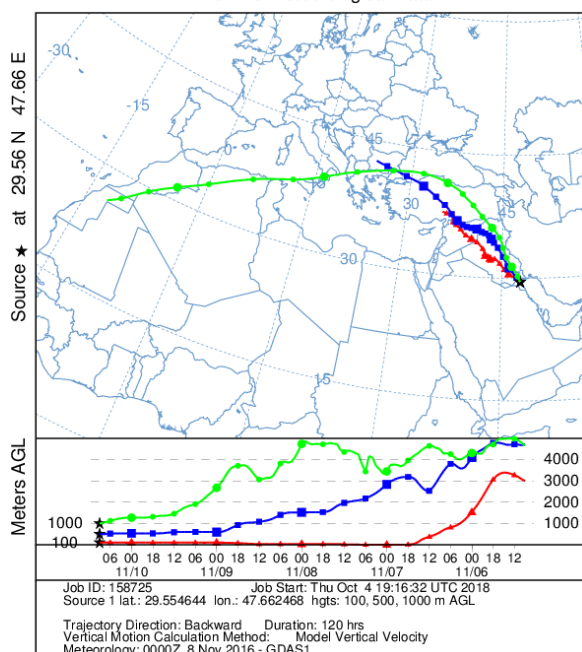
NOAA HYSPLIT MODEL
Backward trajectories ending at 0800 UTC 20 Oct 16
GDAS Meteorological Data



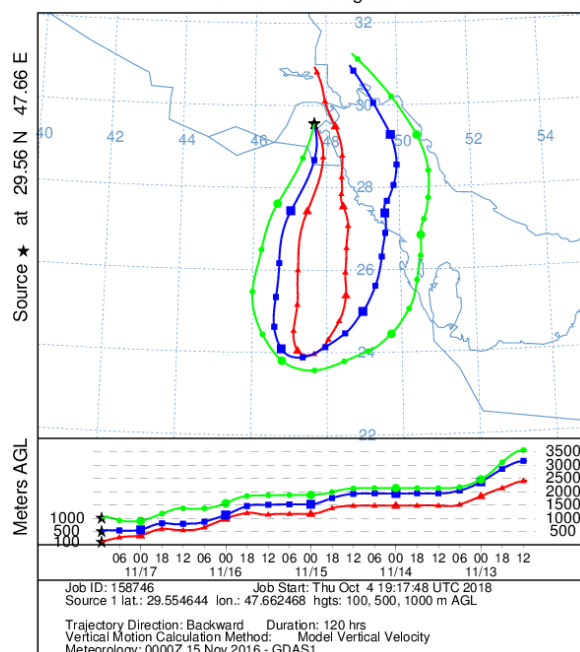
NOAA HYSPLIT MODEL
Backward trajectories ending at 0800 UTC 03 Nov 16
GDAS Meteorological Data



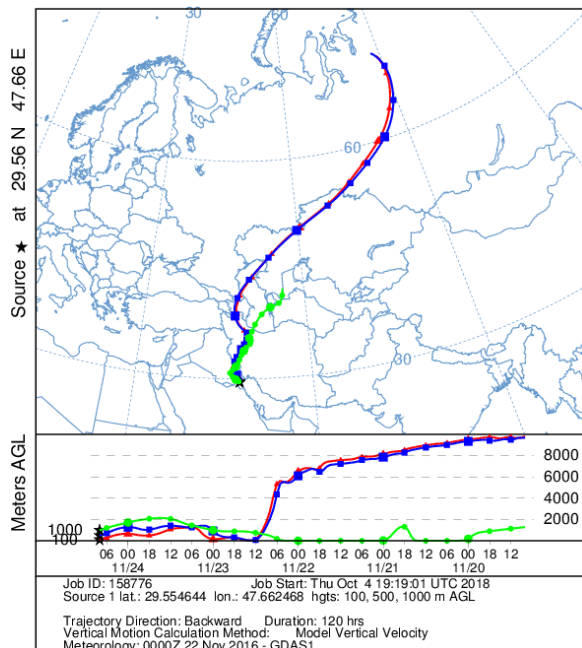
NOAA HYSPLIT MODEL
Backward trajectories ending at 0900 UTC 10 Nov 16
GDAS Meteorological Data



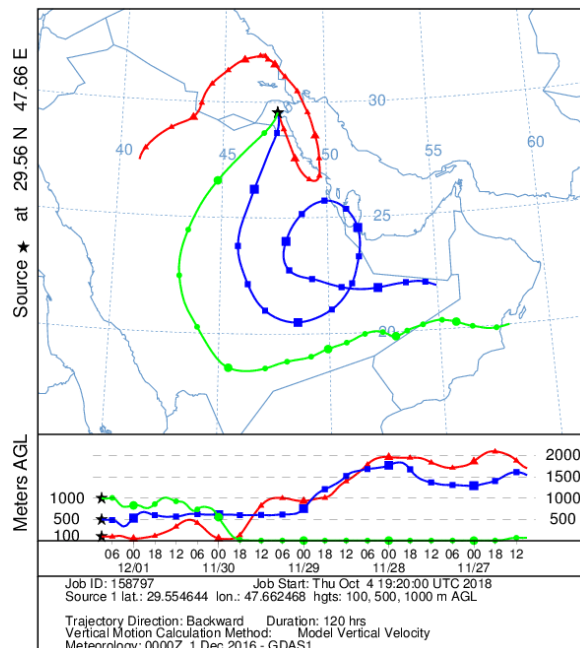
NOAA HYSPLIT MODEL
Backward trajectories ending at 1100 UTC 17 Nov 16
GDAS Meteorological Data



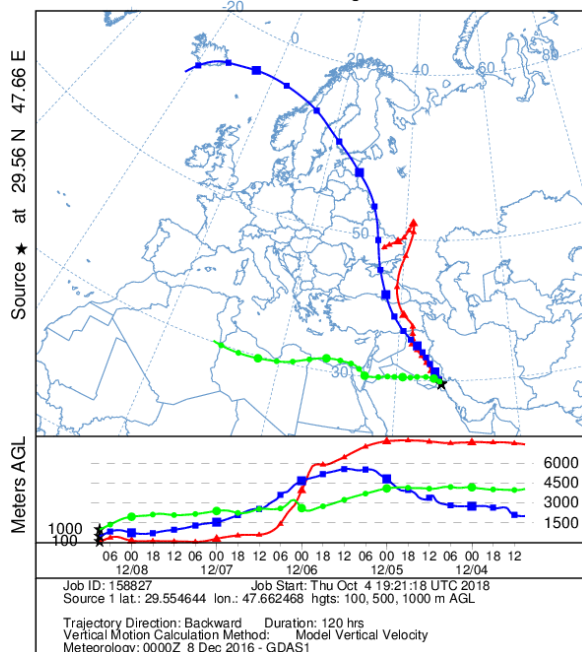
NOAA HYSPLIT MODEL
Backward trajectories ending at 0800 UTC 24 Nov 16
GDAS Meteorological Data



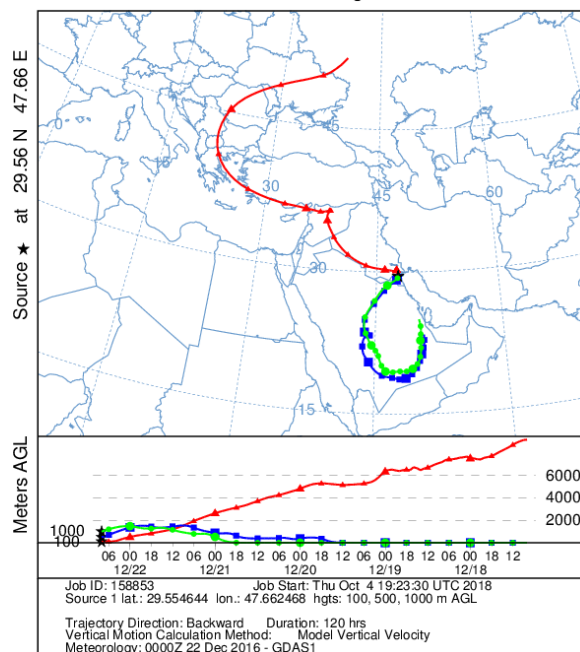
NOAA HYSPLIT MODEL
Backward trajectories ending at 0900 UTC 01 Dec 16
GDAS Meteorological Data



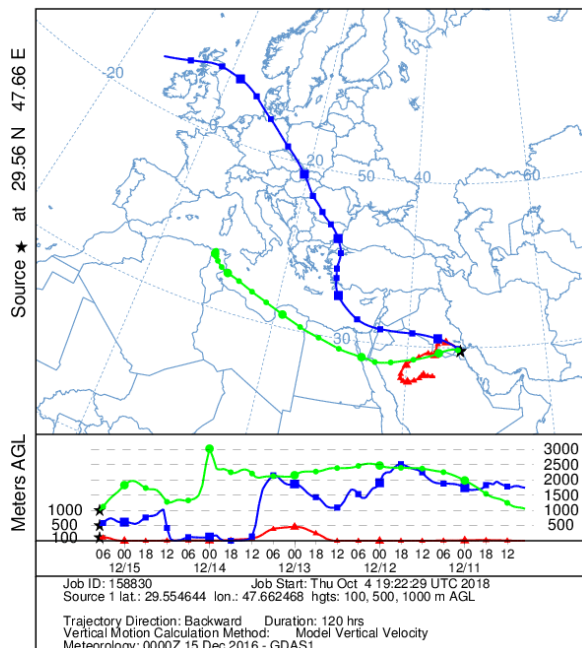
NOAA HYSPLIT MODEL
Backward trajectories ending at 0900 UTC 08 Dec 16
GDAS Meteorological Data



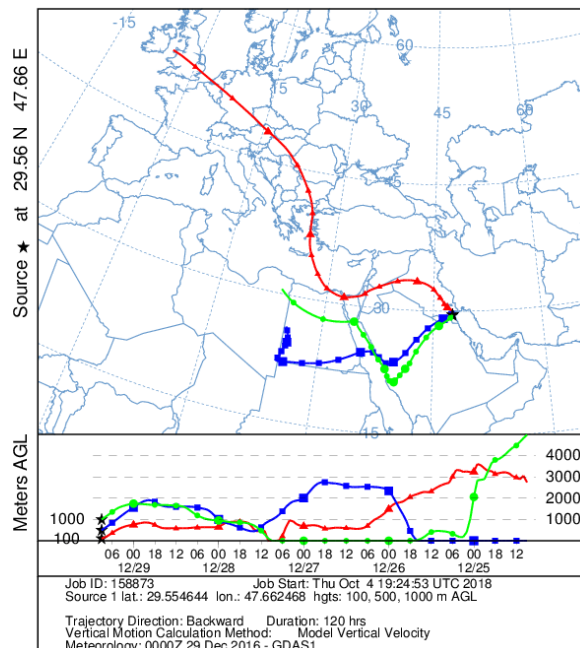
NOAA HYSPLIT MODEL
Backward trajectories ending at 0800 UTC 22 Dec 16
GDAS Meteorological Data



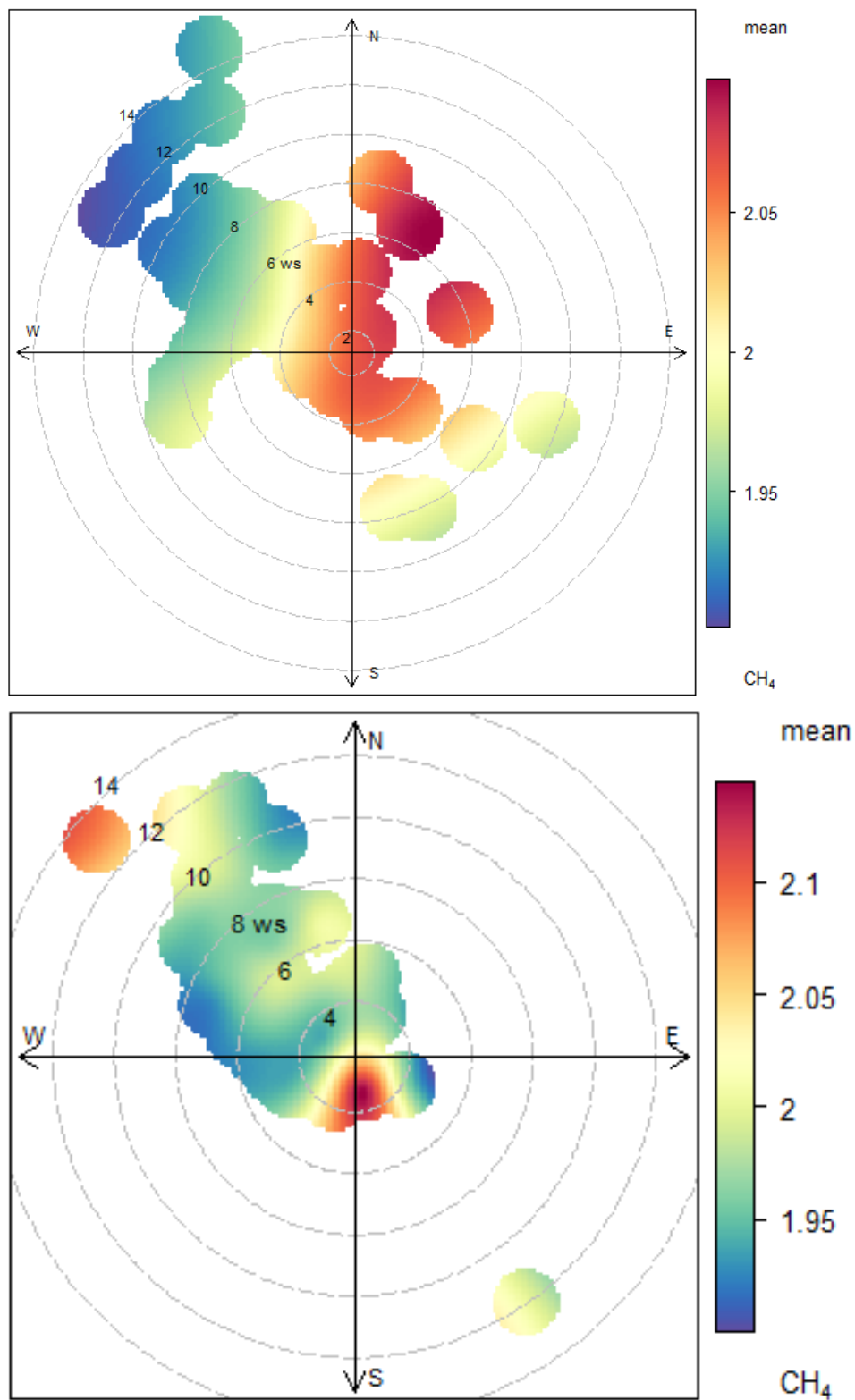
NOAA HYSPLIT MODEL
Backward trajectories ending at 0700 UTC 15 Dec 16
GDAS Meteorological Data



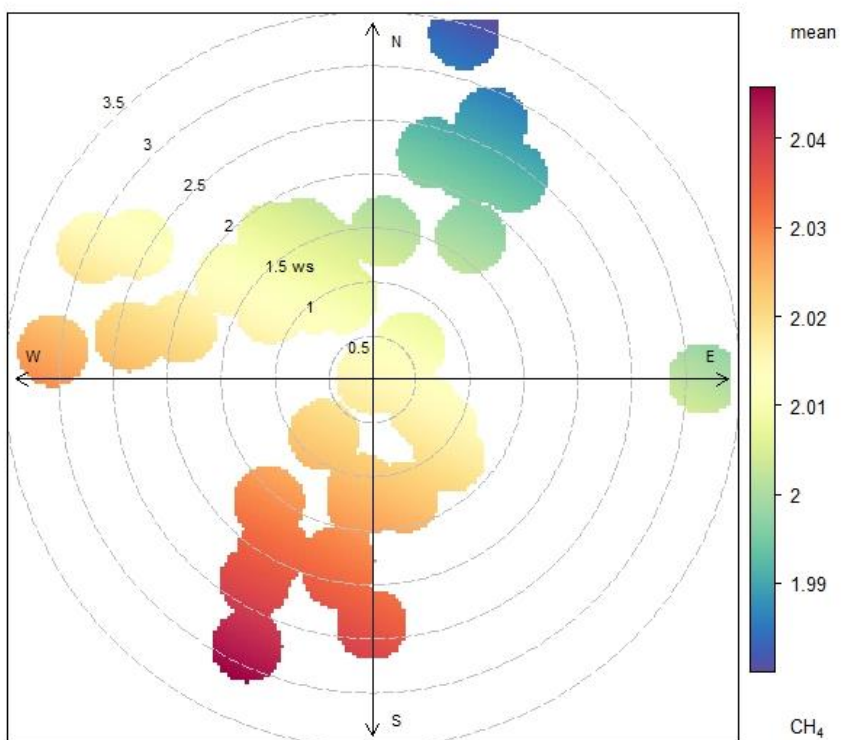
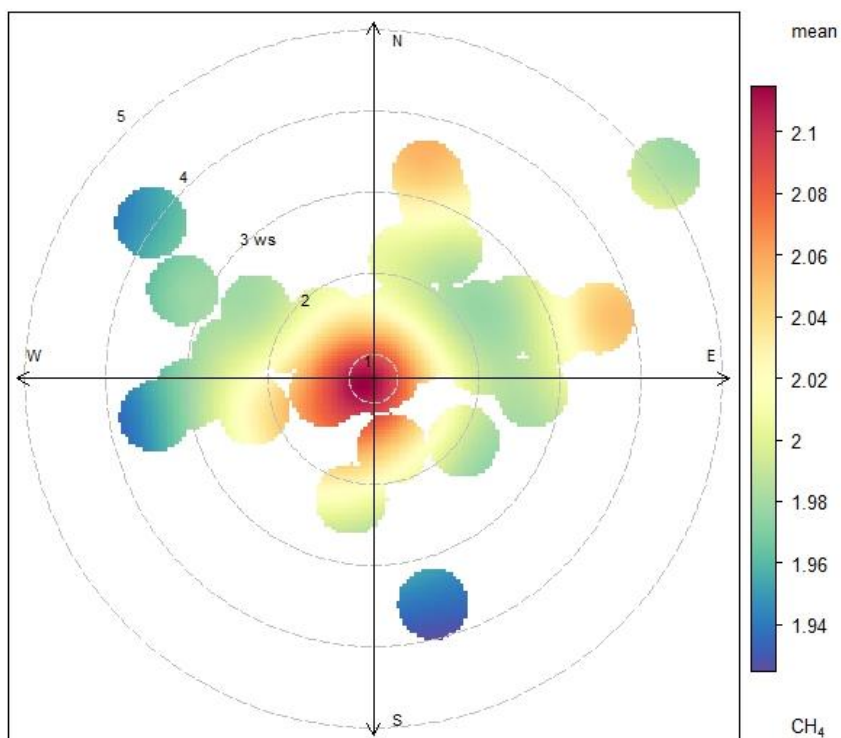
NOAA HYSPLIT MODEL
Backward trajectories ending at 0900 UTC 29 Dec 16
GDAS Meteorological Data



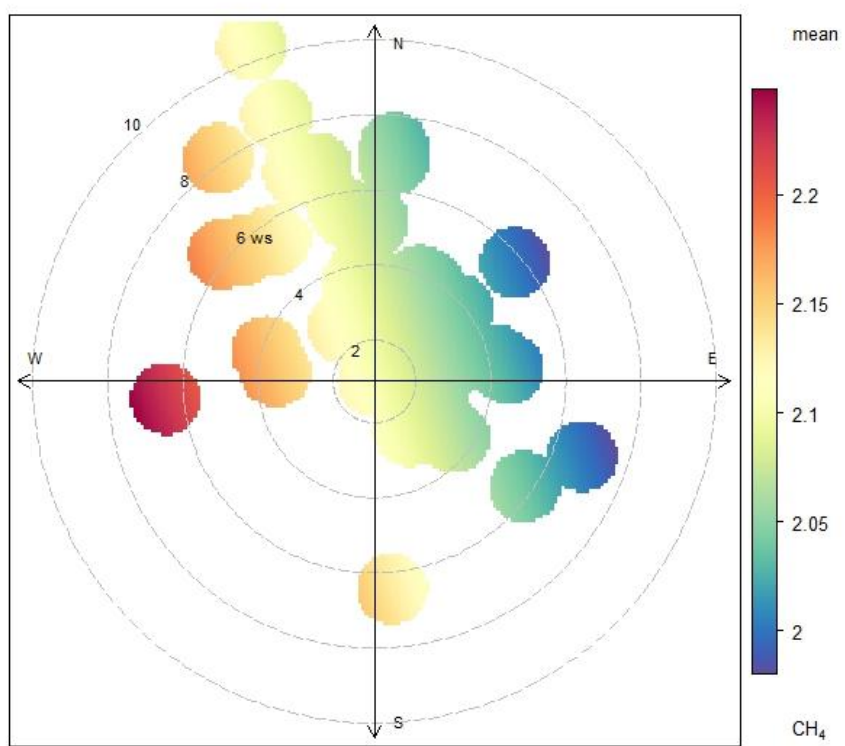
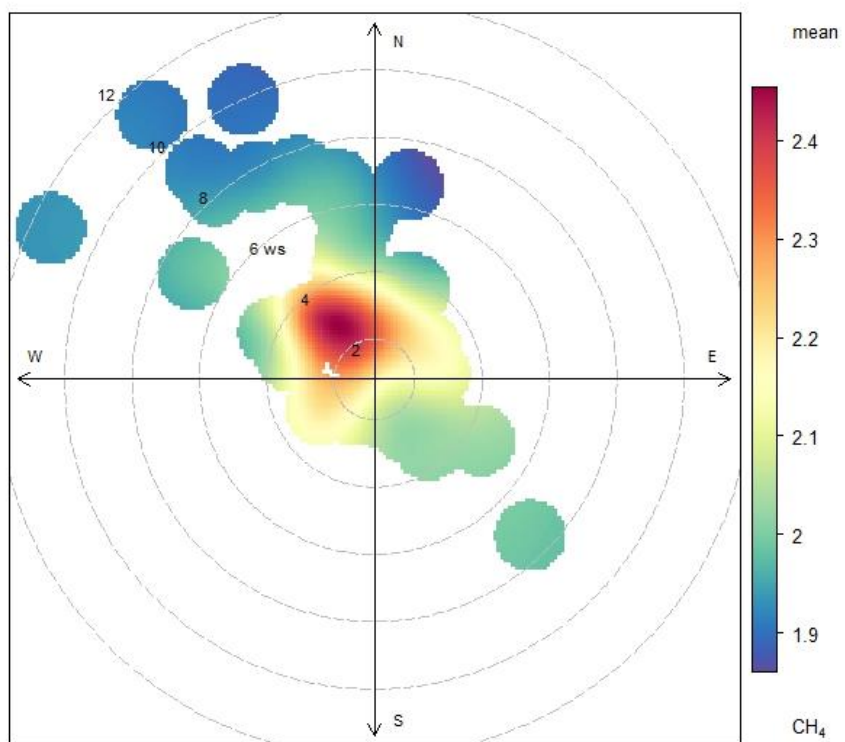
Appendix 2: Methane mole fraction (ppm) for the three sites of long-term measurements in Kuwait for the period 2015 and 2016.



Al-Mutla site: methane mole fraction (ppm) measurements 2015 (Top) 2016 (Bottom).



Khaldiya site: methane mole fraction (ppm) measurements 2015 (Top) 2016 (Bottom).



Fahaheel site: methane mole fraction (ppm) measurements 2015 (Top) 2016 (Bottom).